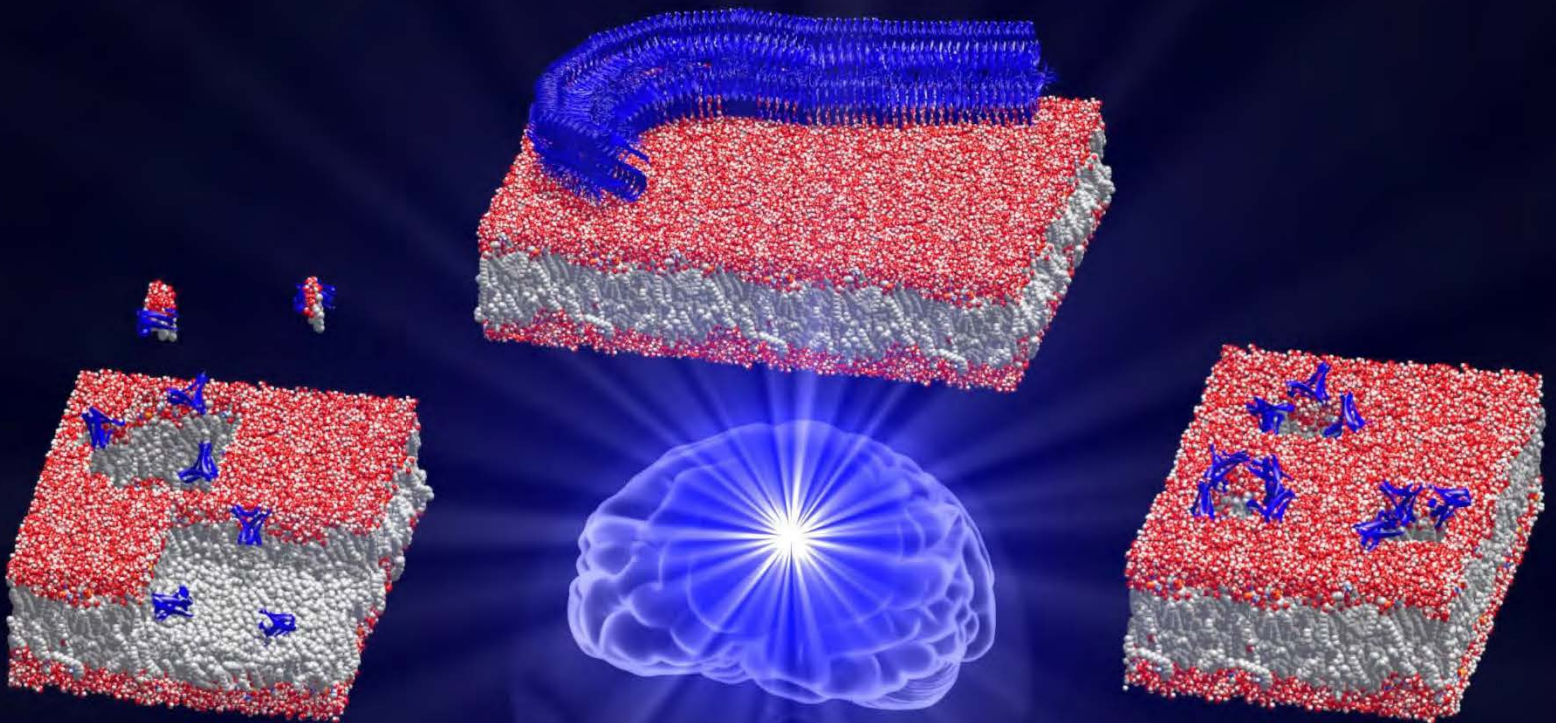


Ph.D. thesis

Amyloid β interaction with model cell membranes – insight into the mechanism of the Alzheimer's disease etiology and a novel therapeutic approach

Dusan Mrdenovic



Ph.D. thesis

**Amyloid β interaction with model cell membranes
– insight into the mechanism of the Alzheimer's disease etiology
and a novel therapeutic approach**

Dusan Mrdenovic

Supervisors: Prof. Włodzimierz Kutner

Auxiliary supervisor: Dr. Piotr Pieta

The present thesis was prepared within the International Doctoral Studies in Chemistry at the Institute of Physical Chemistry of the Polish Academy of Sciences in the Molecular Films Research group in collaboration with the group of Prof. Jacek Lipkowski at the University of Guelph.



Biblioteka Instytutu Chemii Fizycznej PAN

F-B.526/21



80000000342007

A-21-7, K-5-161, K-6-219, K-7-137
Warsaw, December 2020

To my family



B. 526/21

Acknowledgments

The road to my Ph.D. was the most challenging and most rewarding experience in my life. I entered that journey without knowing what amyloids, lipids, atomic force microscopy, or infrared spectroscopy are. Now, I am happy to write the first page of my doctoral thesis, describing the knowledge I gained during my Ph.D. study. I owe this knowledge to many supportive people I was lucky to work with, and I would like to express my gratitude to them.

First, I would like to thank Piotr for the endless effort in supervising me. I am grateful for the fruitful discussions and knowledge that he shared. Importantly, I am thankful for his understanding, advice, and support regarding personal matters as well. His open, kind, and friendly attitude created a delightful atmosphere that allowed for open and effective communication, one of the key ingredients for my success. Moreover, I would like to thank Prof. W. Kutner for many significant inputs and guidance that shaped me into a better writer, better thinker, and better scientist. I will always appreciate his advice on dealing with various scientific duties, ranging from the very basic up to those more advanced. My eternal gratitude goes to Jacek for, first of all, introducing me to this opportunity. I am indebted to him for sharing his tremendous expertise and providing an enjoyable and productive working environment. Many of his personal stories taught me about both the private and professional side of scientist life. These will serve me as a guide in the future. I would like to thank Prof. R. Nowakowski for many useful discussions concerning my research. I am grateful for the time and effort he spent to counsel and help me with my professional future. Importantly, I am thankful for the many coffees and enjoyable stories that he shared in the office every day.

I would like to thank Marta for the enormous patience and help that I needed (especially at the beginning of my Ph.D. study) with various tasks, ranging from sample preparation, AFM imaging to administrative paperwork. I am grateful to Zhangfei for teaching me electrochemistry and spectroscopy. Moreover, I appreciate the help he provided regarding personal matters during my stay in Canada. Many thanks go to colleagues of the Molecular Films research group - Piyush, Jarek, Maciej, Zofia, Kuba, Patrycja, Kamila, Jyoti, Nabila, Vicky, and others, but also other colleagues from the Institute of Physical Chemistry – Iza, Agnieszka (M.-N.), Klaudyna, Agnieszka (L.-G.). I am grateful for the many coffees, beers, parties, and stories that we enjoyed together.

Finally, most immense gratitude goes to the people that were always there for me – my family. I am grateful to my grandparents for the love, care and for being a role model for many life aspects. I am forever thankful to my sister, mother, and father, who raised me and shaped me into the man I am today. Their selfless patience, compassion, love, and guidance helped me to go forward in life. My eternal gratitude goes to my wife Nevena for the support, understanding, and love I have been receiving from the moment I met her. I always like to remember when she introduced me to science and helped me reveal my passion for it. I am most grateful to her for being my life companion and an infinite source of energy and happiness.

Declaration of originality

I hereby declare that the research included within this thesis was carried out by myself or with support by others included in acknowledgments.


I state that I have exercised care to ensure that the work is original and contains no previously published material or written by another person, except where citations have been made in the text. To the best of my knowledge, the content provided here does not violate any copyrights.

I accept that the Polish Academy of Sciences has the right to use plagiarism detection software to ensure the thesis's legitimacy.

I certify that no part of my thesis has been or will be submitted for obtaining a degree or diploma by the Institute of Physical Chemistry, Polish Academy of Science, or any other educational institution.

This thesis's copyright rests with the author, and no information derived from it may be published without the author's consent.

Warsaw, 13.12.2020.

A handwritten signature in blue ink, appearing to read 'L. M. Kozłowski', is written above a horizontal dotted line.

(signature)

Funding

The present research was financed by

- the European Union Horizon 2020 Research and Innovation Programme under the Marie Skłodowska-Curie grant agreement no. 711859 and the Polish Ministry of Science and Higher Education for implementing an international co-financed project in the years 2017–2021.
- the Polish National Science Centre, grant no. OPUS12 2016/23/B/ST4/02791



Horizon 2020
European Union Funding
for Research & Innovation



NATIONAL SCIENCE CENTRE
POLAND



Ministry of Science
and Higher Education

Republic of Poland

List of publications

Publications included in the thesis:

1. **Mrdenovic, D.**; Majewska, M.; Pieta, I. S.; Bernatowicz, P.; Nowakowski, R.; Kutner, W.; Lipkowski, J.; Pieta, P. Size-Dependent Interaction of Amyloid β Oligomers with Brain Total Lipid Extract Bilayer—Fibrillation Versus Membrane Destruction. *Langmuir* 2019, 35 (36), 11940–11949.
2. **Mrdenovic, D.**; Su, Z.; Kutner, W.; Lipkowski, J.; Pieta, P. Alzheimer's Disease-Related Amyloid β Peptide Causes Structural Disordering of Lipids and Changes the Electric Properties of a Floating Bilayer Lipid Membrane. *Nanoscale Adv.* 2020, 2 (8), 3467–3480.
3. **Mrdenovic, D.**; Zarzycki, P.; Majewska, M.; Pieta, I. S.; Nowakowski, R.; Kutner, W.; Lipkowski, J.; Pieta, P. Inhibition of amyloid β -induced lipid membrane permeation and amyloid β aggregation by K162. 2020, submitted.
4. **Mrdenovic, D.**; Lipkowski, J.; Pieta, P. Analyzing properties of early-stage toxic amyloid β oligomers by atomic force microscopy. 2020, submitted.
5. **Mrdenovic, D.**; Pieta, I. S.; Nowakowski, R.; Kutner, W.; Lipkowski, J.; Pieta, P. Amyloid β interaction with model cell membranes – what are the toxicity-defining properties of amyloid β ? 2020, submitted.

Other publications:

1. Majewska, M.; **Mrdenovic, D.**; Pieta, I. S.; Nowakowski, R.; Pieta, P. Nanomechanical Characterization of Single Phospholipid Bilayer in Ripple Phase with PF-QNM AFM. *Biochim. Biophys. Acta - Biomembr.* 2020, 1862 (9), 183347.
2. Su, Z.; **Mrdenovic, D.**; Sek, S.; Lipkowski, J. Ionophore Properties of Valinomycin in the Model Bilayer Lipid Membrane 1. Selectivity towards a Cation. *J. Solid State Electrochem.* 2020, 24 (11–12), 3125–3134.
3. Pieta, I. S.; Kadam, R. G.; Pieta, P.; **Mrdenovic, D.**; Nowakowski, R.; Bakandritsos, A.; Tomanec, O.; Petr, M.; Otyepka, M.; Kostecki, R.; Khan, M. A. M.; Zboril, R.; Gawande M. B. The Hallmarks of Copper Single-Atom Catalysts in Direct Alcohol Fuel Cells and Electrochemical CO₂ fixation. 2020, submitted.

Conference presentations

1. 12-2018, the 10th Workshop on Applications of Scanning Probe Microscopy – STM/AFM in Zakopane (Poland), oral contribution, **Dusan Mrdenovic**, Robert Nowakowski, and Piotr Pieta, "The mechanism of amyloid β and total brain lipid extract interaction".
2. 06-2019, 102nd Canadian Chemistry Conference and Exhibition in Quebec City (Canada), oral contribution, **Dusan Mrdenovic**, Marta Majewska, Izabela Pieta, Robert Nowakowski, Wlodzimierz Kutner, Jacek Lipkowski, and Piotr Pieta, "Oligomer size-dependent interaction of amyloid β with a model cell membrane – mechanisms relevant to understand origins of Alzheimer disease".
3. 06-2019, 2nd Annual ECS Guelph young researcher symposium in Guelph (Canada), oral contribution, **Dusan Mrdenovic**, Marta Majewska, Izabela Pieta, Robert Nowakowski, Wlodzimierz Kutner, Jacek Lipkowski, and Piotr Pieta, "Oligomer size-dependent interaction of amyloid β with a model cell membrane – mechanisms relevant to understand origins of Alzheimer disease".

List of abbreviations

2D-COS – two-dimensional correlation spectroscopy

AD – Alzheimer's disease

AFM – atomic force microscopy

APP – amyloid precursor protein

A β – amyloid β

A β ₄₀ – 40-amino acids-long form of A β

A β ₄₀F – A β ₄₀ fibril

A β ₄₀M – A β ₄₀ monomer

A β ₄₀O – A β ₄₀ oligomer

A β ₄₂ – 42-amino acids-long form of A β

A β ₄₂F – A β ₄₂ fibril

A β ₄₂M – A β ₄₂ monomer

A β ₄₂O – A β ₄₂ oligomer

A β F – A β fibril

A β M – A β monomer

A β O – A β oligomer

BLM – bilayer lipid membrane

BTLE – brain total lipid extract

C – cell

CD – circular dichroism

CE – counter electrode

Chol – cholesterol

CSF – cerebrospinal fluid

D – detector

DC – differential capacitance

DEPE – 1,2-dielaidoyl-*sn*-glycero-3-phosphoethanolamine

DHPC – 1,2-dihexanoyl-*sn*-glycero-3-phosphocholine
DLPC – 1,2-dilauroyl-*sn*-glycero-3-phosphocholine
DLS – dynamic light scattering
DMPC – 1,2-dimyristoyl-*sn*-glycero-3-phosphocholine
DMPE – 1,2-dimyristoyl-*sn*-glycero-3-phosphoethanolamine
DMSO – dimethyl sulfoxide
DOPC – 1,2-dioleoyl-*sn*-glycero-3-phosphocholine
DOPE – 1,2-dioleoyl-*sn*-glycero-3-phosphoethanolamine
DOPG – 1,2-dioleoyl-*sn*-glycero-3-phospho-(1'-*rac*-glycerol)
DOPS – 1,2-dioleoyl-*sn*-glycero-3-phospho-L-serine
DOTAP – 1,2-dioleoyl-3-trimethylammonium-propane
DPC – dodecylphosphocholine
DPPC – 1,2-dipalmitoyl-*sn*-glycero-3-phosphocholine
DPPG – 1,2-dipalmitoyl-*sn*-glycero-3-phospho-(1'-*rac*-glycerol)
DSPE – 1,2-Distearoyl-*sn*-glycero-3-phosphoethanolamine
EIS – electrochemical impedance spectroscopy
ETD – effective tip diameter
F – optical filter
fBLM – floating bilayer lipid membrane
FD curve – force-distance curve
FM – flat mirror
FRET – Förster resonance energy transfer assay
FSD – Fourier self-deconvolution
GD1a – ganglioside GD1a
GD1b – ganglioside GD1b
GM1 – monosialotetrahexosylganglioside
GM2 – monosialoganglioside GM2

GM3 – monosialodihexosylganglioside
GPI – glycosylphosphatidylinositol
GT – glass tube
GT1b – ganglioside GT1b
hBLM – hybrid bilayer lipid membrane
HFIP – 1,1,1,3,3,3-hexafluoro-2-propanol
HMW – high-molecular-weight
IR – infrared
IRRAS – infrared reflection-absorption spectroscopy
L – lens
LMW – low-molecular-weight
LPC – lysophosphatidylcholine
LS – large size
LUV – large unilamellar vesicle
MA β – mutant A β ₄₂
MA β M – mutant A β ₄₂ monomer
MA β O – mutant A β ₄₂ oligomer
MCI – mild cognitive impairment
MD – molecular dynamics
OG – octyl glucoside
OW – optical window
PBS – phosphate buffer saline
PC – phosphatidylcholine
PE – phosphatidylethanolamine
PEM – photoelastic modulator
PF-QNM – peak force quantitative nanomechanical mapping
PH – piston handle

PM – parabolic mirror
PM-IRRAS – polarization-modulation IR reflection-absorption spectroscopy
POPC – 1-palmitoyl-2-oleoyl-*sn*-glycero-3-phosphocholine
POPE –1-palmitoyl-2-oleoyl-*sn*-glycero-3-phosphoethanolamine
POPS –1-palmitoyl-2-oleoyl-*sn*-glycero-3-phospho-L-serine
PS – phosphatidylserine
P-to-L – peptide-to-lipid
RE – reference electrode
SAM – self-assembled monolayer
SCE – saturated calomel electrode
SD – second derivative
SM – sphingomyelin
SP – static polarizer
SS – small size
SSD – synchronous sampling demodulator
SUV – small unilamellar vesicle
tBLM – tethered bilayer lipid membranes
TF – Teflon flange
TFA – trifluoroacetic acid
TH – Teflon holder
ThT – thioflavin T
TP – Teflon piston
W – gold wire
WE – working electrode
YM – Young's modulus

$\langle E^2 \rangle$ – mean square electric field of the photon, $V\ m^{-1}$

\vec{E} – electric field vector of incident IR light
 Δi – current amplitude, A
 ΔU – voltage amplitude, V
 A – intensity of the absorption band (absorbance)
 A_{exp} – intensity of the absorption band from the PM-IRRAS experiment
 A_{sim} – intensity of the absorption band from the PM-IRRAS simulation
 C – capacitance, F
 C_{H} – Helmholtz layer capacitance, F
 C_{m} – membrane capacitance, F
 C_{mH} – capacitance of the membrane and Helmholtz layer, F
 CPE_{m} – membrane constant phase element
 CPE_{mH} – constant phase element of the membrane and Helmholtz layer
 C_{pseudo} – pseudocapacitance, F
 C_{true} – true capacitance, F
 d – distance between the charged surfaces, m
 d_{sp} – thickness of the spacer region, m
 E – applied potential, V
 E_{pzfc} – potential of zero free charge, V
 f_{min} – frequency at the minimum of the phase angle vs. frequency curve, Hz
 h – indentation depth, m
 I – incident IR light
 I_0 – transmitted IR light
 j – complex unit
 N_{def} – defect density, m⁻²
 P – applied load, N
 Q – constant phase element coefficient
 Q_{m} – membrane capacitance, F

Q_{sp} – spacer layer capacitance, F
 R – sample radius, m
 r_0 – defect radius, m
 R_i – indenter radius, m
 R_m – membrane resistance, Ω
 R_p – p-polarized light reflectivity
 R_{sol} – solution resistance, Ω
 R_s – s-polarized light reflectivity
 T – transmittance
 Z – impedance, Ω
 Z_{CPE} – impedance of the constant phase element, Ω
 Z_{def} – defect impedance, Ω
 Z'_m – impedance associated with the membrane capacitance, Ω
 Z_{sp} – spacer region impedance, Ω
 Z_{tot} – total impedance, Ω

Γ – Gibbs surface excess, mol m⁻²
 γ – half-width at the band half maximum, m⁻²
 δ – defect occupancy radius, m
 $\delta(\text{CH}_2)$ – methylene scissoring vibration
 ε – electric permittivity of insulating membrane hydrocarbons
 ε_0 – electric permittivity of free space, F m⁻¹
 η – Poisson's ratio
 θ – the angle between two vectors, °
 $\theta_{C=O}$ – C=O bond angle against the surface normal, °
 θ_{chains} – tilt angle of the lipid acyl chain against the surface normal, °
 $\vec{\mu}$ – transition dipole moment vector

$|\mu|^2$ – square of the absolute value of the transition dipole moment, C m

$\nu(\text{CH}_2)_{\text{as}}$ – asymmetric methylene stretching vibration

$\nu(\text{CH}_2)_{\text{s}}$ – symmetric methylene stretching vibration

ν – frequency (wavenumber), Hz

ξ – molar extinction coefficient, $\text{M}^{-1} \text{m}^{-1}$

ρ_{sp} – specific resistance of the spacer region, Ω

σ_{M} – charge of the metal electrode, C

$\Phi(\nu_1, \nu_2)$ – synchronous component of the 2D correlation intensity

ϕ_{min} – phase angle at the minimum of the phase angle vs. frequency curve, $^\circ$

$\Psi(\nu_1, \nu_2)$ – asynchronous component of the 2D correlation intensity

ω – cyclic frequency, rad s^{-1}

Abstract

Aggregation of misfolded proteins, named amyloids, is associated with more than fifty so-called protein misfolding diseases. Alzheimer's disease (AD) is related to the amyloid β ($A\beta$) aggregation and aggregates' deposition in the patients' brains. Despite many research efforts, $A\beta$ properties and behavior are not entirely understood. Moreover, mechanistic links between $A\beta$ and AD etiology is unclear. Consequently, AD remains incurable. For this reason, more than 46 million people worldwide suffer from AD, and it is estimated that this number will increase to 131.5 million by 2050. Therefore, AD is a global health problem that requires more research effort to be solved.

The amyloid cascade hypothesis attempts to connect $A\beta$ with AD development. This hypothesis suggests that $A\beta$ over-production, aggregation, and accumulation in the human brain triggers a cascade of molecular and cellular events leading to progressive neurodegeneration. $A\beta$ can form various kinds of aggregates, including different $A\beta$ oligomers ($A\beta$ Os) and $A\beta$ fibrils ($A\beta$ Fs). Initially, $A\beta$ Fs were the main subject of research studies. However, the latest research showed that both $A\beta$ monomers ($A\beta$ M) and $A\beta$ Fs are not toxic, while $A\beta$ Os demonstrate high toxicity. $A\beta$ Os cause various kinds of toxicity, and one of them is cell membrane permeation. However, the cell membrane can also catalyze $A\beta$ aggregation, thus surviving the presence of some $A\beta$ forms. Unfortunately, $A\beta$ Os are polymorphic and metastable, representing the major challenge in distinguishing between different $A\beta$ O behavior and toxicity.

The present dissertation's main objective is to decipher the mechanism of membrane permeation by $A\beta$ Os and identify the kind of $A\beta$ Os that causes this toxicity. Atomic force microscopy (AFM) imaging was used to monitor $A\beta$ aggregation and distinguish between different types of $A\beta$ aggregates produced. The formed $A\beta$ Os are classified into small size (SS) and large size (LS) $A\beta$ Os based on their size. LS $A\beta$ Os fibrillate on the membrane surface without compromising the membrane integrity. In contrast, SS $A\beta$ Os permeate the membrane via a mechanism that consists of both pore formation and lipid extraction. First, SS $A\beta$ Os form pores in the membrane. These pores expand with time, and then, SS $A\beta$ Os insert into the membrane through these pores, thus clogging the pores. Being inside the membrane, SS $A\beta$ Os extract the membrane lipids either by simultaneous extraction of lipids from both membrane leaflets or by sequential extraction of lipids from the outer and then from the inner membrane leaflet. Interestingly, although SS and LS $A\beta$ Os interact with the membrane differently, they both reduce the membrane Young's modulus by $\sim 45\%$.

The second part of the research consists of expanding the knowledge of $A\beta$ O-lipid interaction by studying it with electrochemical and IR spectroscopic techniques. Moreover, the interaction of non-toxic $A\beta$ M with lipid membrane was studied as a control measurement. Electrochemical techniques showed that the membrane electrical properties change significantly only in the presence of $A\beta$ Os. That is a consequence of membrane permeation by $A\beta$ Os. Polarization-modulation infrared reflection-absorption spectroscopy (PM-IRRAS) showed that both $A\beta$ M and

A β O β s disorder membrane lipids. Both A β forms interact with the membrane hydrophobic core, i.e., lipid acyl chains, causing changes in these chains' conformation and orientation. However, these changes are more pronounced in the presence of A β O β s. Interestingly, A β M β s and A β O β s interact with lipid heads differently. A β M β s dehydrate lipid heads but do not affect their orientation. In contrast, A β O β s do not change the lipid head hydration levels but significantly affect their orientation. Two-dimensional correlation spectroscopy (2D-COS) showed that structural changes in lipids precede those in A β . Moreover, it showed a sequential change of the A β secondary structure in line with the A β aggregation mechanism.

The final part of the research elucidates inhibition of A β O β toxicity by a fluorene-based active drug candidate, named K162. It was previously reported that K162 is an effective A β toxicity inhibitor *in vivo*. However, the mechanism of this inhibition was not revealed. Our electrochemical impedance spectroscopy (EIS) investigations showed that K162 prevents membrane permeation by A β O β s. These findings were confirmed by AFM, which showed no membrane pores in the K162 presence, typically formed by A β O β s in the K162 absence. AFM and molecular dynamics (MD) simulations were employed to study A β aggregation in the K162 presence to gain insight into K162-A β interaction. MD simulations showed that the aggregation of K162-bound A β is energetically very costly, thus unfavorable. However, AFM results showed that A β aggregates in the K162 presence. Apparently, K162 also aggregates itself, and not all K162 molecules bind to A β . Consequently, A β aggregation in the K162 presence is not entirely prevented. Notably, the aggregation pathway is modified by K162. In the K162 presence, only non-toxic A β forms, i.e., A β M β s, A β D β s, and A β F β s, are formed, and the production of membrane-permeating A β O β s is bypassed. Unlike other A β toxicity inhibitors, K162 preserves neurologically beneficial A β M β s. The deciphered A β toxicity inhibition mechanism explains previously-reported *in vivo* results and provides a novel therapeutic approach for AD that might be explored in the future.

Table of contents

Acknowledgments.....	3
Declaration of originality	4
Funding	5
List of publications	6
Conference presentations	7
List of abbreviations.....	8
Abstract.....	15
Table of contents	17
Chapter 1. Introduction	19
1.1. Alzheimer's disease and amyloid β	19
1.1.1. Alzheimer's disease.....	19
1.1.2. Amyloid β	20
1.2. Cell membrane.....	23
1.2.1. Lipid self-assembled nanostructures and phase transitions	26
1.2.2. Lipid rafts	28
1.2.3. Model cell membranes	29
1.3. Amyloid β interaction with model cell membranes	32
1.3.1. Ion channels in bilayer lipid membranes.....	32
1.3.2. Lipid extraction from bilayer lipid membranes	34
1.3.3. Non-specific bilayer lipid membrane permeation.....	35
1.3.4. Influence of bilayer lipid membrane properties on A β -membrane interaction	39
1.4. The objective of the thesis.....	42
Chapter 2. Experimental section.....	44
2.1. Chemicals and materials	44
2.2. Experimental techniques and methods.....	45
2.2.1. Supported lipid bilayer preparation	45
2.2.2. Atomic force microscopy	45
2.2.3. Electrochemical methods	50
2.2.3.1. Differential capacitance measurement	51



2.2.3.2. Immersion method	53
2.2.3.3. Electrochemical impedance spectroscopy	53
2.2.4. IR spectroscopy	58
Chapter 3. Size-dependent interaction of amyloid β oligomers with brain total lipid extract bilayer — fibrillation versus membrane destruction.....	70
3.1. Introduction	71
3.2. Experimental section	71
3.3. Results and discussion	74
3.4. Conclusions	88
Chapter 4. Alzheimer's disease-related amyloid β peptide causes structural disordering of lipids and changes the electric properties of a floating bilayer lipid membrane	90
4.1. Introduction	91
4.2. Experimental section	91
4.3. Results and discussion	96
4.4. Conclusions	114
Chapter 5. Inhibition of amyloid β -induced lipid membrane permeation and amyloid β aggregation by K162	116
5.1. Introduction	117
5.2. Experimental section	117
5.3. Results and discussion	121
5.4. Conclusions	133
Chapter 6. Research summary and future perspectives	135
References	138

Chapter 1. Introduction

This chapter provides background knowledge essential for understanding the findings presented in the thesis. The first part of the chapter discusses Alzheimer's disease (AD) and its impact on the human population. Next, amyloid β ($A\beta$) is introduced through the amyloid cascade hypothesis, demonstrating the connection between $A\beta$ and AD. Then, $A\beta$ production, structural properties, and behavior are described. The second part of this chapter introduces a cell membrane and its essential components. Then, the concept of model cell membranes is introduced as well as its importance in research studies. The third part of the chapter consists of a critical review of the literature regarding the $A\beta$ interaction with a model cell membrane. This part provides an insight into the current state of the field and the challenges it faces. The final part of the introduction describes the thesis objectives.

1.1. Alzheimer's disease and amyloid β

1.1.1. Alzheimer's disease

Advances in science and technology resulted in the extension of the human life duration.¹ Unfortunately, the chance of getting a neurodegenerative disease increases with age. Alzheimer's disease (AD) is the most prevalent type of neurodegenerative disease.² Aging,³ genetics,⁴ and having a family history of AD⁵ are the greatest risk factors for AD, with aging being the most significant one. The percentage of people suffering from AD increases remarkably with age, i.e., 3% of 65-74 years old, 17% of 75-84 years old, and 32% of 85 years old people (or older) have AD.⁶ Over 46 million people worldwide live with AD (more than the population of Spain). This number is estimated to increase to 131.5 million by 2050.⁷ This trend shows that a new AD case appears every three seconds. Based on this trend, the number of patients will double every 20 years. Besides affecting the welfare of the human population, AD has a significant impact on the world economy. The global costs associated with AD patients' care have increased from 604 billion US\$ in 2010 to 818 billion US\$ in 2015 (35.4% increase).⁷ Estimations, based on this trend, show that this cost will be higher than 2 trillion US\$ by 2030. If worldwide AD care is a country, it would be the 18th largest economy globally with a market value higher than those of Google or Apple.⁷ Therefore, AD represents one of the most significant worldwide problems of the 21st century.

AD, a type of dementia, involves progressive neurodegeneration that severely impairs cognition.^{8,9} Difficulties in remembering information learned recently are an early clinical symptom of AD because the brain's learning centers are affected first. With the progression of AD, new symptoms appear, such as impaired communication, disorientation, confusion, poor judgment, and behavioral changes. Ultimately, difficulties in speaking, swallowing, and walking occur.

AD was first reported about a century ago.¹⁰ In 1907, Alois Alzheimer, a German clinical psychiatrist and neuroanatomist, documented the progression of an unusual illness in a 51-year-old woman in the asylum in Frankfurt. Alzheimer reported a "peculiar substance" in the form of extra- and intracellular deposits present in the patient's brain. Polish-Jewish neurologist and neuropathologist Teofil Simchowicz, also Alzheimer's student, named the extracellular deposits "senile plaques."¹¹ Almost 80 years later, it was discovered that these senile plaques (Figure 1.1a) are composed of amyloid β ($A\beta$),¹² and the intracellular deposit, known as neurofibrillary tangles (Figure 1.1b), are composed of hyperphosphorylated tau protein.¹³ These discoveries made senile plaques and neurofibrillary tangles hallmarks of AD, and they put a spotlight on $A\beta$ and tau protein as the main suspects behind AD-related toxicity.

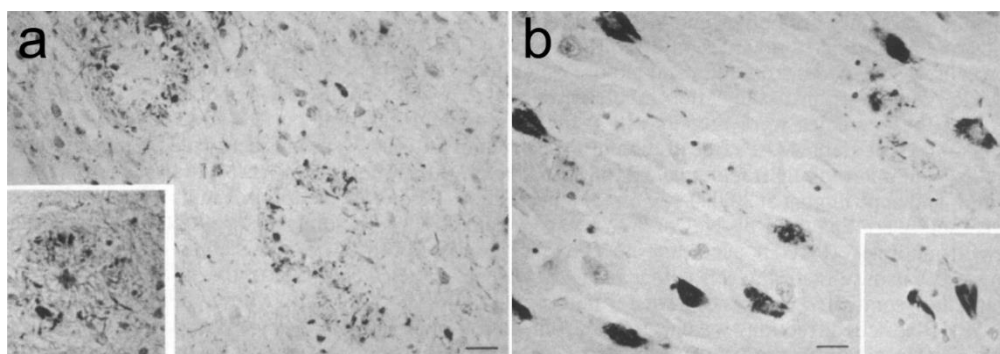


Figure 1.1. Immunocytochemistry of AD brain sections showing (a) senile plaques and (b) neurofibrillary tangles [adapted from ¹³].

1.1.2. Amyloid β

The amyloid cascade hypothesis proposes that the $A\beta$ protein plays a central role in AD development.^{14,15} This hypothesis suggests that $A\beta$ over-production, aggregation, and accumulation in the human brain parenchyma triggers a cascade of molecular and cellular events leading to a progressive synaptic and neuritic injury, disturbance of ionic homeostasis, oxidative damage of cells that result in neuronal death, and consequently, AD.¹⁶

$A\beta$ is a 39-44 amino acids long peptide produced from proteolytic cleavage of a large, type I transmembrane protein called amyloid precursor protein (APP).^{17,18} APP can be processed in two ways, i.e., according to the non-amyloidogenic and amyloidogenic pathway.¹⁹ In the non-amyloidogenic pathway (Figure 1.2a), α -secretase cleaves APP to produce a soluble N-terminal ectodomain of APP (sAPP α) and an 83-amino acid C-terminal fragment (C83). Next, γ -secretase cleaves C83 to split it into an APP intracellular domain (AICD) and a non-pathogenic fragment p3. In the amyloidogenic pathway (Figure 1.2b), β -secretase cleaves APP, forming a soluble N-terminal ectodomain of APP (sAPP β) and a 99-amino acid C-terminal fragment (C99). Finally, γ -secretase cleaves C99 at one of the several different sites to produce AICD and amyloid β ($A\beta$) of variable length, i.e., with 39-44 amino acids. Under normal physiological conditions, the most

abundant A β form consists of 40 amino acids (A β_{40}). In comparison, the 42 amino acids-long form of A β (A β_{42}) is significantly less produced, i.e., the A β_{42} -to-A β_{40} molar ratio is \sim 1:9.²⁰ However, the production of A β_{42} is elevated in body fluids of AD patients.²¹ The A β_{42} is more toxic^{22,23} and more aggregation-prone than A β_{40} .^{24–26} Inherited mutations in APP and γ -secretase facilitate the production of more toxic A β_{42} relative to the usually abundant A β_{40} , leading to the development of familial (early-onset) AD.^{16,17} Hence, A β_{42} was the objective of studies presented in this doctoral thesis.

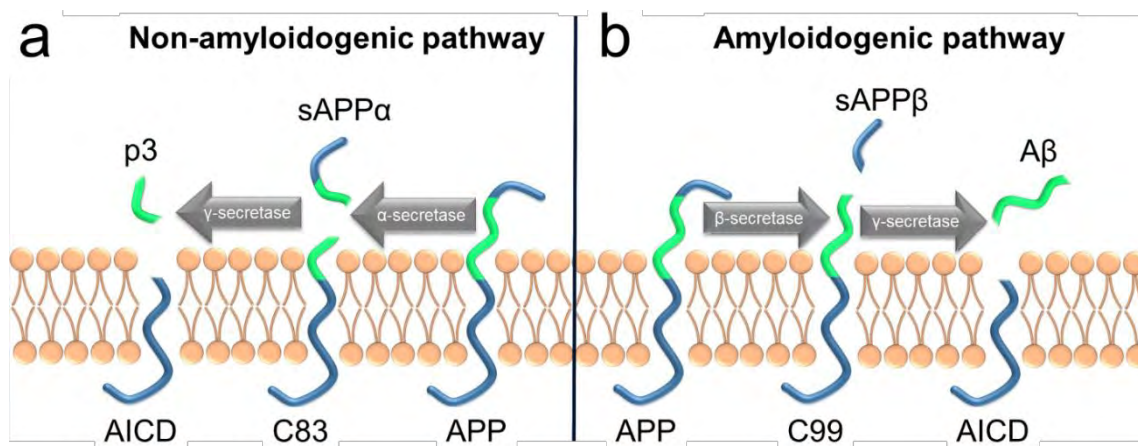


Figure 1.2. Proteolytic cleavage of APP according to (a) non-amyloidogenic and (b) amyloidogenic pathway. (a) In the non-amyloidogenic pathway, sequential proteolytic cleavage of APP by α - and γ -secretase leads to the formation of a soluble N-terminal ectodomain of APP (sAPP α), an 83-amino acid C-terminal fragment (C83), an APP intracellular domain (AICD), and a non-pathogenic fragment p3. (b) In the amyloidogenic pathway, β -secretase cleaves APP to produce the soluble N-terminal ectodomain of APP (sAPP β), 99-amino acid C-terminal fragment (C99), AICD, and A β .

In its native form, A β exhibits neuroprotective abilities and stimulates brain development.²⁷ The native state of any protein, although thermodynamically favorable, is not necessarily stable. A protein or polypeptide consisting of \sim 100 amino acids can adopt as many as 10^{49} conformations.²⁸ The human body's cellular environment contains a so-called "quality control" system (QCS) that assists proteins in adopting their native folding and degrade misfolded proteins.^{29,30} Protein misfolding can occur for several reasons, e.g., (i) intrinsic nature of a protein to adopt many non-native conformations, (ii) malfunctioning of QCS, (iii) mutations in gene sequence that participate in protein production, (iv) translation and transcription errors, (v) failures in the post-translational modifications and trafficking, (vi) cross-seeding and seeding of misfolded proteins, and (vii) environmentally-induced structural modifications of a protein.^{31,32} Misfolded proteins are unstable because their hydrophobic residues are exposed. To stabilize themselves, they aggregate into highly-ordered structures with an energy minimum even lower than that of the native state.³³

The A β aggregation mechanism is under debate, and many different aggregation pathways have been proposed (Figure 1.3).^{34–42} The "on-pathway" mechanism follows nucleation-dependent aggregation of misfolded A β monomers (A β Ms) into A β oligomers (A β O), A β protofibrils (A β PFs), and mature A β fibrils (A β Fs). This process also involves the conversion of the dominant A β secondary structure from random coils (present in A β Ms) to β -sheet (present in A β aggregates). Notably, there are unique β -sheet arrangements in different A β aggregates. A β O adopt the anti-parallel β -sheet configuration, while A β Fs contain an in-register parallel β -sheet arrangement, where individual β -strands are perpendicular to the fibril axis (the β -strands of A β Fs are rotated by 90° in comparison to β -strands of A β O).^{34–36,43–45} Production of A β Fs is still under debate. Some studies propose that small A β O combine into thin protofilaments that intertwine to form protofibrils, and then, these protofibrils intertwine to produce A β Fs.^{46–48} On the other hand, some studies propose that A β O directly assemble into A β Fs without forming protofilaments and protofibrils.^{49,50} Moreover, A β Ms can aggregate according to the "off-pathway" mechanism (Figure 1.3), forming unstructured, amorphous aggregates.^{37,38} These "off-pathway" aggregates can dissociate into smaller aggregates that can further undergo "on-pathway" aggregation. Furthermore, the "on-pathway" aggregates also dissociate (aggregate fragmentation).^{39,51} As a result of these complex processes, many different A β aggregates may coexist.

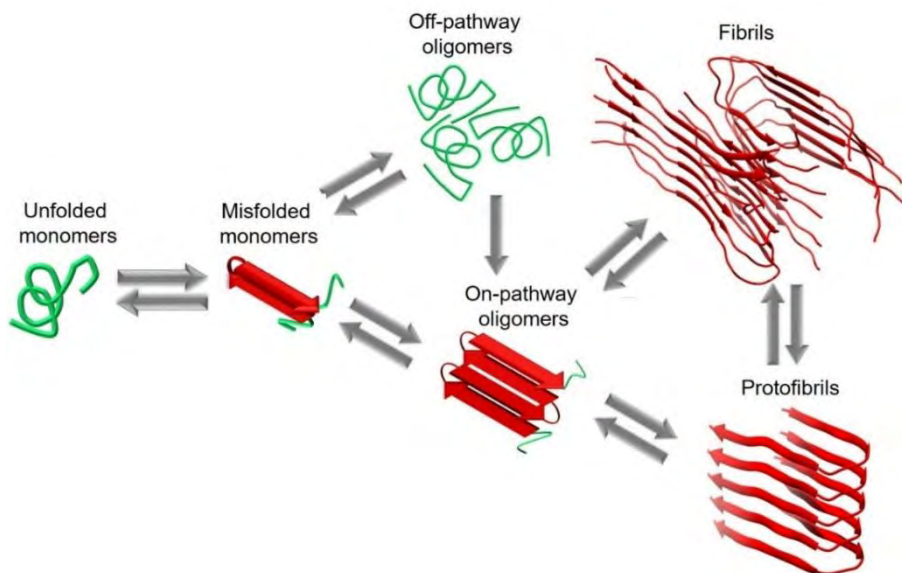


Figure 1.3. Unfolded A β Ms get misfolded, and then, they aggregate and adopt various conformational states according to different aggregation pathways. The scheme was produced with UCSF Chimera software⁵² using PDB files 1Z0Q,⁵³ 2BEG,⁵⁴ and 2LMN⁵⁵ for misfolded monomers/on-pathway oligomers, protofibrils, and fibrils, respectively.

The A β aggregates deposit in the brain as amyloid plaques, which leads to AD pathology. Genetic risk factors can indirectly facilitate A β aggregation and deposition. The ApoE4 gene is associated

with decreased brain clearance of A β , promoting A β aggregation and deposition in the brain. This event is associated with sporadic (late-onset) AD.¹⁶

Therefore, A β misfolding, overproduction, and imbalance in the A β_{40} -to-A β_{42} ratio (in favor of A β_{42}) lead to accelerated A β aggregation into insoluble A β Fs. According to the amyloid cascade hypothesis, these fibrils deposit to produce amyloid plaques, the AD hallmark. However, many in vivo studies showed individuals with a significant amyloid burden and no memory impairment symptoms, demonstrating that amyloid deposition does not correlate well with neuronal loss and cognitive decline.⁵⁶⁻⁶⁰ These findings suggested that the amyloid cascade hypothesis needs revision.

Since various A β forms coexist, it was necessary to perform systematic studies analyzing each of the A β forms separately to determine their respective toxicities. It was demonstrated that A β M and A β Fs exhibit low toxicity both in vitro and in vivo.⁶¹⁻⁶⁷ They fail to permeate lipid vesicles,⁶¹ exhibit low toxicity towards PC12 cells,⁶² glial cells in CGC cultures, and macrophage J774 cells,⁶³ demonstrate low impairment of memory and learning functions,^{64,66,67} low inhibition of long-term hippocampal potentiation,^{65,66} low enhancement of long-term depression⁶⁶ in rat models. A β Fs, the main component of amyloid plaques,⁶⁸ exhibit low toxicity, explaining the absence of correlation between the amyloid plaques and the cognitive decline mentioned above.

In contrast to A β M and A β Fs, A β O are incredibly toxic. A β O cause memory impairment,⁶⁷ long-term hippocampal potentiation,⁶⁵ learning and cognition deficiency,^{66,69} deterioration of synapses,^{70,71} suppression of synaptic activity,⁷² cell death via leakage of lysosomal enzymes,⁷³ inhibition of mitochondrial activity,⁷⁴ the increase of production of reactive oxygen species,⁷⁵ and neuroinflammation.^{76,77} Interestingly, A β O build up in the human brain before amyloid plaques are deposited.⁷⁸⁻⁸⁰ Post-mortem analysis revealed that A β O, unlike A β Fs, accumulate in meningeal vessels⁸¹ and cortical lysates⁸² of AD brains. These findings shifted the research focus towards A β O, leading to the so-called "Amyloid β Oligomer" hypothesis.⁸³

1.2. Cell membrane

The cell membrane, or plasma membrane, is one of the most vital components of every cell. The cell membrane envelopes the cell cytoplasm, shielding the cell interior from the extracellular environment. Eukaryotic cells also contain subcellular membranes that divide cell cytoplasm into different sections, allowing multiple functions to be performed simultaneously in different cell parts.⁸⁴ Moreover, the cell membrane plays an active role in connecting the cytoskeleton to define the cell shape and attaching to the extracellular matrix and other cells to form tissues. Furthermore, the cell membrane is selectively permeable and controls the transport of molecules exchanged between the cell and its environment. Therefore, the cell membrane has an essential role in maintaining cell protection, homeostasis, and communication with the environment.

In 1972, the "fluid mosaic" model of the cell membrane was formulated (Figure 1.4).⁸⁵ This model suggests that the cell membrane is a lipid bilayer that encompasses carbohydrates and proteins.⁸⁶

All molecules present in the cell membrane are amphipathic, i.e., they have hydrophobic and hydrophilic parts. These molecules arrange to satisfy as many hydrophilic and hydrophobic interactions as possible, adopting the most stable structure in a polar environment.⁸⁷ This arrangement results in formation of a planar two-dimensional structure with a hydrophobic core and hydrophilic sides. Some proteins, like integral proteins, span the entirety of the cell membrane. They establish hydrophobic and hydrophilic interactions with respective lipid counterparts. Other proteins, like peripheral proteins, only temporarily reside on the membrane surface. Carbohydrates can adhere to proteins or lipids to form glycoproteins or glycolipids, respectively.

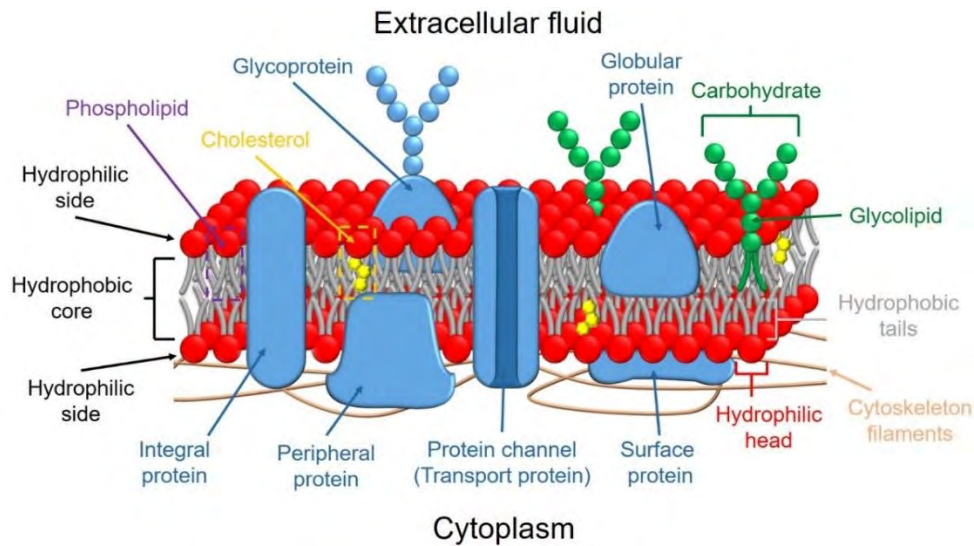


Figure 1.4. Illustration of the "fluid mosaic" model of the cell membrane.

Lipids represent approximately 50% of the cell membrane composition, although the lipid composition varies between different types of cell membranes.⁸⁸ Like other cell membrane components, lipids are also amphipathic molecules, i.e., they have hydrophilic heads and hydrophobic tails. Hydrophobic and van der Waals forces acting between lipids make them assemble into a bilayer structure where hydrophobic tails are hidden, and hydrophilic heads are exposed, i.e., oriented towards the cell interior (cytoplasm) and the cell exterior (extracellular fluid). Even though all lipids consist of heads and tails, the chemical composition of these parts varies significantly. As a result, three different types of lipids are distinguished, i.e., phospholipids, sphingolipids, and steroids.⁸⁹

Phospholipids are the most abundant type of lipids in most cell membranes (Figure 1.5). Typically, phospholipid has a tail composed of two fatty acyl chains. The acyl chains vary in length (usually 16 or 18 carbon-carbon bonds) and degree of saturation. They can be saturated (no double carbon-carbon bonds) or unsaturated (one or more double carbon-carbon bonds). The lipid tail is connected to the lipid head via esterification of acyl chains to two hydroxyl groups of the

glycerol moiety. The glycerol moiety is attached to the phosphate group, linked to different groups (R group) like choline, ethanolamine, or serine. Phospholipids are classified according to the chemical composition of the R group. For example, phosphatidylcholine (PC), the most abundant kind of lipids in the plasma membrane, contains a choline group composed of a positively charged alcohol moiety bound to a negatively charged phosphate group. In phosphatidylethanolamine (PE) and phosphatidylserine (PS), the phosphate groups are attached to OH-containing groups, i.e., ethanolamine and serine, respectively. Depending on the R group, phospholipids can be charged (positively or negatively) or not charged (zwitterionic).

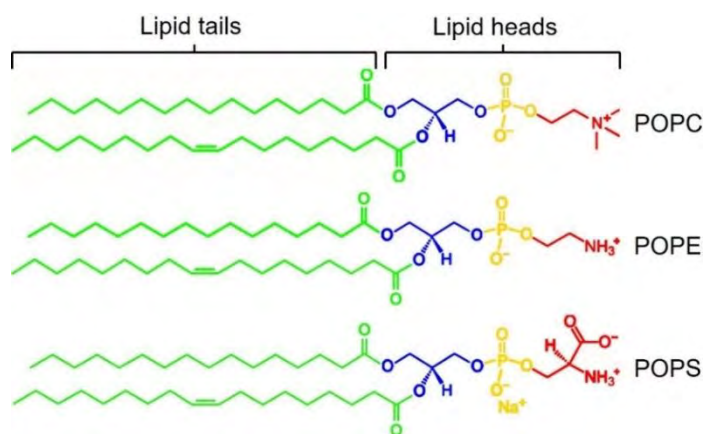


Figure 1.5. Structural formulas of 1-palmitoyl-2-oleoyl-*sn*-glycero-3-phosphocholine (POPC), 1-palmitoyl-2-oleoyl-*sn*-glycero-3-phosphoethanolamine (POPE), and 1-palmitoyl-2-oleoyl-*sn*-glycero-3-phospho-L-serine (POPS). R groups, phosphates, glycerols, and fatty acyl chains are colored in red, yellow, blue, and green, respectively.

In 1884, another class of phospholipids was discovered in the brain extracts – sphingolipids. They are named after the Greek mythological creature, the Sphinx, because of their enigmatic nature.⁹⁰ Sphingolipids consist of a long fatty acyl chain attached to the amino group of sphingosine. Sphingomyelin (SM) is the only non-glycerol lipid present in the cell membranes (Figure 1.6).⁸⁸ In most mammalian cell membranes, SM makes from 2 to 15% of the total lipid composition.⁹¹ Importantly, higher SM concentrations are found in a particular type of tissue, e.g., peripheral nerve and brain.^{91,92} The SM structure is very similar to that of PC lipid, which is why it is also classified as a phospholipid. In SM, phosphocholine is bound to the terminal hydroxyl group of sphingosine.

In other sphingolipids, sugars are present in their heads, and these kinds of sphingolipids are known as glycolipids. Glycolipids represent 2-10% of the plasma membrane lipid content, and they are abundant in nervous tissue.⁸⁹ Gangliosides are complex glycolipids in which sphingosine is bonded with one or two-branched sugar chains that contain sialic acid groups (Figure 1.6). Gangliosides represent 10-12% of the neuronal membranes' lipid content, and 20-25% of them are located in the outer leaflet.⁹³ Monosialotetrahexosylganglioside (GM1) is one of the most

important types of gangliosides in the brain. It represents 10-20% of the brain's ganglioside content.^{94,95}

Steroids are the third important class of membrane lipids. They have a four-ring hydrocarbon structure. Cholesterol (Chol) is the most abundant steroid present in mammalian tissues.⁸⁹ Given that Chol is mostly composed of hydrocarbons, it should be hydrophobic (Figure 1.6). However, one hydrocarbon ring is modified with a hydroxyl group, making that part hydrophilic and the whole molecule amphipathic. Chol is abundant in mammalian cell membranes, but it is absent in prokaryotic cells.⁸⁹ In most mammalian tissues, the Chol concentration is ~2 mg/g tissue, while in the central nervous system is 15-20 mg/g tissue.⁹⁶ About 25% of the total amount of cholesterol in the human body is located in the human brain, mostly in the myelin sheets surrounding the axons. Chol plays a vital role in neuronal development, synaptic plasticity, and brain function.

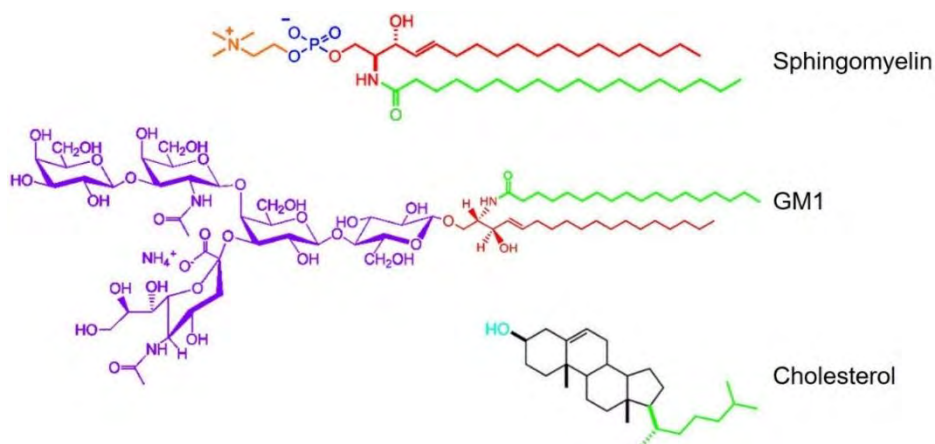


Figure 1.6. Structural formulas of sphingomyelin (SM), monosialotetrahexosylganglioside (GM1), and cholesterol (Chol). Sphingosines, fatty acyl chains, phosphates, cholines, sialic acids are colored in red, green, blue, orange, and violet, respectively. The hydrophilic part of Chol is colored in cyan.

1.2.1. Lipid self-assembled nanostructures and phase transitions

From the biological point of view, the planar lipid bilayer represents the most important lipid structure type. However, lipids' amphipathic nature allows them to self-assemble into various nanostructures (lipid polymorphism).⁹⁷⁻⁹⁹ These structures include micelles, vesicles, cylindrical tubules, and disks (Figure 1.7). The lipid structure and environmental factors, e.g., temperature, hydration, and water content, affect the lipid nanostructure formation.^{98,99} For example, cylindrically-shaped PC lipids are called bilayer lipids or type 0 lipids because they form a planar lipid bilayer.¹⁰⁰ On the other hand, type I lipids, like inversely conical lysolipids, and type II lipids, like conical PE lipids, cannot produce a planar bilayer on their own, thus are known as non-bilayer lipids. In non-bilayer lipids, the head's cross-sectional area is not proportional to that of tails,

causing them to have a conical or inversely conical shape. There is an imbalance of molecular forces (electrostatic, steric, van der Waals, hydration forces) acting on these lipids' heads and tails. As a result, non-bilayer lipids form structures that have an intrinsic curvature. For example, type II lipids have a conical shape forming structures with negative curvatures, i.e., that bend towards aqueous exterior, like inverse micelles and inverse tubules. On the other hand, type I lipids have an inversely conical shape with an intrinsic tendency to form structures with positive curvatures, i.e., away from the water, like micelles.

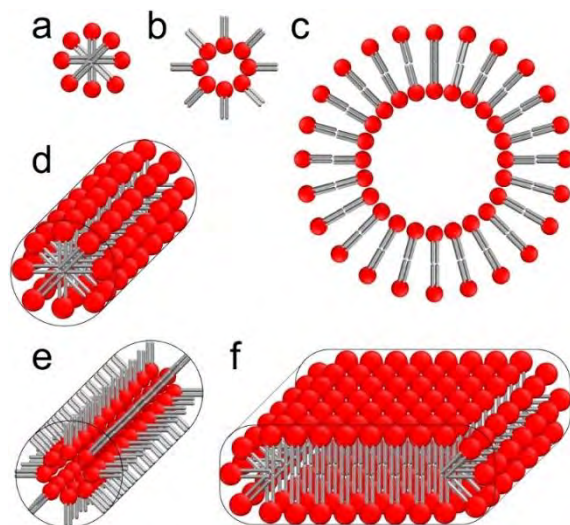


Figure 1.7. Illustration of different lipid nanostructures, i.e., (a) spherical micelle, (b) inverted micelle, (c) vesicle (liposome), (d) cylindrical micelle (tubule), (e) inverted cylindrical micelle (tubule), and (f) disks.

In the cell membrane, the lipid composition is optimized to form a planar lipid bilayer. Having various lipids in the cell membrane, including non-bilayer lipids, is vital for proper cell functioning. Lipid bilayers have to allow material exchange between the cell and its environment while preserving the barrier function and overall structural stability.¹⁰¹ Therefore, both bilayer and non-bilayer lipids participate in maintaining the necessary flexibility and robustness of a lipid bilayer. Moreover, the non-bilayer lipids like PE have an active role in physiological processes like proteolipid interactions¹⁰⁰ and folding of lac permease protein.⁹⁷

Planar lipid bilayer may convert to a non-planar (non-bilayer) structure. Changes in the lipid bilayer environment might be the reason for this conversion.¹⁰¹ The increase in temperature can increase repulsive forces in lipid tails, causing increased stress in lipids. Once the accumulated stress exceeds a critical point, a new lipid structure emerges. Peptides can also induce conversion from a planar to a non-planar lipid structure.¹⁰² Alamethicin converts planar bilayer of 1,2-dielaidoyl-*sn*-glycero-3-phosphoethanolamine (DEPE) into cubic phase,¹⁰³ gramicidin A converts

planar bilayers of various lipids to hexagonal H_{II} phase¹⁰⁴ and lysophosphatidylcholine (LPC) micelles to planar bilayers.¹⁰⁵

A lipid bilayer can undergo phase transitions that do not involve a change of the planar shape. In this case, lipids change their conformation, which affects lipid bilayer thickness and mobility.^{106,107} These phase transitions of lipid bilayers are known as thermotropic phase transitions because they are mostly influenced by temperature. However, also pressure, lipid composition, and water content affect lipid bilayer phase transitions.⁹⁹ At low temperatures, the lipid bilayer is in the crystalline (sub-gel) phase (Figure 1.8a). The temperature increase causes a bilayer transition to the gel phase (Figure 1.8b) in which acyl chains are fully extended in all-*trans* conformation.¹⁰⁸ At this point, some lipids can adopt several other arrangements, like the interdigitated (Figure 1.8c) and tilted (Figure 1.8d) gel phase. In some bilayers, e.g., bilayers composed of DMPC lipids,¹⁰⁹ further temperature increase causes the bilayer's phase transition to the ripple phase, characterized by corrugations on the bilayer surface (Figure 1.8e). At temperatures exceeding the lipid melting temperature (T_m), lipid bilayers convert to liquid crystalline (disordered) phase (Figure 1.8f). In this phase, the lipid acyl chains are melted, i.e., they are no longer fully extended in all-*trans* conformation, and an increased number of *gauche* conformers appear. In this phase, lipids exhibit higher rotational motion, and overall lipid bilayer's mobility is increased.

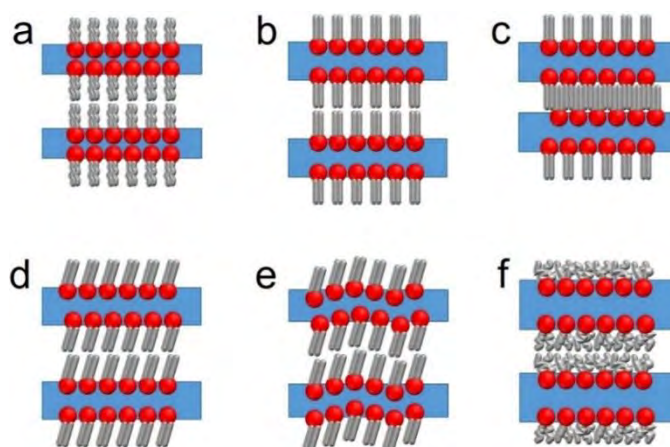


Figure 1.8. Illustration of lipid planar (a) subgel, (b) gel, (c) interdigitated gel, (d) tilted gel, (e) ripple, and (f) liquid crystalline phase.

1.2.2. Lipid rafts

Lipid rafts are small (10-200 nm in diameter) biomembrane regions enriched in Chol, SM, and glycolipids (particularly gangliosides).^{88,110,111} They are named rafts because of their low buoyant density, which allows their isolation from the rest of the membrane.¹¹² Lipid rafts serve as a platform that accommodates various transmembrane and GPI proteins. They play an active role

in multiple cellular functions like cell movement, signaling, division, adhesion, axon guidance, vesicular trafficking, synaptic transmission, membrane-associated proteolysis, and endocytosis.^{88,112,113}

Changes in lipid rafts are associated with the loss of neuron function, leading to cell death and neurodegenerative diseases.^{114,115} For example, the genetic mutation that causes the failure of monosialodihexosylganglioside (GM3) synthesis leads to the infants' developmental retardation and death.¹¹⁶ Decrease in the ganglioside and Chol concentrations is associated with aging,¹¹⁵ and age-related neurodegenerative diseases like AD.¹¹⁷ On the other hand, increased concentrations of GM1 and monosialoganglioside GM2 (GM2), along with Chol decrease, were also observed in lipid rafts of AD brains.¹¹⁸ Moreover, an increase in GM1 and ganglioside GD1a (GD1a), accompanied by a decrease in ganglioside GD1b (GD1b) and ganglioside (GT1b) contents, was found in individuals with AD.¹¹⁹ Chol is another significant component of lipid rafts associated with AD.¹²⁰ An increase in the Chol concentration in midlife people is a risk factor for developing AD.¹²¹ Statins, compounds that lower Chol level, have been associated with the diminished prevalence of AD.^{122,123} Majority of Chol-AD correlation studies comes from in vitro and cell studies which mostly agree that the Chol concentration increase facilitates A β accumulation and the Chol decrease has the opposite effect.^{124–126} However, some studies reported a decreased Chol level in AD individuals.¹²⁰ Apparently, most studies agree that lipid raft components are associated with AD, even though their exact role is under debate and requires further investigation.

1.2.3. Model cell membranes

An incredibly convenient way of studying individual cell membrane components and their interaction with proteins, peptides, drugs, and other biologically active molecules, involves using model cell membranes. Moreover, they can be used to study the effect of environmental changes (changes in temperature, pH, ionic strength, electric field, etc.) on the cell membrane's structure and morphology. Model cell membranes are systems designed to mimic the cell membrane, thus also named biomimetic systems. The most commonly used model cell membranes include lipid monolayers (Figure 1.9) and lipid bilayers (Figure 1.10).⁸⁴

A lipid monolayer, a single layer of lipid molecules, is useful to study a single side (leaflet) of the cell membrane. Amphipathic properties of lipids allow studying this type of biomimetic systems at the air-water interface (Figure 1.9a). Moreover, the lipid monolayer can be deposited onto either hydrophilic or hydrophobic substrates. Lipid monolayer adopts the configuration shown in Figure 1.9b if a hydrophilic substrate is used. In this case, lipid heads contact the substrate, while lipid tails are exposed to the environment.¹²⁷ This configuration mimics the inner (facing cytosol) leaflet of the cell membrane. Substrates made of hydrophilic materials like mica, freshly oxidized surfaces of glass, quartz, and silicon wafers can be used for this purpose.¹²⁸ Importantly, this lipid monolayer arrangement is only stable in the air because hydrophobic tails are exposed to the environment. The lipid monolayer can be constructed, as shown in Figure 1.9c, using a

hydrophobic substrate. In this case, lipid tails contact the substrate, while hydrophilic heads are exposed towards the environment. This system is only stable in the polar environment, and it mimics the outer (facing extracellular space) leaflets of the cell membrane. Silicon dioxide and graphene can be used to achieve this lipid monolayer architecture.¹²⁹

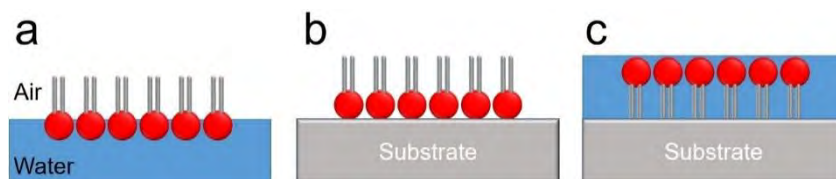


Figure 1.9. The lipid monolayer formed (a) at the air-water interface as well as the lipid monolayer deposited on the (b) hydrophilic and (c) hydrophobic substrate.

In 1962, Muller et al.¹³⁰ reported the first type of lipid bilayer known as the black lipid membrane (Figure 1.10a). In this membrane, the lipid bilayer is formed by creating a small (diameter of tens to hundreds of micrometers) opening in a hydrophobic material. A syringe, brush, or glass applicator is used to apply a solution of lipids dissolved in an organic solvent to the opening, forming a thin lipid bilayer. The destructive interference between the light irradiating from both sides of the chamber makes the bilayer dark, hence the name "black" lipid membrane.¹³¹

Lipid bilayers, also known as bilayer lipid membranes (BLM), deposited on a solid substrate are called supported lipid bilayers (Figure 1.10b). This type of lipid bilayers is more robust and stable than black lipid membranes. Moreover, they can be studied using surface techniques, unlike black lipid membranes.¹³² In a supported lipid bilayer, the lipid heads are oriented towards the hydrophilic substrate, though they do not directly contact it, i.e., they are separated by a ~1 nm thick water layer.^{133,134} Electrostatic, hydration, and van der Waals forces are acting between the lipid bilayer and the substrate.¹³⁵ Various substrates can be used for creating supported lipid bilayers, e.g., fused silica,¹³⁶ borosilicate glass,¹³⁷ mica,¹³⁸ and gold.¹³⁹ It is also possible to deposit multiple lipid bilayers.¹⁴⁰ Another type of supported lipid bilayer is a hybrid BLM (hBLM), formed by deposition of a lipid monolayer on a substrate coated with a hydrophobic monolayer of alkylthiols¹⁴¹ and polymers with hydrophobic side chains (Figure 1.10c).^{142,143} Disadvantage of these supported lipid bilayers is that the underlying substrate imposes stress on the lipid bilayer, affecting lipids' mobility. Moreover, space between the substrate and the bilayer is insufficient for the incorporation of transmembrane proteins.

A way to overcome those disadvantages is to coat the substrate surface with a self-assembled monolayer (SAM) of polymers and chemically-modified lipids before the lipid bilayer deposition.¹⁴⁴ The SAM, located in between the substrate and the lipid bilayer, acts as a cushion that decreases the substrate-induced stress imposed on the lipid bilayer and increases the lipid bilayer's hydration, thus increasing lipids' mobility. Moreover, SAM provides space between the lipid bilayer and the substrate surface sufficient to allow transmembrane protein incorporation

without denaturing the protein.¹³² There are two types of such a membrane architecture, i.e., tethered BLM (tBLM) and floating BLM (fBLM).

In tBLM, lipids are covalently bonded to the substrate by a hydrophilic spacer layer.^{134,145} Neutron reflectivity and IR spectroscopy showed that some spacers' water content is low, and in such an environment, the BLM fluidity is low.^{146–148} This difficulty could be solved using a different spacer layer, like β -mercaptoethanol, where only some lipids from the bottom leaflet are attached to the spacer.¹⁴⁶ This type of tBLM is known as sparsely tBLM (Figure 1.10d). However, the sparsely tBLM production is difficult because this requires functionalized lipids produced by a complex synthesis.¹⁴⁹

A floating bilayer lipid membrane (fBLM) is an improved biomimetic system (Figure 1.10e) because lipid mobility in fBLM is higher than in tBLM. In fBLM, the lipid bilayer can be deposited on top of a supported bilayer¹⁵⁰ or an S-layer protein.¹⁵¹ Alternatively, the lipid bilayer can be deposited on the Au(111) electrode surface functionalized with a hydrophilic monolayer of 1-thio- β -D-glucose (Tg). This fBLM can be studied under electrochemical conditions^{152–154} by applying a static electric field comparable to that experienced by natural cell membranes.^{155,156} Moreover, Tg SAM stabilizes the lipid bilayer via hydrophilic interactions. Furthermore, it prevents metal-induced protein denaturation because the gold substrate does not contact the protein, thus allowing for the protein-lipid interaction studies.^{157–160}

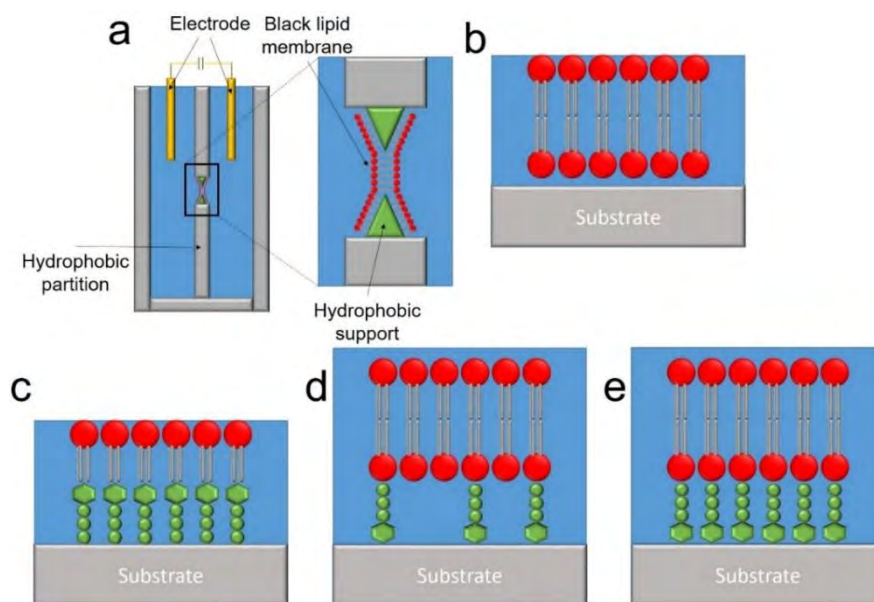


Figure 1.10. Illustration of the (a) black lipid membrane, (b) supported BLM, (c) hybrid BLM, (d) tethered BLM, and (e) floating BLM.

1.3. Amyloid β interaction with model cell membranes

An essential feature of A β O is their ability to permeate cell membranes. This ability is destructive by itself and allows A β O to incorporate into the cell and trigger cell death from the cell interior. The mechanism of cell membrane permeation by A β O is still debated. The two most popular mechanisms proposed are pore/ion channel formation^{161–163} and lipid extraction (Figure 11).^{164–168}

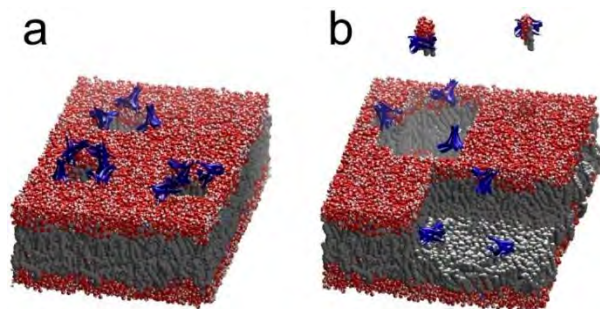


Figure 1.11. (a) Pore formation and (b) lipid extraction mechanism of membrane destruction by A β O s.

1.3.1. Ion channels in bilayer lipid membranes

Ion channels are donut-shaped pores with outer and inner diameters of ~ 10 and $1-2$ nm, respectively, that protrude ~ 0.5 nm above the membrane surface (Figure 1.12a).^{162,163,169–173} A β_{40} form Ca²⁺-permeable channels in POPE or POPE/POPS lipid bilayers. From this observation, it follows that disruption of Ca²⁺ cell homeostasis leads to neuronal death characteristic of AD.^{161,174} Small A β_{40} oligomers (A β_{40} O s), ranging from trimers to hexamers, form ion channels in the 1,2-dioleoyl-*sn*-glycero-3-phosphocholine (DOPC) membrane.^{162,163} Multiple electrical conductance states are observed, indicating the presence of different ion channels formed by oligomers of distinct molecular weights (Figure 1.12b).^{162,163,174–177} In contrast, A β_{40} O s were incapable of forming ion channels in the membrane excised from HEK293 cells.¹⁷⁸ This behavior was also observed for A β_{40} monomers (A β_{40} M s) and fibrils (A β_{40} F s), as well as A β_{42} monomers (A β_{42} M s) and A β_{42} fibrils (A β_{42} F s), while only A β_{42} oligomers (A β_{42} O s), 5-20 nm in diameter, were capable of forming ion channels. Interestingly, A β_{40} M s do not permeate but rather fibrillate on the surface of the dodecylphosphocholine (DPC), octyl glucoside (OG), and 1,2-dihexanoyl-*sn*-glycero-3-phosphocholine (DHPC) membranes.¹⁷¹ In contrast, both A β_{42} M s and A β_{42} O s porate lipid bilayers and induce different types of ionic currents. A β_{42} M s induce fast, transient, and heterogeneous, so-called "spiky" ionic currents, indicating the formation of a heterogeneous population of pores. However, monomers cannot be heterogeneous, which rules out the possibility that A β_{42} M s themselves form ion channels with heterogeneous ionic currents in the

lipid membrane. Most likely, $A\beta_{42}$ Ms aggregate into $A\beta_{42}$ Os of different sizes and molecular weights that produce variable-size ion channels with diverse electrical activity.

The pre-formed $A\beta_{42}$ Os, rich in the β -sheet secondary structure, form barrel-shaped ion channels in lipid bilayers with three distinct ionic currents.¹⁷¹ These currents are different from those of ion channels formed in the presence of freshly-prepared $A\beta_{42}$ Ms. These different ionic currents indicate that structurally distinctive ion channels are formed by pre-formed $A\beta_{42}$ Os and $A\beta_{42}$ Os formed by $A\beta_{42}$ Ms aggregation on the membrane's surface. These channels are most likely formed by two distinct types of $A\beta_{42}$ Os, produced in different aggregation pathways. Freshly-prepared $A\beta_{42}$ Ms, added to the lipid bilayer, aggregated on the bilayer surface, while the pre-formed $A\beta_{42}$ Os aggregated in the bulk solution before their addition to the lipid bilayer. Lipid bilayers catalyze $A\beta$ aggregation^{179–181} (this effect is discussed below). Therefore, another possibility is that the aggregation pathways of $A\beta_{42}$ Ms and $A\beta_{42}$ Os were the same, but ion channel-forming $A\beta_{42}$ Os in the two cases were produced at different aggregation stages. However, these two hypotheses are yet to be verified.

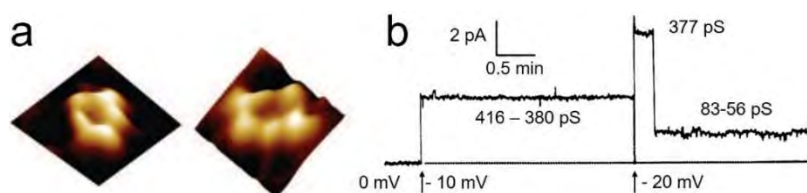


Figure 1.12. (a) AFM images of the ion channels formed in the DOPC membrane by $A\beta_{40}$ Os [adapted from ¹⁶²]. (b) Multiple electrical conductance states of ion channels formed by $A\beta_{40}$ Os in the lipid membrane. Each conductance state is labeled with its conductance value expressed in pS [adapted from ¹⁷⁴].

The above discussion demonstrates that $A\beta_{42}$ Os form ion channels in the membrane, while such behavior for $A\beta_{40}$ Os is still ambiguous. The effect of membrane composition on the $A\beta$ -membrane interaction outcome can be ruled out because, in these cases,^{171,178} the same type of biomimetic system was used for studying membrane interaction with $A\beta_{42}$ and $A\beta_{40}$. This conclusion raises a question - what makes $A\beta_{42}$ Os more effective in forming ion channels in comparison with $A\beta_{40}$? $A\beta_{42}$ Os are more toxic,^{22,23} and the $A\beta_{42}$ aggregation pathway is different from that of $A\beta_{40}$.^{24–26} $A\beta_{42}$ contains two additional hydrophobic amino acids at C-terminus in comparison to $A\beta_{40}$. As mentioned above, increased hydrophobicity of $A\beta_{42}$ Os correlates with their toxicity. However, the mechanism of this phenomenon is still unknown. There are two possibilities to consider. The increased hydrophobicity of $A\beta_{42}$ Ms might be the reason for the formation of structurally unique $A\beta_{42}$ Os in solution bulk, more capable of forming ion channels compared to $A\beta_{40}$ Os. Structural comparison of $A\beta_{40}$ Os and $A\beta_{42}$ Os produced under identical conditions could confirm or negate this hypothesis. The other possibility is that the increased hydrophobicity of $A\beta_{42}$ Ms stimulates their interaction with the membrane hydrophobic core,

thus enhancing A β ₄₂Ms rearrangement into ion channel-forming A β ₄₂Os. However, this aspect also requires further research to be elucidated.

1.3.2. Lipid extraction from bilayer lipid membranes

In the lipid extraction mechanism, a toxic peptide binds to the membrane surface and then extracts the membrane lipids (Figure 1.11b). High-speed AFM imaging showed that a mutant form of A β ₄₂Os dissolve the membrane composed of POPC/Chol/SM/GM1.¹⁸² The diameter and height of these oligomers were ~17.8 and ~9.6 nm, respectively. Moreover, A β ₄₂Os extract lipids from the egg PC/Chol/GM1 lipid bilayer (Figure 1.13), while A β ₄₂Ms and A β ₄₂Fs are inert towards the membrane.¹⁶⁴ Molecular weight and diameter of these toxic A β ₄₂Os was 30-400 kDa and 10-12 nm, respectively. The pores formed are significantly larger (~50 nm in diameter) than ion channels (1-2 nm¹⁶²). The same lipid extraction mechanism was reported but named as detergent-like solubilization, membrane dissolution, membrane fragmentation, or lipid uptake by A β .^{164,167,168,182,183} Mixing of A β ₄₀Ms with POPC/POPG/Chol lipids before lipid vesicle formation (pre-incorporation) leads to the formation of A β -lipid complexes because of A β ₄₀-induced vesicles disruption.¹⁸³ The TEM imaging showed that only 4-h incubation was required for membrane disruption and formation of short A β ₄₀ protofibrils. Noteworthy, the resolution of the TEM image was insufficient to resolve smaller aggregates. On the other hand, mixing A β ₄₀Ms with pre-formed lipid vesicles (external addition) and their incubation for 46 h resulted in A β fibrillation on the membrane surface without the membrane disruption. Continuation of this study showed that the pre-incorporated (membrane-disrupting) A β forms were rich in β -sheets, while externally added (fibrillating) A β forms were unstructured (rich in random coils).^{167,168} Moreover, the CH₂ group of lipids interacts with the C α nuclei of Asp23 and Ser26, suggesting that the A β -lipid binding in a complex is residue-specific. Additional investigations attempted to explain the difference in lipid vesicle interaction with the pre-incorporated and externally added A β ₄₀ by studying the influence of peptide-to-lipid (P-to-L) ratio on these interactions (see discussion in the "Influence of bilayer lipid membrane properties on A β -membrane interaction" section, below).¹⁶⁷

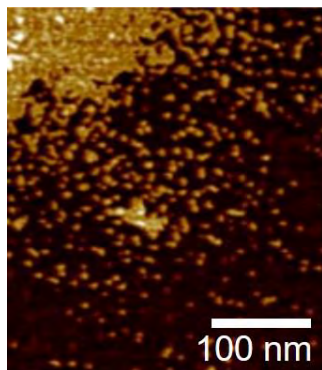


Figure 1.13. The AFM image of the (egg PC)/cholesterol/GM1 membrane after lipid extraction by A β ₄₂Os [adapted from ¹⁶⁴].

1.3.3. Non-specific bilayer lipid membrane permeation

Some studies on lipid bilayer permeation by A β do not support any specific permeation mechanism like the pore formation or the lipid extraction mechanism. In these studies, the membrane permeation mechanism is not specified. Therefore, the present section devoted to this kind of research is named a non-specific BLM permeation.

Unlike A β_{42} Ms or A β_{42} Fs, only A β_{42} O permeate lipid bilayers composed of a POPC/biotinylated POPC mixture.⁶¹ Unfortunately, no details on the secondary structure or size of these A β_{42} forms were provided. Further research showed that a mixture containing monomers and small globular oligomers of a height of 0.5-2.0 nm permeated the POPC/biotinylated POPC lipid bilayer. In comparison, the mixture containing globular oligomers and elongated protofilaments, with a height of 0.4-1.0 nm and a length of several hundreds of nm, caused inflammation of microglia cells.¹⁸⁴ These results suggest that the mechanism of the A β O toxicity depends on the aggregates' size. The activity of small oligomers (lipid bilayer permeation) was inhibited by the antibody that targets the C-terminal regions. On the other hand, the activity of protofilaments (cell inflammation) was hindered by the antibody that targets the N-terminal regions. Evidently, C- and N-terminal residues in small oligomers and protofilaments, respectively, were solvent exposed, thus suggesting that significant structural differences between them govern their respective toxic effects. Interactions of small A β aggregates, extracted from cerebrospinal fluid (CSF) of healthy (control) individuals, and large A β aggregates, extracted from CSF of the mild cognitive impairment (MCI) and AD individuals, were studied.¹⁸⁵ MCI is conceptualized as a stage preceding AD.¹⁸⁶ CSF from healthy individuals contained globular aggregates only (Figure 1.14a). CSF from MCI and AD individuals consisted of globular and elongated aggregates (Figures 1.14b and 1.14c). Notably, the elongated aggregates originating from individuals with MCI and AD differed in size. That is, the elongated aggregates from MCI individuals termed protofilaments were 0.3-1.0 nm high and 50-100 nm long. On the other hand, CSF of AD individuals contained a small fraction of protofilaments and a high population of the 1-3 nm high elongated aggregates, termed protofibrils. The length of both protofilaments and protofibrils characteristic of AD individuals ranged from 50 up to 400 nm. Apparently, the protofilaments present in AD individuals are much longer than those present in MCI individuals. This study confirmed the size-dependent difference in the A β toxic actions showing that small aggregates permeate the cell membrane (Figure 1.14d), while large aggregates induce cell inflammation (Figure 1.14f). However, the cell membrane permeation was not associated with globular but with elongated aggregates,¹⁸⁵ in contrast to the previous study.¹⁸⁴ The cell membrane permeation was inhibited by the C-terminus targeting antibody (Figure 1.14e). The cell inflammation by protofibrils was inhibited only by the N-terminus targeting antibody (Figure 1.14g).

It has been demonstrated successfully that small A β aggregates permeate the lipid bilayer, while large A β aggregates induce cell inflammation. However, it has not been explained why these actions were associated with globular¹⁸⁴ and elongated¹⁸⁵ aggregates, respectively. C-terminal targeting antibodies efficiently inhibit lipid membrane permeabilization by small globular

oligomers¹⁸⁴ and small protofilaments¹⁸⁵, indicating that both forms have solvent-exposed C-terminal residues. These results suggest that A β permeation through the membrane is independent of A β aggregates shape, but only aggregates with C-terminal residues exposed can exert it. Notably, the N-terminus targeting antibody also inhibits lipid bilayer permeation though less than the C-terminal targeting antibody.¹⁸⁵ However, cell inflammation was only observed in the presence of protofibrils with the N-terminal residues exposed. In mature fibrils, the N-terminus is exposed while C-terminus is hidden.⁴⁶ Therefore, it is inaccessible to the C-terminus active antibodies. This property might explain why the cell inflammation, caused by large protofibrils, was inhibited only by N-terminus targeting antibody. Overall, these results indicate that the toxicity mechanism depends on A β aggregates' structure, i.e., whether their C- or N-terminal residues are exposed. However, the origin of the exposition of C- and N-terminal residues is under question. There might be two possibilities.

One possibility is that protofilaments and protofibrils are formed by structurally distinct subunits ("seeds") with C- and N-terminal residues exposed. Conversion from soluble oligomers to fibril seeds involves β -strands rotation by 90°. ⁴³⁻⁴⁵ In this particular A β_{42} O model, the packing of adjacent β -sheets is in a "face-to-back" arrangement with more C-terminal residues exposed, while in A β_{42} F, the C-terminal region is buried inside.⁴⁴ This model suggests that A β_{42} O_s convert into fibril seeds with N-terminal residues exposed. These seeds aggregate into elongated structures with exposed N-terminal residues like protofibrils and fibrils. However, this does not explain the formation of protofilaments with C-terminal residues exposed. Presumably, the globular A β_{42} O_s can also assemble into elongated protofilaments while keeping their C-terminal residues exposed. This hypothesis would explain why membrane permeation is independent of the A β aggregate shape, i.e., why it is observed for both globular and elongated A β aggregates and why it is inhibited by C-terminal targeting antibody.

The other possibility is that the cell-inflaming protofibrils are formed by the intertwining of protofilaments with C-terminal residues exposed. During this process, protofilaments bind with each other with their C-terminal residues creating the C-terminal hydrophobic core of the newly produced protofibril, thus exposing its N-terminal residues. It was proposed that mature fibrils are produced in this way, i.e., by protofilaments intertwining.⁴⁶ This possibility could explain the formation of protofilaments with exposed C-terminal residues. Moreover, it could elucidate why, in some cases, elongated A β aggregates, like A β O_s, also permeate lipid membranes.

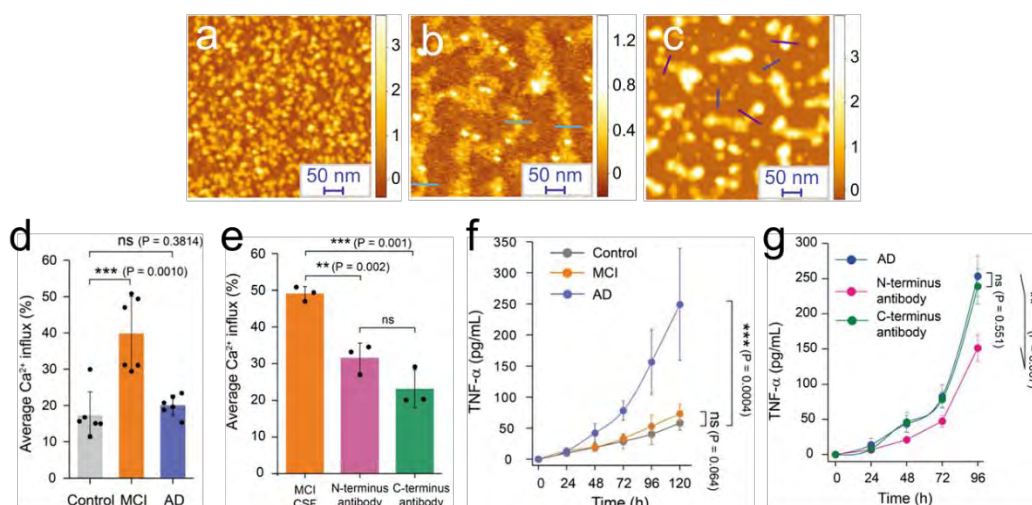


Figure 1.14. (a-c) AFM images of A β aggregates extracted from healthy (control) individuals, as well as individuals with mild cognitive impairment (MCI) and Alzheimer's disease (AD). (d) The membrane permeabilization assay for 16:0 – 18:1 PC and 18:1 – 12:0 biotin PC lipid vesicles in the presence of A β aggregates extracted from CSF of the control, MCI, and AD individuals. (e) The membrane permeabilization assay for 16:0 – 18:1 PC and 18:1 – 12:0 biotin PC lipid vesicles in the presence of A β aggregates extracted from CSF of MCI individuals as well as N- and C-terminus-targeting antibodies. (f) The cell inflammation assay for BV2 cells in the presence of A β aggregates extracted from healthy (control) individuals, as well as individuals with MCI and AD. (g) The cell inflammation assay for BV2 cells in the presence of A β aggregates extracted from AD individuals, as well as N- and C-terminus-targeting antibodies [adapted from ¹⁸⁵].

In any case, one may ask why different residue exposure drives different toxic actions? One possible explanation is the difference in hydrophobicity of the resulting pathogenic species. The C-terminus of A β is highly hydrophobic,^{187,188} while the N-terminus is hydrophilic.^{189,190} These structural features explain why smaller aggregates are more hydrophobic than larger aggregates. A polar physiological solution is not preferable for the smaller aggregates. Therefore, they permeate the lipid bilayer to incorporate themselves into the membrane hydrophobic core. On the other hand, large A β aggregates have their N-terminal residues exposed, which makes them hydrophilic. Therefore, they do not incorporate into the membrane, and they can stay on its surface.

Many other studies suggest the correlation between A β O's hydrophobicity and toxicity.^{191–193} The increase in surface hydrophobicity of (β -sheet)-rich oligomers of E22G (arctic) A β ₄₂, a variant of A β ₄₂, correlates with the increase in the cell death caused by the cell membrane permeabilization.¹⁹¹ Moreover, hydrophobicity-dependent and size-independent A β ₄₂O's toxicity was demonstrated.¹⁹² For this purpose, two types of A β ₄₂O's with similar sizes (~6.1 nm) and secondary structures (no β -sheet, only random coils) but different hydrophobicity were produced. These A β ₄₂O's exhibited different toxicity levels, i.e., only oligomers of higher hydrophobicity exhibited toxic activity towards PC12 cells and increased conductance of L- α -

phosphocholine lipid bilayers.¹⁹² This study is not the only one reporting toxic A β O_s that lack an ordered structure. A β ₄₂O_s with both the β -sheet^{194–196} and random coil secondary structure exhibit toxicity towards the phospholipid membrane.^{188,192,197}

The combinatorial change of A β ₄₀ aggregates' hydrophobicity and size was correlated with their ability to permeate the lipid membrane.¹⁹³ The increase in the A β ₄₀ aggregates size and surface hydrophobicity was associated with both increased cellular toxicity and permeation of the membrane composed of 1,2-dioleoyl-*sn*-glycero-3-phosphoethanolamine (DOPE)/1,2-dioleoyl-*sn*-glycero-3-phospho-L-serine (DOPS)/DOPC lipids. The correlation of large aggregates with increased toxicity is in agreement with some studies¹⁹⁸ but contradicts others.^{62,63,184,185,192} Noteworthy, the size of these aggregates was determined by dynamic light scattering (DLS) measurements. The DLS results can be misleading for heterogeneous samples like A β because they show the average size of all aggregates in the sample (not size distribution).¹⁹⁹ Moreover, the particle shape is assumed to be spherical, which is not valid for all A β aggregates. Therefore, DLS is not a technique suitable for examining anisotropic particles like elongated A β forms, and the DLS results should be verified using a different technique.²⁰⁰

The two studies providing the hypothesis that large aggregates are more toxic^{193,198} showed that their aggregates differed in shape, i.e., globular oligomers vs. elongated protofibrils supporting the shape-independent A β toxicity. Both the size and shape of A β aggregates might depend on the aggregation pathway. A β aggregation can follow many different pathways (Figure 1.3).^{34–42} Some of those involve forming short protofilaments and protofibrils that intertwine with each other to form A β Fs. In contrast, in other pathways, globular oligomers directly assemble into A β Fs, bypassing the formation of protofilaments and protofibrils.^{49,50} Therefore, a similar number of monomeric subunits can rearrange into aggregates of different sizes and shapes because they follow different aggregation pathways. This inference could explain why many studies indicated A β O_s of various sizes and shapes to be either toxic or non-toxic. One difficulty in establishing the size- and shape-toxicity correlation is the lack of consensus on A β aggregates' classification according to their size, molecular weight, and shape. Each research group classifies A β aggregates into small and large based on their size measurements. Moreover, it is unclear whether A β protofilaments and protofibrils should be regarded as A β O_s or A β Fs or separate classes. Providing an official classification of A β aggregates would facilitate the comparison of published results and determination of the size- and shape-toxicity correlation.

As mentioned above, both small, globular A β M_s and large, elongated A β Fs are not toxic. However, intermediate aggregates formed along the aggregation pathway are toxic. This behavior implies that significant structural changes occur at two steps of the aggregation, i.e., during aggregation of non-toxic A β M_s into toxic A β O_s and conversion of toxic A β O_s into non-toxic A β Fs. First, unfolded A β M_s transform into the (β -sheet)-rich A β O_s. Moreover, these A β M_s may form transiently stable α -helical A β M_s before converting to A β O_s rich in β -sheets. Next, β -strands of A β O_s rotate by 90° to create fibril seeds that elongate into A β Fs.^{43,195,201} These results indicate that toxic A β O_s are transiently stable structures that lose their toxicity upon conversion

to fibril seeds. However, this inference does not explain the formation of toxic A β O_s lacking the β -sheet structure.^{188,192,197} Different experimental conditions either stimulate various aggregation pathways or simply render structurally different A β M_s that prefer to follow unique aggregation pathways. In both cases, toxic A β aggregates of different shapes, sizes, and secondary structures are produced along these different aggregation pathways, making the size- and shape-toxicity correlation challenging. However, to the best of the author's knowledge, there is no study demonstrating toxic A β aggregates that are not hydrophobic. This inference suggests that the critical moment for A β toxicity along any aggregation pathway is when the aggregates with the highest surface hydrophobicity are formed. These aggregates might have different shapes, sizes, secondary structures, and be formed at different aggregation stages. This hypothesis would explain the conflicting results of the studies reporting toxic A β O_s of different shapes, sizes, and secondary structures.

1.3.4. Influence of bilayer lipid membrane properties on A β -membrane interaction

As mentioned above, alterations in the lipid rafts are associated with neuronal loss and neurodegeneration.¹¹⁴ Therefore, understanding how changes in the composition of the lipid raft-mimicking membranes affect their interaction with A β is essential.

Toxicity of mutant A β ₄₂ (MA β) peptide, in which cysteine replaces glycine as the 37th residue, was studied.^{182,202} A high-speed AFM imaging showed that MA β form oligomers (MA β O_s) with average diameter and height of \sim 20 and \sim 10 nm, respectively.¹⁸² These MA β O_s are very stable and do not aggregate into A β F_s. The study of the MA β O_s interaction with lipid bilayers of different lipid compositions revealed that MA β O_s were inactive toward the POPC/Chol/SM bilayer.¹⁸² Replacement of Chol with GM1 in the lipid bilayer resulted in MA β O_s adsorption on the bilayer surface, without compromising the membrane integrity. The addition of both Chol and GM1 into the lipid bilayer resulted in MA β O_s-induced membrane destruction via the lipid extraction mechanism. Other studies demonstrated that only Chol presence in the membrane is necessary for MA β O_s binding to the lipid bilayer.²⁰² Interactions of MA β monomers (MA β M_s) and MA β O_s, as well as two other A β ₄₂ variants, with lipid membranes, were compared.²⁰³ Interestingly, both MA β M_s and MA β O_s permeate the 1,2-dioleoyl-*sn*-glycero-3-phospho-(1'-rac-glycerol) (DOPG) but not DOPC vesicles. Under physiological conditions, A β ₄₂ is negatively charged. Therefore, it might seem surprising that the negatively charged A β ₄₂ prefers binding to negatively charged lipids than to zwitterionic lipids. However, this higher affinity has already been demonstrated.^{181,204–206} The reason for this phenomenon is the hydrogen bonding of A β ₄₂ side chains with the surface-exposed OH groups in DOPG lipids' heads rather than electrostatic interaction. The same interaction was proposed in the case of A β binding to gangliosides, also rich in OH groups.^{204,207} The A β ₄₂ aggregation is significantly accelerated if the Chol content in the 1,2-dimyristoyl-*sn*-glycero-3-phosphocholine (DMPC) and DMPC/1,2-dimyristoyl-*sn*-glycero-3-phosphoethanolamine (DMPE) vesicles is increased (Figure 1.15).²⁰⁸ Apparently, the A β interaction with lipid membranes depends on the lipid composition even though membrane Chol's role is ambiguous, i.e., whether A β binds to Chol-containing membranes or not.^{182,202}

Some studies disagree with the weak binding of A β ₄₂ to zwitterionic lipids.^{209–211} For instance, α -helical A β ₄₀Ms not only bind but also perturb the POPC bilayer while changing its secondary structure to β -sheet.²⁰⁹ Moreover, they induce spiky, fast cation channel formation in the POPC/POPE membranes. A β ₄₂ incurs perturbation in both the genuine POPC and POPC/SM/Chol vesicles.²¹⁰ Interestingly, 1,2-dilauroyl-*sn*-glycero-3-phosphocholine (DLPC) vesicles inhibit A β ₄₀ aggregation by stabilizing unstructured aggregates that disrupt both DLPC vesicles and bilayers via the lipid extraction mechanism.²¹¹ On the other hand, the DOPC and POPC membranes accelerate A β ₄₀ aggregation, causing (β -sheet)-rich A β Fs to be formed within 24 h.

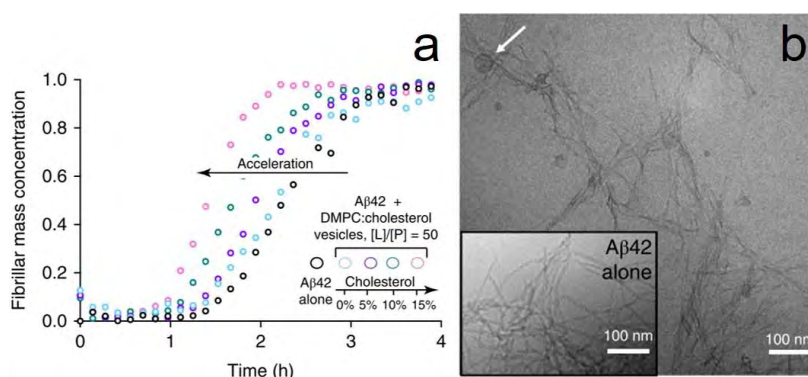


Figure 1.15. (a) Thioflavin T (ThT) dye fluorescence kinetic profiles for the A β ₄₂ aggregation in the presence of either DMPC or DMPC/Chol vesicles containing cholesterol of increasing concentrations up to 15%. (b) TEM images of A β ₄₂Fs formed in the (inset) absence and presence of DMPC/Chol vesicles containing 15% of Chol. The arrow points toward DMPC/Chol vesicle [adapted from ²⁰⁸].

Remarkably, DLPC lipids remodel pre-formed A β ₄₀Fs. This remodeling leads to the formation of thin fibrils incapable of binding to the thioflavin T (ThT) dye. This result implies that DLPC-remodeled fibrils are structurally unique even though they contain β -sheets, a secondary structure typical of A β Fs.²¹¹ Presumably, in DLPC-remodeled A β ₄₀Fs, the ThT binding sites are occupied by DLPC lipids. However, this hypothesis remains to be confirmed.

A β ₄₀Ms either perturb the POPC membrane²⁰⁹ or aggregate on its surface without permeating it.²¹¹ Most likely, this contradiction arises from different sample preparation procedures used in these two studies. In both studies, the A β concentration and P-to-L ratio were varied depending on the type of measurement performed. The A β aggregation rate depends on the A β concentration. Therefore, it is essential to keep the A β concentration and P-to-L ratio constant so that all measurements' results could be supplemented.

The catalytic effect of Chol-containing vesicles on the A β ₄₂ aggregation was studied.²⁰⁸ The lipid vesicles used were composed of lipids with PC heads and acyl chains of different lengths and degrees of unsaturation. Apparently, the higher the A β ₄₂ aggregation rate, the higher is the degree of unsaturation in lipids (DMPC < POPC < DOPC).²⁰⁸ This effect is attributed to the

increased bulkiness and exposure of acyl chains in unsaturated lipids. Additionally, the lipid vesicle size has no impact on the A β ₄₂ aggregation rate. The initially disordered globular A β ₄₂ form (β -sheet)-rich fibrils after 12 h of aggregation. The ThT fluorescence analysis confirmed that variation of the P-to-L ratio to increase lipid concentration resulted in acceleration of the A β ₄₂ aggregation.²⁰⁸

Some studies highlight the significance of electrostatic interaction between A β and lipids.^{204–206} Variations in pH of the A β /lipid vesicle solution induce variations in electrostatic interaction of A β M with 1,2-dioleoyl-3-trimethylammonium-propane (DOTAP) and egg yolk PG lipids.²⁰⁴ This phenomenon is absent for the lipid raft-mimicking membrane composed of Chol, SM, and GM1. The strength of the electrostatic interaction of A β M with lipid monolayers can vary significantly, ranging from strongly attractive (A β -DOTAP in PBS), through moderately attractive (A β -1,2-dipalmitoyl-*sn*-glycero-3-phospho-(1'-*rac*-glycerol) (DPPG) and (A β -DPPC in water), to strongly repulsive (A β -DPPG in PBS).²⁰⁵ The change in the peptide charge and charge screening effects, adjusted by the appropriate change of pH and ionic strength of the solution, respectively, affects the A β M-lipid interaction strength because of its electrostatic nature. The increase in the bilayer negative surface charge, caused by the increase in the DMPG content in the DMPC/DMPG mixture, leads to the increase in the amount of (β -sheet)-rich A β ₄₀ bound to the membrane surface.²⁰⁶ Apparently, positively charged A β ₄₀ residues (Arg5, Lys16, and Lys28) are electrostatically attracted to negatively charged lipid heads. The electrostatic interaction occurred when A β ₄₀M were externally added to the pre-formed lipid vesicles. However, when A β ₄₀M were pre-mixed with lipids before forming lipid vesicles, the C-terminal hydrophobic part of the peptide was inserted into the membrane.²⁰⁶ In this case, the increase in the anionic lipid content leads to electrostatic anchoring of charged A β ₄₀ residues with lipid heads. Consequently, the α -helical secondary structure content increases, and the hydrophobic peptide segments insert further into the membrane.

GM1 is an essential component of lipid rafts present in neuronal membranes. It influences A β -membrane interaction.^{212,213} An increase in the GM1 content in the cell membrane increases the amount of A β ₄₂O_s adsorbed on the membrane surface, stimulating the cell membrane permeation and transfer of Ca²⁺ across the membrane.²¹² However, a decrease in the GM1 concentration decreases this neurotoxic effect. This toxicity can be inhibited by blocking GM1 interaction with A β ₄₂O_s using Cholera Toxin Subunit-B. This blocking evidences the importance of GM1 in the A β ₄₂O_s toxicity. The supported DMPC bilayers and vesicles perturbations by A β ₄₀O_s are enhanced in the presence of GM1.²¹³ This A β ₄₀O_s-lipid interaction results in the formation of hexagonal micelles. Moreover, the GM1 presence stimulates the A β ₄₀M insertion into the DPPC/GM1 monolayer.²¹⁴ At low GM1 concentration, A β ₄₀ disrupts the membrane morphology, causing the fluid phase expansion. In contrast, A β ₄₀ disrupts both the fluid and condensed (gel phase) domains at high GM1 concentrations. Variation in pH and ionic strength of water solutions may lead to either strong attractive or repulsive A β -GM1 interaction, indicating the interaction's electrostatic nature. Surprisingly, the incubation of A β ₄₀ with POPC/GM1 vesicles results in A β fibrillation.²¹⁴ Why does GM1 stimulate disruption of DPPC monolayers by A β ₄₀, while when

incorporated into POPC vesicles, it enhances A β fibrillation? One possible explanation originates from the difference in the A β ₄₀ concentrations employed in the two experiments. In the experiments involving DPPC monolayers, the A β ₄₀ concentration was 250 nM, while in experiments with POPC vesicles, it was 100 μ M. However, whether this was the cause of the discrepancy remains to be elucidated.

Some studies suggest that A β ₄₀ interaction with lipid vesicles is independent of lipid composition, but the P-to-L ratio influences it.²¹⁵ At a high P-to-L ratio, the A β ₄₀ converts from the α -helix to the β -sheet secondary structure within 4 h, without forming protofibrils or fibrils. Only the (β -sheet)-rich A β ₄₀O_s are formed, which induce the membrane content leakage during this time frame. At a low P-to-L ratio, the peptide's structural conversion from α -helix to the random coil is accompanied by the formation of off-pathway A β ₄₀O_s. These A β ₄₀O_s stimulate the mixing of lipid molecules between neighboring lipid vesicles, resulting in their fusion. Other studies by the same group^{166,167} associated a low P-to-L ratio with the same lipid mixing-vesicle fusion mechanism. However, in these cases, this mechanism was associated with A β ₄₀M_s, and not with off-pathway A β ₄₀O_s, like in the previous study.²¹⁵ Interestingly, both the off-pathway A β ₄₀O_s from the former study²¹⁵ and the A β ₄₀M_s from the latter,^{166,167} that induced lipid mixing-vesicle fusion, were unstructured, i.e., they had a high content of the random coil secondary structure. On the other hand, (β -sheet)-rich A β ₄₀O_s from the previous study²¹⁵ induced leakage of the membrane content. Therefore, these studies suggest that different A β -lipid interactions result from variations in the A β secondary structures and the P-to-L ratio. However, these results are contradicted by previous studies, which show that unstructured A β O_s could also permeate lipid membranes.^{188,192,197} Therefore, this rules out the secondary structure of A β O_s as a factor influencing the A β -lipid interaction. However, these studies strongly indicate that A β -lipid interaction is affected by the P-to-L ratio.^{166,167,208,215} The overall conclusion is that a low P-to-L ratio facilitates A β aggregation, and a high P-to-L ratio facilitates membrane permeation by A β aggregates. It would be interesting to define the P-to-L ratio's threshold value, thus determining the border between these two processes. Determining the P-to-L ratio value at which the membrane starts decomposing would unravel the A β concentration on the membrane surface lethal to the cell.

1.4. The objective of the thesis

A β O_s are the most toxic forms of A β .⁸³ However, there are A β O_s of various sizes, shapes, and structures. Therefore, it is not clear which type of A β O_s exerts a particular toxic activity. Some studies imply that small^{62,63,184,185} and highly hydrophobic^{191-193,216} A β O_s are most toxic. On the contrary, other studies suggest that large A β O_s are more harmful than the small oligomers.^{193,198} Some studies indicate a lack of toxicity difference between small and large A β O_s, but their respective toxic activities are different. That is, small A β O_s permeate lipid membranes, while large A β O_s induce cell inflammation.^{184,185} Interestingly, a size-independent difference in A β O_s toxicity levels, somewhat influenced by distinct A β O conformations, was also shown. Both (β -

sheet)-rich A β O_s¹⁹⁴⁻¹⁹⁶ and unstructured A β O_s (abundant in a random coil secondary structure)^{188,192,197} are toxic.

Evidently, there is a lot of discrepancy among A β -membrane studies, suggesting that further research is required. Identification of the A β -induced lipid membrane permeation mechanism is necessary to understand the AD pathophysiology and develop an effective therapeutic strategy against AD.

Therefore, the research goals of the present thesis are to unravel (i) the mechanism of A β -induced permeation of physiologically-relevant model cell membranes, (ii) the type of A β aggregate responsible for the membrane permeation, (iii) the morphological and structural properties of the toxic A β form, (iv) changes in the morphological, nanomechanical, and electrical properties of the membrane because of its damaging by A β , (v) changes in the conformation and orientation of membrane lipids resulting from their interaction with A β , and (vi) testing potential inhibitors of A β -induced membrane permeation.

A combination of single-molecule and bulk techniques were used to achieve these goals. Chapter 3 discusses the AFM study of A β -membrane interaction and unravels the mechanism of membrane permeation by A β O_s, the consequent changes in the membrane morphological and nanomechanical properties, and the type of toxic and non-toxic A β O_s. Chapter 4 describes the electrochemical and IR spectroscopy study of A β -membrane interaction that identifies the changes in the membrane electric properties, conformation and orientation of membrane lipids, and the A β secondary structure changes. Chapter 5 focuses on the electrochemical, AFM, and molecular dynamics (MD) study that identified a novel mechanism of inhibition of A β -induced membrane permeation, revealing a potential therapy for AD.

Chapter 2. Experimental section

2.1. Chemicals and materials

- 1,1,1,3,3,3-Hexafluoro-2-propanol (HFIP) for GC derivatization, purity $\geq 99.8\%$, from Sigma Aldrich
- 1-Thio- β -D-glucose, purity $\geq 98\%$, from Sigma Aldrich
- Au(111) electrodes from MaTeck
- BL-AC40TS cantilevers from Olympus
- Chloroform, HPLC grade, purity $\geq 99\%$, from Sigma Aldrich
- Desiccator with an attachment for a vacuum pump
- Deuterated TFA, purity $\geq 99.0\%$, from Eurisotop
- Deuterium oxide, purity $> 99\%$, from Sigma Aldrich
- Dimethyl sulfoxide (DMSO) Hybri-Max™, sterile-filtered, BioReagent, purity $\geq 99.7\%$, from Sigma Aldrich
- Disposable, Luer-lock, sterilized syringes of 5 ml volume from BD
- DIVAC 1.4 HV3C vacuum pump from Leybold
- Ethanol, purity $\geq 99\%$, from Linegal Chemicals
- Finnpiptette F1 pipettes of 100-1000 μ l and 2-20 μ l in volume equipped with Finntip Flex 200 and 1000 tips from ThermoFisher Scientific
- Human amyloid β (1–42) peptide from Bachem and rPeptide
- Isopropanol, ACS reagent, purity $\geq 99.5\%$, from Sigma Aldrich
- Magnetic discs (15 mm in diameter) from Ted Pella
- Methanol, HPLC grade, purity $\geq 99\%$, from Sigma Aldrich
- Milli-Q® water, 18.2 M Ω cm, from EMD Millipore
- Phosphate buffer saline (PBS) tablets from Sigma Aldrich
- Phospholipids, purity $> 99\%$, from Sigma Aldrich – brain total lipid extract (BTLE), 1,2-distearoyl-*sn*-glycero-3-phosphoethanolamine (DSPE), 1,2-dipalmitoyl-*sn*-glycero-3-phosphocholine (DPPC), Chol, SM, GM1
- Protein LoBind polypropylene tubes of 2 ml in volume from Eppendorf
- Qp-BioAC cantilevers from Nanosensors
- RTESPA-300 cantilevers from Bruker
- Trifluoroacetic acid (TFA), HPLC grade, purity $\geq 99.0\%$, from Sigma Aldrich
- V1 grade mica discs (12 mm in diameter) from Ted Pella
- Whatman Puradisc PTFE, non-sterile syringe filters of 25 mm in diameter and 0.1 μ m porosity from GE Healthcare

2.2. Experimental techniques and methods

2.2.1. Supported lipid bilayer preparation

Most of the techniques used in the present study require sample deposition on a solid substrate. Supported lipid bilayers can be deposited using a combination of Langmuir-Blodgett/Langmuir-Schaeffer or the vesicle fusion technique (Figure 2.1).^{144,217} In the present thesis, the vesicle fusion technique was utilized. The technique involves adhesion, fusion, and then rupture of unilamellar vesicles to produce a lipid bilayer at the substrate surface.^{218,219} This process is significantly influenced by the lipid vesicles' radius. If the radius is smaller than the critical adsorption radius, the vesicles do not adsorb on the substrate surface. Moreover, if the radius is larger than the rupture radius, the vesicles rupture and spread to form a bilayer. Suppose the vesicle radius is larger than the adsorption but smaller than the rupture radius. In that case, vesicles adsorb at the substrate surface and fuse to produce larger vesicles that rupture and spread to form a bilayer. The vesicle fusion method is convenient for the protein/peptide incorporation into the lipid bilayer. Moreover, it allows for studying the lipid bilayer interaction with proteins/peptides.

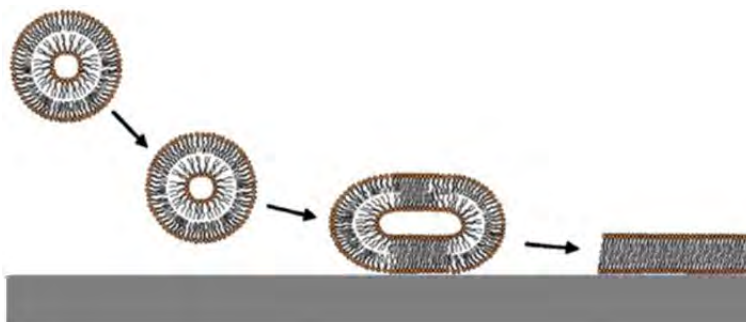


Figure 2.1. Supported lipid bilayer preparation via the vesicle fusion technique [adapted from ¹⁴⁴].

2.2.2. Atomic force microscopy

Atomic force microscopy (AFM) uses a cantilever with a sharp tip to probe the sample surface and acquire information about the sample morphology (Figure 2.2). The AFM tip scans the sample surface in the raster fashion, i.e., it scans across one horizontal scan line (X direction in Figure 2.2) at a time, slowly moving along the vertical scan line (Y direction in Figure 2.2). Every line is divided into pixels, and for each pixel, the tip-sample interaction forces are monitored. These forces cause cantilever deflection (bending). The cantilever deflection is monitored using a laser beam directed on the cantilever's back and reflected from it into a four-quadrant photodiode detector. The AFM user controls the extent of the cantilever deflection by defining the setpoint value. Deviations of the cantilever deflection from the setpoint (due to the tip-sample interactions) change the laser position on the detector. This change triggers feedback

electronics to drive piezoelectric elements in a vertical direction to compensate for any excessive cantilever deflections caused by the tip-sample interaction forces. The movement of piezoelectric elements along the vertical direction (Z direction in Figure 2.2) is used to obtain information about the sample height. This process is repeated for every pixel of the scanning area, providing the 3D map of the sample morphology.

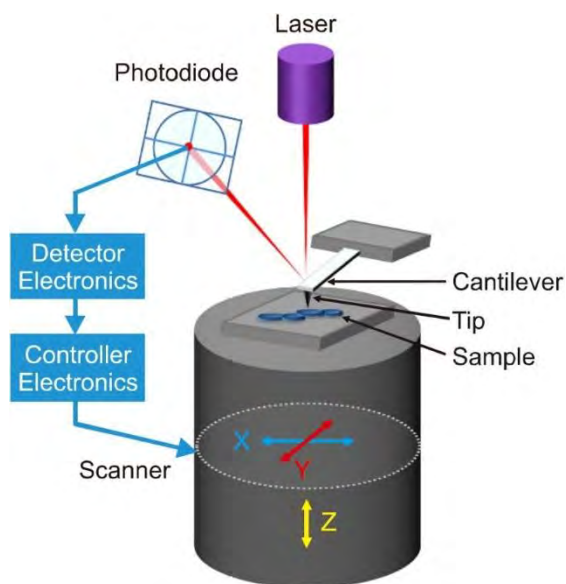


Figure 2.2. Schematic representation of an atomic force microscope [adapted from ²²⁰].

AFM cantilevers have different shapes (rectangular, triangular, etc.), and their length, width, and thickness typically range between 60-200, 10-40, and 0.3-2 μm , respectively. The AFM tip radius can range from a few to ~ 30 nm. The AFM cantilever can be considered a spring, and Hook's law defines the cantilever deflection as $F = kx$, where F is force, k is the elastic constant, and x is displacement. The piezoelectric elements can precisely regulate the cantilever deflection, causing displacements as small as 1 \AA up to 100 μm .²²¹ This means that AFM can record forces in the sub-pN range.²²² This sensitivity allows very gentle imaging force, a feature essential for studying delicate samples like biological molecules. Different forces might act during the tip-sample interactions (Figure 2.3a).²²³ These forces can be classified into attractive and repulsive forces. They depend on the tip-sample distance (Figure 2.3b). Attractive forces dominate at a large tip-sample distance, while repulsive forces dominate when the tip is close to the sample.²²¹ In the absence of an external electromagnetic field, van der Waals, short-range repulsive, capillary, the adhesive forces dominate.

AFM can operate in the contact, non-contact, and tapping mode (Figure 2.3c). In the contact mode, the tip is in contact with the sample while scanning the sample surface. In this mode, the AFM operates under a regime where strong repulsive forces ($\sim 1-10$ nN) dominate. In the non-contact mode, the oscillating AFM tip is brought close to the sample surface, typically a few to

tens of nanometers. At this tip-sample distance, the main tip-sample interaction forces monitored are weak attractive forces such as van der Waals forces. In the tapping mode (also known as the intermittent mode), the tip periodically contacts the sample surface and withdraws from it. Similarly, as in the non-contact mode, the change in either amplitude, frequency, or phase of the cantilever oscillation can be used as a feedback signal to record the sample topography and control the tip movement. The tapping mode is useful for studying loosely-bound molecules, like DNA and proteins.²²⁴

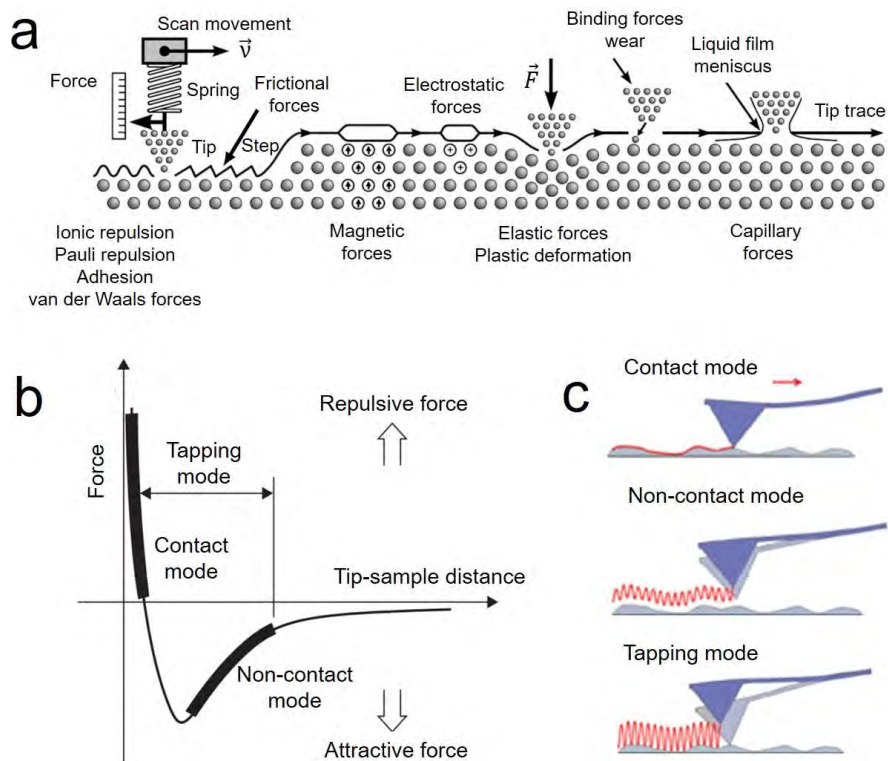


Figure 2.3. (a) Schematic representation of the AFM tip-sample interaction forces [adapted from²²³]. (b) Tip-sample interaction forces as a function of the tip-sample distance. (c) Scheme of the AFM imaging modes.

Moreover, AFM can operate in the force spectroscopy mode, known as the force-distance curve (FD curve) based AFM. In this mode, the AFM probe is ramped up and down on the sample surface by extending and retracting the scanner (Figure 2.4a). The cantilever deflection is recorded as a function of the scanner position in the vertical direction (Z direction in Figure 2.2). This relation can also be expressed as the tip-sample interaction force vs. tip-sample distance, forming the FD curve (Figure 2.4b). Two FD curves that correspond to the tip-sample interaction forces during the tip approach (red curve in Figure 2.4b) and the tip retraction (black curve in Figure 2.4b) are recorded for each image pixel. At position 1 in the approach curve, the probe is not in contact with the sample surface. The scanner moves in the Z direction, decreasing the tip-

sample distance, and at point 2, the tip contacts the sample. If the attractive tip-sample forces are higher than the cantilever spring constant, then the tip will "snap-in" contact with the sample, which manifests itself as negative force values at point 2 of the approach curve (not shown in Figure 2.4b). Further scanner movement in Z direction pushes the sample against the probe, causing the cantilever to bend up and increase the tip-sample interaction force until the setpoint value is reached (F_i force in Figure 2.4b). Next, the scanner moves in the opposite direction, thus causing the probe retraction. During the tip retraction from the sample surface, adhesive forces might bend down the cantilever, manifested as negative force values in the FD curve. At point 4 of the retraction curve (Figure 2.4b), the tip-sample adhesive force is equal to the force exerted by the probe. The negative force value at point 4 in the retraction curve is used to measure the tip-sample adhesion force. It can be exploited to do molecular recognition studies, measure chemical bonds' strength, capillary forces, etc.²²⁴ Further scanner movement allows the probe to overcome the tip-sample adhesion forces and "snap-off" the sample surface (point 5 in the retraction curve).

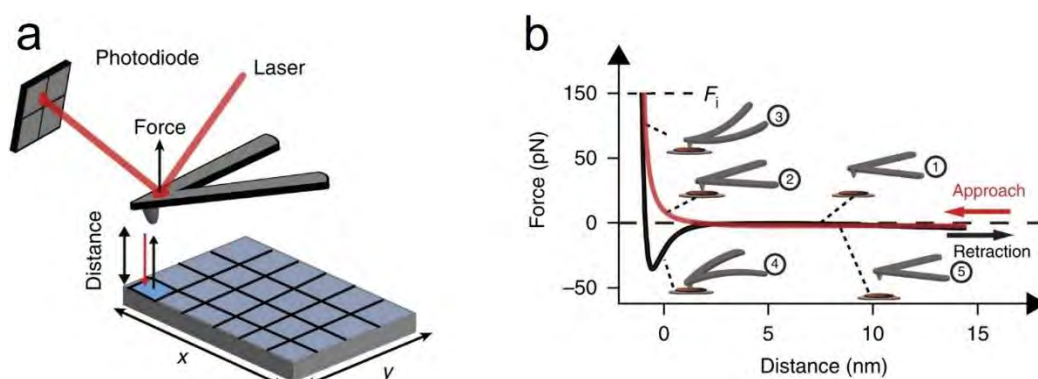


Figure 2.4. (a) Schematic representation of the force-distance curve-based atomic force microscopy operation and (b) force-distance curves [adapted from ²²⁵].

Analysis of the FD curves provides information about the sample nanomechanical properties (Figure 2.5). Young's modulus (YM) is a measure of the tensile stiffness of a material. The YM measurement is gaining importance in biology. For example, the YM values of healthy and cancer cells are different.^{226,227} To extract YM values from the FD curves, appropriate contact mechanics models must be used. Some of the most commonly used models include the Hertz,²²⁸ DMT,²²⁹ JKR,²³⁰ and Sneddon²³¹ models. The most widely used model for studying nanomechanical properties of biological samples is the Hertz model.²³² This model describes YM of a spherical sample in contact with spherical indenter as:

$$YM = \frac{3(1 - \eta^2)P}{4} \left(\frac{1}{R_i} + \frac{1}{R} \right)^{\frac{1}{2}} h^{-\frac{3}{2}} \quad (2.1)$$

where P is the load applied, η is Poisson's ratio, R_i is the indenter's radius, R is the sample's radius, and h is the indentation depth. Poisson's ratio is a measure of a material compression or expansion in the directions perpendicular to the applied force's direction. This ratio value can range from 0 to 0.5. Biological samples are treated as isotropic incompressible materials ($\eta = 0.5$).^{233,234}

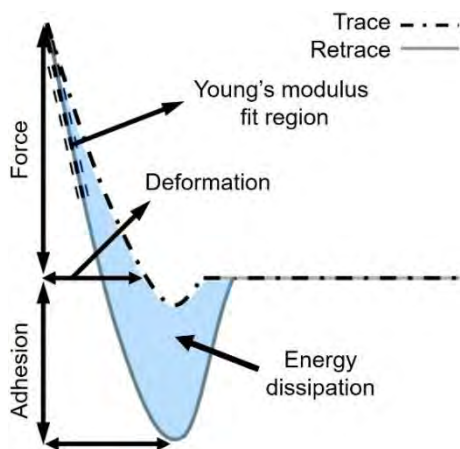


Figure 2.5. Force-distance (FD) curve regions relevant for determining the sample's nanomechanical properties [adapted from ²³⁵].

The Peak Force tapping mode is one of the newest tapping modes of AFM. The maximum force (F_i in Figure 2.4b), also called Peak Force, is used as the feedback signal. Therefore, in this mode, the cantilever force is directly controlled, minimizing the chance for the tip or sample damage. The cantilever resonance frequency in the regular tapping mode depends on the environment's nature (air or fluid), temperature, and the cantilever itself. Therefore, the cantilever must be tuned under the same conditions. In contrast, the Peak-Force tapping mode does not rely on the cantilever dynamics. Therefore, there is no need to determine the cantilever resonance frequency, an advantage particularly beneficial for the measurement in a fluid.²²⁴ The probe oscillates at a frequency significantly lower than its resonance frequency (typically 1-2 kHz). Such a slow tapping rate allows recording FD curve for each tap. This mode, known as Peak Force Quantitative Nanomechanical Mapping (PF-QNM) mode, allows simultaneous recording of topographic and nanomechanical maps.

AFM has two distinctive resolutions, i.e., lateral and vertical resolution. The lateral and vertical resolutions are ~ 1 and ~ 0.1 nm, respectively.²³⁶ Interestingly, high-speed AFM also provides a high temporal resolution of ~ 100 ms.

The vertical resolution depends on the detector's noise and thermal noise (thermal fluctuations) of the cantilever.²³⁷ The detector noise defines the minimum displacement of the laser on the detector. Using cantilevers with low spring constant solves this problem because these cantilevers deflect more under the same load, causing more evident laser position movement on

the detector, thus easing the force detection measurement. However, these soft cantilevers suffer more from thermal noise. Cantilevers with low spring constant experience more thermal drift with the temperature variation. The AFM laser heats the cantilever, causing these temperature variations.²²⁴

Three factors that affect the lateral resolution are instrument resolution, the precision of the piezo elements in the lateral direction, and the probe radius. The instrument resolution is expressed as a ratio of the scanning area size and the number of image pixels. Both the scanning area size and the number of image pixels should be adjusted according to the sample size so that the sample could be resolved. As mentioned above, the piezo elements have angstrom-level precision in controlling the cantilever movement, which is sufficient in most cases.²²¹ Therefore, the most significant parameter limiting the lateral (spatial) resolution of AFM is the probe radius. The AFM tip size and shape do not influence the scanned object's height, but they affect its lateral size. If an AFM tip radius of curvature is equal or higher than the scanned object's width, the tip's side is in contact with the sample sooner than the tip's apex (Figure 2.6a). The detector and feedback system react accordingly, causing an image artifact where the object's lateral size in the image is larger than its actual size. This artifact is known as the convolution effect. Therefore, the sharper the AFM tip, the more realistic is the object's lateral size obtained from the AFM image (Figure 2.6b).

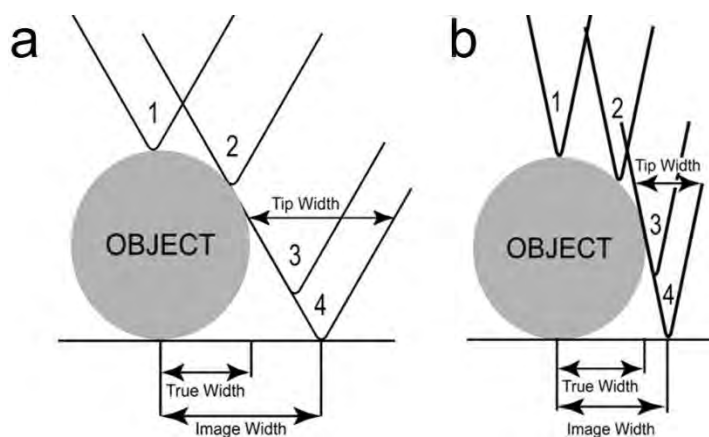


Figure 2.6. Schematic representation of AFM tip shape convolution with the shape of the object scanned using (a) blunt and (b) sharp AFM tip [adapted from ²³⁸].

2.2.3. Electrochemical methods

In membrane studies, electrochemical methods, as macroscopic interfacial techniques, provide average information about membrane integrity in the presence of toxins, thus supplementing the single-molecule information obtained by AFM. Moreover, these techniques provide information about the electric properties of lipid membranes.

2.2.3.1. Differential capacitance measurement

A conducting electrode coated with BLM can be treated as a parallel plate capacitor where the charge is accumulated on both sides of the membrane.¹⁰⁸ For this system, capacitance (C) is defined as:

$$C = \frac{\varepsilon\varepsilon_0}{d} \quad (2.2)$$

In this equation, ε and ε_0 are electric permittivity of insulating membrane hydrocarbons ($\varepsilon = 2$) and free space ($\varepsilon_0 = 8.85 \times 10^{-12} \text{ F m}^{-1}$), respectively, and d is the distance between the charged surfaces.

The charge of the metal electrode (σ_M) covered with adsorbed molecules is a function of the Gibbs surface excess (Γ) and applied potential (E). The differential of this charge is defined as:

$$d\sigma_M = \left(\frac{\partial\sigma_M}{\partial E}\right)_\Gamma dE + \left(\frac{\partial\sigma_M}{\partial\Gamma}\right)_E d\Gamma \quad (2.3)$$

Derivation of Eq. 2.3 against applied potential yields the expression for the differential capacitance (DC):

$$C = \frac{d\sigma_M}{dE} = \left(\frac{\partial\sigma_M}{\partial E}\right)_\Gamma + \left(\frac{\partial\sigma_M}{\partial\Gamma}\right)_E \frac{d\Gamma}{dE} \quad (2.4)$$

The differential capacitance has two contributions, i.e., true (C_{true}) and pseudo (C_{pseudo}) capacitance:

$$C_{\text{true}} = \left(\frac{\partial\sigma_M}{\partial E}\right)_\Gamma \quad C_{\text{pseudo}} = \left(\frac{\partial\sigma_M}{\partial\Gamma}\right)_E \frac{d\Gamma}{dE} \quad (2.5)$$

The measured capacitance corresponds to true capacitance in the potential range where surface coverage is constant ($d\Gamma/dE = 0$). This potential-independent capacitance is generally small for lipid bilayers ($\sim 1 \mu\text{F cm}^{-2}$).¹⁰⁸ Outside of this potential range, so-called pseudocapacitive peaks appear due to changes in the electrode charge or Gibbs surface excess (equivalent to the electrode surface coverage by adsorbed molecules). Therefore, these peaks indicate the adsorption-desorption of molecules present on the electrode surface.

The DC measurements can be used to assess BLM's quality and stability on the electrode surface.¹⁰⁸ These measurements provide three essential findings, i.e., (i) the potential range where BLM is stable on the electrode surface (the range where capacitance does not change), (ii) the minimum capacitance value in this stable potential range that indicates membrane quality (capacitance value higher than $1 \mu\text{F cm}^{-2}$ indicates the presence of the BLM defects), and (iii) the potential range where BLM detaches from the electrode surface (electrode wetting).^{108,153,239} During the electrode wetting, the BLM first becomes thicker because water incorporates into the

BLM, and then BLM detaches from the electrode surface. Interestingly, the neutron reflectivity study showed that BLM stays in the electrode vicinity after detaching from its surface.²⁴⁰

2.2.3.2. Immersion method

When surface coverage of the electrode is constant ($d\Gamma/dE = 0$, Eq. 2.3), the variation of the electrode potential causes a change in the free charge density as follows:

$$\sigma_M = \int_{E_{pzfc}}^E \left(\frac{\partial \sigma_M}{\partial E} \right)_T dE \quad (2.6)$$

The potential at which free charge is equal to zero is called the potential of zero free charge (E_{pzfc}).

The immersion method is useful for measuring E_{pzfc} of the metal or SAM-coated metal electrodes.²⁴¹ This method consist of recording current transients at different electrode potentials when the SAM-coated metal electrode contacts the electrolyte. These transients arise from the flow of charge to the metal-electrode interface to build the electrical double layer. Therefore, when the electrode contacts the electrolyte, the interface becomes charged, and σ_M can be obtained by integrating the immersion current (I) against time (t) at a given electrode potential as follows:

$$\sigma_M = \int_0^E I(E, t) dt \quad (2.7)$$

The information about the E_{pzfc} value is needed to determine the potential drop across BLM supported on the metal electrode.¹⁰⁸

2.2.3.3. Electrochemical impedance spectroscopy

Electrochemical impedance spectroscopy (EIS) is an electrochemical technique that measures the electrical impedance by applying harmonic perturbation as alternating current or voltage. The impedance (Z) is defined as:

$$Z = \frac{\Delta U}{\Delta i} \quad (2.8)$$

where ΔU and Δi are complex amplitudes of voltage and current, respectively. Impedance is a function of frequency. This dependence allows EIS to distinguish a single process of interest from other processes in the system. For example, the Helmholtz layer's contribution to the BLM impedance can be decreased by applying sufficiently high modulation frequency. Removal of this contribution allows studying the BLM impedance change because of BLM damage by membrane-permeating proteins.¹⁴⁵ This is an advantage of EIS over DC-based electrochemical techniques. EIS is a modeling technique, i.e., the appropriate equivalent electric circuit¹⁴⁵ model must be fitted to the measured EIS signal to interpret the EIS results. The equivalent electric circuit is a

virtual electric circuit model consisting of various electric elements like capacitors, resistors, etc. This model is designed to simulate the response of the real electrochemical system.

In membrane studies, a simple RC electric circuit represents simple systems like black lipid membrane systems.¹⁴⁵ That is because the black lipid membrane system consists of two ideally nonpolarizable (zero impedance) Ag/AgCl electrodes submerged into a high conductivity electrolyte solution separated by a lipid bilayer. This system is different from tBLM or fBLM, where the lipid bilayer is supported on a polarizable electrode (Figure 2.7a). The absence of a polarizable electrode underneath the membrane results in the electric current distribution in fBLM quite different from that in black lipid membranes. For tBLM or fBLM, the capacitance is defined as follows:

$$C = C_{mH} = (C_m^{-1} + C_H^{-1})^{-1} \quad (2.9)$$

where C_m and C_H are capacitance of the membrane and the Helmholtz layer, respectively. Joint contribution from these capacitances is denoted as C_{mH} . Notably, tBLMs and fBLMs deviate from the idealized RC model behavior in the low-frequency region of EIS spectra. The capacitance dispersion on the electrode surface arises from the atomic-scale surface heterogeneities.²⁴² To take it into account, C_{mH} is substituted by the constant phase element (CPE_{mH}), and its impedance (Z_{CPE}) is defined as follows:

$$Z_{CPE} = -\frac{1}{Q(j\omega)^\alpha} \quad (2.10)$$

where Q is the constant phase element coefficient ($Q = |CPE_{mH}|$), j is the complex unit, $j = (-1)^{0.5}$, and ω is the cyclic frequency. If α is close to 1, the impedance is dominated by capacitance, and Q can be considered a capacitance. However, if α is close to 0, the impedance is dominated by resistance. Therefore, defect-less tBLM or fBLM are represented by a model involving an equivalent electric circuit shown in Figure 2.7a. This circuit combines electric elements that represent solution resistance (R_{sol}), membrane constant phase element (CPE_m), and membrane resistance (R_m). The model implies that electric potential is the same at all points of the metal-electrolyte interface, i.e., the space separating the lipid bilayer and the Helmholtz layer is equipotential.

In the presence of membrane defects, the ionic current flowing through membrane defects bends because of the significant impedance of the underlying electrode surface (Figure 2.7b). The electric field propagating along the Helmholtz layer's outer plane is attenuated due to the displacement current flowing through the Helmholtz layer. Consequently, the equipotentiality is not satisfied, and the electric field distribution changes. An electrolyte layer of a size comparable to that of the membrane separates the membrane from the electrode surface. This submembrane (spacer) region is only partially hydrated, which means that its polarity is lower than that of the bulk solution. Consequently, mobility and specific electrolyte conductance in such confined, water-depleted areas are significantly lower than that in the bulk solution.²⁴³

The equivalent electric circuit shown in Figure 2.7b is used to consider the alternative conductance pathway present in the defected membrane. This model consists of R_{sol} , CPE_m , R_m , and the constant phase element corresponding to the spacer region (CPE_{sp}).

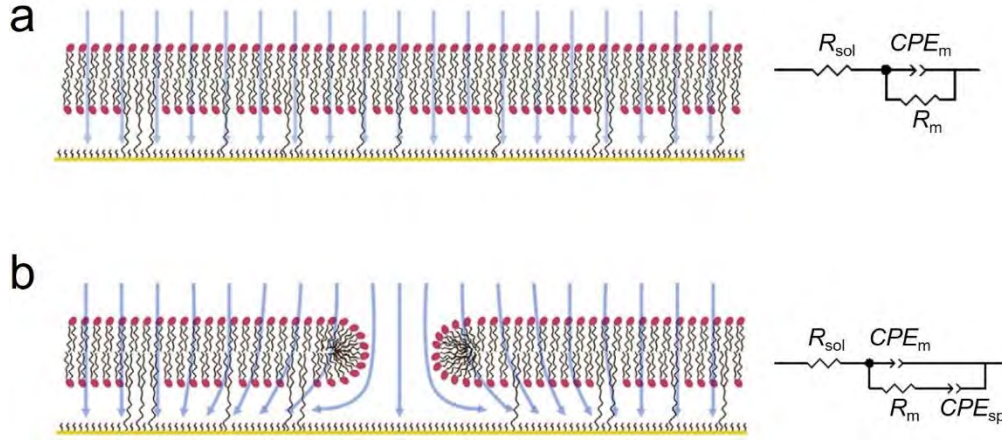


Figure 2.7. Ionic current pathways and corresponding equivalent electric circuits for (a) defect-less and (b) defect-containing tBLM/fBLM [adapted from ¹⁴⁵].

The total impedance (Z_{tot}) of defected fBLM is defined as:²⁴⁴

$$Z_{tot} = R_{sol} + \frac{1}{N_{def}} \frac{1}{(Z'_m)^{-1} + (Z_{def} + Z_{sp})^{-1}} \quad (2.11)$$

where N_{def} is the defect density, Z'_m is the impedance associated with the membrane capacitance, Z_{def} is the impedance of the defect, and Z_{sp} is the impedance of the spacer region. Assuming a hexagonal arrangement of defects, N_{def} is defined as:

$$N_{def} = \frac{0.907}{\pi\delta^2} \quad (2.12)$$

where δ is the defect occupancy radius, i.e., the radius of a circular area that hosts a circular defect with radius r_0 . Z'_m is defined as follows:

$$Z'_m = \frac{1}{j\omega C'_{mH}} \quad (2.13)$$

where C'_{mH} is defined as:

$$C'_{mH} = (C_m^{-1} + C_H^{-1})^{-1} \pi(\delta^2 - r_0^2) + C_H \pi r_0^2 \quad (2.14)$$

C'_{mH} (Eq. 2.14) differs from C_{mH} (Eq. 2.9) because it considers the capacitance of the individual defect site, while C_{mH} is capacitance for the defect-less membrane. Helmholtz capacitance (C_H)

for SAM that anchor the membrane typically varies between 5-10 $\mu\text{F cm}^{-2}$.²⁴⁴ C_m from Eq. 2.14 is defined, similarly as capacitance from Eq. 2.2, as follows:

$$C_m = \frac{\varepsilon_m \varepsilon_0}{h_m} \quad (2.15)$$

In this equation, ε_m and ε_0 are electric permittivity of the membrane hydrophobic core and free space, respectively, while h_m is the thickness of the membrane hydrophobic core.

Z_{def} is the impedance related to the resistance of a single defect. It can be determined from a single-channel conductance measurement for small pores ($r_0 < 1$ nm), while for larger pores, it can be calculated using the numerical finite element analysis.²⁴⁵ Impedance of the spacer region is defined as:

$$Z_{\text{sp}}^{-1} = 2\pi \frac{d_{\text{sp}}}{\rho_{\text{sp}}} (1 - j)\lambda H(\lambda) \quad (2.16)$$

where d_{sp} and ρ_{sp} are thickness and specific resistance of the spacer region, respectively. Complex function, $H(\lambda)$, is defined as:

$$H(\lambda) = \frac{H_1^{(2)}(L\Lambda)H_1^{(1)}(\Lambda) - H_1^{(1)}(L\Lambda)H_1^{(2)}(\Lambda)}{H_1^{(2)}(L\Lambda)H_0^{(1)}(\Lambda) - H_1^{(1)}(L\Lambda)H_0^{(2)}(\Lambda)} \quad (2.17)$$

where $H_0^{(1)}$ and $H_1^{(1)}$ are the first-kind Hankel functions of the zeroth and first-order, respectively, $H_0^{(2)}$ and $H_1^{(2)}$ are the second-kind Hankel functions of the zeroth and first-order, respectively, $L = \delta/r_0$, $\Lambda = (1-j)\lambda$, and λ is dimension-less frequency defined as:

$$\lambda = r_0 \sqrt{\frac{\omega}{2k}} \quad (2.18)$$

where k is defined as:

$$k = \frac{d_{\text{sp}}}{\rho_{\text{sp}} C_H} \quad (2.19)$$

The electric permittivity of peptides is higher than that of the lipid membrane. Therefore, the thickness of the membrane dielectric sheet can change because of the peptide-membrane interaction. Consequently, the electric membrane properties, e.g., membrane capacitance, changes (see Eq. 2.15). The electric membrane properties can be analyzed using Bode plots. These plots display frequency-dependent changes in the impedance magnitude and phase angle. Bode plots for non-permeated (in the peptide absence) and permeated (in the peptide presence) membranes have distinct EIS spectral features (Figure 2.8). The linear impedance vs. frequency curve characterizes non-permeated membranes. The phase angle vs. frequency curve displays a plateau region where the phase angle value exceeds 80° , typical for a highly capacitive system. In contrast, for permeated membranes, the slope of the impedance vs. frequency curve changes

in the low-frequency region, forming the so-called "step-like" feature.²⁴⁶ Moreover, the phase angle vs. frequency curve displays a downward-pointing peak, the so-called curve "minimum".

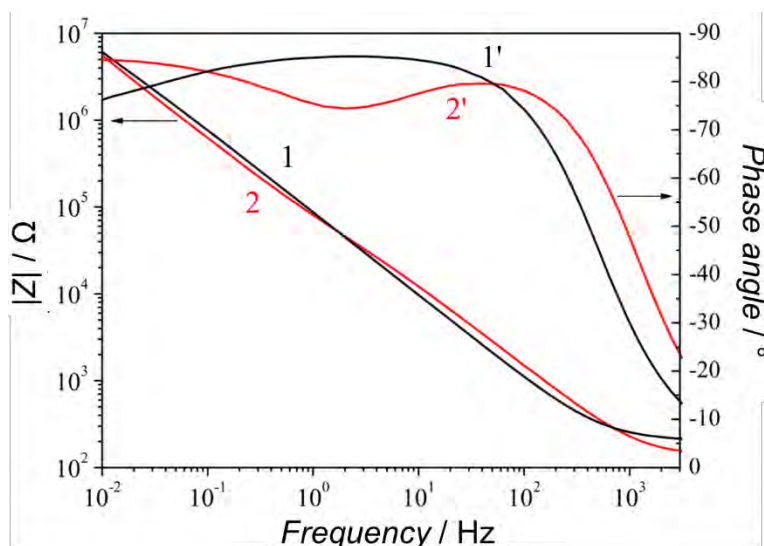


Figure 2.8. Bode plots showing frequency-dependent (curves 1 and 2) impedance and (curves 1' and 2') phase angle for (black curves 1 and 1') DPhPC fBLM and (red curves 2 and 2') DPhPC fBLM permeated by valinomycin [adapted from ²⁴⁷].

As evident from Eq. 2.11, the impedance magnitude depends on the density of membrane defects. Moreover, the impedance phase angle is affected by the defect density because N_{def} affects δ (see Eq. 2.12) that influences L on which Hankel functions depend (see Eq. 2.17). Moreover, EIS spectral features change as a function of the defect distribution (Figure 2.9).¹⁴⁵ If defects are homogeneously distributed across the membrane surface, an increase of defect density causes a shift of the step-like feature in the impedance vs. frequency plot towards higher frequencies and lower impedance values, as indicated by the arrow in Figure 2.9a. The same N_{def} change causes a shift of the minimum in the corresponding phase angle vs. frequency curve (Figure 2.9c) towards higher frequencies, while the phase angle value remains constant (within 1°). If defects are heterogeneously distributed, a N_{def} increase causes a modest shift of the impedance vs. frequency step compared to that of homogeneously distributed pores (Figure 2.9b). Moreover, an increase in the density of heterogeneously distributed defects causes a shift of the phase angle vs. frequency minimum towards both higher frequencies and phase angles (Figure 2.9d). Therefore, different defect distributions can be detected by analyzing the direction of EIS spectral feature shifts.

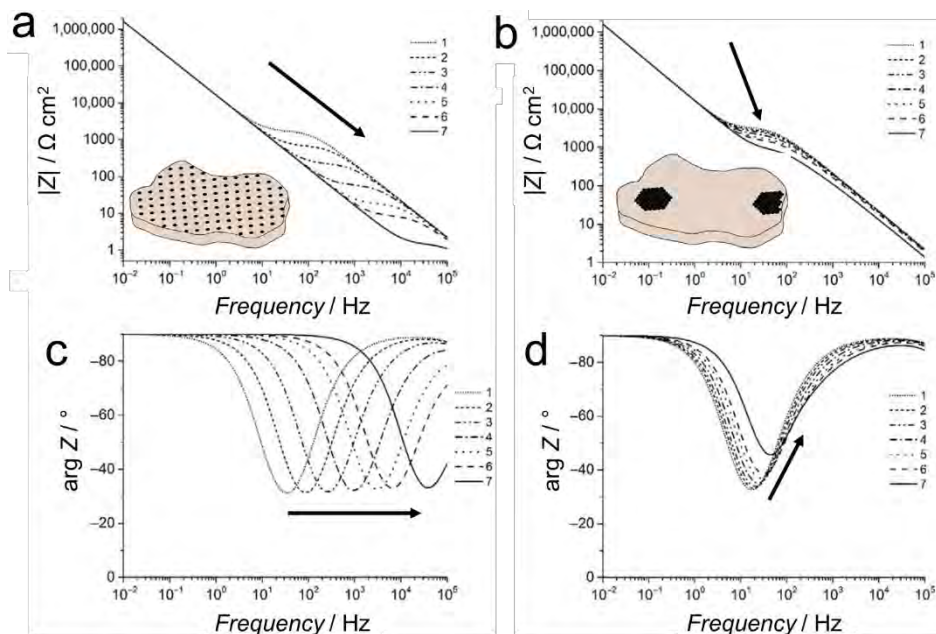


Figure 2.9. Calculated Bode plots for (a, c) homogeneous and (b, d) heterogeneous distribution of membrane defects. Modeling was carried out using Eq. 2.11. N_{def} equals (curve 1) 3, (curve 2) 7, (curve 3) 19, (curve 4) 61, (curve 5) 169, (curve 6) 331, and (curve 7) 1519 μm^2 . Other modeling parameters: $C_H = 10^{-5} \text{ F cm}^{-2}$, $\rho_{\text{sp}} = 10^5 \Omega \text{ cm}$, $d_{\text{sp}} = 1.5 \text{ nm}$, $\varepsilon = 2.9$, $h_m = 3.0 \text{ nm}$, $R_s = 0.1 \Omega$. [adapted from ¹⁴⁵].

2.2.4. IR spectroscopy

Infrared (IR) spectroscopy is an excellent technique used to study the sample structure. In IR spectroscopy, a sample is irradiated by IR light. If the frequency of IR radiation matches the frequency of molecular bond vibration, IR light is absorbed. IR spectroscopy measures the wavelength and intensity of IR radiation absorbed by the sample. The IR absorption probability and frequency of the molecule's vibrational mode depend on molecular bonds' strength and polarity. These properties are influenced by molecules' inter- and intra-molecular interactions. Therefore, IR spectroscopy provides structural information about the sample. However, this technique can detect only IR active molecules, i.e., molecules whose bond vibration is accompanied by a change in the electric dipole moment.

Transmission IR spectroscopy is an averaging technique. It is useful for studying the properties of biomolecules in solution bulk. In this technique, IR light is passed through the transmission cell that contains the sample. The intensities of the incident (I) and transmitted (I_0) light are recorded (Figure 2.10a). The I/I_0 ratio is transmittance (T), while absorbance (A) is expressed as $A = -\log T$. According to Beer-Lambert's law, absorbance is directly proportional to the sample concentration (c) and optical path length (l):

$$A = \xi lc \quad (2.20)$$

where ξ is the molar extinction coefficient. Two critical issues should be considered in the transmission IR spectroscopy. On the one hand, molar extinction coefficients are generally very low for biomolecules (e.g., it is only a few hundreds of $M^{-1} \text{ cm}^{-1}$ for the amide I band of proteins).²⁴⁸ On the other hand, water absorption bands overlap with some bands of proteins and lipids. Therefore, transmission IR spectroscopy requires a high sample concentration (typically $\geq 1 \text{ mg ml}^{-1}$). Moreover, short path lengths are needed because IR absorption by water causes huge intensity loss if the path length exceeds $10 \text{ }\mu\text{m}$.^{249,250}

Transmission IR spectroscopy is not a surface-sensitive technique, and it cannot be used to study biomolecules at solid-liquid interfaces. For that, IR reflection-absorption spectroscopy (IRRAS) was utilized in the present study. In this spectroscopy, an IR beam is externally reflected from the substrate surface (Figure 2.10b). A planar atomically flat reflective substrate (usually metal) covered with adsorbed molecules is pressed against the optical window in the so-called "thin layer cell" configuration.²⁵¹ In this configuration, a thin layer of aqueous solution (several micrometers thick) separates the optical window from the sample-covered substrate. The IR beam passes through the optical window and the aqueous solution and is then reflected from the metal surface. In this case, a single-crystal metal surface can be used, which also allows studying the effect of the metal surface crystallography on the adsorbed molecule structure. The sample and background spectra are superimposed. Therefore, to get the sample spectrum, it is necessary to determine the background spectrum and subtract it from the recorded signal. Under the same thin-layer cell configuration, i.e., at the same cavity thickness, it is difficult (if not impossible) to obtain the background spectrum. Fortunately, the background signal can be removed from the sample spectrum by polarization modulation, exploited in polarization-modulation IR reflection-absorption spectroscopy (PM-IRRAS).²⁵¹

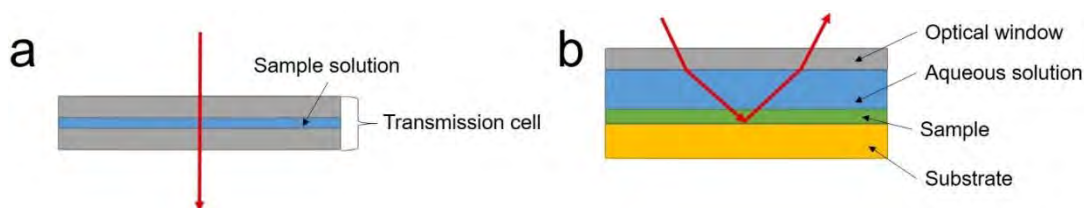


Figure 2.10. The IR spectroscopy (a) transmission, and (b) reflection-absorption sampling mode.

In PM-IRRAS, incident IR light is modulated in two orthogonal directions, i.e., parallel (p-polarization) and perpendicular (s-polarization) to the plane of incidence of IR light (Figure 2.11).¹⁰⁸ Surface selection rules²⁵² dictate that illumination of a smooth metal surface with the p-polarized light at the grazing angle of incidence leads to constructive interference between incident and reflected IR beams. The constructive beam interference causes an

enhancement of the electric field component perpendicular to the substrate surface. In contrast, illumination under the same conditions using the s-polarized light causes a destructive interference between beams, resulting in almost complete disappearance of the electric field component parallel to the substrate surface. Therefore, the s-polarized light reflectivity (R_s) is insensitive to molecules adsorbed at the metal surface. Consequently, it is used to obtain the background spectrum. In contrast, the p-polarized light (R_p) reflectivity is sensitive to the adsorbed molecules with transition dipole moments perpendicular to the substrate surface. The reflection-absorption spectrum ($\Delta R/\langle R \rangle$) is calculated as follows:²⁵¹

$$\frac{\Delta R}{\langle R \rangle} = \frac{|R_p - R_s|}{\frac{R_p + R_s}{2}} \quad (2.21)$$

In this spectrum, the signal due to the IR absorption by atmospheric water and CO₂ is also removed. Therefore, only IR absorption by the surface molecules is detected. Biological samples are often studied in aqueous solutions that absorb IR light. The thin-layer cell configuration is employed to minimize this effect. Proper alignment of the optical elements causes the cancelation of the p- and s-polarized light absorption by solvent molecules, thus increasing the analyte signal. However, it is challenging to cancel this absorption entirely. Therefore, PM-IRRAS is not suitable for studying soluble organic molecules present both on the metal surface and in the bulk solution. However, it is an excellent technique for examining films adsorbed irreversibly, like biomembranes.

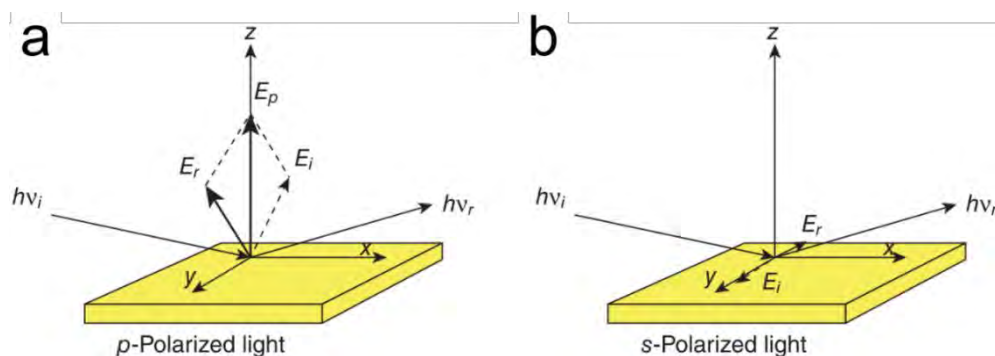


Figure 2.11. Reflection of (a) p- and (b) s-polarized IR light from a smooth metal surface. Incident and reflected IR beam interfere constructively, enhancing the electric field vector of p-polarized light. For s-polarized IR light, the incident and reflected beam interfere destructively; thus, the electric field vector component of s-polarized light nearly vanishes [adapted from ¹⁰⁸].

The spectroelectrochemical setup for PM-IRRAS measurements used in the present study is shown in Figure 2.12. It consists of a spectroelectrochemical cell and IR spectroscopic elements. The glass electrochemical cell is connected to the CaF₂ optical window by a Teflon flange. A gold wire in a Teflon sealer, inserted into a glass tube, is attached to a disk-shaped Au(111) single-

crystal, used as the working electrode. The glass tube is connected to a micrometer-precise screw used to position the working electrode. A Pt foil, sealed into the electrochemical cell, is the counter electrode. An Ag/AgCl electrode mounted to the electrochemical cell via a glass capillary serves as the reference electrode. The IR beam coming from the spectrometer is reflected from the flat mirror into the parabolic mirror and then refocused into the static polarizer. After passing the polarizer, it enters the photoelastic modulator (PEM). The modulated beam illuminates the working electrode and gets reflected from its surface into a ZnSe lens, which refocuses the beam into the MCT-A detector. Signals from the detector and PEM (reference signal) are fed into the synchronous sampling demodulator (SSD). SSD and PEM are phased using the oscilloscope. SSD demodulates the signal, giving the difference and average of the p- and s-polarized light needed to acquire the sample spectrum (see Eq. 2.21).

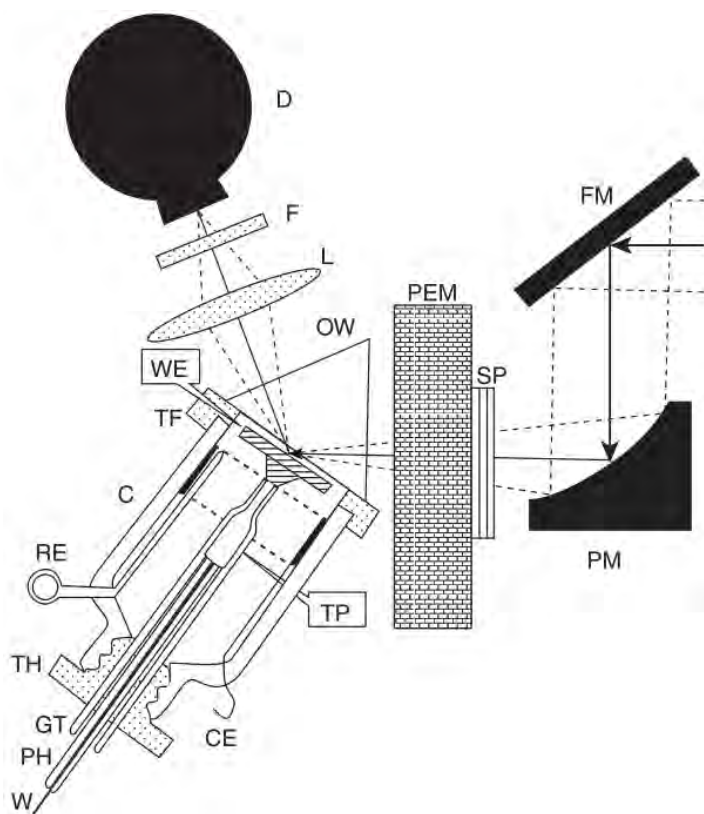


Figure 2.12. The spectroelectrochemical setup for PM-IRRAS measurement. FM - flat mirror, PM - parabolic mirror, SP - static polarizer, PEM - photoelastic modulator, OW - optical window, L – lens, F - optical filter, D – detector, WE - working electrode, TF - Teflon flange, C – cell, RE - reference electrode, TH - Teflon holder, GT - glass tube, PH - piston handle, W - gold wire, CE - counter electrode, and TP - Teflon piston [adapted from ¹⁰⁸].

For biomolecules, the essential IR spectral regions are the fingerprint region ($600\text{--}1,450\text{ cm}^{-1}$), the amide (amide I/II) region ($1,500\text{--}1,700\text{ cm}^{-1}$), and the higher-wavenumber region ($2,550\text{--}3,500\text{ cm}^{-1}$) associated with the S-H, C-H, N-H, and O-H stretching vibrations (Figure 2.13).

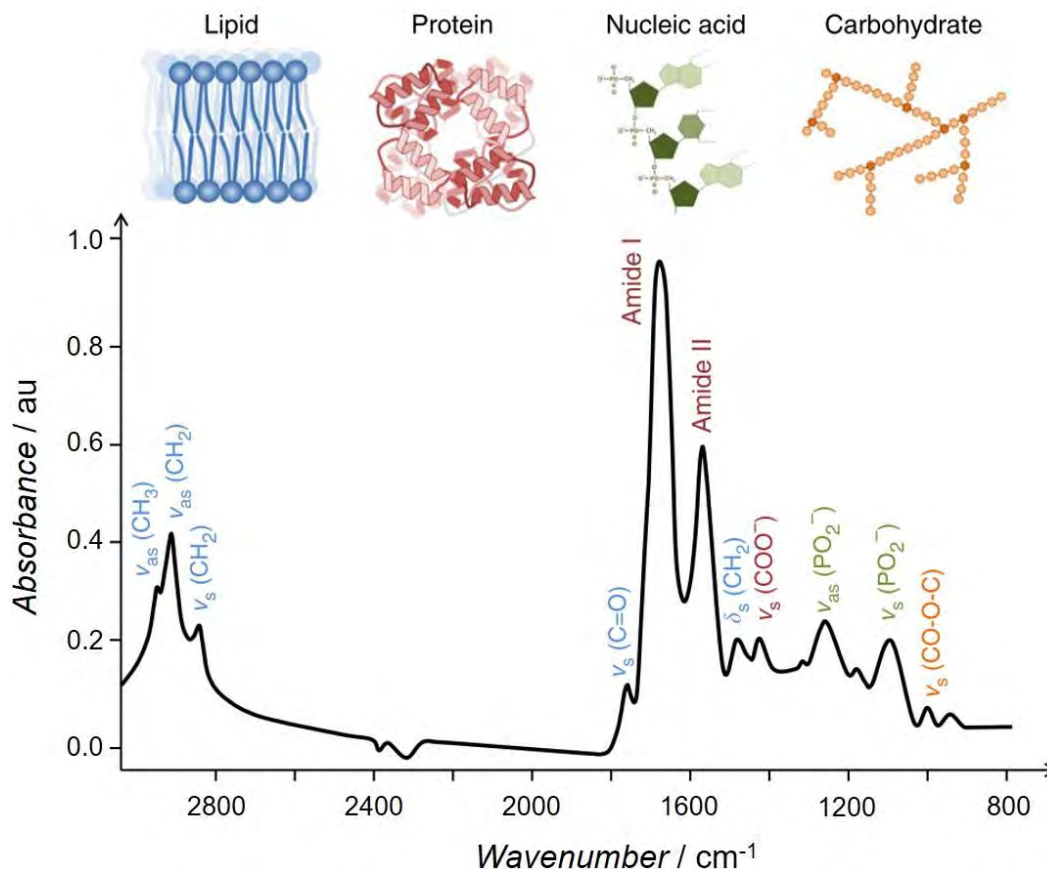


Figure 2.13. IR spectrum typical for a biological sample. Vibrational modes are indicated as ν_s - symmetric stretching vibrations, ν_{as} - asymmetric stretching vibrations, and δ_s - symmetric bending vibrations [adapted from ²⁵³].

The IR bands of lipids can roughly be divided into two groups, i.e., bands containing information about lipid heads and lipid acyl chains (Table 2.1).

Lipid acyl chains are composed of hydrocarbons. Therefore, their IR active vibrations (Table 2.1) include CH_3 symmetric ($2865\text{--}2885\text{ cm}^{-1}$) and asymmetric stretching ($2950\text{--}2975\text{ cm}^{-1}$), CH_2 symmetric ($2840\text{--}2870\text{ cm}^{-1}$) and asymmetric stretching ($2915\text{--}2940\text{ cm}^{-1}$), CH_2 scissoring ($1460\text{--}1480\text{ cm}^{-1}$), CH_3 asymmetric (1460 cm^{-1}) and symmetric (1378 cm^{-1}) bending, CH_2 wagging ($1340\text{--}1370\text{ cm}^{-1}$) and rocking ($720\text{--}740\text{ cm}^{-1}$) vibrations.^{108,248} The most intense lipid bands are in the C-H stretching region ($2800\text{--}3100\text{ cm}^{-1}$). This region is used to detect lipids and study the lipid structural changes occurring during the phase transition. As mentioned in Chapter 1.2.1., membrane transition from the gel to fluid phase is accompanied by lipid acyl chain disordering

(melting), i.e., conversion from the all-*trans* to *gauche* conformation. This conversion can be monitored by analyzing the width and position of methylene symmetric, $\nu_s(\text{CH}_2)$, and asymmetric, $\nu_{as}(\text{CH}_2)$, stretching bands. The $\nu_s(\text{CH}_2)$ and $\nu_{as}(\text{CH}_2)$ wavenumbers below 2850 and 2920 cm^{-1} , respectively, are characteristic for the membrane in the gel phase, where lipid acyl chains are fully stretched (all-*trans* conformation).^{108,254} A shift of these bands to higher wavenumbers indicates the presence of *gauche* conformers typical for the lipid membrane in the fluid phase, where acyl chains are melted. Moreover, the gel-fluid phase transition of membrane lipids is characterized by increased lipid acyl chain mobility. This change manifests itself in the IR spectrum as the broadening of the $\nu_s(\text{CH}_2)$ and $\nu_{as}(\text{CH}_2)$ bands.^{255,256} The C-H scissoring vibration band, $\delta(\text{CH}_2)$, is interesting for studying the lateral packing of lipid acyl chains in the membrane because it is sensitive to the interchain interactions.^{257–260} Orthorhombic lipid arrangement is characterized by two bands, at ~ 1474 and ~ 1463 cm^{-1} , while the hexagonal and triclinic arrangements are characterized by single bands at ~ 1468 and ~ 1473 cm^{-1} , respectively.²⁵⁵

Lipid heads reveal many IR active vibrations (Table 2.1), i.e., ester carbonyl stretches (1724-1742 cm^{-1}), PO_2 asymmetric (1220-1260 cm^{-1}) and symmetric (1085-1110 cm^{-1}) stretches, C–O single bond stretches of the phosphate ester (1040-1090 cm^{-1}). Some additional vibrations of the head group are unique for each type of lipids, like the choline group (present only in PC lipids). The ester carbonyl C=O stretching vibration of the glycerol moiety is studied the most. This band usually consists of two subbands at 1738-1742 and 1724-1729 cm^{-1} . Initially, the two subbands were assigned to the sn-1 and sn-2 ester groups, but this was disputed later by showing that they correspond to non-hydrogen-bonded and hydrogen-bonded C=O bonds that indicate the hydration level of lipid heads.^{261,262}

Protein and peptide biomolecules are composed of chains of amino acids. In these chains (backbones), amino acids are connected by a peptide (amide) bond, a covalent bond formed between an amine and carboxyl groups. Amide bonds have nine IR active vibrational modes, i.e., the amide A (~ 3300 cm^{-1}), amide B (~ 3100 cm^{-1}), amide I (1600-1700 cm^{-1}), amide II (1480-1600 cm^{-1}), amide III (1200-1300 cm^{-1}), amide IV (625-770 cm^{-1}), amide V (640-800 cm^{-1}), amide VI (530-610 cm^{-1}), and amide VII (200 cm^{-1}) mode.^{263,264} Amide I and amide II bands are mostly studied because they are the most prominent bands. They correspond to the protein/peptide backbone vibrations. The amide I band almost entirely arises from C=O stretches (~ 80 %), while the remaining two contributions represent the C-N stretching (~ 10 %) and the in-plane N-H bending (~ 10 %) vibrations. Amide I frequency depends on the nature of carbonyl group hydrogen bonding and the coupling of transition dipoles, unique for each secondary structure. Therefore, bands corresponding to different secondary structures arise at different frequencies (Table 2.1), i.e., β sheet (1620-1642 cm^{-1}), random coil (~ 1645 cm^{-1}), α -helix (~ 1656 cm^{-1}), β -turn (1662-1686 cm^{-1}), and anti-parallel β sheet (1675-1695 cm^{-1}).^{249,264} The amide I band is most sensitive to the peptide backbone vibrations. Therefore, it is used as the main band for studying protein/peptide secondary structure. The amide II band arises from two contributions, i.e., the in-plane N-H bending (~ 40 – 60 %) and the C-N stretching (~ 18 – 40 %) vibrations. This band is much less sensitive to the protein secondary structure than the amide I band. Other amide vibrations

are very complex. They depend on different factors like hydrogen bonding, amino acid side chains, etc. Therefore, they are less useful for secondary structure determination.

Table 2.1. Proteins/peptides and lipids IR band and subband frequencies.^{108,248,249,264}

Sample	Band	Frequency / cm ⁻¹
Lipids	CH ₃ asymmetric stretching	2975-2950
	CH ₂ asymmetric stretching	2940-2915
	CH ₃ symmetric stretching	2885-2865
	CH ₂ symmetric stretching	2870-2840
	C=O stretching (non-hydrogen-bonded)	1742-1738
	C=O stretching (hydrogen-bonded)	1729-1724
	CH ₂ scissoring (orthorhombic)	1474, 1463
	CH ₂ scissoring (triclinic)	1473
	CH ₂ scissoring (hexagonal)	1468
	CH ₃ asymmetric bending	1460
	CH ₃ symmetric bending	1378
	CH ₂ wagging	1370-1340
	PO ₂ asymmetric stretching	1260-1220
	PO ₂ symmetric stretching	1110-1085
	C–O stretching	1090-1040
CH ₂ rocking	740-720	
Proteins/Peptides	anti-parallel β sheet	1695-1675
	β turn	1686-1662
	α-helix	1656
	random coil	1645
	β sheet	1642-1620

Some of the protein and lipid bands overlap, forming a single complex band. In this case, the sample quantitative analysis becomes more challenging. The number and frequencies of the overlapping subbands can be obtained by the second derivative (SD), Fourier self-deconvolution (FSD), or two-dimensional correlation spectroscopy (2D-COS) analysis.^{249,265,266}

Even order derivatives (usually second-, rarely fourth-order) are used as a spectroscopy tool to resolve subbands.^{267,268} Shape of a single IR absorption line is approximated by Lorentzian function:

$$A = \frac{\frac{\gamma}{\pi}}{\gamma^2 + \nu^2} \quad (2.22)$$

where A is absorbance, γ is half-width at the band half maximum, and ν is frequency. The SD of that is:

$$A^{II} = -\left(\frac{1}{\pi\gamma}\right) \frac{2a(1 - 3a\nu^2)}{(1 + a\nu^2)^3} \quad (2.23)$$

where $a = 1/\gamma^2$. The frequencies of the second derivative and the original peak are identical. The relation of the half widths of the second derivative and the original peak is $\gamma/\gamma^{II} = 2.7$. Intensities of the second derivative and original peak are related as $I^{II} = -2I/\gamma^2$. The second derivative is usually smoothed using a 7- or 9-point Savitsky-Golay filter.^{249,269} One of the main advantages of the SD analysis is that it can be performed objectively because subjective choosing of deconvolution parameters is not needed.

FSD is another useful tool for improving the visibility of overlapping subbands present in a complex band. FSD considers that the IR band profile has a Lorentzian line shape.²⁴⁹ Therefore, an IR band with Lorentzian shape can be defined as:

$$A(\nu) = \frac{A_0\gamma^2}{\gamma^2 + (\nu - \nu_0)^2} \quad (2.24)$$

where A_0 is the maximum band absorbance, and ν_0 is the frequency (wavenumber) at A_0 . The Fourier transform of $A(\nu)$ gives:

$$I(x) = F\{A(\nu)\} = 0.5A_0\gamma \cos(2\pi\nu_0x) e^{-2\pi\gamma x} \quad (2.25)$$

where x is spatial frequency. From Eq. 2.25, it follows that the exponential term is determined by γ . Therefore, the wider the absorbance band, the faster the $I(x)$ decays. Consequently, the bandwidth would decrease if the decay rate could be decreased. This decrease can be achieved by multiplying $I(x)$ with the exponential function, $\exp(2\pi\gamma'x)$, to obtain a new function, $I'(x)$, with the decreased decay rate:

$$I'(x) = 0.5A_0\gamma \cos(2\pi\nu_0x) e^{2\pi(\gamma' - \gamma)x} \quad (2.26)$$

This band processing step enhances the noise as well. Therefore, $I'(x)$ is smoothed by multiplying it by the apodization function. Finally, the reverse Fourier transform is applied to $I'(x)$ to obtain a new band, $A'(\nu)$, with the half-width of γ' . The γ/γ' ratio is known as the resolution enhancement factor (K). The choice of the enhancement factor and bandwidth values is

subjective, and variations of these values influence FSD results. Therefore, the FSD analysis should be applied carefully, and it is recommended to verify the obtained results using another spectroscopic method for improving the subband resolution.

Two-dimensional correlation spectroscopy (2D-COS) is the data analysis technique that improves spectral resolution by spreading the unresolved bands across the second dimension.²⁶⁶ In typical, one-dimensional spectroscopy, electromagnetic radiation probes the sample, thus providing the sample spectrum that contains information about the sample components. In 2D-COS, additional external perturbation, i.e., time, temperature, pressure, concentration, voltage, is applied. This perturbation causes the intensity variations of the spectral features, resulting in the so-called "dynamic spectrum." A set of dynamic spectra is collected sequentially, and this set is mathematically processed to obtain the 2D correlation spectrum. The dynamic spectra are cross-correlated, a quantitative comparison of spectral intensity variations at two chosen spectral variables (ν_1, ν_2) over some finite perturbation interval. The 2D correlation intensity, $X(\nu_1, \nu_2)$, can be treated as a complex number defined as:

$$X(\nu_1, \nu_2) = \Phi(\nu_1, \nu_2) + i\Psi(\nu_1, \nu_2) \quad (2.27)$$

where $\Phi(\nu_1, \nu_2)$ and $\Psi(\nu_1, \nu_2)$ correspond to the synchronous and asynchronous component of the 2D correlation intensity, respectively, and i is the imaginary unit. 2D COS spectra are usually represented as contour maps of correlation intensities as a function of the selected wavenumbers (Figure 2.14), where negative intensity regions are shaded.²⁷⁰

The synchronous correlation intensity, $\Phi(\nu_1, \nu_2)$, corresponds to the simultaneous changes of spectral intensity variations at wavenumbers ν_1 and ν_2 generated by the external perturbation (Figure 2.14a). Peaks at the main diagonal line, where $\nu_1 = \nu_2$, mathematically correspond to the autocorrelation function, thus are named auto-peaks. Auto-peaks are always positive, and their magnitudes represent the extent of the spectral variation at the given wavenumber. That is, the larger the intensity change caused by the perturbation, the higher the auto-peak magnitude. Peaks located outside the diagonal, known as cross-peaks, represent simultaneous signal intensity changes at two different wavenumbers. Unlike auto-peaks, cross-peaks can be either positive or negative. Suppose the intensities of two spectral signals, located at wavenumbers ν_1, ν_2 , change in the same direction, i.e., either increasing or decreasing as a function of perturbation. In that case, the cross-peak will be positive. In contrast, if the intensities are changing in opposite directions, the cross-peak will be negative. Cross-peaks, located at opposite sides of the diagonal, drawn through corresponding auto-peaks, can be joint with correlation square to detect coherent variations of the signal intensities at wavenumbers of interest.

The asynchronous correlation intensity, $\Psi(\nu_1, \nu_2)$, indicates sequential changes of the spectral intensities with perturbation (Figure 2.14b). An asynchronous cross-peak appears only if the two signals' intensities do not change simultaneously, i.e., one change occurs before or after the other. The cross-peaks' signs indicate the order of sequential intensity changes. If $\Phi(\nu_1, \nu_2)$ and

$\Psi(\nu_1, \nu_2)$ signs are the same, the spectral intensity change at ν_1 occurs before that at ν_2 . If signs are different, the order is the opposite. If $\Psi(\nu_1, \nu_2) = 0$, changes at ν_1 and ν_2 are synchronized, while if $\Phi(\nu_1, \nu_2) = 0$, the sequential order of changes cannot be determined.

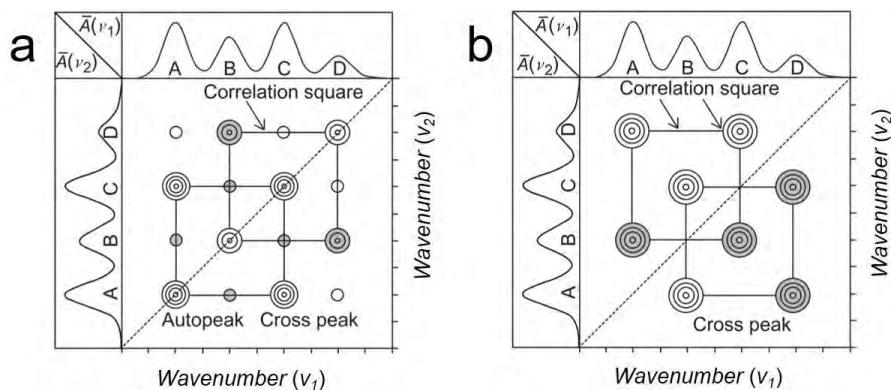


Figure 2.14. Simulated (a) synchronous and (b) asynchronous 2D correlation spectra [adapted from ²⁷⁰].

SD, FSD, and 2D COS provide information about the subbands' numbers and frequencies. The subbands are assigned to specific vibrations based on the literature data. This information is an input for the peak fitting procedure used to extract quantitative information about the subbands. PeakFit software can be used to perform the peak fitting. The goal is to achieve fitting with appropriate band shapes that will yield $R^2 \geq 99\%$ by choosing appropriate band shapes. Either Gaussian, Lorentzian, or a mixture of these two band shapes can be selected. The Lorentzian band shape should be selected for vibrational modes of homogeneous samples, i.e., where all molecules experience the same state, like C-H stretching bands that show changes in lipid acyl chains.¹⁰⁸ The Gaussian band shape is useful for vibrational modes of inhomogeneous samples, where molecules experience different states. For example, lipid heads might be either non-hydrated or hydrated, which is manifested in the C=O stretching region as subbands that correspond to non-hydrogen-bonded and hydrogen-bonded C=O bonds, respectively. Similarly, proteins can contain many different secondary structures. In that case, the amide I band consists of multiple subbands corresponding to each structure. Therefore, the Gaussian band shape is used.²⁴⁹ In some cases, a mixture of Gaussian and Lorentzian bands, with a different Gaussian-to-Lorentzian ratio, is used.²⁷¹

By resolving the subbands, conformational changes of molecules can be determined. Moreover, the subbands' information obtained from the PM-IRRAS spectrum can be used to calculate the molecules' orientation. When sample molecules absorb the linearly polarized light, the integrated intensity of the absorption band (A) is defined as follows:

$$\int A dv \propto |\vec{\mu} \cdot \vec{E}|^2 = |\mu|^2 \langle E^2 \rangle \cos^2 \theta \quad (2.28)$$

where $\vec{\mu}$ is the transition dipole moment vector, \vec{E} is the electric field vector of incident IR light, θ is the angle between the two vectors, $|\mu|^2$ is the square of the absolute value of the transition dipole moment, and $\langle E^2 \rangle$ is the mean square electric field of the photon. The symbol \propto denotes proportionality. The direction of the photon's electric field vector is perpendicular to the metal surface plane. Therefore, the absorption band's integrated intensity is proportional to $\cos^2 \theta$, where θ is the angle between the surface normal and the direction of the transition dipole moment. This angle can be determined using the previously developed protocol.²⁷² A simulated PM-IRRAS spectrum of a film with randomly oriented molecules is calculated using the same conditions as those applied in the PM-IRRAS experiment. If randomly oriented molecules absorb the linearly polarized light, $\cos^2 \theta = 1/3$. The θ angle is proportional to the ratio of the integrated intensity of the absorption band obtained from the PM-IRRAS experimental spectrum (A_{exp}) to the integrated intensity of the absorption band obtained from the PM-IRRAS simulation (A_{sim}), as follows:

$$\cos^2 \theta = \frac{1 \int A_{\text{exp}} dv}{3 \int A_{\text{sim}} dv} \quad (2.29)$$

This method is employed to determine the orientation of lipid acyl chains and lipid heads in a lipid bilayer deposited on the gold surface. Refractive index (n) and attenuation coefficient (k) of each component of the PM-IRRAS experiment (metal, optical window, electrolyte, and lipid bilayer) must be known to simulate the PM-IRRAS spectrum of the lipid membrane. The optical constants for the metal, optical window, and electrolyte are obtained from the literature.^{273,274} The optical constant for the lipid bilayer is determined by recording a transmission IR spectrum of lipid vesicles.²⁵¹ Finally, to calculate the θ angle, it is necessary to know the surface concentration of lipids or the lipid bilayer thickness. With known θ , it is possible to determine the orientation of molecules adsorbed on the metal surface by considering the direction of the transition dipole of the vibration with respect to the molecule's spatial coordinates. Directions of transition dipole moments can be obtained from the literature or ab initio calculations.

This method can be used to determine the lipid head and acyl chain orientations in the supported lipid bilayers (Figure 2.15). The lipid acyl chains' orientation is estimated from the calculation of the acyl chains' tilt angle (θ_{chains}), i.e., the angle between the surface normal and the plane of fully-stretched (all-*trans*) acyl chains. Directions of transition dipole moments of methylene symmetric, $\nu_s(\text{CH}_2)$, and asymmetric, $\nu_{\text{as}}(\text{CH}_2)$, stretches, and the plane of fully-stretched (all-*trans*) acyl chains are perpendicular to each other. Therefore, the acyl chains' tilt angle (θ_{chains}) can be calculated using the following expression:

$$\cos^2 \theta_s + \cos^2 \theta_{\text{as}} + \cos^2 \theta_{\text{chains}} = 1 \quad (2.30)$$

where θ_s and θ_{as} are angles between the surface normal and average directions of transition dipole moments of methylene symmetric, $\nu_s(\text{CH}_2)$, and asymmetric, $\nu_{as}(\text{CH}_2)$, stretches, respectively. These angles can be determined using Eq. 2.29. Moreover, this equation can be used to determine the angle between the surface normal and the direction of the transition dipole moment for C=O bond stretches ($\theta_{\text{C=O}}$). This angle provides information about the lipid heads' orientation. In most supported lipid bilayers, θ_{chains} and $\theta_{\text{C=O}}$ are $\sim 30^\circ$ and 70° , respectively.^{275,276} Orientation of the biomembrane-adsorbed peptides can also be determined using Eq. 2.29, provided that the crystallographic structure of the peptide is known.^{277,278}

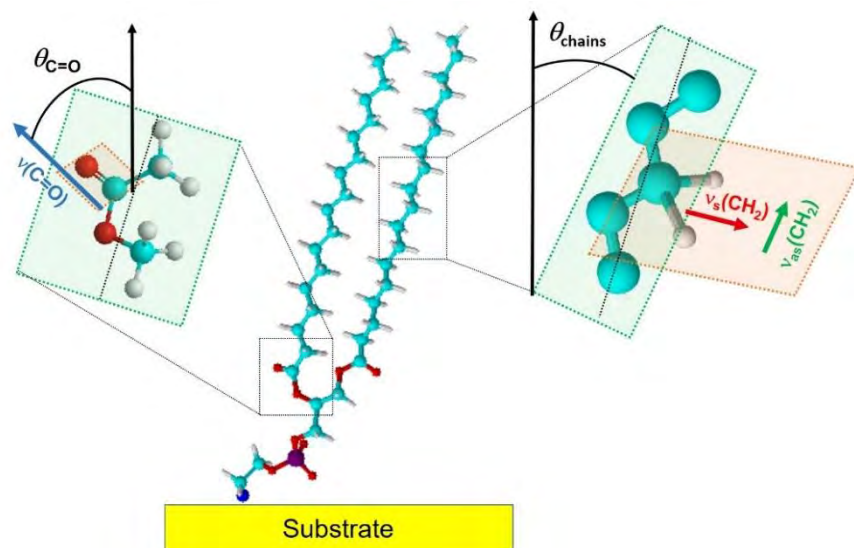


Figure 2.15. The DSPE molecule structure with marked directions of the transition dipole moments of the symmetric, $\nu_s(\text{CH}_2)$, and asymmetric, $\nu_{as}(\text{CH}_2)$, methylene stretches of a lipid acyl chain as well as the C=O bond stretch, $\nu_{\text{C=O}}$, in lipid heads. Moreover, the acyl chain tilt angle (θ_{chains}), i.e., the angle between the surface normal (black arrow) and acyl chains plane (green rectangle), and the C=O bond angle ($\theta_{\text{C=O}}$), i.e., the angle between the surface normal (black arrow) and direction of the C=O stretch transition dipole moment, are shown. The orange rectangle marks the C-H bond plane.

Chapter 3. Size-dependent interaction of amyloid β oligomers with brain total lipid extract bilayer — fibrillation versus membrane destruction

This chapter discusses the research work published in *Langmuir* **2019**, *35* (36), 11940–11949.

Dusan Mrdenovic,^{†,§} Marta Majewska,[†] Izabela S. Pieta,[†] Piotr Bernatowicz,[†] Robert Nowakowski,[†] Wlodzimierz Kutner,^{†,‡} Jacek Lipkowski,[§] and Piotr Pieta,^{†*}

[†]Institute of Physical Chemistry, Polish Academy of Sciences, Kasprzaka 44/52, 01-224 Warsaw, Poland

[‡]Faculty of Mathematics and Natural Sciences, School of Sciences, Cardinal Stefan Wyszyński University in Warsaw, Wóycickiego 1/3, 01-815 Warsaw, Poland

[§]Department of Chemistry, University of Guelph, 50 Stone Road East, Guelph, Ontario N1G 2W1, Canada

Abstract

Amyloid β , A β (1-42), is a component of senile plaques present in the brain of Alzheimer's disease patients and one of the main suspects responsible for pathological consequences of the disease. Herein, we directly visualize the A β activity toward a brain-like model membrane and demonstrate that this activity strongly depends on the A β oligomer size. PeakForce Quantitative Nanomechanical Mapping mode of atomic force microscopy (PF-QNM AFM) imaging revealed that interaction of large-size (LS) A β oligomers, corresponding to high-molecular-weight (HMW) A β oligomers, with brain total lipid extract (BTLE) membrane results in accelerated A β fibrillogenesis on the membrane surface. Significantly, the A β fibrillogenesis does not compromise membrane integrity. In contrast, small-size (SS) A β oligomers, corresponding to low-molecular-weight (LMW) A β oligomers, create pores and disintegrate the BTLE membrane. Both forms of the A β oligomers change the nanomechanical properties of the BTLE membrane. Our results demonstrate that both forms of A β oligomers induce the brain cells' neurotoxicity, but their action toward the membrane differs significantly.

3.1. Introduction

The objective of the study described in the present chapter is to elucidate the A β O toxicity mechanisms. For that, A β O of controlled size and concentration were introduced to the suspension of small unilamellar vesicles (SUVs) with lipid composition similar to that of the brain cell membranes. An aliquot of SUV solution was dropcast on a mica substrate, and SUVs ruptured after contacting the substrate surface, forming a model cell membrane. The effectiveness of the A β action toward SUVs was examined by unraveling changes in the topography and nanomechanical properties of the model membrane interacting with A β using atomic force microscopy (AFM). This examination allowed identifying the mechanisms of action of A β O of different sizes. AFM studies of the A β interaction with model cell membranes have already been performed.^{162,177,279} However, the present results provide unique information allowing one to distinguish between the mechanisms of small-size (SS) and large-size (LS) A β O interactions with the model membrane. SS and LS oligomers correspond to LMW and HMW oligomers, respectively. The high-resolution AFM images show that LS A β O fibrillate through both primary and secondary nucleation mechanism on the brain total lipid extract (BTLE) vesicle surface without affecting the membrane integrity. Moreover, SS A β O destroy the BTLE membrane by a combination of the pore formation and lipid extraction mechanisms.

3.2. Experimental section

A β peptide preparation. Lyophilized A β (1-42), named A β , was purchased from Bachem (Bubendorf, Switzerland). Its purity was determined to be 92% using ¹H NMR spectroscopy (Figure 3.1). The A β sample was pretreated by following the earlier developed procedure²⁸⁰ illustrated in Figure 3.2.

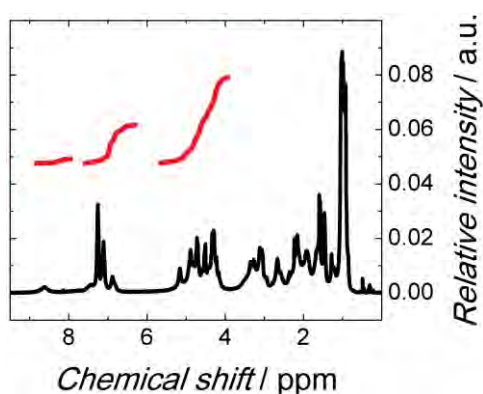


Figure 3.1. The ¹H NMR spectrum of the A β in deuterated trifluoroacetic acid.

A 1-mg A β sample was dissolved in 1 ml of trifluoroacetic acid (TFA), then sonicated for 15 min in a cold water bath followed by solvent evaporation under an Ar stream to break pre-existing

aggregates. Next, the sample was dissolved in 1 ml of 1,1,1,3,3,3-hexafluoro-2-propanol (HFIP) from Sigma-Aldrich by 10-min bath sonication; HFIP was then removed under an Ar stream. HFIP addition, sonication, and solvent removal were repeated once more, and then 1 ml of HFIP was added for the third time. The sample was stored for 24 h at 4 °C. Next, the sample was vortexed for 5 min and then aliquoted. Afterward, HFIP was evaporated under Ar stream, which resulted in transparent A β films left on centrifuge tubes' bottoms. Residual HFIP was removed from the films under decreased pressure in a desiccator for 1 h. The films were stored at -80 °C in a freezer. For each experiment, an aliquot taken from the freezer was allowed to equilibrate to room temperature for 15 min. Next, the A β film was dissolved in anhydrous dimethyl sulfoxide (DMSO) from Sigma-Aldrich to reach the 5 mM concentration. It was then diluted to the 10- μ M concentration using 0.01 M PBS (pH = 7.4) from Sigma-Aldrich. This solution was filtered through the Whatman syringe filter (GE Healthcare Life Sciences) of 0.02 μ m porosity before use.

The size of the A β O_s was controlled by varying their aggregation time in the mixed solvent solution of 0.01 M PBS (pH = 7.4) and anhydrous DMSO. The A β O_s size distribution was characterized by depositing 5 μ L of 5 μ M A β solution on mica. After subsequent washing with Milli-Q[®] water (18.2 M Ω cm) and drying, the sample was AFM imaged in air.^{281–283}

Brain total lipid extract (BTLE) supported lipid bilayer preparation. A chloroform solution of the porcine BTLE, purchased from Avanti Polar Lipids, was used without further purification. Supported lipid bilayers were prepared using the vesicle fusion method.²¹⁷ The BTLE vesicle solution was prepared by transferring 4 μ L of the BTLE stock solution in chloroform (25 mg mL⁻¹) to a glass vial followed by solvent evaporation with an Ar stream under vortexing until a dry film appeared on the bottom of the vial (Figure 3.2). After solvent evaporation, the lipid film was dried in a desiccator overnight. It was then re-suspended in a filtered PBS (pH = 7.4) solution to reach the 1-mg mL⁻¹ concentration and subsequently sonicated for 20 min at 40 °C. The BTLE vesicle solution was used either immediately or stored at 4 °C until further use.

The BTLE bilayer in the A β absence was studied by depositing a 40- μ L sample of the BTLE vesicles solution on the mica surface and then left for 45 min to allow for the bilayer formation. Next, the sample was washed with filtered Milli-Q[®] water, subsequently immersed in the PBS (pH = 7.4) solution, and immediately imaged with AFM.

A β -BTLE mixture preparation. The SS or LS A β O_s were mixed with BTLE vesicles at the 1:20 or 1:50 peptide-to-lipid mass ratio (Figure 3.2). Then, the mixture was sonicated for 10 min at RT. The time-dependent mechanism of the A β -BTLE vesicles interaction was studied by sampling 40- μ L aliquots of the A β -BTLE mixture at different time intervals and depositing them on the mica surface. After 45 min, the sample was rinsed with Milli-Q[®] water, immersed in the PBS (pH = 7.4) solution, and immediately imaged.

The DMSO solvent can cause membrane thinning, pore formation, and membrane disintegration.^{284,285} In the present studies, the DMSO concentration in the lipid bilayer presence

was 0.1% (v/v). DMSO has no adverse effect at this low concentration on the lipid bilayer's stability and topography (Figure 3.3a).

For control measurements, a sample of the supported BTLE bilayer was prepared and then imaged in the AFM fluid cell. After acquiring images of an intact BTLE membrane, a 40- μ L sample of \sim 5- μ M SS A β O was added to the BTLE membrane. This concentration of SS A β O corresponds to the concentration of A β in the A β -BTLE vesicles mixtures. Next, the AFM cell was filled with the PBS (pH = 7.4) solution and immediately imaged with AFM.

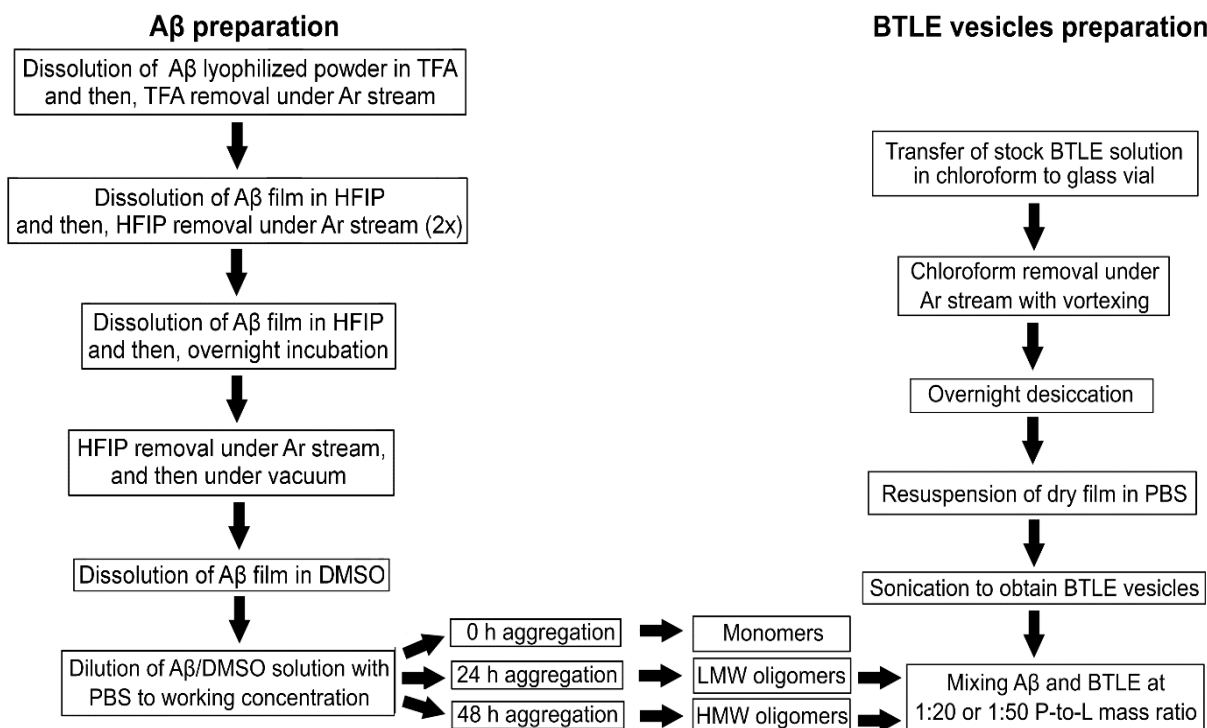


Figure 3.2. The flowchart describing the experimental steps for preparing solutions of A β , BTLE vesicles, and A β -BTLE mixture.

Atomic force microscopy (AFM) experiments. AFM with Multimode 8 system (Bruker) equipped with E scanner (scan size $10 \times 10 \mu\text{m}^2$) and the PF-QNM mode (PBS, pH = 7.4) was used for imaging samples in liquid, at 21 °C. The Scanasyst mode was used for sample imaging in the air. Before the imaging, the fluid cell and AFM accessories were cleaned in a detergent bath, followed by consecutive rinsing with ethanol and then Milli-Q[®] water. The V1 grade mica disks (Ted Pella, Inc.) were mounted on metallic disks using an adhesive tape. Immediately before sample deposition, mica was cleaned in ethanol and then in Milli-Q[®] water. After drying with an Ar stream, its top layer was pilled off using an adhesive tape, resulting in a clean and atomically flat surface. The Qp-BioAC (NanosensorsTM) and RTESPA300 (Bruker) cantilevers of 0.1 and 40 N m⁻¹, respectively, spring constant and corresponding resonance frequency of 50 and 300 kHz,

respectively, were used for imaging in the liquid and air, respectively. The AFM cantilevers were cleaned by consecutive immersing in a detergent bath, 2-propanol, and Milli-Q® water for 10 min. Next, the cantilevers were ozonized in the UVC-1014 UV ozone cleaner (Nanobioanalytics, Berlin, Germany) for 10 min. The cantilevers were calibrated using the thermal tune method. The tip radius was determined by imaging the Ti roughness sample (Bruker), routinely used for tip radius determination.^{286,287} The PF-QNM images were obtained using a 1-2 Hz scan rate. Images were processed and analyzed using Nanoscope Analysis of Bruker and Gwyddion software.²⁸⁸

Nanomechanical properties analysis. Data were analyzed using AtomicJ software.²⁸⁹ The contact point was found on the extended curve. All Young's modulus fitting was performed on the retraction curve using the Hertz model.

NMR spectroscopy study. The purity of the A β sample was assessed with ¹H NMR spectroscopy. First, 1 mg of A β was dissolved in 1 ml of deuterated trifluoroacetic acid (TFA-d), then sonicated for 15 min at RT, and then subjected to the ¹H NMR spectroscopy analysis. The latter was performed at 298 K using BRUKER AVANCE II 300 MHz spectrometer. At first, longitudinal relaxation time (T_1) values of ¹H nuclei were determined to be 20 to 180 ms using the inversion-recovery technique²⁹⁰. Then, a quantitative ¹H NMR spectrum of a high resolution was acquired with 2048 scans. The recycle delay between scans was 2 s to avoid signal oversaturation. The pulse duration was 11.7 μ s, spectral width was 7.5 kHz, and the acquisition time was 2.2 s. Before integration, the spectrum was carefully phased and subjected to baseline correction to avoid integral distortion.

3.3. Results and discussion

AFM characterization of BTLE bilayer without A β . The AFM PF-QNM mode served to study topography and nanomechanical properties of the BTLE bilayer deposited on the mica surface. The topography image of the BTLE bilayer supported on the mica surface is shown in Figure 3.3a. This bilayer has a smooth surface without defects or discontinuities. The average thickness of this bilayer, determined by the height profile measured along the line shown in Figure 3.3a, is 6.1 (\pm 0.3) nm (Figure 3.3c). This thickness is in agreement with the typical height of the supported lipid bilayers.^{291–294}

Figure 3.3b shows the YM map, determined from the FD curves collected simultaneously with the topography imaging. Bright areas visible on Young's modulus map correspond to the mica surface. YM was determined by fitting the Hertz model to the retracted part of the FD curves.²⁸⁹ Figure 3.3d shows the YM distribution of the bilayer presented in Figure 3.3a. The distribution is narrow, confirming that the membrane is homogeneous, with the average modulus value of 11.8 (\pm 3.2) MPa.

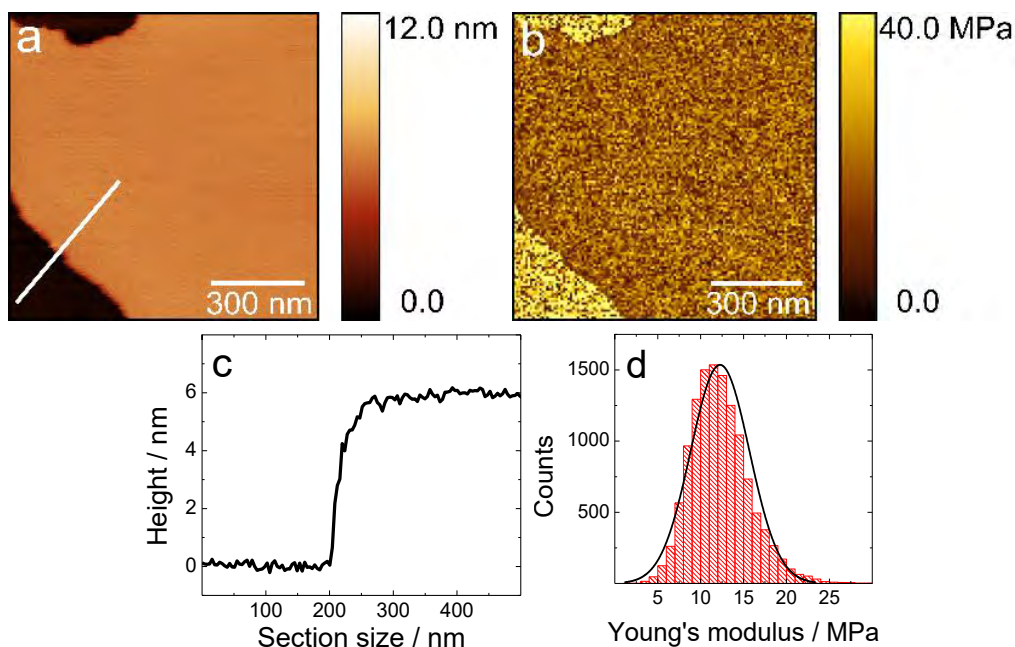


Figure 3.3. (a) The AFM topography image and (b) corresponding Young's modulus map of the BTLE supported lipid bilayer on mica in 0.01 M PBS (pH = 7.4) acquired at 21 °C. (c) The cross-sectional profile of the membrane measured along the line shown in Panel (a). (d) Young's modulus distribution determined from 12,000 FD curves acquired for different points of the bilayer shown in Panel (b).

AFM characterization of A β oligomers. Different forms of A β Os induce different levels of cell toxicity.^{62,63,295–300} Hence, the mechanism of A β interaction with a cell membrane should depend on the molecular weight of A β . Therefore, A β samples with different size distribution were prepared. The molecular weight of the studied A β Os was not measured, and the LMW and HMW A β Os are distinguished only based on their size (SS or LS oligomers, respectively). Initially, freshly prepared samples of 10 μ M A β in a PBS-DMSO mixture were analyzed to confirm that pre-existing aggregates were eliminated, i.e., A β M dominated in the sample. An aliquot of this solution was deposited on the mica substrate. After 5-min deposition, the sample was washed, then dried under an Ar stream, and then immediately imaged by AFM in the air. Figure 3.4a shows many globular aggregates on the mica surface. Statistical analysis of the sample revealed that globular aggregates with a height of \sim 0.3 nm and an average diameter of \sim 2 nm populated the most abundant fraction (Figures 3.4d and 3.14a). This height corresponds to the height of the A β M.¹⁸⁴ Therefore, in a freshly prepared A β solution (0 h aggregation time, Figure 3.2), A β M dominated, and only a minor amount of LMW A β Os was distinguished. At this stage, A β M and LMW A β Os are in equilibrium.^{301–303} After establishing that a freshly prepared sample is mostly populated with A β M, the A β fibrillogenesis was monitored as a function of the aggregation time. First, A β was allowed to aggregate for 24 h at 4 °C. At this point, a significant amount of A β M aggregate into SS A β Os with the height of \sim 1-3 nm and average diameter of \sim 6 nm (Figures 3.4b, 3.4e, and

3.14b). After 48 h, A β aggregation progressed further, and both SS and LS A β O were formed (Figure 3.4c). Statistical analysis of the height of the A β aggregates generated after 48-h aggregation shows a bimodal height distribution of aggregates with heights of \sim 0.5-2 and \sim 3-5 nm corresponding to the SS and LS A β O, respectively (Figure 3.4f). The average diameter of the formed LS A β oligomers is \sim 10 nm (Figure 3.14c). These sizes of A β oligomers are in agreement with those determined by AFM,^{63,188,283,297,303-306} dynamic light scattering (DLS),⁶³ fluorescence correlation spectroscopy (FCS),⁶³ and transmission electron microscopy (TEM).^{188,303} Their corresponding molecular weights were determined by electrophoresis^{188,283,297,304,305} and mass spectrometry.³⁰³ Using the literature data mentioned above, one could roughly estimate that A β O with a height of \sim 1-3 nm correspond to trimers and tetramers with the molecular weight of \sim 30 kDa.³⁰⁵ Most likely, the molecular weight of the A β O with the height of \sim 3-5 nm exceeds \sim 60 kDa, which is that of dodecamer.³⁰⁵ Noteworthy, amyloid plaques from AD patient brains contain A β aggregates of similar shapes and sizes.³⁰⁷

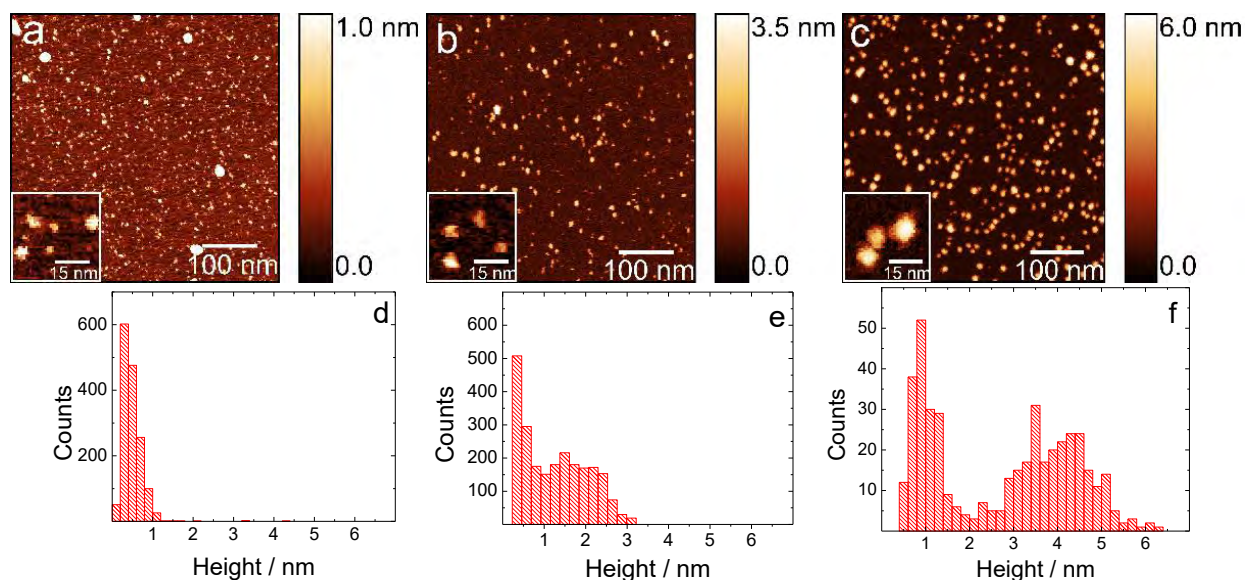


Figure 3.4. The AFM topography images of (a) A β M as well as (b) SS and (c) LS A β O deposited on the mica surface. Insets exhibit magnified parts of the corresponding topography images showing the shape of the aggregates in greater detail. The height distribution of the (d) A β M, as well as (e) SS and (f) LS A β O. The aggregates were formed in the PBS-DMSO solution in the BTLE vesicles' absence.

Interestingly, only the globular aggregates were formed if the A β aggregation time was shorter than 48 h. However, protofibrils and fibrils of A β were produced if the aggregation time exceeded 48 h (Figure 3.5).

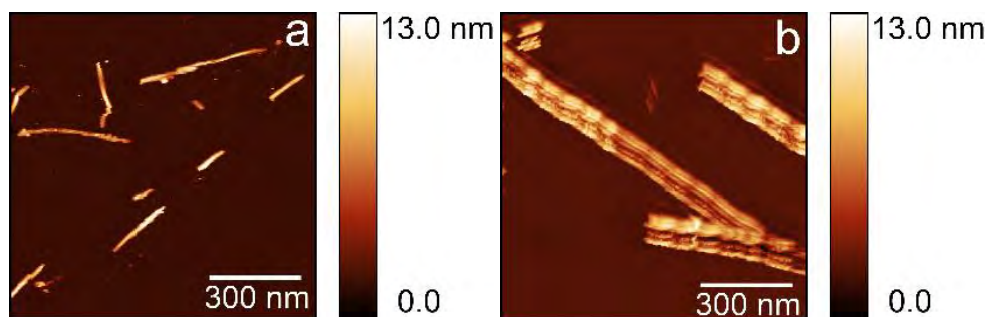


Figure 3.5. The AFM topography image of A β (a) protofibrils and (b) fibrils deposited on the mica surface.

Interaction of LS A β oligomers with BTLE vesicles. The PF-QNM AFM technique was employed to study the A β -BTLE vesicles interaction. The LS A β Os (Figure 3.4c) solution was mixed with the BTLE vesicle solution at the A β -to-lipid mass ratio of 1:20. Forty- μ L aliquots of the mixture were taken at different interaction times and dropcast onto the mica surface to monitor the time-dependent interaction of LS A β Os with BTLE vesicles. The vesicles were allowed to fuse for 45 min. The sample was then carefully washed with filtered Milli-Q[®] water, and then imaged with AFM in the PBS (pH = 7.4) solution. The A β -BTLE bilayer, deposited after mixing solutions of the LS A β Os and BTLE vesicles (0 h interaction time), is shown in Figure 3.6a. Many globular A β aggregates are present on the BTLE bilayer surface. These aggregates' height mostly exceeds 3 nm (Figure 3.6c), indicating that these are mostly LS A β Os. Comparing the height distribution of the A β aggregates formed in solution in the absence (Figures 3.4e and 3.4f) and presence (Figure 3.6c) of BTLE vesicles, it is evident that the BTLE vesicles promote the large A β Os growth on the membrane surface. Moreover, the aggregation rate is significantly increased in the BTLE presence. Both the phospholipid composition and the presence of cholesterol decrease the half time of A β aggregation.^{179,208} Apparently, the BTLE bilayer very efficiently catalyzes LS A β O aggregation. This inference is consistent with that of previous studies showing the catalytic role of lipid bilayers in amyloid fibrillation by ThT fluorescence,¹⁷⁹ Förster resonance energy transfer (FRET) assay,¹⁷⁹ circular dichroism (CD),¹⁸⁰ NMR spectroscopy,¹⁸⁰ X-ray scattering,¹⁸¹ neutron reflectivity,¹⁸¹ TEM,¹⁸¹ and DLS.¹⁸¹ Moreover, AFM imaging showed A β fibrils growth along with the unfused large unilamellar vesicles (LUVs).¹⁷⁹

The cross-sectional profile of the BTLE bilayer (Figure 3.6d) shows that the thickness of the BTLE bilayer exposed to LS A β Os is 5.9 (\pm 0.2) nm, which is similar to the BTLE bilayer thickness in the A β absence (Figure 3.3c). Nanomechanical properties of the BTLE bilayer with adsorbed LS A β Os are significantly different from those of the A β -free membrane. Figure 3.6b shows the YM map corresponding to the topography image shown in Figure 3.6a. The YM distribution (Figure 3.6e) shows the average value of 6.5 (\pm 2.5) MPa, half of that determined for the intact bilayer (Figure 3.3d).

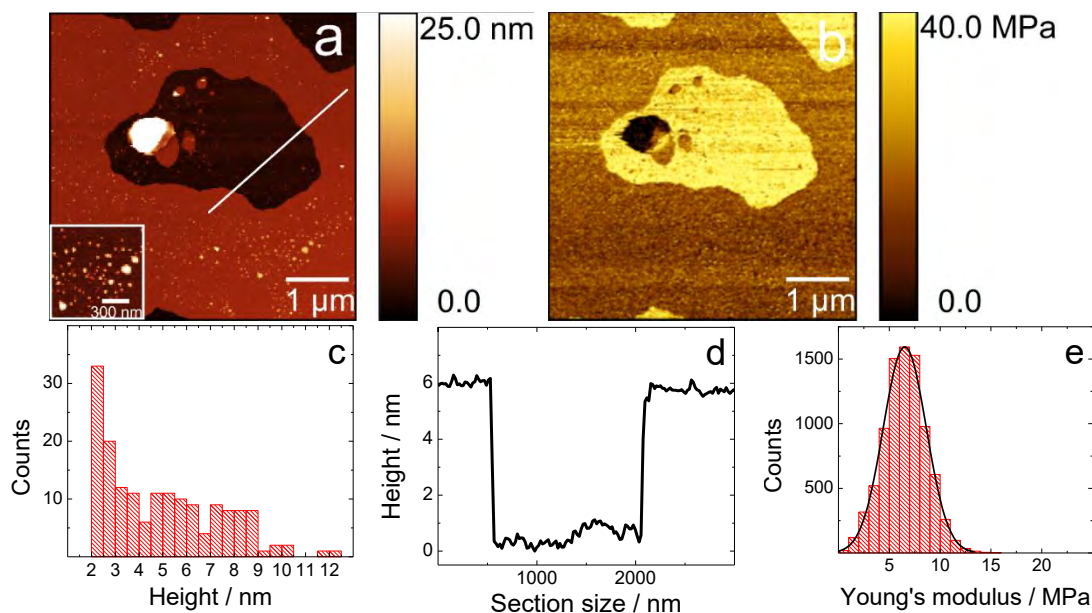


Figure 3.6. (a) The AFM topography image and (b) the corresponding Young's modulus map of the BTLE bilayer with adsorbed LS A β oligomers deposited on mica immediately after mixing solutions of LS A β oligomers and BTLE vesicles. Inset in Panel (a) exhibits a magnified section of the same topography image showing the LS A β oligomers' shape on the membrane surface. The images are acquired for the bilayer in the PBS (pH = 7.4) solution at 21 °C. (c) The LS A β oligomers' height distribution determined from the AFM image shown in Panel (a). (d) The cross-sectional profile, measured along the line shown in Panel (a), exhibiting the BTLE bilayer thickness. (e) Young's modulus distribution determined from 6000 FD curves acquired for different points of the BTLE bilayer shown in Panel (b).

Interestingly, many A β Fs are formed on the BTLE membrane surface after 3 h of the A β -BTLE vesicles interaction (Figure 3.7a). Additionally, both individual globular aggregates and long fibrillar structures are visible on the fibril surface. It suggests that the secondary nucleation mechanism of A β aggregation is observed. Aggregation through secondary nucleation is the only step that occurs on the surface of already formed A β fibrils, thus being easily distinguished from other steps in the aggregation pathway.^{208,308} This process is a surface reaction involving the coalesce of A β aggregates rather than their deposition from the solution bulk. The secondary nucleation aggregates are clearly seen in Figures 3.7c and 3.7d. Here, the aggregation through secondary nucleation resulted in the formation of A β Fs (Figure 3.7c) and globular A β aggregates (Figure 3.7d) on the surface of A β Fs pre-formed through primary nucleation. Cross-sectional profiles measured along and across the aggregates are analyzed to compare heights of the A β Fs formed via primary and secondary nucleation mechanisms (Figures 3.7e-3.7g). Figures 3.7h-3.7j show the corresponding height histograms of these aggregates. A narrow Gaussian distribution of the primary nucleation fibrils' height indicates that the average height is 5.4 (\pm 0.6) nm (Figure 3.7h).

In contrast, the height distribution for the secondary nucleation fibrils is wide, with an average height of 7.09 (± 1.62) nm (Figure 3.7i). The height distribution of globular aggregates formed through secondary nucleation is quite broad, covering the range of 1 – 12 nm (Figure 3.8j). The height of the larger population of secondary globular aggregates is 1 – 2 nm, which corresponds to that of the SS A β O₂. This result is not surprising because these oligomers aggregate to form fibrils. Notably, LS A β O₂s seen at the initial interaction time (Figure 3.6a) are also visible after 3 h of interaction (Figure 3.7a). The presence of these aggregates indicates accelerated A β aggregation on the BTLE surface. Therefore, the aggregates observed directly on the membrane surface are formed during aggregation catalyzed by the membrane surface, which occurred via the primary nucleation mechanism. The aggregates observed on the fibril surface are formed during aggregation catalyzed by the fibril surface, which is the secondary nucleation mechanism.^{44,47}

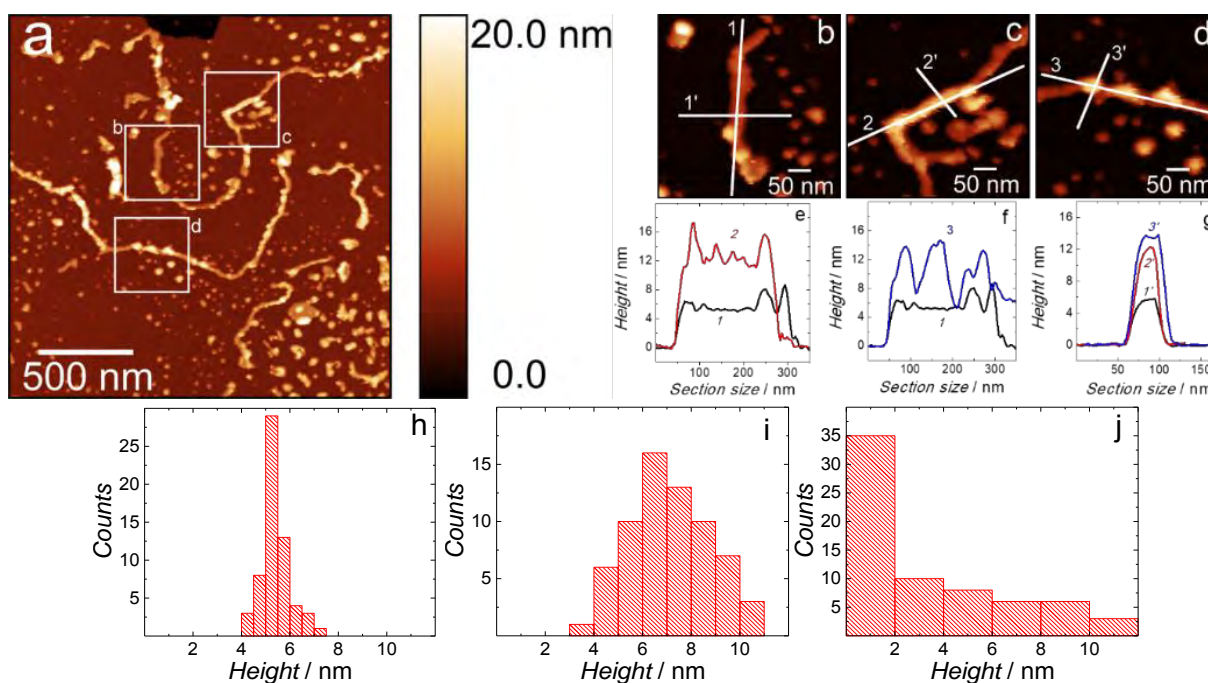


Figure 3.7. (a) The AFM topography image of the A β aggregates formed on the BTLE supported bilayer in 0.01 M PBS (pH = 7.4). (b-d) High-resolution topography images, acquired for the areas depicted as squares in Panel (a), showing the (b) primary nucleation fibril, (c) secondary nucleation fibril, and (d) secondary nucleation globular aggregates. (e-g) The cross-sectional profiles measured along (e) primary and secondary nucleation fibrils (lines 1 and 2) and (f) primary nucleation fibril and secondary nucleation globular aggregate (lines 1 and 3) as well as (g) across the primary and secondary nucleation aggregates (lines 1', 2', and 3'). (h-j) The height distribution of (h) primary nucleation fibrils, (i) secondary nucleation fibrils, and (j) secondary nucleation globular aggregates of A β .

Interaction of SS A β oligomers with BTLE vesicles. Exposure of SS A β O to BTLE vesicles (the A β -to-lipid mass ratio of 1:20) results in the A β -BTLE bilayer's deposition, significantly different from that shown in Figure 3.6. Figure 3.8a shows the A β -BTLE film deposited on the mica substrate immediately after mixing solutions of SS A β O and BTLE vesicles. There are numerous pores of different sizes and shapes on the BTLE bilayer surface. Long A β Fs and large globular A β aggregates, seen previously in Figures 3.6a and 3.7a, are absent. Clearly, SS A β oligomers' interaction with BTLE vesicles results in the lipid vesicles spreading different from that described above for LS A β O. The cross-sectional profile of the membrane shown in Figure 3.8a indicates that the BTLE film thickness is 6.3 (\pm 0.6) nm (Figure 3.8c), a value comparable to that of the intact BTLE bilayer (Figure 3.3c).

Figure 3.8b shows a YM map corresponding to the topography image shown in Figure 3.8a. The average YM value of this bilayer is 6.7 (\pm 2.2) MPa (Figure 3.8d), a value comparable to that of the membrane with adsorbed LS A β oligomers. Therefore, both LS and SS A β O effectively change the nanomechanical properties of the BTLE membrane by causing a decrease in its YM by \sim 45%. Force spectroscopy measurements revealed that the POPC/POPS supported lipid bilayer rupture in the absence and presence of the A β 42 at 3.5 and 1.2 nN, respectively, indicating a decrease in the bilayer stiffness by 65.71%.²⁷⁹ This significant membrane nanomechanical properties change incurred by the A β activity implies both conformational and organizational changes of the phospholipid molecules in the membrane.

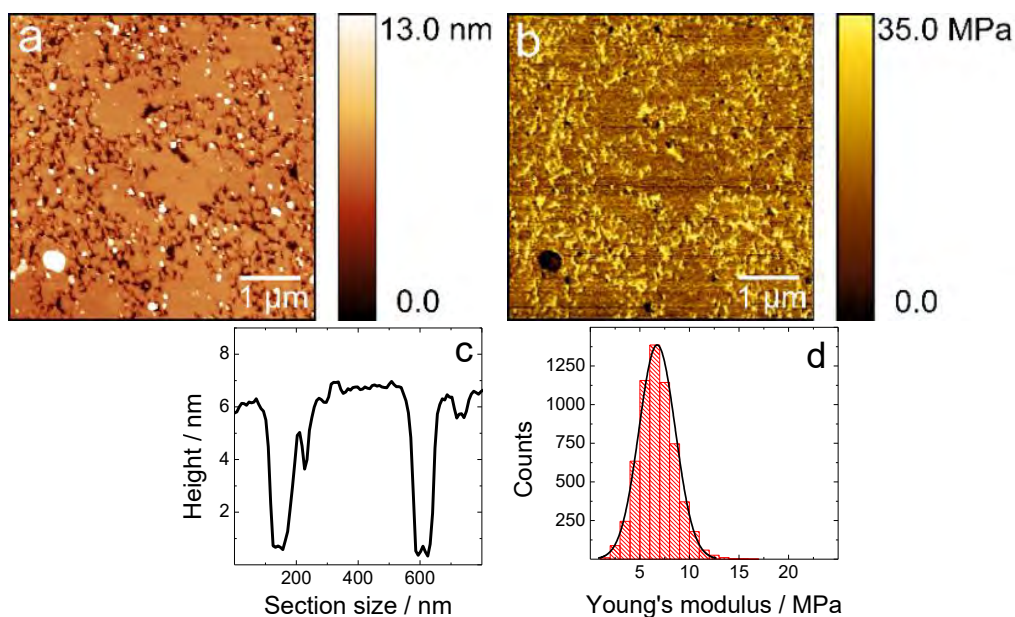


Figure 3.8. (a) The AFM topography image and (b) the corresponding Young's modulus map of the A β -BTLE supported bilayer in 0.01 M PBS (pH = 7.4), at the initial interaction time. (c) A representative cross-sectional profile showing the depth of the pores formed in the BTLE lipid bilayer depicted in Panel (a). (d) Young's modulus distribution determined from 6000 FD curves acquired for different points of the bilayer shown in Panel (b).

A porous bilayer was repeatedly formed from BTLE vesicles mixed with SS A β O_s (Figure 3.8a). Occasionally, a partial BTLE bilayer was also formed (Figure 3.9a). There are numerous pores in both the outer and inner leaflets of the BTLE bilayer shown in Figure 3.9a. The cross-sectional profile, measured along the line shown in Figure 3.9a, demonstrates that the outer and inner leaflet's heights are equal, being ~ 3.1 nm (Figure 3.9b). The average depth of the pores formed in the inner leaflet is $2.8 (\pm 0.4)$ nm (Figure 3.9c). These results evidence that the bottom part of the film has the thickness of a monolayer. Only the upper part of this film is covered with a second monolayer, forming a complete bilayer (Figure 3.9a).

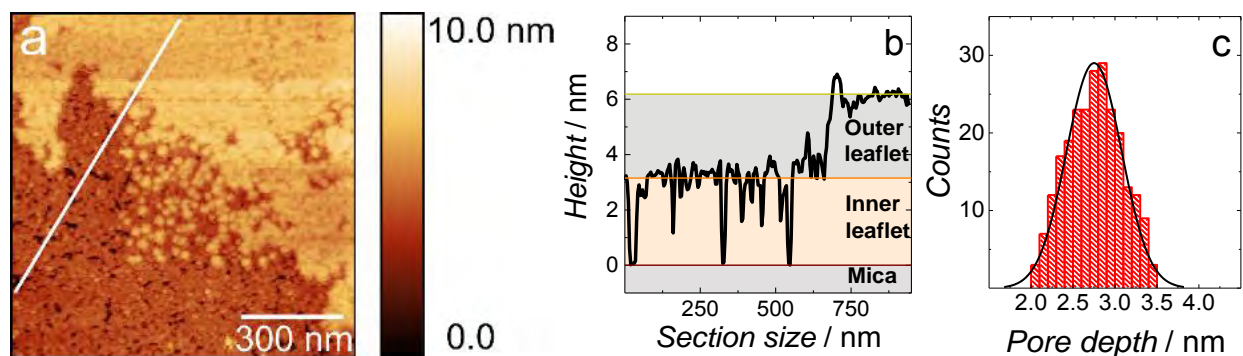


Figure 3.9. (a) The AFM topography image of the A β -BTLE supported bilayer in 0.01 M PBS (pH = 7.4) showing lipid extraction from the outer leaflet of the BTLE bilayer. (b) The corresponding height profile, measured along the line in Panel (a), showing the height difference between the outer and inner leaflets of the BTLE lipid bilayer. (c) The depth distribution of the pores formed in the inner leaflet of the BTLE bilayer.

Only pores of a diameter larger than that of the AFM tip are considered in the present analysis. The diameter and quality of the AFM tips were estimated by using a well-established procedure. This procedure consists of imaging the Ti roughness sample (Bruker) and analyzing the obtained image (Figure 3.10a) using the Tip Qualification option in NanoScope Analysis software. This analysis results in obtaining the software model of the tip (Figure 3.10b) and effective tip diameters (ETDs) at different distances from the tip apex (Figure 3.10c and 3.10d). The tip characterization analysis showed that ETDs are 8.5 and 26.3 nm at 3 and 20 nm distance, respectively, from the tip apex (Figure 3.10e). In Figure 3.10f, it is illustrated how ETD is calculated based on the tip cross-section.

The ETD limits the tip's ability to measure the true pore depth. The tip cannot reach the pore's bottom if the tip's diameter is larger than the pore diameter. Consequently, the pore depth cannot be determined. Therefore, it is essential to determine whether the tip is sufficiently sharp to measure the depth of the BTLE bilayer's pores. Pores formed in the inner leaflet of the BTLE bilayer (Figure 3.9a) are analyzed by measuring diameters and depths of the big, medium, and small size pores. Green, cyan, and blue arrows in the magnified region of the BTLE bilayer's inner leaflet show big, medium, and small size pores, respectively (Figure 3.11a).

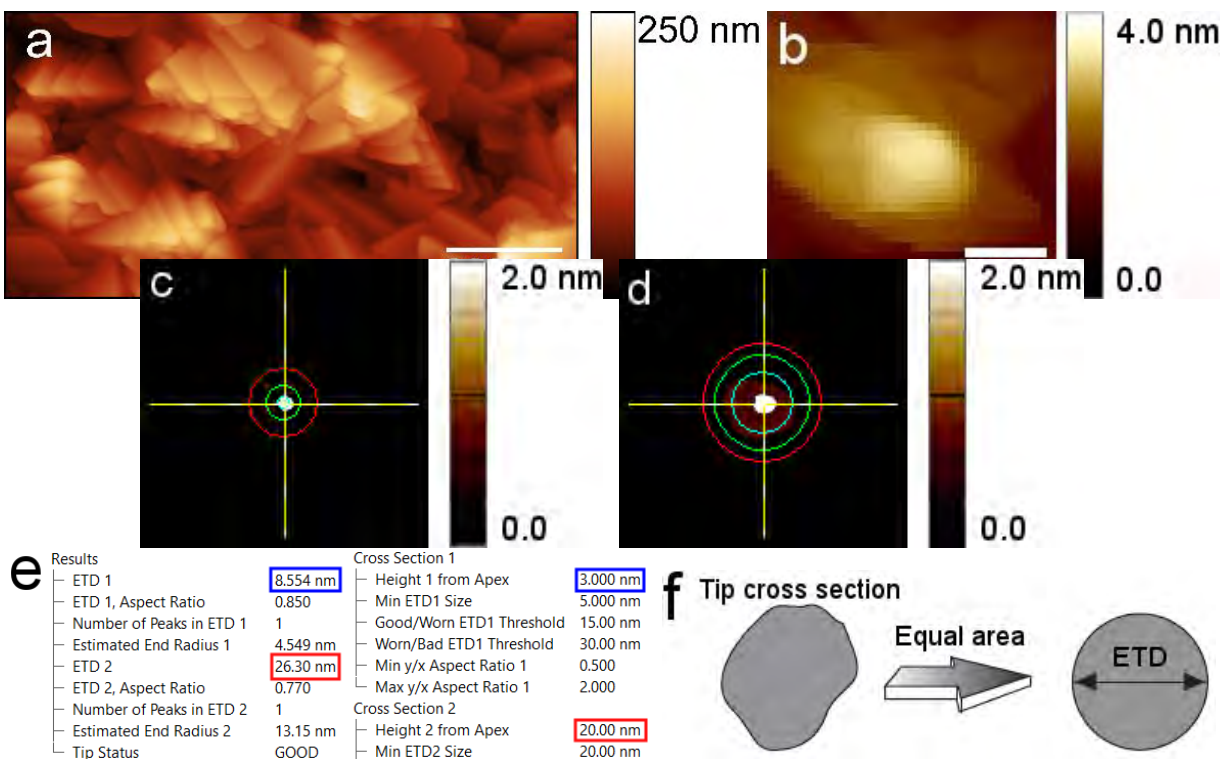


Figure 3.10. (a) The AFM topography image of a Ti roughness sample used for the tip radius and quality determination. (b) The top-view image of the software model of the tip. Cross-section diagrams showing the tip's size and shape at the distance of (c) 3 and (d) 20 nm from the tip apex. (e) Results of the tip radius and quality determination. (f) Scheme of the effective tip diameter calculation from the tip cross-section.

The cross-section profile of the BTLE bilayer shows that the bilayer thickness is 6.1 (± 0.3) nm (Figure 3.3c). This result suggests that the thickness of a single leaflet is ~ 3 nm. The tip characterization analysis indicates that the tip diameter is 8.5 nm at a distance of 3 nm from its apex. If the pore diameter exceeds 8.5 nm, the tip can reach the bottom of the 3-nm deep pore. Therefore, the tip can measure the depth of the pores formed in a single leaflet. These pores' depth cannot exceed 3 nm because a single leaflet's thickness is 3 nm. Figure 3.11b shows the relation between the measured depth and diameter of pores. Apparently, the measured pore depths did not exceed 2 nm if the pore diameter was less than 10 nm. On the other hand, the pore depth ranged from 2.5 to 3.5 nm if the pore diameter exceeded 10 nm. This result suggests that the diameter of small pores is smaller than the tip diameter, and the tip could not measure depths deeper than 2 nm. Presumably, this is why the depth distribution for small pores is small (Figure 3.11b). On the other hand, the tip can measure the true depth of medium and big pores and, therefore, their depth distribution is broad.

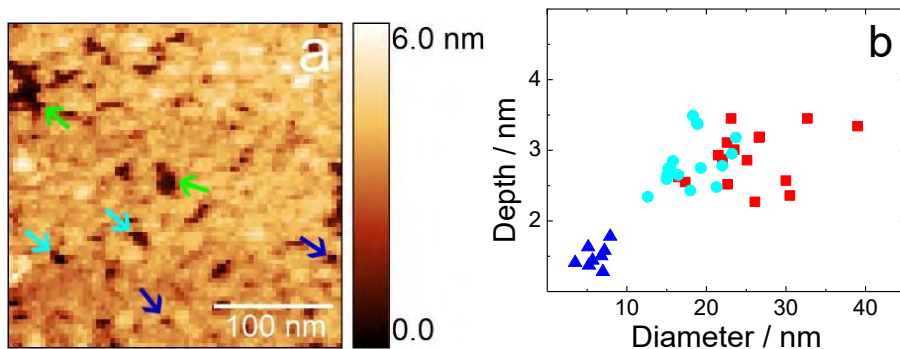


Figure 3.11. (a) The AFM topography image of pores in the inner leaflet of the BTLE lipid bilayer. (b) Correlation between depth and diameter of (■) big, (●) medium, and (▲) small pores.

Our AFM studies demonstrate that SS A β O_s are harmful to the spreading of BTLE vesicles and bilayer formation. The partial absence of the outer membrane leaflet, shown in Figure 3.9a, suggests that SS A β O_s extract lipids from this leaflet. A β O_s uptake lipid molecules, inducing lipid extraction/release from, e.g., a neuronal membrane, also known as membrane fragmentation or detergent-like solubilization.^{36,165,167,207,213,309} Only SS A β O_s (dimers, trimers, and tetramers) extract phospholipid molecules from neuronal cells, forming A β -lipid complexes, also named lipoprotein particles.¹⁶⁵ Moreover, A β interaction with lipid vesicles results in the formation of lipoprotein complexes.^{167,207,213,309} Importantly, these complexes diffuse away from neuronal cells. Lipid extraction is intensified by the increase in A β concentration, A β -cell interaction time, and it depends upon cell membrane composition.^{167,213,309} These studies suggest that the adverse effect of SS A β O_s on the BTLE vesicles spreading results from the lipoprotein complex formation.

Figures 3.12a and 3.12b are images previously shown in Figures 3.8a and 3.9a with the globules marked with green circles. Equivalent disk radii distributions of these objects are presented in Figures 3.12c and 3.12d, respectively. The most dominant populations of globules are characterized by a radius between 10 and 20 nm. A similar size of the globules suggests the formation of similar nanoclusters.

Equivalent disk radii of all globular A β forms, as well as unruptured BTLE vesicles, were measured and compared (Figure 3.13) to verify that the observed nanoclusters are not A β aggregates or unfused BTLE vesicles. The range of equivalent disk radii of the A β M_s, SS A β O_s, LS A β O_s, and unfused BTLE vesicles are ~1, 2-4, 4-6, and 40-80 nm, respectively. The nanoclusters' radii (Figures 3.13c and 3.13d) are significantly different from those of A β aggregates and BTLE vesicles, thus confirming that the nanoclusters are unique entities. These nanoclusters are formed only in the LMW A β O_s presence, thus suggesting that these are A β -lipid complexes.

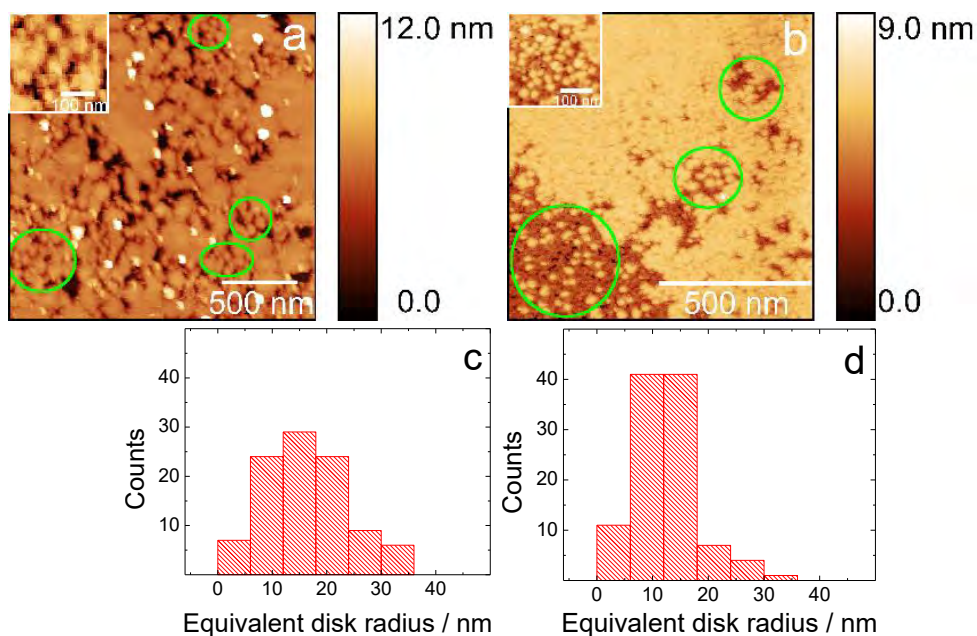


Figure 3.12. The AFM topography images showing nanoclusters (green circled) formed by the BTLE lipids interacting with SS A β O₂s in the cases of (a) Figure 3.9 and (b) Figure 3.10. Insets exhibit high-resolution AFM topography images showing the size and shape of the A β -lipid nanoclusters. (c) and (d) Equivalent disk radii distributions of the A β -lipid nanoclusters, green circled in Panel (a) and Panel (b), respectively. Scan sizes of images presented in Panels (a) and (b) are different to show a sufficient number of nanoclusters.

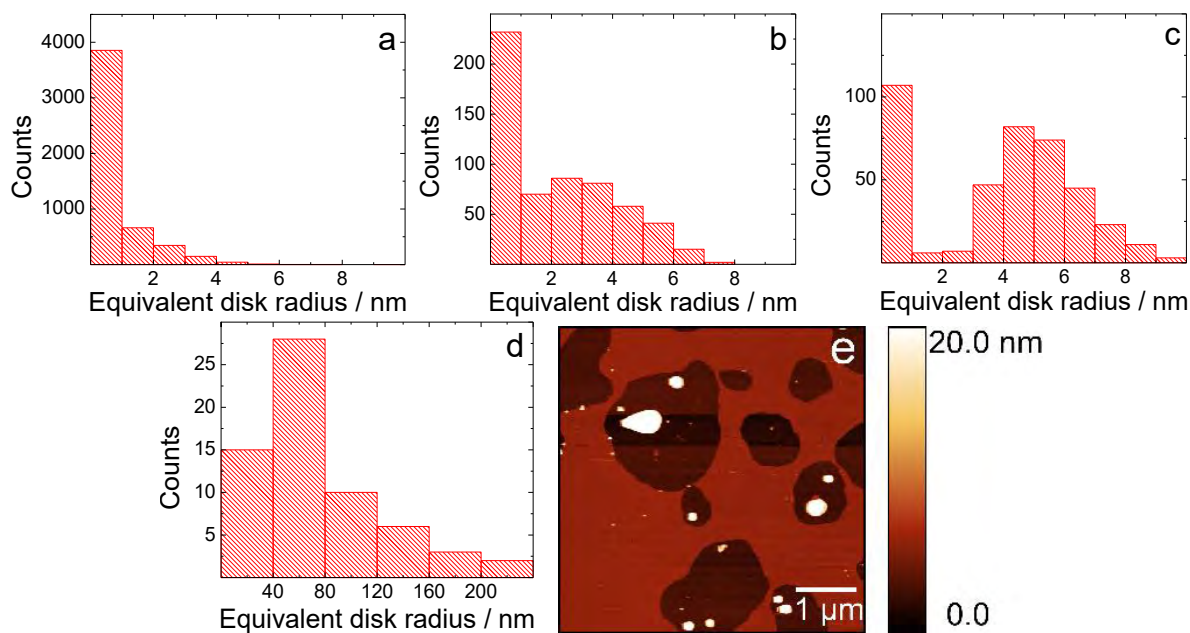


Figure 3.13. The equivalent disk radii distribution of (a) A β M_s, (b) SS A β O₂s, (c) LS A β O₂s, and (d) BTLE vesicles. (e) The AFM topography image of unfused BTLE vesicles and the BTLE lipid bilayer deposited on the mica support.

Temporal changes of the bilayer formed by a mixture of BTLE vesicles and SS A β oligomers. To observe temporal changes in the bilayer formed by the fusion of a mixture of BTLE vesicles and SS A β O₂s, the mixture of the A β -to-lipid mass ratio of 1:50 was used. This solution condition allows direct imaging of individual pores formed by SS A β oligomers. Similar measurements for LS A β were not performed because the decrease of the LS oligomers concentration should only affect the aggregation rate.³⁴ This rate directly correlates with the A β concentration, i.e., the higher the concentration, the higher is the aggregation rate. Figure 3.14 shows the time-lapse AFM images of a single pore formed in the A β -BTLE bilayer deposited on the mica surface from the mixed SS A β O₂s and BTLE vesicle solution. The A β aggregates surrounding the pore protrude ~1 nm above the BTLE membrane surface (Figures 3.14a). This protrusion is much lower than that observed for LS A β O₂s (Figure 3.6c). Moreover, equivalent disk radii of the A β aggregates shown in Figure 3.14a range between 2.4 and 4.2 nm, similar to that of SS A β O₂s, thus suggesting that the pores are formed by SS A β O₂s indeed.

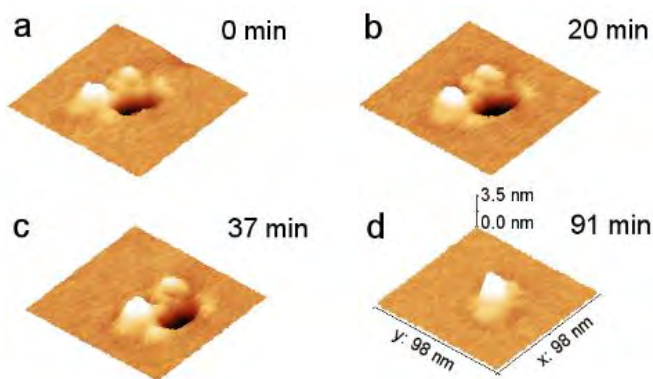


Figure 3.14. Time-resolved AFM topography images of a single pore in the outer BTLE leaflet formed in 0.01 M PBS (pH = 7.4) by the LMW A β O₂s after (a) 0, (b) 20, (c) 37, and (d) 91 min of interaction.

A different number of A β O₂s could surround the BTLE bilayer pores. For instance, Figure 3.15a shows an AFM image of the membrane pore surrounded by eight A β O₂s that protrude ~1 nm above the BTLE membrane surface (Figure 3.15b). Within the first ~37 min, the pore expands (Figures 3.14a-c), and then A β O₂s insert into the pore, clogging it (Figure 3.14d and movie M1). The pore filled with SS A β O₂s does not change during the next 90 min. Similar behavior is observed for multiple pores. Movie M2 shows that all pores initially expand and, eventually, become filled with SS A β O₂s. Penetration of the membrane by SS A β oligomers and their subsequent insertion into the cell can trigger cell death via leakage of lysosomal enzymes,^{73,310} inhibition of mitochondrial activity,^{74,311} increasing production of reactive oxygen species,⁷⁵ or cytosolic proteasome impairment.^{312–314}

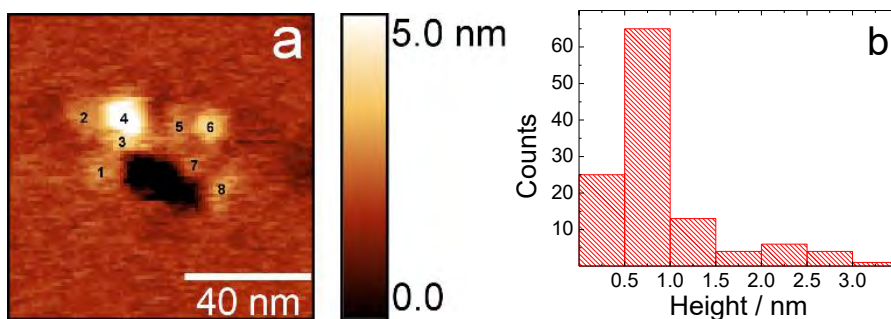


Figure 3.15. (a) The AFM topography image of the BTLE bilayer in 0.01 M PBS (pH = 7.4) with the pore surrounded by eight A β oligomers. (b) Histogram showing protrusion distribution of the LMW A β oligomers above the BTLE bilayer.

Evidently, BTLE membrane exposure to SS A β O_s results in the pore formation and subsequent SS A β O_s insertion in the BTLE bilayer, leading to membrane destruction. In detail, first, SS A β O_s form pores in the BTLE membrane. Then, the pores expand with time, and SS A β O_s insert themselves into the pores. Once inside the membrane, these oligomers have access to hydrophobic acyl chains of the BTLE membrane. The A β O_s hydrophobic residues interact with the hydrophobic BTLE acyl chains. Hiding hydrophobic parts and exposing hydrophilic parts of both nanocluster components to the solvent increases the A β -lipid complexes' stability in the polar environment.



Movie M1. Movie of a single pore expansion and A β O_s incorporation into the BTLE lipid bilayer.



Movie M2. Movie of a multiple pore expansion and A β O_s incorporation into the BTLE lipid bilayer.

Interaction of SS A β oligomers with supported BTLE bilayer. Additional measurements were performed to understand how SS A β O_s influence the behavior of BTLE vesicles. Control measurements were performed to determine whether the BTLE membrane topography changed (Figures 3.8a and 3.9a) because of SS A β O_s activity or ineffective disruption and fusion of vesicles. The control measurements for the LS A β O_s were not performed because the AFM images, shown in Figures 3.6a and 3.7a, clearly indicate the LS A β oligomers' presence on the membrane surface and their mechanism of interaction with the BTLE bilayer. The BTLE bilayer was first deposited on mica and then exposed to SS A β oligomers. For this purpose, 40 μ L of \sim 5 μ M SS A β solution was

added to the AFM cell. This concentration of SS oligomers corresponds to the A β concentration in the A β -BTLE vesicles mixtures. Figure 3.16 shows a sequence of AFM images acquired for the SS A β oligomers interacting for (a) 0, (b) 24, and (c) 72 h with the mica-supported BTLE bilayer. Initially, only single A β Os, protruding 2-3 nm above the bilayer plane, were visible (Figure 3.16a). These oligomers surround small (0.5 nm deep) pores (inset in Figure 3.16a). The interaction of A β with the membrane for 24 h resulted in the formation of \sim 5 nm-deep pores with a radius of \sim 22 nm (Figure 3.16b). Inset to Figure 3.16b shows that SS A β Os are present at the edges of these pores. Therefore, the pore depth increases from 0.5 to 5 nm after exposing the BTLE membrane to SS A β Os for 24 h. After 72 h, the bilayer is almost entirely disintegrated (Figure 3.16c). Numerous globular objects with radii of 10-20 nm (Figure 3.16d) and remnants of the 5.7-nm thick bilayer (Figure 3.16e) are observed.

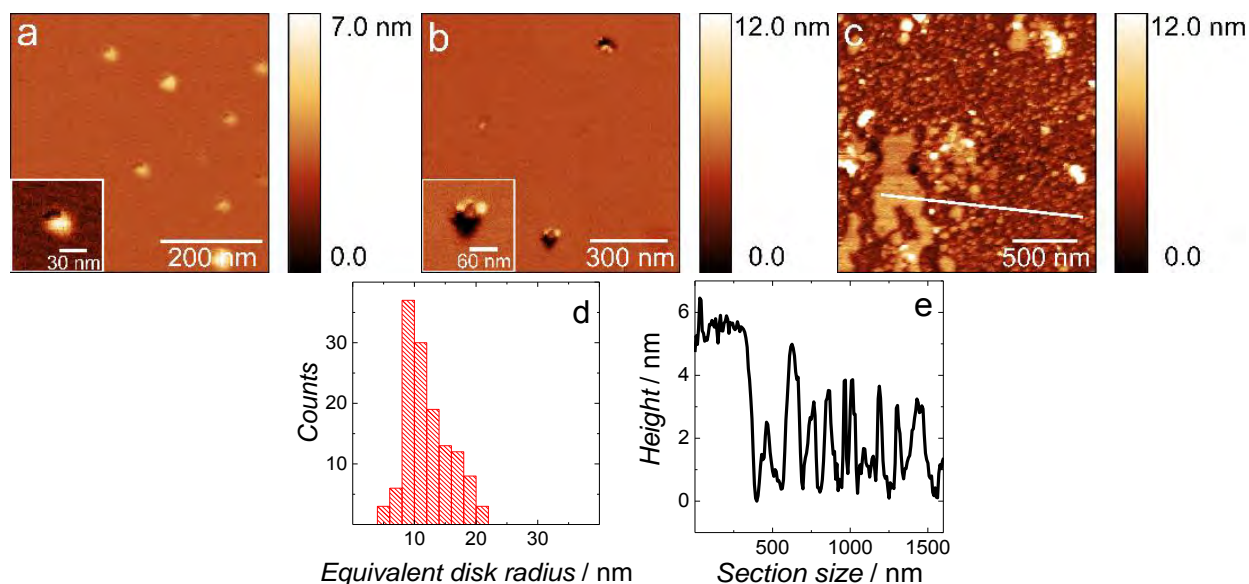


Figure 3.16. AFM topography images of the mica-supported BTLE bilayer, in 0.01 M PBS (pH = 7.4), exposed to the SS A β Os for (a) 0, (b) 24, and (c) 72 h. (d) Radius distribution of the nanoclusters observed in the AFM image in Panel (c). (e) Corresponding height profile showing thickness of the supported BTLE bilayer exposed to SS A β Os for 72 h shown in Panel (c).

For comparison, the intact supported BTLE bilayer, imaged after 0 and 72 h, is shown in Figure 3.17. Apparently, the bilayer is stable for 3 days, and its disintegration, shown in Figure 3.16, results from interaction with the SS A β Os. The size of globular objects seen in Figure 3.16c is comparable to that of globules shown in Figures 3.12a and 3.12b. This result indicates that both the formation of porous bilayer by spreading a mixture of BTLE vesicles and SS A β Os (Figure 3.12) and the pre-formed BTLE bilayer disintegration after exposure to SS A β Os (Figure 3.16) involves A β -lipid complex formation, a result of A β -induced lipid extraction.

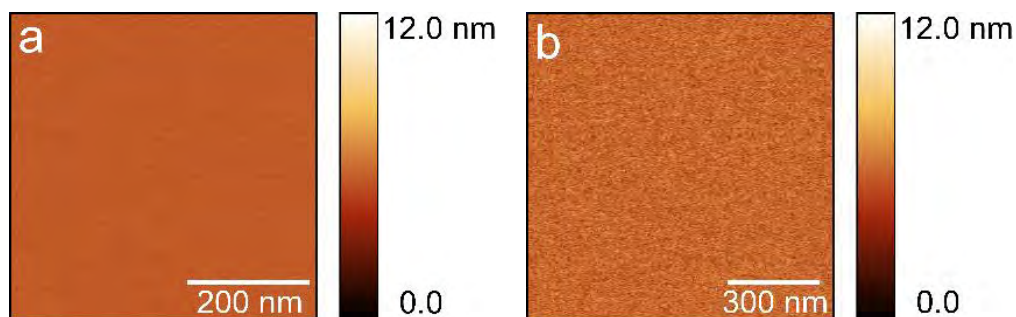


Figure 3.17. AFM topography images of the mica-supported BTLE bilayer in the absence of the SS A β O_s after (a) 0 and (b) 72 h in 0.01 M PBS (pH = 7.4) solution.

This study clearly shows that A β oligomers of different sizes interact differently with the BTLE membrane. During A β aggregation, both the secondary structure and the number of solvent-exposed hydrophobic residues of A β aggregates changes.^{201,315} LMW A β oligomers are more hydrophobic than HMW A β oligomers.²⁰¹ Moreover, the hydrophobicity correlates with the toxicity of A β oligomers of different sizes.¹⁹¹ That is, the higher the availability of hydrophobic sites on the aggregate surface, the higher is their toxicity. The high hydrophobicity of SS oligomers is the reason for their instability in polar solvent solutions. In these solutions, individual A β molecules spontaneously aggregate and minimize the number of exposed hydrophobic residues. However, in the presence of a biological membrane, LMW A β oligomers adsorb on the membrane surface and interact with hydrophobic phospholipid chains to form stable lipid-A β complexes. In contrast, the pre-formed HMW A β oligomers' hydrophobicity is lower because of their β -sheet secondary structure. This secondary structure is a matrix for extending and forming fibrils by intermolecular hydrogen bonding and also by side-chain interactions with other HMW oligomers.^{201,315}

3.4. Conclusions

Utilizing high-resolution AFM imaging, the unique direct BTLE lipid bilayer visualization allowed distinguishing between two different mechanisms of interaction of various size A β oligomers with a model brain-like phospholipid membrane. Large size (LS) A β oligomers aggregate on the BTLE bilayer surface via both primary and secondary nucleation mechanisms, but the bilayer's integrity remains intact. Unlike the LS A β oligomers, small size (SS) A β oligomers destroy the BTLE bilayer. The destruction mechanism consists of two consecutive events, i.e., pore formation followed by lipid extraction. After pore formation, the pores expand with time. Then SS A β oligomer molecules insert into these pores. The next step involves the extraction of phospholipid molecules from the membrane, leading to A β -lipid complexes' formation. Lipid extraction from the membrane, most likely, proceeds either via simultaneous involvement of phospholipids from both bilayer leaflets or, first, phospholipids from the outer and then, from the inner leaflet are

extracted. Figure 3.18 illustrates the proposed mechanisms of A β fibrillation and BTLE membrane destruction.

Both SS and LS A β oligomers cause a ~50% decrease in the bilayers Young's moduli. This decrease indicates that both forms of A β oligomers affect membrane stability, but each in a different way. These differences in membrane destabilization may imply differences in the toxicity, which should be investigated in future cytotoxicity studies.

Our results explain the toxicity mechanisms of A β oligomers formed at different aggregation stages and reconcile contradictory reports encountered in the literature. Moreover, our findings correlate well with the two distinct features found in AD patients, i.e., amyloid plaques and pathological consequences of neuronal death. The differences in the mechanism of SS and LS A β oligomers' interaction with a model cell membrane suggest that each of the oligomer forms may require unique treatment to inhibit their toxicity.

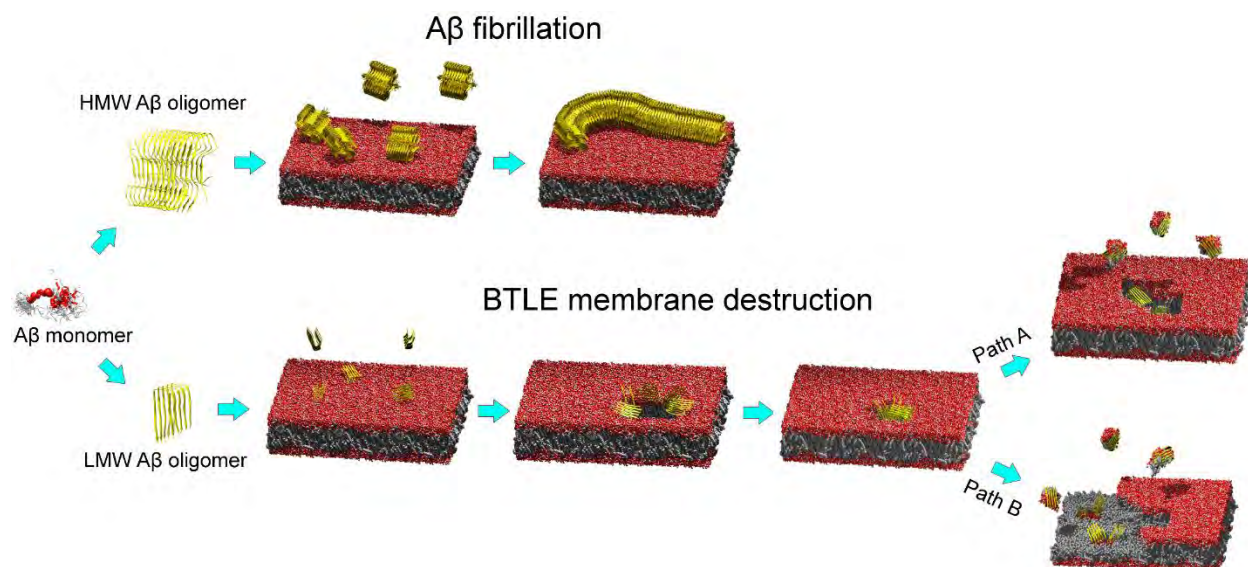


Figure 3.19. Illustration of the proposed mechanisms of the LS and SS A β O interaction with the BTLE bilayer. The illustration is produced in UCSF Chimera software⁵² using the 2OMP,³¹⁶ 1Z0Q,⁵³ 5V63,³¹⁷ and 5KK3³¹⁸ PDB files for lipid bilayer, A β M, SS and LS A β O, and A β fibrils, respectively.

Chapter 4. Alzheimer's disease-related amyloid β peptide causes structural disordering of lipids and changes the electric properties of a floating bilayer lipid membrane

This chapter discusses the research work published in *Nanoscale Adv.* **2020**, 2 (8), 3467–3480.

Dusan Mrdenovic,^{†,§} Zhangfei Su,[§] Wlodzimierz Kutner,^{†,‡} Jacek Lipkowski,^{§,*} Piotr Pieta^{†,*}

[†]Institute of Physical Chemistry, Polish Academy of Sciences, Kasprzaka 44/52, 01-224 Warsaw, Poland

[§]Department of Chemistry, University of Guelph, 50 Stone Road East, Guelph, Ontario N1G 2W1, Canada

[‡]Faculty of Mathematics and Natural Sciences, School of Sciences, Cardinal Stefan Wyszyński University in Warsaw, Wóycickiego 1/3, 01-815 Warsaw, Poland

Abstract

Neurodegeneration in Alzheimer's disease is associated with disruption of the neuronal cell membrane by the A β peptide. However, the disruption mechanism and the resulting changes in membrane properties remain to be elucidated. To address this issue, herein the interaction of amyloid β monomers (A β Ms) and amyloid β oligomers (A β Os) with a floating bilayer lipid membrane (fBLM) was studied using electrochemical and IR spectroscopy techniques. IR spectroscopy measurements showed that both A β forms interact similarly with the hydrophobic membrane core (lipid acyl chains). They cause conformational and orientational changes of the lipid acyl chains, decrease acyl chain mobility, and alter the lipid packing unit cell. In the presence of A β Os, these changes are more pronounced than in the A β Ms presence. However, the respective interactions of A β Ms and A β Os with the membrane hydrophilic exterior (lipid heads) are quite different. A β Ms dehydrate lipid heads without affecting their orientation, while A β Os change lipid heads' orientation, keeping their hydration level intact. Electrochemical measurements showed that only A β Os permeate the fBLM, significantly changing its electrical properties. The present results provide new molecular-level insight into the mechanism of membrane destruction by A β Os and changes in the membrane properties.

4.1. Introduction

The results of our previous AFM study lacked information about the changes inside the membrane. Therefore, the present chapter's research goal is to study the A β O-induced changes in the floating bilayer lipid membrane (fBLM) using polarization-modulation infrared reflection-absorption spectroscopy (PM-IRRAS) and different electrochemical techniques. These techniques have already been successfully applied to study the effect of antimicrobial peptides on the fBLM properties.^{153,278,319,320} The interaction of A β O with fBLM is compared with the interaction of fBLM with non-toxic A β M.

Only A β O form defects in the membrane. This defect formation results in a significant change in the membrane electric properties. These defects differ from the ion channels formed by other pore-forming peptides/proteins. Moreover, both A β M and A β O cause conformational and orientational changes of lipid molecules in the fBLM. All changes in fBLM are more pronounced in the presence of A β O, thus indicating that the interaction of A β O with the membrane is stronger than that of A β M. Our results provide new insight into the A β O-lipid interaction expanding knowledge about our previously proposed A β O-induced membrane destruction mechanism.

4.2. Experimental section

A β peptide preparation. Recombinant amyloid β (1-42) peptide was purchased from rPeptide (Watkinsville, USA). Its purity was high, as evidenced by MS analysis showing molecular mass identical to that expected for a monomer (Figure 4.1). The peptide was prepared following the previously developed protocol,²⁸⁰ with slight modifications that were introduced in our previous study (Chapter 3). First, a 1-mg sample of A β was dissolved in TFA from Sigma-Aldrich to reach the final concentration of 0.5 mg ml⁻¹. This dissolution is necessary to dissociate pre-existing A β aggregates that may act as seeds accelerating A β aggregation, causing irreproducibility in the experiments. The TFA addition to the peptide was followed by 5-min vortexing, and then the solvent was removed under an Ar stream. The resulting peptide film was left on the vial glass wall. Next, HFIP from Sigma-Aldrich was added to reach the 0.5 mg ml⁻¹ A β concentration. HFIP is another solvent used for A β disaggregation, and it also helps to remove traces of TFA. The A β -HFIP solution was vortexed for 5 min, and then HFIP was evaporated under an Ar stream. The addition and then removal of HFIP were repeated once more. Next, the peptide film was dissolved in HFIP to achieve the 0.25 mg ml⁻¹ A β concentration, and subsequently, the solution was vortexed for 5 min. This A β solution was divided into 20 aliquots, each containing 50 μ g of the peptide per centrifuge tube. The tubes were covered with Kimtech wipes to protect them from dust and then left under the fume hood overnight to allow for HFIP evaporation. Next, residual HFIP was removed under decreased pressure in a desiccator for 1 h. This HFIP removal resulted in the peptide film deposition on the bottom of the tubes. Those were then stored in the freezer at -20 °C. A single aliquot was used for each experiment. First, the aliquot was allowed

to equilibrate to room temperature for several minutes. Then, the peptide film was resuspended in 20 μl of DMSO. Finally, it was diluted with 0.01 M PBS (pH = 7.4) to reach the 50- $\mu\text{g ml}^{-1}$ A β concentration. The PBS solution was prepared by dissolving PBS tablets from Sigma-Aldrich in 200 mL of Milli-Q[®] water, 18.2 M Ω cm (EMD Millipore, Billerica, MA, US), thus obtaining the 0.01 M phosphate buffer, 0.0027 M KCl, and 0.137 M NaCl (pH = 7.4) solution. The A β solution prepared that way contained A β M. Our previous AFM study showed that A β M molecules are globular and are \sim 0.3 nm high. This A β M solution was immediately used to study A β M-lipid bilayer interaction. To analyze the A β O-lipid bilayer interaction, the A β M solution was stored in the fridge at 4 $^{\circ}\text{C}$ for 24 h, thus allowing aggregation of A β M into A β O. Our previous AFM study showed that toxic, globular A β O, with the height of \sim 1-3 nm and average diameter of \sim 6 nm (Figures 3.4b, 3.4e, and 3.14b), are formed under these conditions.

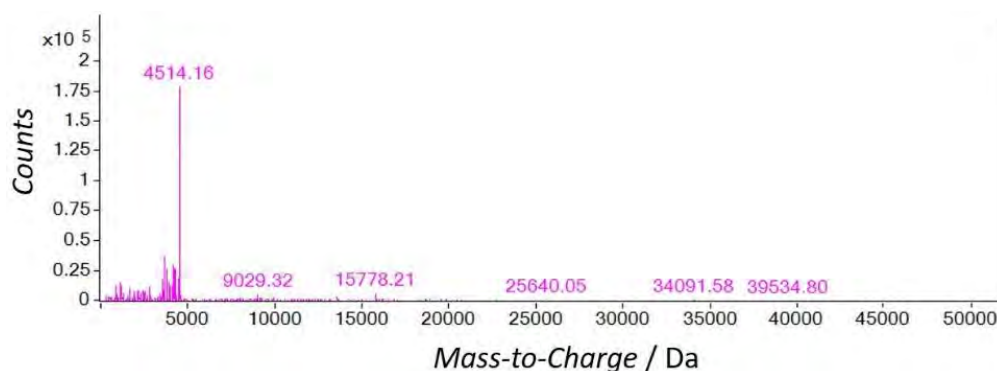


Figure 4.1. The A β mass spectrum showing A β molecular weight.

Lipid vesicle preparation. DSPE, DPPC, Chol, porcine brain SM, and ovine brain GM1 were purchased from Sigma-Aldrich and used without further purification. Structural formulas of lipids used are shown in Figure 4.2. DSPE was dissolved in the chloroform:methanol (9:1, v:v) mixed solvent solution at 50 $^{\circ}\text{C}$. Other lipids were dissolved in chloroform at room temperature. Lipid stock solutions were stored in the freezer at -20 $^{\circ}\text{C}$. An aliquot of the lipid stock solution was transferred to a glass vial, and the final solution contained 1 mg of lipids. The lipid mixture contained 50% DSPE, 15% DPPC, 25% Chol, 8% SM, and 2% GM1 by weight. This lipid composition was used to mimic aged lipid rafts formed in the membrane of the human frontal cortex cells found in AD patients' brains.³²¹ Next, the solvent was evaporated under an Ar stream accompanied by vortexing. The solvent removal resulted in the formation of a lipid film on the bottom of the glass vial. This film was then resuspended in PBS (pH = 7.4) to reach the 1 mg ml⁻¹ lipid concentration. Subsequently, the solution was sonicated using an ultrasonic cleaner (VWR Model 50D, 120V) for 20 min at 45 $^{\circ}\text{C}$, which resulted in the formation of lipid vesicles.

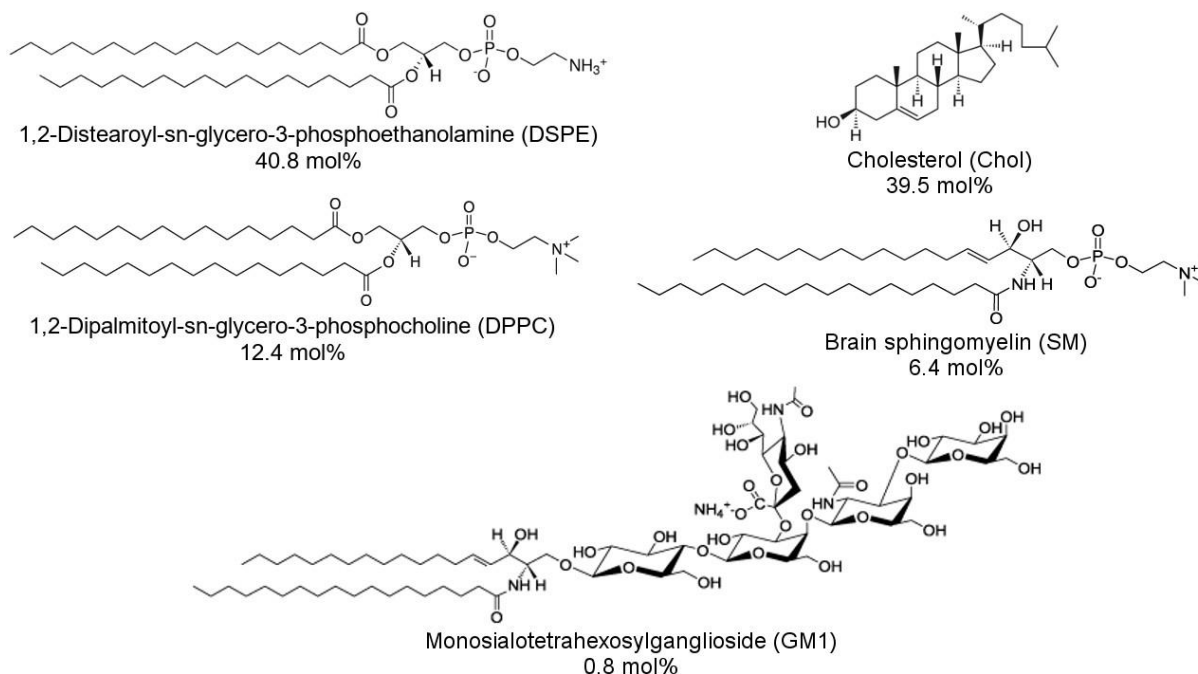


Figure 4.2. Structural formulas of lipids used to construct a model membrane of the human brain cell and their corresponding concentrations expressed in molar percentages.

Floating bilayer lipid membrane (fBLM) preparation. The vesicle fusion method was used to prepare an fBLM.²¹⁷ Small and big single-crystal Au(111) electrodes (surface area of 0.172 and 1.33 cm², respectively) were used as the working electrodes for electrochemical and PM-IRRAS measurements, respectively. Before use, the Au electrodes were pretreated according to the previously developed procedure.³²² Briefly, the electrodes were rinsed with Milli-Q® water, and then flame annealed using a Bunsen burner. After cooling down to room temperature, the electrodes were immersed in a 0.4 mg ml⁻¹ 1-thio-β-D-glucose (Tg) solution from Sigma-Aldrich for 5 h, which resulted in the formation of a self-assembled monolayer of Tg (SAM-Tg) on the gold surface. The SAM-Tg provides a hydrophilic cushion layer that enhances vesicle fusion and relieves stress imposed by the gold substrate on the fBLM.³²³ Moreover, it provides a water-rich layer underneath the lipid bilayer, thus mimicking the natural cell membrane environment. After SAM-Tg formation, the electrodes were rinsed with Milli-Q® water and then immersed in the lipid vesicle solution (either containing or not containing Aβ) overnight. Finally, the electrodes were taken out of the solution, and then the excess of the solution was gently removed with a Kimtech wipe.

Preparation of the Aβ-lipid bilayer mixture. In all experiments, the Aβ and lipid vesicle solutions were mixed to reach the peptide-to-lipid mass ratio of 1:20. The mixture was then sonicated for 10 min at room temperature, followed by overnight immersion of the Au(111) electrode in this mixture.

Electrochemical measurements. An all-glass three-electrode cell was used for all electrochemical measurements. An Au(111), Pt wire, and saturated Ag/AgCl electrode were used as the working, counter, and reference electrode, respectively. Before each measurement, the solution was deoxygenated with a 30-min Ar stream purge. During the experiments, a cushion of Ar was flowing over the solution. A small Au(111) electrode coated with the fBLM was assembled in the electrochemical cell in the hanging meniscus configuration. Namely, the electrode was slowly lowered vertically towards the electrolyte solution until it touched the solution surface. Then, it was raised to form a meniscus between the electrode surface and the electrolyte.

The immersion method^{241,324} was employed to determine the potential of zero free charge (E_{pzfc}) at the electrode surface. For that, the electrode freshly coated with the fBLM in the A β absence was used for each immersion measurement. The transient of the current flowing to the electrode, brought into contact with the electrolyte at a controlled potential (E), was measured. Insets (a) and (b) to Figure 4.3 show characteristic current transients recorded at potentials negative and positive to E_{pzfc} , respectively. The transients were integrated, and the corresponding charge was plotted as a function of the applied potential. From the intercept corresponding to zero charge density, the E_{pzfc} value was determined to be 0.11 (± 0.02) V vs. Ag/AgCl.

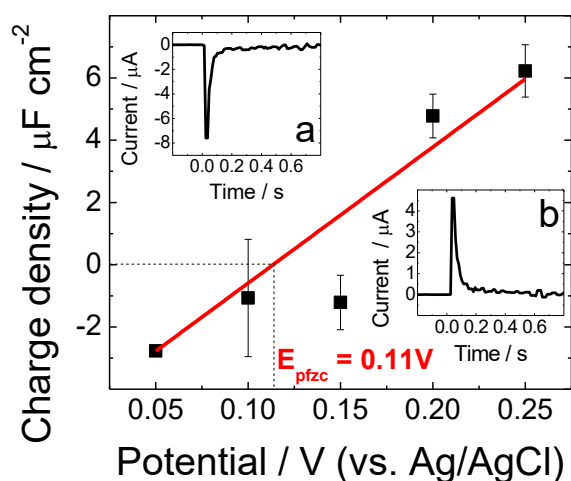


Figure 4.3. Charge density as a function of potential for fBLM in the PBS (0.01 M phosphate buffer, 0.0027 M KCl and 0.137 M NaCl, pH = 7.4) solution. Insets show current transients recorded for fBLM at (a) 0.05 V and (b) 0.25 V vs. Ag/AgCl in the same PBS solution.

Differential capacitance (DC) measurements were performed using PG590 potentiostat/galvanostat (HEKA, Pfalz, DE) and a lock-in amplifier (EG&G Instruments 7265 DSP, Wellesley, MA, US). The DC vs. potential curves were measured in the potential range of 0.3 to -0.9 V vs. Ag/AgCl at a scan rate of 20 mV s⁻¹. The resulting data were acquired using custom-designed software. The capacity was calculated from the in-phase and out-of-phase components

of the AC signal treating the electrochemical interface as a simple series *RC* equivalent electric circuit.

Electrochemical impedance spectroscopy (EIS) measurements were conducted using the Solartron SI 187 electrochemical interface and Solartron SI 1260 impedance/gain-phase analyzer (Ametek Scientific Instruments, Depew, NY). The EIS spectra were acquired in the potential range of 0.3 to -0.4 V vs. Ag/AgCl. During EIS measurements, an excitation sinusoidal signal of the amplitude of 10 mV was applied, and the spectra were recorded in the frequency range of 10^3 to 0.06 Hz. The data were analyzed, and the interface modeled using ZView software (Scribner Associates Inc.).

PM-IRRAS measurements. PM-IRRAS experiments were performed using Thermo Nicolet Nexus 8700 spectrometer (Madison, WI). The spectrometer was equipped with an external tabletop optical mount (TOM) box. A CaF_2 equilateral prism (BoXin, Changchun, CN) was used. The prism was first washed with methanol and then with Milli-Q[®] water, followed by 15-min treatment in the UV-Ozone cleaner (Jelight, Irvine, USA). The PM-IRRAS spectra for each spectral region of interest were recorded in a separate experiment. For significant enhancement of the mean-square electric-field strength, the half-wave retardation of the photoelastic modulator (PEM) was adjusted at 1600 and 2900 cm^{-1} , and the incidence angle was adjusted to 60° and 57° for spectra recording in the C=O stretching/ CH_2 scissoring and C-H stretching vibration regions, respectively. The spectroelectrochemical cell was filled with PBS (pH = 7.4) prepared with D_2O to avoid the H_2O bands' spectral interference. The spectral resolution was 4 cm^{-1} . For spectra recording, 4000 scans were acquired and then averaged in the potential range of 0.40 to -0.40 V vs. Ag/AgCl. The PEM response functions were corrected, as previously described.²⁵¹ Fourier self-deconvolution (FSD)²⁶⁵ analysis was performed using the bandwidth of 25-32 cm^{-1} and the enhancement factor of 2.5 depending on the spectral region of examination.

Tilt angle calculations. The angles between the surface normal and the direction of transition dipoles for symmetric (ν_s) and asymmetric (ν_{as}) methylene stretches, as well as C=O bond stretches, were calculated using Eq. 2.29, as described above (Chapter 2.2.4.). Simulated IR spectra were generated using custom-written software that solved the Fresnel equations by employing the transfer matrix method, as described previously.²⁵¹ The optical constants of gold, D_2O , and CaF_2 were taken from literature.²⁷³ The optical constants of the fBLMs with and without $\text{A}\beta$ were determined from the transmission IR spectra of lipid vesicle solutions with and without $\text{A}\beta$, respectively (Figure 4.4). The bands of symmetric (ν_s) and asymmetric (ν_{as}) methylene stretches were used to calculate the average tilt angle of the lipid molecules' acyl chains using Eq. 2.30, as described above (Chapter 2.2.4.).

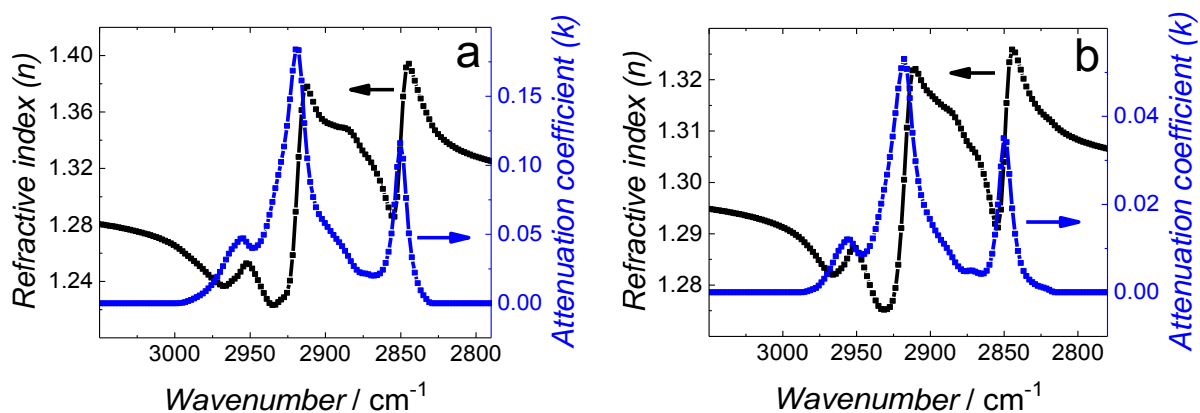


Figure 4.4. The refractive index and attenuation coefficient dependence on frequency for fBLM vesicles in the (a) absence and (b) presence of A β Os in the PBS/D₂O (0.01 M phosphate buffer, 0.0027 M KCl, and 0.137 M NaCl, pH = 7.4) solution.

4.3. Results and discussion

Electrochemical measurements. Differential capacitance (DC) measurements were performed to assess the quality and stability of the floating bilayer lipid membrane in the A β absence (fBLM) as well as in the presence of A β M (fBLM-A β M) and A β O (fBLM-A β O). Figure 4.5 shows DC vs. potential curves for the membrane-free Au electrode (curve 1 in Figure 4.5) as well as the Au electrode coated with fBLM (curve 2 in Figure 4.5), with fBLM-A β M (curve 3 in Figure 4.5), and with fBLM-A β O (curve 4 in Figure 4.5) in the potential range of 0.30 to -0.90 V vs. Ag/AgCl. The upper abscissa label is the transmembrane potential equal to $E - E_{pzfc}$. For all fBLMs, the capacitance was the lowest at 0.10 V vs. Ag/AgCl, indicating the highest stability at E_{pzfc} . The lowest capacitance for the fBLM was $7.3 \mu\text{F cm}^{-2}$, a value typical for fBLMs.^{153,325} In the presence of either A β M or A β O, the minimum value of capacitance increased to 14.6 or 16.8 $\mu\text{F cm}^{-2}$, respectively, indicating a decrease in the membrane quality. When the applied potential became more negative, the capacitance of the electrodes, coated with the three membranes, gradually increased. The bilayer started detaching at -0.60 V vs. Ag/AgCl, as manifested by a characteristic desorption/detachment peak at -0.70 V vs. Ag/AgCl. The DC vs. potential curves indicate that all three membranes are unstable at potentials more negative than -0.60 V vs. Ag/AgCl. Therefore, all further measurements were performed at $E > -0.40$ V vs. Ag/AgCl, i.e., where electrode wetting does not occur.

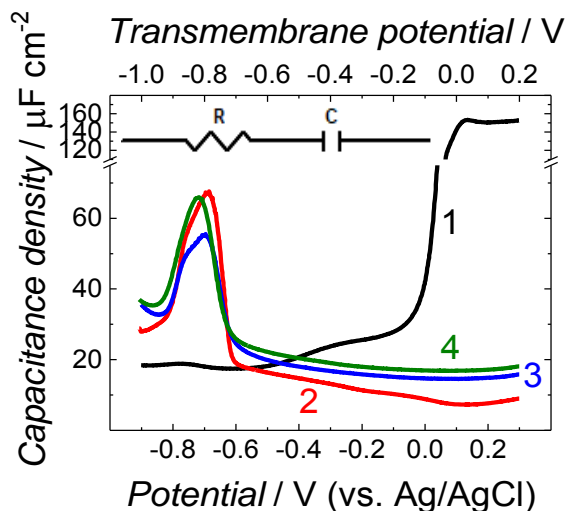


Figure 4.5. Differential capacitance vs. potential curves for (curve 1) the membrane-free Au electrode, (curve 2) the Au electrode coated with fBLM, (curve 3) fBLM-A β M, and (curve 4) fBLM-A β O in the PBS (0.01 M phosphate buffer, 0.0027 M KCl, and 0.137 M NaCl, pH = 7.4) solution. The upper abscissa label is the transmembrane potential that accounts for the potential of zero free charge ($E_{pzc} = 0.11$ V vs. Ag/AgCl). Inset shows an equivalent electric circuit used to determine the capacitance values.

The capacitance values (Figure 4.5) were determined using a simplified RC in series equivalent electric circuit (Inset in Figure 4.5). They provide useful information about the potential range where the bilayers are stable. More precise information about the membrane electrical properties can be obtained from electrochemical impedance spectroscopy (EIS) measurements and fitting an appropriate equivalent electric circuit to the EIS data acquired. Moreover, these data can provide information about the pore/defect forming abilities of A β . Figure 4.6 shows plots of Bode impedance vs. frequency in the range of 1000 to 0.06 Hz for fBLM (Figure 4.6a and 4.6b), fBLM-A β Ms (Figure 4.6c and 4.6d), and fBLM-A β Os (Figure 4.6e and 4.6f) at constant potentials in the range of 0.30 to -0.40 V vs. Ag/AgCl.

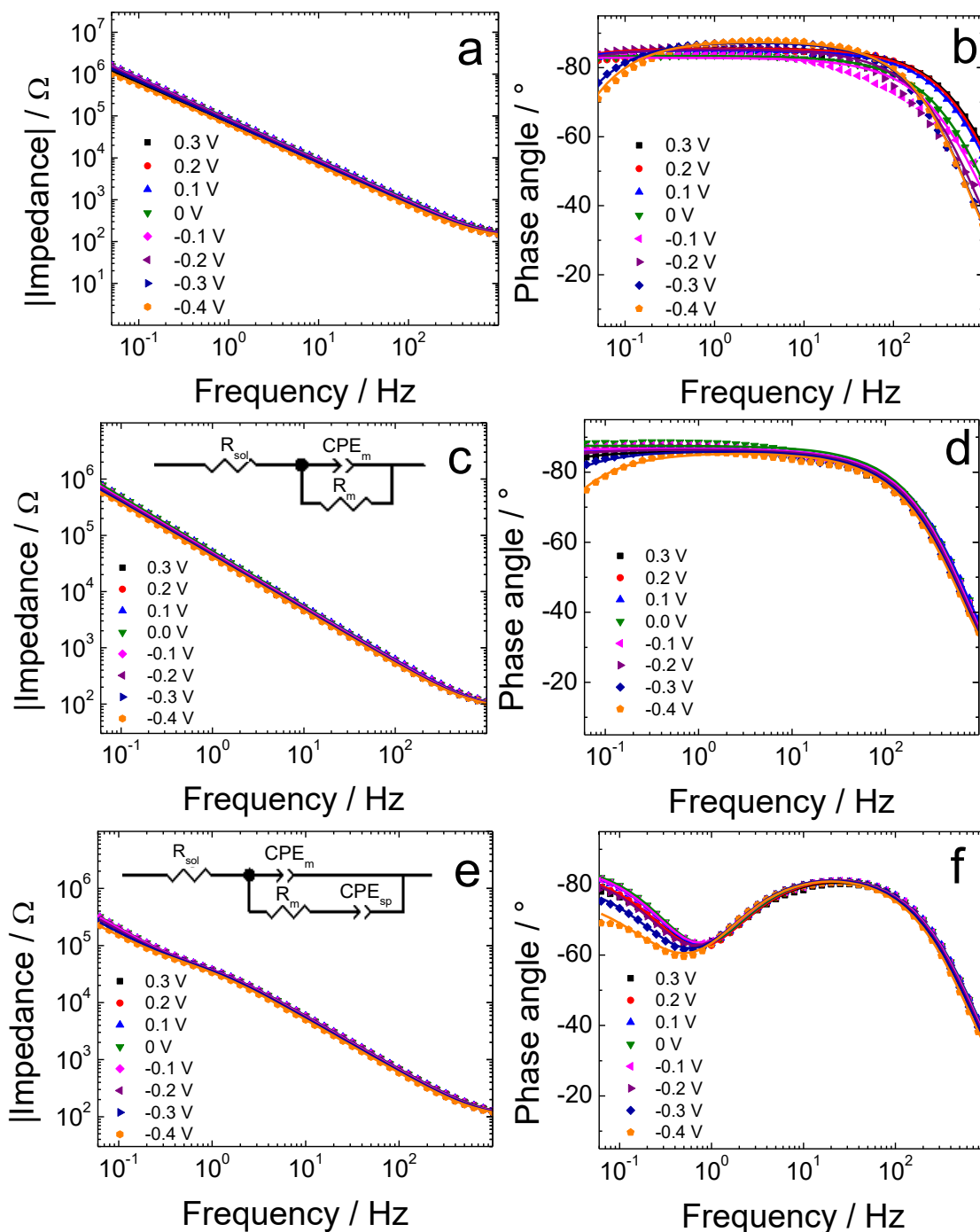


Figure 4.6. (a, c, e) Impedance and (b, d, f) phase angle as a function of frequency for (a, b) fBLM, (c, d) fBLM- β Ms, and (e, f) fBLM- β O_s in the PBS (0.01 M phosphate buffer, 0.0027 M KCl, and 0.137 M NaCl, pH = 7.4) solution at different potentials. Symbols and lines of the same colors represent experimental data and results of fitting of parameters of the equivalent electrical circuits to the EIS data, respectively, for the same measurement at a single potential. R_s and R_m – solution and membrane resistance, respectively; CPE_m and CPE_{sp} – constant-phase element for the membrane and submembrane (spacer) region, respectively.

Figures 4.6a, 4.6c, and 4.6e show the dependence of absolute impedance on frequency for fBLM, fBLM-A β Ms, and fBLM-A β Os, respectively. The impedance vs. frequency curves are almost linear for fBLM and fBLM-A β Ms, typical for capacitive systems.²⁴⁶ Their respective phase angle vs. frequency plots (Figures 4.6b and 4.6d) display a plateau with the phase angle values exceeding 80°, thus indicating that the membrane capacitance primarily controls the impedance. The phase angle decreases with the frequency decrease below 1 Hz for the two most negative potentials, i.e., -0.30 and -0.40 V vs. Ag/AgCl. This behavior is characteristic of pores/defects formation in the membrane because of electroporation.^{240,244,326} For the fBLM-A β Os membrane, the impedance vs. frequency curve (Figure 4.6e) displays a “step-like” feature below 1 Hz. The corresponding phase angle vs. frequency curve (Figure 4.6f) reveals a characteristic minimum at ~0.8 Hz. This minimum indicates that A β Os permeate the membrane.^{145,246} This experiment was repeated four times. The average values of frequency (f_{\min}) and phase angle (ϕ_{\min}) at the minimum of the phase angle curve are plotted as a function of potential in Figures 4.7a and 4.7b, respectively. Apparently, the f_{\min} and ϕ_{\min} are potential independent for transmembrane potentials more positive than -0.20 V. Besides, the minimum in the phase angle vs. frequency plot (Figure 4.6f) is symmetric. Both f_{\min} and ϕ_{\min} decrease with the transmembrane potential decrease at potentials more negative than -0.20 V. Concomitantly, the minimum in the phase angle vs. frequency plot (Figure 4.6f) becomes asymmetric.

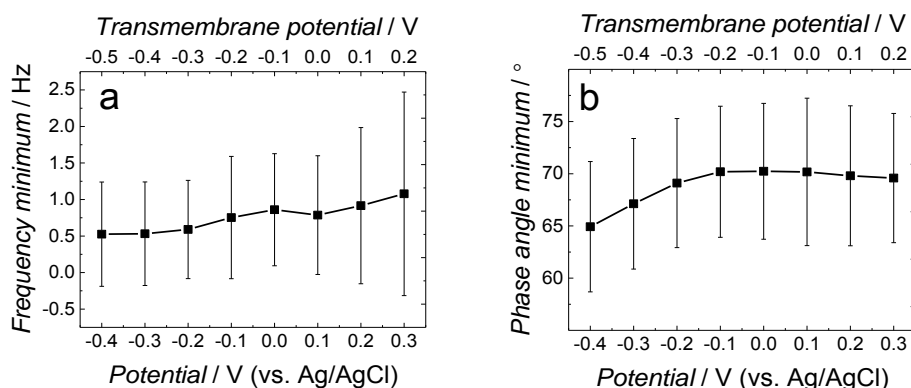


Figure 4.7. The change of (a) frequency and (b) phase angle at the phase angle vs. frequency minimum as a function of potential for fBLM-A β O in the PBS (0.01 M phosphate buffer, 0.0027 M KCl, and 0.137 M NaCl, pH = 7.4) solution. The upper abscissa label is the transmembrane potential that accounts for the potential of zero free charge ($E_{pzfc} = 0.11$ V vs. Ag/AgCl).

The shape and position of the phase angle vs. frequency minimum depend on the density and distribution of membrane defects.¹⁴⁵ For homogeneous defect distribution, the ϕ_{\min} is independent of the defect density, and the f_{\min} shifts towards higher frequencies with the increase of the defect density. Typically, defect distribution is homogeneous in the lipid bilayers in the presence of peptides, such as α -hemolysin and alamethicin.^{145,319,327} For heterogeneous defect distribution (defect clusters), the defect density increase causes the ϕ_{\min} increase and the

f_{\min} shift towards higher frequencies. This shift is much less pronounced than that for homogeneous defect distribution. In the presence of vaginolysin, membrane pores cluster in the lipid bilayers, having a heterogeneous defect distribution.²⁴⁶ Therefore, the phase angle vs. frequency minimum shifts towards lower phase angles and a minor shift with frequency at transmembrane potentials below -0.20 V (Figures 4.6f and 4.7) would suggest a decrease in the defect density. However, the membrane is electroporated in this potential range. That is, there are small pores formed in addition to the pores generated by A β Os. Therefore, the defect density should be higher and not lower, as earlier suggested.¹⁴⁵ However, all simulations concerning homogeneous and heterogeneous defect distributions were performed for membranes containing pores of the same radius.¹⁴⁵ Our AFM data showed that A β generated pores of different sizes in the lipid bilayers (Figures 3.8 and 3.9). It is unclear if the pore radius change affects the position of the phase angle vs. frequency minimum.

To determine that, the EIS spectra for the membrane with pores of different radii were simulated (Figures 4.8a and 4.8b). This simulation was performed using the previously adopted approach.¹⁴⁵ Figure 4.8b shows that the pore radius increase causes a shift of the phase angle vs. frequency minimum towards both higher phase angles and frequencies. Therefore, changes in both pores' density and the pore size significantly influence the phase angle position vs. frequency minimum. If this behavior (Figures 4.6f and 4.7) is considered, then it is evident that only big pores generated by A β Os are present in the membrane at transmembrane potentials exceeding -0.20 V vs. Ag/AgCl. However, at potentials below -0.20 V vs. Ag/AgCl, additional small pores are generated because of electroporation. Hence, a shift of the phase angle vs. frequency minimum towards lower phase angles and frequencies indicates a decrease of the average pore radius. These results demonstrate that the pore size change significantly affects EIS spectral features and should be considered when interpreting the EIS results. Moreover, this change reveals the fundamental difference between the properties of ion channels formed by other peptides, like α -hemolysin or alamethicin,^{145,319,327} and defects/pores formed by A β Os.

Figure 4.8c compares absolute impedance values determined at 0.8 Hz, i.e., the frequency of the phase angle vs. frequency minimum (Figure 4.6f), for all three fBLMs as a function of the electrode potential. For all three membranes, the impedance displays a maximum at ~ 0 V vs. Ag/AgCl, i.e., the potential slightly more negative than E_{pzc} . Apparently, either positive or negative charging of the electrode decreases membrane impedance. Significantly, this impedance is the highest for fBLM and the lowest for fBLM-A β Os.

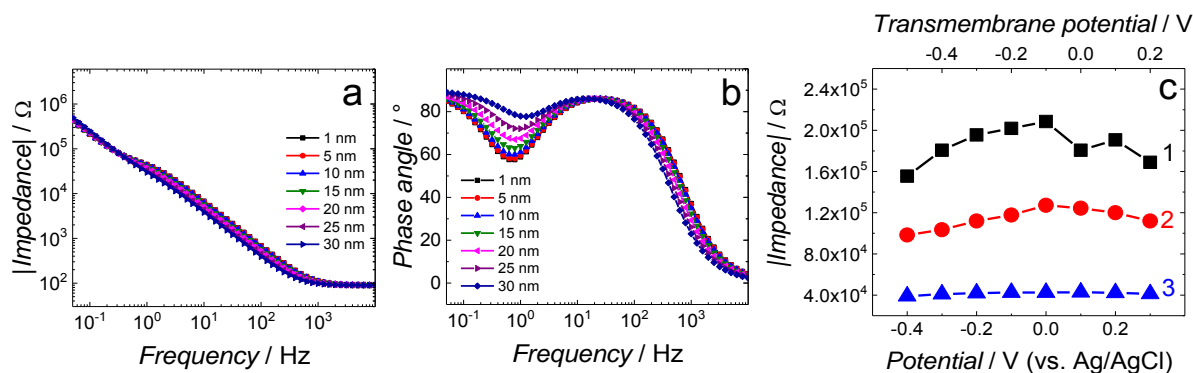


Figure 4.8. The EIS simulated curves of the (a) impedance and (b) phase angle dependence on frequency for the membrane with pores of different radii. Modeling was performed using the pore radii from 1 to 30 nm. Other parameters are: defect density, $N_{\text{def}} = 190 \mu\text{m}^{-2}$; Helmholtz layer capacitance, $C_H = 0.06 \text{ F cm}^{-2}$; membrane capacitance, $C_m = 0.045 \text{ F cm}^{-2}$; solution resistance, $R_{\text{sol}} = 90 \Omega$; pore conductance, $Y_{\text{def}} = 0.7 \text{ pS}$; thickness of the submembrane spacer layer, $d_{\text{sub}} = 1.7 \text{ nm}$; specific resistance of the conducting media in the submembrane spacer layer, $\rho_{\text{sub}} = 10^5 \Omega \text{ cm}$. (c) Experimental impedance as a function of potential at the phase angle vs. frequency minimum for (curve 1) the fBLM, (curve 2) fBLM-A β M, and (curve 3) fBLM-A β O in the PBS (0.01 M phosphate buffer, 0.0027 M KCl, and 0.137 M NaCl, pH = 7.4) solution. The upper abscissa label is the transmembrane potential that accounts for the potential of zero free charge ($E_{\text{pzfc}} = 0.11 \text{ V vs. Ag/AgCl}$).

Further information concerning the electrical properties of the three fBLMs is obtained by fitting an equivalent electric circuit to the EIS data. For fBLM and fBLM-A β Ms, a simple equivalent circuit (Inset in Figure 4.6c) is used, where R_s and R_m are solution and membrane resistance, respectively, and CPE_m is the membrane constant-phase element. The EIS measurements indicate that the presence of A β Ms does not lead to the formation of pores in the membrane (there is no minimum in the phase angle vs. frequency plot). For the fBLM-A β Os, the equivalent circuit proposed by Valincius²⁴⁴ (Inset in Figure 4.6e) is used. This circuit introduces a constant-phase element of the submembrane (spacer) region (CPE_{sp}), separating the membrane from the gold surface. This element accounts for the electric properties of the hydrated Tg monolayer. In the pores' presence, ions may migrate between the submembrane region and the solution bulk, affecting this region's properties. The impedance of the constant-phase element is defined by Eq. 2.10. If α is close to 1, the impedance is dominated by capacitance, and Q can be considered capacitance. If α is close to 0, the impedance is dominated by resistance.

Symbols in Figure 4.6 show experimental data, and solid curves represent the fitting of the equivalent circuits to the experimental data. The numerical values of elements of the equivalent circuits are reported in Table 4.1. The Q_m values can be considered as representing membrane capacitance because α_m parameters are close to 1.

Table 4.1. Numerical results of the equivalent electric circuits fittings to the EIS data for fBLM in the A β absence (fBLM), fBLM in the presence of A β monomers (A β Ms), and fBLM in the presence of A β oligomers (A β Os) at different potentials in 0.01 M PBS (pH = 7.4), 0.0027 M KCl, and 0.137 M NaCl.

E V vs Ag/AgCl	Q_m (fBLM) $\mu\text{F cm}^{-2}$	Q_m (A β Ms) $\mu\text{F cm}^{-2}$	Q_m (A β Os) $\mu\text{F cm}^{-2}$	α_m (fBLM)	α_m (A β Ms)	α_m (A β Os)	R_m (fBLM) $\text{M}\Omega \text{ cm}^2$	R_m (A β Ms) $\text{M}\Omega \text{ cm}^2$	R_m (A β Os) $\text{M}\Omega \text{ cm}^2$	Q_{sp} (A β Os) $\mu\text{F cm}^{-2}$	α_{sp} (A β Os)
0.3	15.03 ± 0.06	18.19 ± 0.06	20.61 ± 0.08	0.924 ± 0.001	0.956 ± 0.001	0.941 ± 0.006	4.71 ± 0.77	1.83 ± 0.05	0.0124 ± 0.0001	28.37 ± 0.12	0.927 ± 0.003
0.2	14.14 ± 0.04	15.69 ± 0.04	19.83 ± 0.05	0.930 ± 0.002	0.964 ± 0.001	0.943 ± 0.005	9.42 ± 1.78	2.37 ± 0.06	0.0127 ± 0.0000	28.17 ± 0.09	0.938 ± 0.002
0.1	13.83 ± 0.05	14.32 ± 0.04	19.68 ± 0.04	0.936 ± 0.001	0.968 ± 0.001	0.945 ± 0.004	11.92 ± 2.59	2.77 ± 0.07	0.0133 ± 0.0000	26.21 ± 0.07	0.963 ± 0.001
0	13.59 ± 0.04	14.18 ± 0.03	19.67 ± 0.04	0.951 ± 0.001	0.974 ± 0.001	0.946 ± 0.003	12.01 ± 1.63	2.892 ± 0.07	0.0131 ± 0.0000	25.37 ± 0.07	0.969 ± 0.001
-0.1	13.31 ± 0.03	14.64 ± 0.03	20.12 ± 0.05	0.963 ± 0.002	0.970 ± 0.001	0.946 ± 0.004	11.71 ± 0.83	2.75 ± 0.06	0.0135 ± 0.0000	26.01 ± 0.08	0.964 ± 0.002
-0.2	13.69 ± 0.02	15.29 ± 0.04	20.75 ± 0.05	0.967 ± 0.002	0.969 ± 0.001	0.946 ± 0.004	6.60 ± 0.17	2.15 ± 0.04	0.0134 ± 0.0000	29.24 ± 0.08	0.935 ± 0.002
-0.3	14.69 ± 0.04	16.54 ± 0.06	21.64 ± 0.07	0.968 ± 0.001	0.965 ± 0.001	0.945 ± 0.006	2.881 ± 0.05	0.980 ± 0.02	0.0130 ± 0.0001	33.87 ± 0.13	0.898 ± 0.003
-0.4	16.72 ± 0.08	19.26 ± 0.14	23.07 ± 0.13	0.972 ± 0.002	0.957 ± 0.002	0.944 ± 0.009	1.193 ± 0.01	0.331 ± 0.01	0.0119 ± 0.0002	41.01 ± 0.26	0.845 ± 0.005

Figure 4.9a compares membrane capacitance (Q_m) vs. potential curves for the three fBLMs. Qualitatively, they agree well with the corresponding DC vs. potential curves (Figure 4.5). All three curves display a broad minimum at $(E - E_{pzfc}) \sim -0.1$ V. The addition of A β M or A β O to the fBLM results in the Q_m increase at all potentials. For fBLM, the Q_m in the presence of A β O is higher than that in the A β M presence. Figure 4.9b compares membrane resistance changes with potential for the three membranes. Each curve displays a maximum at the transmembrane potential of ~ -0.10 V, which corresponds well to the minima position in the Q_m vs. potential curves in Figure 4.9a. The R_m rapidly decreases at both positive and negative potentials (Figure 4.9b). The maximum R_m value for the fBLM is ~ 4 and ~ 1200 times higher than that for fBLM-A β M and fBLM-A β O, respectively. Very low R_m values for fBLM-A β O are consistent with the pore formation by A β O, observed in our previous study (see Chapter 3, above).

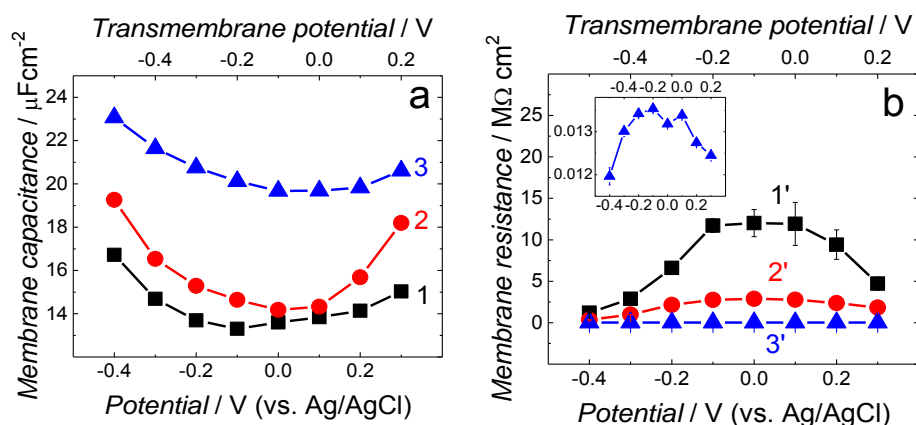


Figure 4.9. Potential dependence of membrane (a) capacitance (Q_m) and (b) resistance (R_m) for the fBLM (curves 1 and 1'), fBLM-A β Ms (curves 2 and 2'), and fBLM-A β O (curves 3 and 3') at different potentials in the PBS (0.01 M phosphate buffer, 0.0027 M KCl, and 0.137 M NaCl, pH = 7.4) solution. Inset shows the magnified R_m vs. potential curve for fBLM-A β O. The upper abscissa plots the transmembrane potential that accounts for the potential of zero free charge ($E_{pzfc} = 0.11$ V vs. Ag/AgCl).

Figure 4.10 presents plots of the spacer layer capacitance (Q_{sp}) and coefficient α_{sp} for fBLM-A β O as a function of electrode potential. The minimum of Q_{sp} and maximum of α_{sp} is displayed at transmembrane potential ~ -0.10 V, indicating the highest impedance of the submembrane region and demonstrating capacitive behavior at this potential. The Q_{sp} increase (Z_{sp} decrease) at both more positive and more negative potentials is associated with the decrease of α_{sp} , thus suggesting that the impedance of CPE_{sp} at this potential is more resistive. This behavior is consistent with electroporation and A β O-assisted membrane poration.

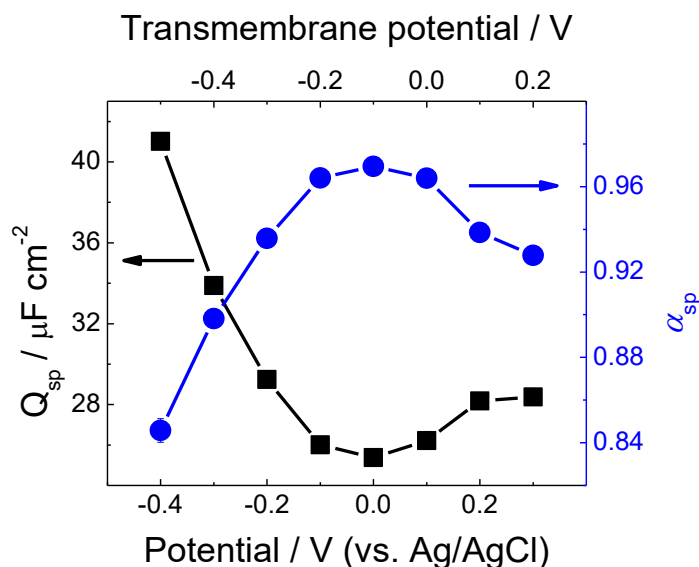


Figure 4.10. The constant phase element, Q_{sp} , and α_{sp} coefficient, representing the spacer layer's impedance, as a function of electrode potential for the fBLM with A β O in 0.01 M PBS (pH = 7.4), 0.0027 M KCl, and 0.137 M NaCl.

IR spectroscopy measurements. PM-IRRAS studies allow determining conformation and orientation of both phospholipids and A β molecules in the membrane and their dependence on the external electric field. The C-H vibration modes (located in the spectral range of 3100-2800 cm^{-1}), C=O vibration modes (1800-1700 cm^{-1}), and CH₂ vibration modes (1550-1350 cm^{-1}) provide information about the geometric properties of phospholipid molecules. The amide I band region (1700-1600 cm^{-1}) is useful for determining A β properties. Present PM-IRRAS measurements are performed in the potential range of 0.40 to -0.40 V vs. Ag/AgCl.

C-H bond stretching vibration modes of lipids. The C-H stretching vibration region (3100-2800 cm^{-1}) of the PM-IRRAS spectra contains useful information about lipid acyl chains' conformation and orientation.¹⁰⁸ Figures 4.11a-4.11c show PM-IRRAS spectra in the C-H stretching region for fBLM, fBLM-A β Ms, and fBLM-A β O. Spectra deconvolution in the C-H stretching region shows bands of both CH₂ symmetric ($\nu(\text{CH}_2)_s$) and asymmetric ($\nu(\text{CH}_2)_{as}$) vibrations, as well as CH₃ symmetric ($\nu(\text{CH}_3)_s$) and asymmetric ($\nu(\text{CH}_3)_{as}$) vibrations. Moreover, two bands corresponding to Fermi resonances (Figure 4.11d) are present.

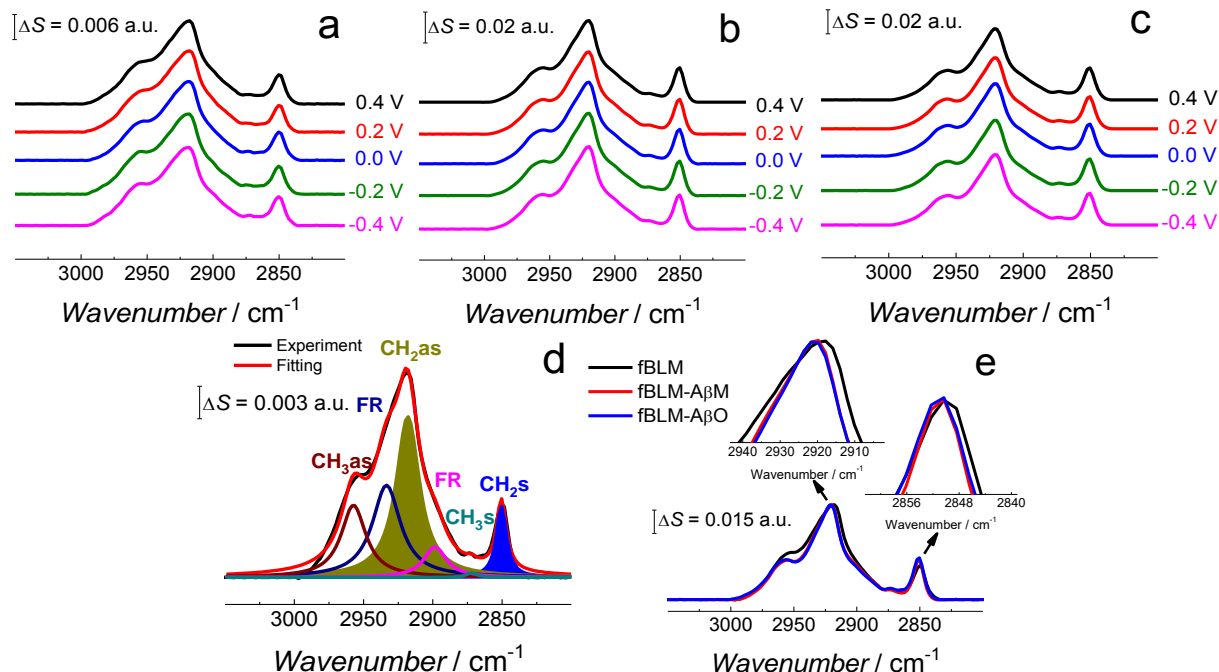


Figure 4.11. The PM-IRRAS spectra in the C-H stretching band region for (a) fBLM, (b) fBLM-AβMs, and (c) fBLM-AβOs at different potentials in the PBS (0.01 M phosphate buffer, 0.0027 M KCl, and 0.137 M NaCl, pH = 7.4) solution. (d) The deconvoluted PM-IRRAS spectra in the C-H stretching band region showing the methyl asymmetric (CH₃as), methylene asymmetric (CH₂as), methyl symmetric (CH₃s), methylene symmetric (CH₂s), and Fermi resonance (FR) bands. (e) Overlaid PM-IRRAS spectra for the bare fBLM (black curve), fBLM-AβM (red curve), and fBLM-AβO (blue curve) showing the change in the width and position of C-H stretching bands. Insets show magnified spectra regions of CH₂as (top inset) and CH₂as (right inset) bands for clarity.

Integrated intensities of the symmetric and asymmetric CH₂ bands are used to calculate the average tilt angle of *trans* fragments of acyl chains (Figure 4.12a), as described in Chapter 2.2.4. The optical constants of membrane lipids needed for these calculations are obtained from the transmission IR measurements (Figure 4.4). Figure 4.12b plots the calculated average tilt angle of *trans* fragments of acyl chains vs. potential. These values could be used as an approximate measure of the orientation of acyl chains. The lipid acyl chains' orientation is potential-independent for all three membranes. For fBLM, the tilt angle is 31(±1)°, typical of acyl chains in BLMs.^{277,328} The average tilt angle of acyl chains increases in the presence of either AβMs or AβOs at all potentials. It is equal to 54(±7)° and 64(±1)° for fBLM-AβMs and fBLM-AβOs, respectively. This significant increase suggests that both AβMs and AβOs interact with the membrane hydrophobic core, and this interaction is more pronounced for AβOs.

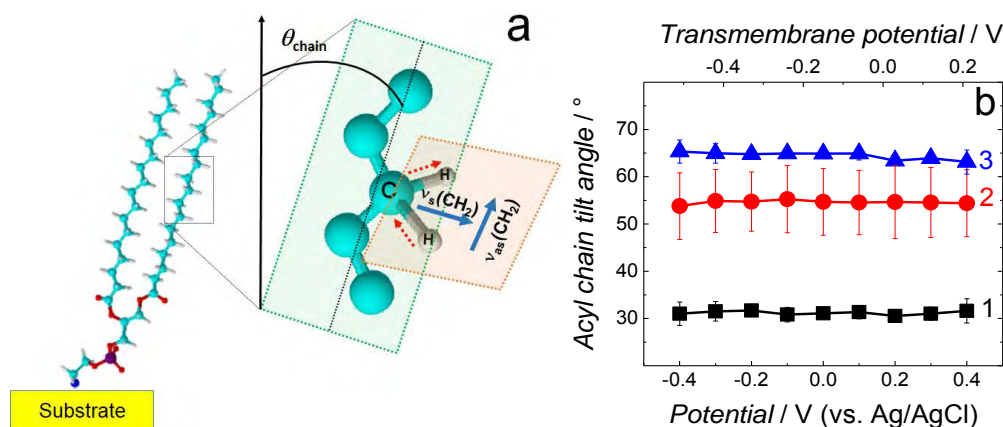


Figure 4.12. (a) Schematic view of the DSPE molecule adsorbed on Au(111) showing directions of the transition dipole moments of the symmetric, $\nu_s(\text{CH}_2)$, and asymmetric, $\nu_{as}(\text{CH}_2)$, methylene stretches for a lipid acyl chain and the tilt angle (θ_{chain}) of acyl chains [adapted from ¹⁰⁸]. (b) The tilt angle of lipid acyl chains as a function of potential for the (curve 1) fBLM, (curve 2) fBLM-A β M, and (curve 3) fBLM-A β O in the PBS/D₂O (0.01 M phosphate buffer, 0.0027 M KCl, 0.137 M NaCl, pH = 7.4) solution. The upper abscissa label is the transmembrane potential that accounts for the potential of zero free charge ($E_{\text{pzfc}} = 0.11$ V vs. Ag/AgCl).

Position and width of $\nu(\text{CH}_2)_s$ and $\nu(\text{CH}_2)_{as}$ bands provide information on the phospholipid acyl chain conformation and mobility in the membrane.^{254–256} The two CH₂ stretching bands' positions are potential independent for both fBLM-A β M and fBLM-A β O (Figures 4.13a and 4.13b, respectively). In contrast, these bands for fBLM are shifted to higher wavenumbers at negative potentials. This shift is more pronounced for the asymmetric band (curve 1 in Figure 4.13b). The $\nu(\text{CH}_2)_s$ and $\nu(\text{CH}_2)_{as}$ wavenumbers below 2850 and 2920 cm^{-1} , respectively, are characteristic of the bilayer's gel state, in which acyl chains are fully stretched and assume the all-*trans* conformation.¹⁰⁸ Wavenumbers' values of the two bands correspond to the gel state of fBLM in the absence of A β (Figures 4.13a and 4.13b). In the presence of either A β M or A β O, these bands shift towards higher wavenumbers, indicating partial melting of the lipid acyl chains. This shift is more distinct for the $\nu(\text{CH}_2)_{as}$ band than for the $\nu(\text{CH}_2)_s$ band. These results indicate that lipids have an increased number of *gauche* conformers in the presence of both A β M and A β O, suggesting lipid acyl chains' melting by both A β forms.^{255,329} The chain melting is more pronounced in the A β O's presence than in the A β M's presence. For all three membranes, widths of the $\nu(\text{CH}_2)_{as}$ and $\nu(\text{CH}_2)_s$ bands are potential independent (Figures 4.13c and 4.13d). However, the presence of either A β M or A β O induces a significant decrease in both bands' width. This width decrease indicates an A β -induced decrease of lipid acyl chain mobility.^{255,256}

The spectra in the C-H stretching region indicate that the amyloid presence induces changes in lipid acyl chains' orientation and conformation and decreases chains' mobility. These changes differ from typical temperature-induced phospholipid chain melting, where conformational disordering is accompanied by increased lipid acyl chain mobility.²⁶²

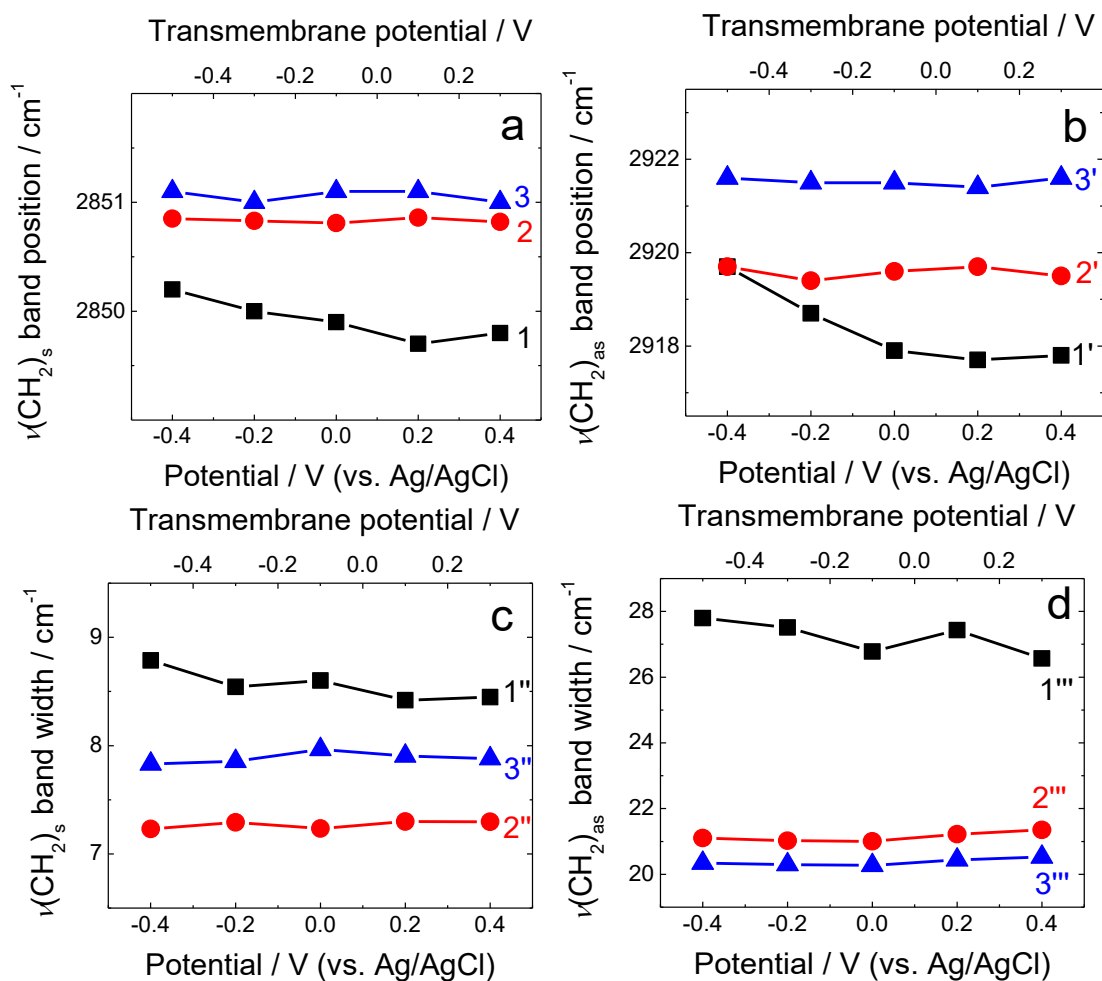


Figure 4.13. (a, b) Position and (c, d) width of the (a, c) $\nu(\text{CH}_2)_s$ and (b, d) $\nu(\text{CH}_2)_{as}$ bands as a function of potential for (curves 1, 1', 1'', and 1''') fBLM, (curves 2, 2', 2'', and 2''') fBLM- $\alpha\beta$ M, and (curve 3, 3', 3'', and 3''') fBLM- $\alpha\beta$ O in the PBS/ D_2O (0.01 M phosphate buffer, 0.0027 M KCl, and 0.137 M NaCl, pH = 7.4) solution. $\text{CH}_2(s)$ and $\text{CH}_2(as)$ stand for the CH_2 stretching symmetric and asymmetric vibrations, respectively. The upper abscissa label is the transmembrane potential that accounts for the potential of zero free charge ($E_{\text{pzfc}} = 0.11$ V vs. Ag/AgCl).

C-H scissoring vibration mode of lipids. The C-H scissoring vibration band, $\delta(\text{CH}_2)$, provides useful information concerning interchain interactions and packing of lipid molecules in the bilayer. Figure 4.14 shows PM-IRRAS spectra in the $1550\text{-}1420\text{ cm}^{-1}$ region containing a wide band for all three membranes. The FSD analysis allows the deconvolution of the broad spectral region. The bands seen in the FSD spectra can be assigned to the asymmetric $\delta(\text{N}^+(\text{CH}_3)_3)_{as}$ vibration (band at $\sim 1490\text{ cm}^{-1}$), the $\delta(\text{CH}_2)$ scissoring vibration (band at $\sim 1470\text{ cm}^{-1}$), the $\delta(\text{CH}_3)_{as}$ asymmetric vibration of terminal CH_3 groups of acyl chains (band at $\sim 1450\text{ cm}^{-1}$), and $\delta(\text{N}^+(\text{CH}_3)_3)_s$ symmetric vibration of terminal CH_3 groups of acyl chains (band at $\sim 1437\text{ cm}^{-1}$ overlapping with that for $\delta(\text{CH}_3)_s$).^{255,260}

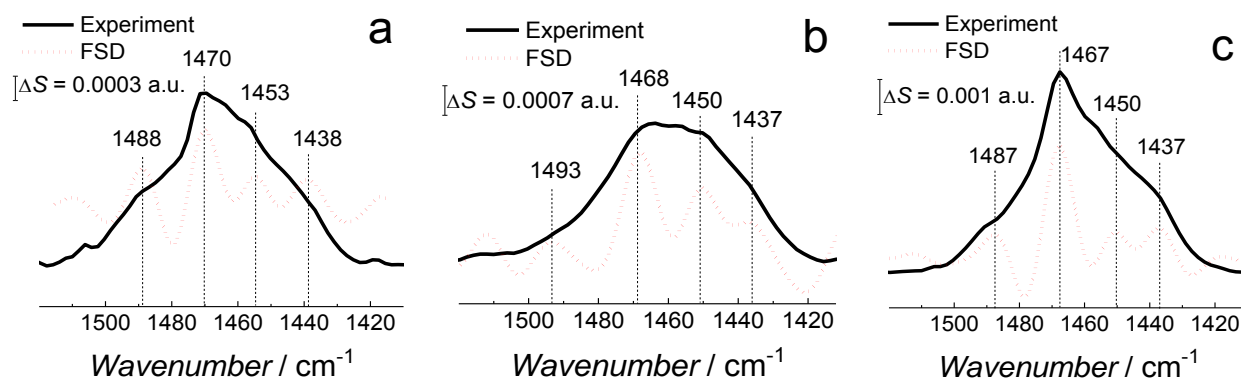


Figure 4.14. (solid black curves) The PM-IRRAS spectra in the CH₂ scissoring vibration band region and (red dotted curves) the corresponding Fourier self-deconvolution (FSD) spectra for (a) fBLM, (b) fBLM- $\alpha\beta$ Ms, and (c) fBLM- $\alpha\beta$ Os in the PBS/D₂O (0.01 M phosphate buffer, 0.0027 M KCl, and 0.137 M NaCl, pH = 7.4) solution.

The δ (CH₂) scissoring band is shifted from 1470 cm⁻¹ for fBLM to 1468 and 1467 cm⁻¹ for fBLM- $\alpha\beta$ Ms and fBLM- $\alpha\beta$ Os, respectively. These shifts indicate that in both $\alpha\beta$ forms presence, lipid molecule packing changes from the triclinic to the hexagonal unit cell.^{257–260}

C=O stretching vibration mode of lipids. The 1800-1700 cm⁻¹ region of the PM-IRRAS spectrum contains a band corresponding to the ester carbonyl C=O stretching vibration of the glycerol moiety of the phospholipid molecule. The PM-IRRAS spectra and the corresponding FSD analysis for the three bilayers at different potentials are shown in Figure 4.15.

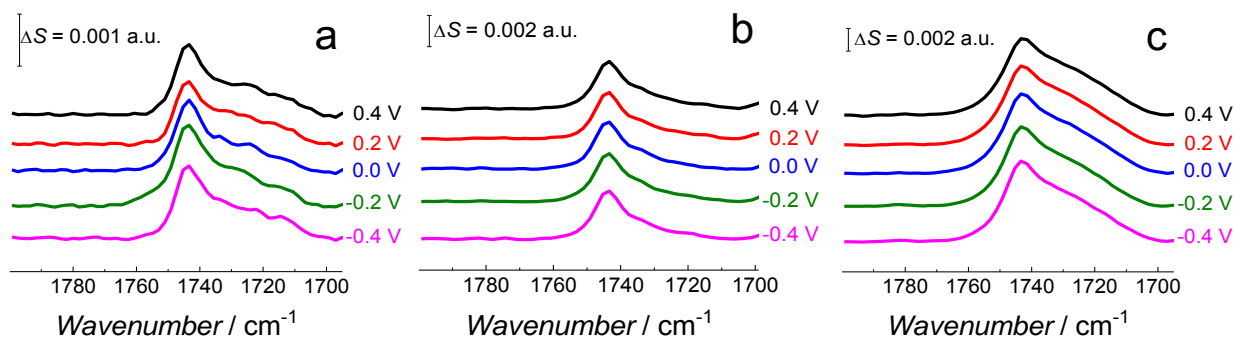


Figure 4.15. The PM-IRRAS spectra in the C=O stretching band region for (a) fBLM, (b) fBLM- $\alpha\beta$ Ms, and (c) fBLM- $\alpha\beta$ Os at different potentials in the PBS/D₂O (0.01 M phosphate buffer, 0.0027 M KCl, and 0.137 M NaCl, pH = 7.4) solution.

The FSD analysis shows a band at $\sim 1743\text{ cm}^{-1}$ corresponding to a non-hydrogen bonded (dehydrated) carbonyl group and two bands at ~ 1731 and $\sim 1724\text{ cm}^{-1}$ corresponding to a hydrogen-bonded (hydrated) carbonyl group (Figures 4.16a-c). The C=O band's deconvolution revealed that sub-bands corresponding to non-hydrogen-bonded and hydrogen-bonded carbonyl groups occupy areas of similar size in fBLM and fBLM-A β O (Figures 4.16d and 4.16f). This feature indicates that the content of non-hydrated and hydrated lipid heads in these two samples is similar. In fBLM, 52 and 48% of the lipid heads were non-hydrated and hydrated, respectively. In fBLM-A β O, 55 and 45% of the lipid heads were non-hydrated and hydrated, respectively. However, in fBLM-A β M, 67 and 33% of the lipid heads were non-hydrated and hydrated, respectively (Figure 4.16e). These results suggest that A β Ms, unlike A β O, dehydrate lipid heads.

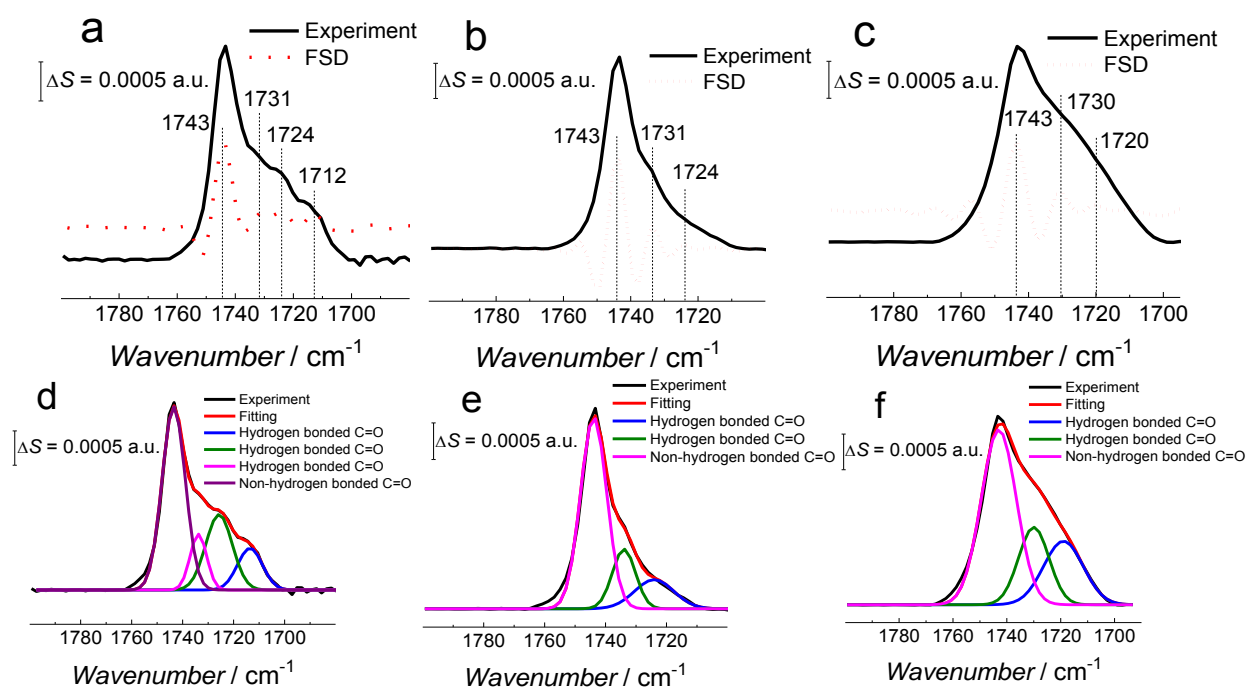


Figure 4.16. (solid black curves) The PM-IRRAS spectra and (red dotted curves) the corresponding Fourier self-deconvolution (FSD) spectra of the C=O band region for (a) fBLM, (b) fBLM-A β M, and (c) fBLM-A β O in the PBS/D₂O (0.01 M phosphate buffer, 0.0027 M KCl, and 0.137 M NaCl, pH = 7.4) solution at different potentials. The PM-IRRAS spectra deconvoluted in the C=O band region for (d) fBLM, (e) fBLM-A β M, and (f) fBLM-A β O.

The spectra are independent of the potential applied (Figure 4.15). Therefore, they are averaged and normalized to improve the *S/N* ratio (Figure 4.17b). The integrated intensity of the C=O band and Eq. 2.29 are used to calculate the angle between the direction of the transition dipole moment of the C=O bond and the surface normal, i.e., the direction of the C=O bond angle (Figure 4.17a). Figure 4.17c plots the C=O bond angle as a function of the potential applied for all three

membranes. The C=O bond angle is potential independent (within limits of experimental errors) for all three membranes. The C=O bond is nearly perpendicular to the fully stretched acyl chain.

Therefore, the sum of the acyl chains and the C=O bond angles against the surface normal should be $\sim 90^\circ$. Indeed, the determined C=O angle of $\sim 70^\circ$ is consistent with the acyl chain tilt angle of $\sim 30^\circ$ determined for fBLM (Figure 4.12b). However, the C=O bond angle of $\sim 73^\circ$ for fBLM-A β Ms is unexpectedly high because the acyl chain tilt angle is $\sim 50^\circ$, thus resulting in the sum of these two angles of $\sim 120^\circ$. Notably, the sum of tilt angles for C=O bonds and acyl chains for the fBLM-A β O is again close to 100° . The sum of the C=O bond and acyl chain angles for fBLM-A β Ms higher than those of fBLM and fBLM-A β O, as well as dehydration of lipid heads only in the presence of A β Ms, suggest that A β Ms interact with the membrane lipids in a fundamentally different way than A β O do.

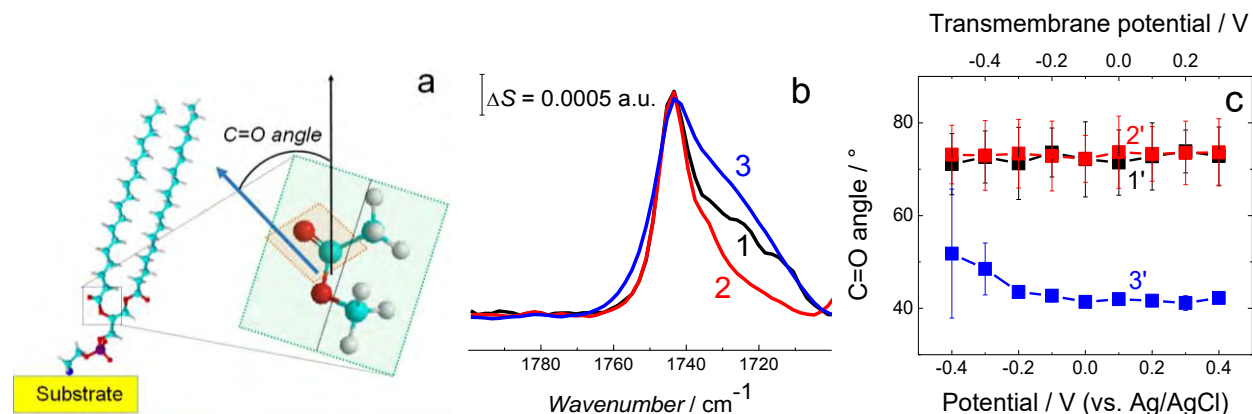


Figure 4.17. (a) Schematic view of DSPE molecule adsorbed on Au(111) showing the C=O bond angle between the (black arrow) surface normal and (blue arrow) direction of the transition dipole moment of the C=O bond. (b) Normalized and averaged PM-IRRAS spectra in the C=O stretching vibration region for the (curve 1) fBLM, (curve 2) fBLM-A β M, and (curve 3) fBLM-A β O in the PBS/D₂O (0.01 M phosphate buffer, 0.0027 M KCl, and 0.137 M NaCl, pH = 7.4) solution. Each spectrum is an average of five spectra shown in Figure 4.15. (c) The C=O bond angle for the (curve 1') fBLM, (curve 2') fBLM-A β M (curve 2'), and (curve 3') fBLM-A β O as a function of the potential applied. The upper abscissa label is the transmembrane potential that accounts for the potential of zero free charge ($E_{pzfc} = 0.11$ V vs. Ag/AgCl).

The amide I band spectra. The amide I band of peptides and proteins is used to determine their secondary structure. A β aggregation is accompanied by the conversion of a structure rich in α -helices and random coils present in A β M to β -sheet secondary structure characteristic of A β aggregates.^{330–332} Therefore, the secondary structure's determination can help identify the A β form that interacts with fBLM. The amide I band is usually very broad and, therefore, requires spectral deconvolution for interpretation. Figures 4.18a and 4.18b show PM-IRRAS spectra of the amide I band for fBLM-A β M and fBLM-A β O, respectively, at different potentials.

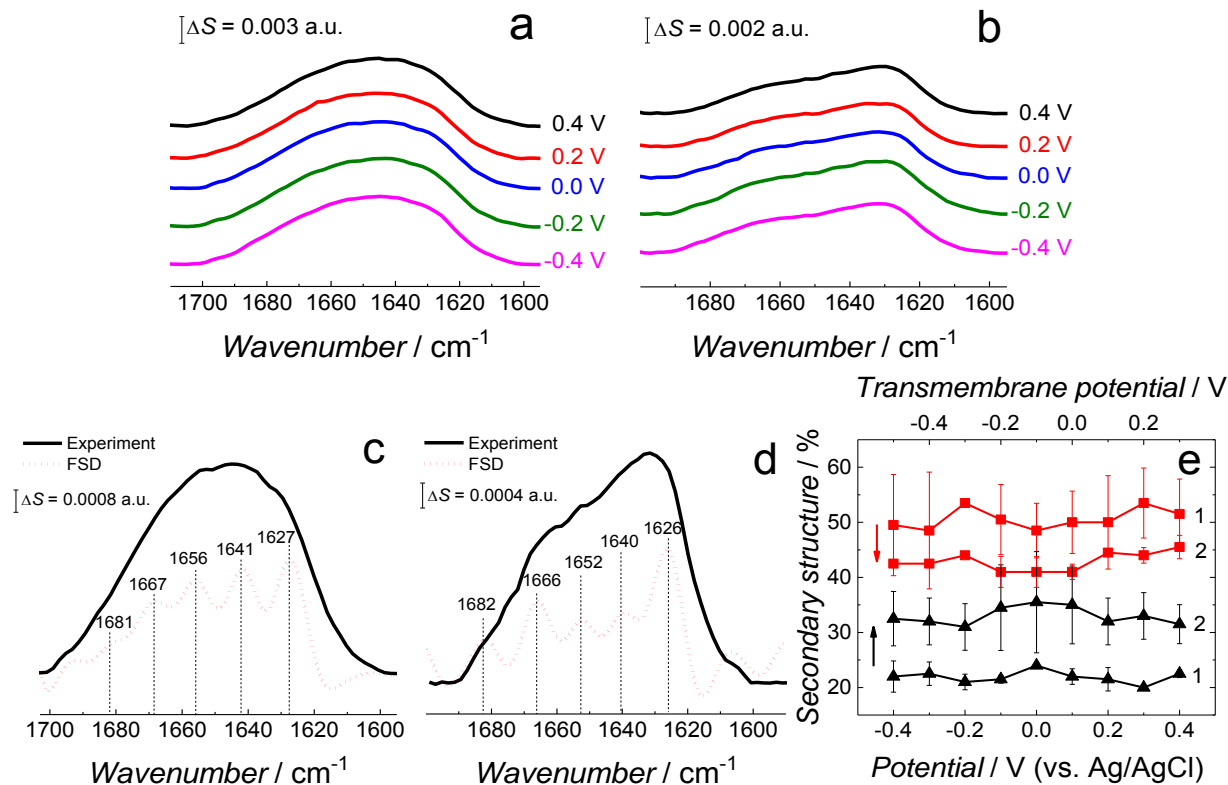


Figure 4.18. The PM-IRRAS spectra in the amide I band region for (a) fBLM-A β M and (b) fBLM-A β O in the PBS/D₂O (0.01 M phosphate buffer, 0.0027 M KCl, and 0.137 M NaCl, pH = 7.4) solution at different potentials. (solid black curves) The PM-IRRAS spectra and (red dotted curves) the corresponding FSD spectra in the amide I band region for (c) fBLM-A β M and (d) fBLM-A β O at 0 V vs. Ag/AgCl. (e) The content of (black curves) β -sheet and (red curves) random coil/ α -helix secondary structure, estimated by deconvolution of the PM-IRRAS spectra of (curve 1) fBLM-A β M and (curve 2) fBLM-A β O vs. potential. The black arrow indicates an increase in the β -sheet content, and the red arrow indicates a decrease in the content of the random coil/ α -helix secondary structures in fBLM-A β O compared to the corresponding contents in fBLM-A β M.

The amide I band is weakly potential dependent for both fBLM-A β M and fBLM-A β O. The spectra recorded at different potentials are averaged and plotted in Figure 4.19. The FSD analysis is used to reveal the sub-bands in a broad envelope of this spectral region (Figures 4.18c and 4.18d). With this information, the spectra in Figure 4.19 are deconvoluted to show sub-bands corresponding to the random coil, β -sheet, β -turn, and α -helix secondary structures. For both fBLM-A β M and fBLM-A β O, the secondary structures did not change with the potential applied (Figure 4.18e). The amide I band in fBLM-A β M (Figure 4.19a) contains strong α -helix and random coil bands, characteristic of A β M.³³³ In contrast, Figure 4.19b shows weaker α -helix and random coil bands and a stronger β -sheet band for fBLM-A β O compared to those for fBLM-A β M. This

result indicates higher β -sheet as well as lower α -helix and random coil content in fBLM-A β Os compared to those in fBLM-A β Ms (Figure 4.18e). This change in the dominant secondary structure of A β signifies the presence of A β aggregates.^{280,333,334}

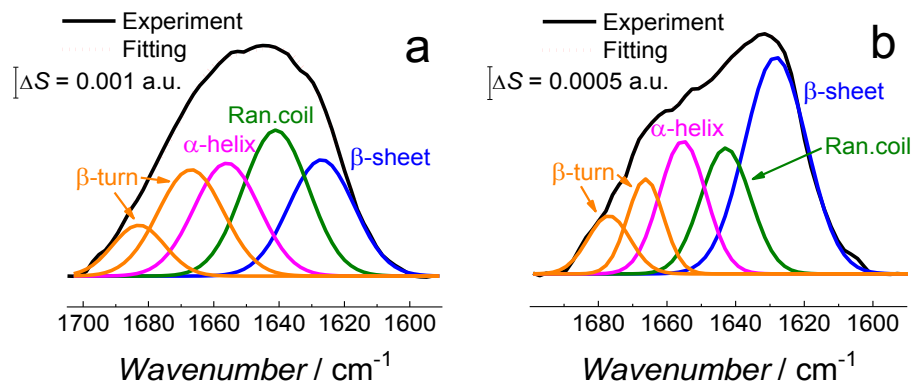


Figure 4.19. Deconvoluted amide I band region of the PM-IRRAS spectra averaged at all potentials for (a) fBLM-A β Ms and (b) fBLM-A β Os in the PBS/D₂O (0.01 M phosphate buffer, 0.0027 M KCl, and 0.137 M NaCl, pH = 7.4) solution.

Figure 4.20 shows the correlation between the secondary structure content of both A β forms (A β Ms and A β Os) and the C=O bond angle against the surface normal. The aperture had to be adjusted accordingly, and every spectral region of interest had to be studied in a separate experiment to obtain high enhancement of the signal in the spectral region of interest in the PM-IRRAS experiment. The lipid C=O band is located close to the amide I band of A β . Therefore, the signal from both regions is expected to be enhanced similarly. Hence, it is easy to directly correlate changes in the C=O angle of the carbonyl glycerol ester group in the lipids with changes of the amide I band in the A β secondary structure in a single experiment. Figure 4.20 was constructed using four independent measurements. A cluster of points at $\sim 78^\circ$ and $\sim 68^\circ$ correspond to two separate measurements for fBLM-A β Ms, and the remaining points correspond to measurements for fBLM-A β Os. Because the spectra were recorded at several potentials for each measurement, the data point spread within the cluster accounts for small changes induced by the electrode potential variation. The content of the random coil and α -helix secondary structures is high, and that of β -sheet is low for fBLM-A β Ms, thus indicating a high population of A β Ms and a low population of A β Os, respectively. As expected for fBLM-A β Os, the random coil and α -helix secondary structures' content is low, and the content of the β -sheet is high. Apparently, the population of A β Os dominates over that of A β Ms as expected because the A β Os population increases at the expense of the A β Ms population during A β aggregation. Interestingly, the higher the A β Os population, the lower is the C=O bond angle. This relation directly shows that the change in the C=O bond angle in each membrane is influenced by the presence of A β O only.

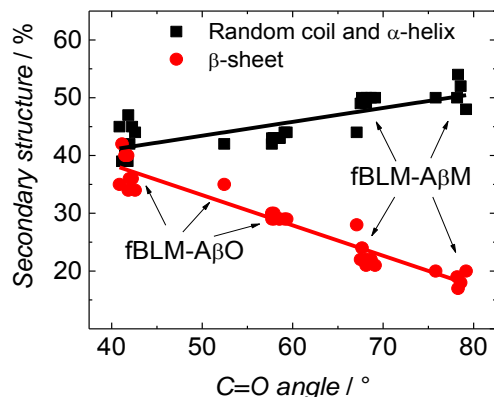


Figure 4.20. The correlation between the content of dominant A β secondary structure and changes in the C=O bond angle against the surface normal for fBLM-A β M and fBLM-A β O samples. The secondary structure percentage corresponds to the fraction of the sub-bands' area to the total area under the amide I band.

Generalized two-dimensional correlation spectroscopy (2D-COS)³³⁵ was employed to analyze spectra used to construct Figure 4.20. The perturbation applied to obtain these spectra was the change in the angle of the C=O bond in the membrane lipids. The 2D-COS analysis provides two significant pieces of information, i.e., (i) it allows identifying bands corresponding to different elements of the secondary structure, thus verifying the FSD analysis, and (ii) it provides information about sequential changes of analyzed bands.^{266,335} Synchronous (Figure 4.21a) and asynchronous (Figures 4.21b and 4.21c) 2D-COS spectra were constructed for 1800-1600 cm^{-1} region. The synchronous spectra show poorly resolved broad auto-correlation bands located at the diagonal (Figure 4.21a). The low resolution and the absence of sub-bands indicate that the spectral changes are predominantly asynchronous (out of phase).¹⁰⁸ There are two negative cross-correlation bands between bands corresponding to C=O vibrations in lipids and amide I sub-bands of A β . These bands' negative sign indicates that the bands of lipids and amide I bands change in opposite directions.

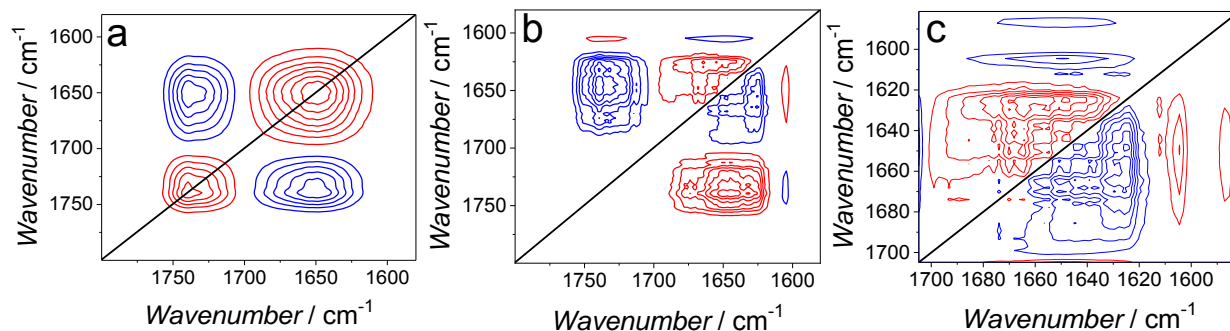


Figure 4.21. (a) Synchronous and (b) asynchronous 2D-COS spectra used to calculate data plotted in Figure 4.20. (c) Enlarged asynchronous 2D-COS spectra of the amide I band region for A β .

The resolution of asynchronous spectra is high, and all sub-bands identified by FSD are seen (Figure 4.21b). This performance confirms that the observed changes are out of phase. The asynchronous spectrum consists of cross-correlation bands only and provides information about sequential changes of the bands. The positive sign of a band (ν_1 , ν_2) indicates that the ν_1 band changes precede changes in the ν_2 band.^{266,335} The cross-correlation of amide I bands of A β and C=O bands of lipids is positive. However, the corresponding cross-correlation band in the synchronous spectrum is negative, and, hence, it inverts the sequence predicted by the asynchronous bands. This feature indicates that changes in the C=O bands precede changes in the amide I bands, i.e., first, changes in the lipids, and then changes in the peptide occur.

Figure 4.21c shows magnified asynchronous spectra corresponding to amide I bands of A β . The synchronous spectra for this region are absent. The analysis shows negative cross-correlation between the β -sheet band at 1626 cm^{-1} and all other amide I sub-bands. This feature indicates that the β -sheet band changes after other sub-bands change. In general, the analysis indicates that a higher wavenumber band changes before a lower wavenumber band. That is, the β -turn (1681 cm^{-1}) change is followed by changes in β -turn (1667 cm^{-1}), α -helix (1556 cm^{-1}), random coil (1640 cm^{-1}), and finally, in β -sheet (1626 cm^{-1}). Changes in α -helix/random coil (A β Ms structure) precede changes in β -sheet (A β O structure). This sequence of changes suggests that the cause of changes shown in Figure 4.20 is A β M aggregation into A β O, involving the transformation of the α -helix/random coil structure to that of β -sheet. This inference is consistent with the A β aggregation mechanism.³³⁰

4.4. Conclusions

The interactions of A β M and A β O with fBLM were investigated using electrochemical and IR spectroscopic techniques. Electrochemical measurements demonstrated that A β O significantly altered the electric properties of the membrane. These changes resulted from the membrane poration by A β O. The electric properties of the fBLM-A β O were different from those reported for lipid bilayers containing ion channels, thus evidencing the fundamental difference between pores formed by A β O and ion channels formed by other toxins, such as α -hemolysin and alamethicin.^{145,319,327} Moreover, the change in the average pore size significantly affected the EIS results and should be considered when analyzing the EIS data for phospholipid bilayers. This finding demonstrates a novel way of interpreting the EIS results.

PM-IRRAS studies show that both A β M and A β O cause significant lipid molecules disordering, as evidenced by conformational and orientational changes of lipid molecules in the fBLM. Both A β forms interact with the membrane hydrophobic core. They increase the tilt angle of lipid acyl chains, increase the number of *gauche* conformers in the lipid acyl chains, decrease lipid acyl chains' mobility, and change the lipid molecule packing. All these changes were more significant in the presence of A β O than in the A β M presence. For fBLM-A β M, the phospholipid carbonyl groups were dehydrated, and there was no change in the angle of the C=O bond located in the lipid heads. In contrast, A β O changed the angle of the C=O bond, causing the reorientation of

lipid heads without affecting their hydration. These results demonstrate that the respective interactions of A β M and A β O with lipid heads are significantly different. The 2D-COS spectroscopy results showed that structural changes of lipids preceded those of A β . Moreover, they confirmed that changes in the random coil and α -helix bands preceded changes in the β -sheet band. These results comply with the A β aggregation mechanism assuming structural transformation from the random coil/ α -helix to the β -sheet secondary structure.

The present results provide novel information on the A β -induced changes in the fBLM properties, thus enabling a deeper understanding of the mechanism of interaction of A β with bilayer lipid membranes and, consequently, pathology of Alzheimer's disease.

Chapter 5. Inhibition of amyloid β -induced lipid membrane permeation and amyloid β aggregation by K162

The present chapter discusses the research work submitted for publishing.

Dusan Mrdenovic,^{†,§} Piotr Zarzycki,[#] Marta Majewska,[†] Izabela S. Pieta,[†] Robert Nowakowski,[†] Włodzimierz Kutner,^{†,‡} Jacek Lipkowski,[§] Piotr Pieta^{†,*}

[†]Institute of Physical Chemistry, Polish Academy of Sciences, Kasprzaka 44/52, 01-224 Warsaw, Poland

[§]Department of Chemistry, University of Guelph, 50 Stone Road East, Guelph, Ontario N1G 2W1, Canada

[#]Energy Geosciences Division, Lawrence Berkeley National Laboratory, 1 Cyclotron Road, Berkeley, California, United States

[‡]Faculty of Mathematics and Natural Sciences, School of Sciences, Cardinal Stefan Wyszyński University in Warsaw, Wóycickiego 1/3, 01-815 Warsaw, Poland

Abstract

Alzheimer's disease (AD) is characterized by progressive neurodegeneration associated with amyloid β (A β) peptide aggregation. The aggregation of A β monomers (A β Ms) leads to the formation of A β oligomers (A β Os), the neurotoxic A β form, capable of permeating the cell membrane. Here, we investigated the effect of a fluorene-based active drug candidate, named K162, on both A β aggregation and A β O toxicity towards the bilayer lipid membrane (BLM). Electrochemical impedance spectroscopy (EIS), atomic force microscopy (AFM), and molecular dynamics (MD) were employed to show that K162 inhibits A β Os-induced BLM permeation, thus preserving BLM integrity. In the presence of K162, only shallow defects on the BLM surface are formed. Apparently, K162 modifies A β aggregation by bypassing the formation of toxic A β Os, and only non-toxic A β Ms, dimers (A β Ds), and fibrils (A β Fs) are produced. Unlike other A β toxicity inhibitors, K162 preserves neurologically beneficial A β Ms. This unique K162 inhibition mechanism provides an alternative AD therapeutic strategy for future exploration.

5.1. Introduction

Recent studies consider A β O to be the most toxic A β form, while A β M and A β F are considered non-toxic.^{61–63} A β O can permeate the cell membrane.^{161,162,164,167} Once incorporated into the cell, they may cause learning and cognition deficiency,^{66,69} deterioration of synapses,^{70,71} leakage of lysosomal enzymes,⁷³ inhibition of mitochondrial activity,⁷⁴ increased production of reactive oxygen species,⁷⁵ and neuroinflammation.^{76,77}

A β inhibitors act either by (i) stimulating A β M aggregation into non-toxic off-pathway oligomers,^{336–338} (ii) binding to fibril surface, thus preventing A β O formation via secondary nucleation,^{339,340} or (iii) accelerating A β aggregation, thus decreasing the lifetime of toxic A β O and stimulating the formation of non-toxic A β F.^{341–343} In all these therapeutic strategies, A β M are consumed. A β M stimulate brain development,²⁷ positively contribute to differentiation and proliferation of neural progenitor cells,³⁴⁴ human neural stem cells,³⁴⁵ enhance survival of neurons,³⁴⁶ and protect neurons from excitotoxic cell death.³⁴⁷ Therefore, the disadvantage of previously developed therapeutic strategies is that with the elimination of A β M, many beneficial physiological abilities of A β M are lost.

A fluorene-based compound known as K162 decreases A β O toxicity in vivo.³⁴⁸ Evidently, K162 penetrates the blood-brain barrier, inhibits A β O binding to synapses, and decreases amyloid load inside MC65 cells and hippocampus of 5xFAD mice brain. However, the mechanism of these K162 in vivo effects is not described.

Here, we reveal that K162 prevents A β O-induced bilayer lipid membrane (BLM) permeation by altering the A β aggregation pathway. In the K162-modified A β aggregation, A β M dimerize. Then, these A β dimers (A β D) do not oligomerize but fibrillate. This way, the formation of membrane-permeating A β O is bypassed. Unlike other amyloid inhibitors, K162 preserves the neurologically beneficial A β M.

5.2. Experimental section

A β peptide preparation. Lyophilized amyloid β (1-42) peptide was purchased from rPeptide (Watkinsville, USA) and Bachem (Bubendorf, Switzerland). The MS analysis showed that the peptide purity was high (Figure 4.1). The peptide solution was prepared by following the previously developed procedure²⁸⁰ with slight modifications introduced in our previous studies (Chapters 3.2 and 4.2, above). Briefly, A β was first dissolved to reach the 0.5-mg ml⁻¹ concentration in TFA from Sigma-Aldrich by 5-min vortexing to remove pre-existing A β aggregates. Then, TFA was removed under an Ar stream, leaving the peptide film on the glass vial wall. Next, the peptide film was dissolved to reach the 0.5 mg ml⁻¹ concentration in HFIP from Sigma-Aldrich by 5-min vortexing. Subsequently, HFIP was evaporated under an Ar stream, leaving the A β film on the glass vial wall. The dissolution of A β film in HFIP and subsequent removal of HFIP were repeated once more. Next, the A β film was dissolved at the 0.25 mg ml⁻¹

concentration in HFIP by 5-min vortexing. The A β solution was divided into 20 aliquots, each containing 50 μg of the peptide per centrifuge tube. The tubes were covered with Kimtech wipes to protect aliquots from dust contamination and then left under the fume hood overnight to allow for HFIP evaporation. Next, residual HFIP was removed under decreased pressure in a desiccator for 1 h, and the resulting transparent peptide films were stored in the freezer at $-20\text{ }^{\circ}\text{C}$. A single aliquot was used for each experiment. The peptide film was resuspended in a 20- μl sample of DMSO from Sigma-Aldrich. The A β aggregation was initiated by diluting the A β /DMSO solution to 50- $\mu\text{g ml}^{-1}$ A β concentration with 0.01 M PBS solution. The PBS solution was prepared by dissolving PBS tablets from Sigma-Aldrich in 200 mL of Milli-Q[®] water, 18.2 M Ω cm, thus obtaining the 0.01 M phosphate buffer, 0.0027 M KCl, and 0.137 M NaCl (pH = 7.4) solution. Initially, the 50- $\mu\text{g ml}^{-1}$ A β solution contained mostly A β Ms. The A β Ms solution was then immediately stored in the fridge at $4\text{ }^{\circ}\text{C}$ and allowed to aggregate for 24 h. The A β aggregation rate is lower at lower temperatures.³⁴⁹ Therefore, storing the A β Ms solution at $4\text{ }^{\circ}\text{C}$ for 24 h allowed us to obtain a solution of small, membrane-permeating A β Os, as shown previously.

Incorporation of K162 into A β solution. A powder of K162 (Figure 5.1) from Sigma-Aldrich was dissolved at the 5-mM concentration in DMSO to make a K162 stock solution. Then, K162 was incorporated into A β solutions in two ways. In one way, named the pre-incorporation procedure, the 20 μl of K162/DMSO stock solution was used to resuspend the 50- μg A β aliquot, thus obtaining the A β Ms/K162/DMSO solution. This solution was then diluted to reach the 50- $\mu\text{g ml}^{-1}$ A β concentration and subsequently allowed to aggregate in the fridge at $4\text{ }^{\circ}\text{C}$ for 24 h, thus providing the same aggregation conditions as those in the drug absence. In the other way, named the external addition procedure, first, a 50- μg A β Ms sample, dissolved in the 20 μl of DMSO solution and 980 μl of PBS, was allowed to aggregate for 24 h at $4\text{ }^{\circ}\text{C}$. Next, the A β Os solution was mixed with the 20 μl of K162/DMSO stock solution. The final A β Os/K162 solution was stored again at $4\text{ }^{\circ}\text{C}$ for 24 h. In this way, conditions of the K162 interaction with both A β Ms and A β Os were identical. The drug-to-peptide ratio in all samples was 10:1 (v:v).

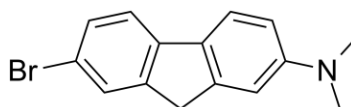


Figure 5.1. The structural formula of K162.

Lipid vesicle preparation. 1,2-Distearoyl-*sn*-glycero-3-phosphoethanolamine (DSPE), 1,2-dipalmitoyl-*sn*-glycero-3-phosphocholine (DPPC), cholesterol (Chol), porcine brain sphingomyelin (SM), and ovine brain monosialoganglioside (GM1), purchased from Sigma-Aldrich, were used without further purification. Structural formulas of these lipids are shown in Figure 4.2. DSPE was dissolved in the chloroform:methanol (9:1, v:v) mixed solvent solution at $50\text{ }^{\circ}\text{C}$. Other lipids were dissolved in chloroform at room temperature. The lipid stock solutions were stored in the freezer at $-20\text{ }^{\circ}\text{C}$. An aliquot of each lipid stock solution was transferred to a

glass vial, and the final solution contained 1 mg of lipids. This mixed lipid solution contained 50% DSPE, 15% DPPC, 25% Chol, 8% SM, and 2% GM1 (w/w). Our previous study (Chapter 4) used this lipid composition to mimic aged lipid rafts formed in the cells' membrane from the human frontal cortex found in AD patients' brains.³²¹ The solvents were evaporated under an Ar stream accompanied by vortexing to produce a lipid film on the bottom of the glass vial. Then, this film was resuspended in the PBS solution to reach the 1 mg ml⁻¹ lipid concentration. Finally, lipid vesicles were formed after 20-min sonication of the lipid solution at 45 °C using ultrasonic cleaner Sonorex Digiplus DL 102 H from Bandelin (Berlin, Germany).

The lipid vesicle and A β O_s solutions (either without or with K162) were mixed to reach the peptide-to-lipid mass ratio of 1:20. Then, the mixture was sonicated for 10 min at room temperature and used immediately afterward.

Electrochemical impedance spectroscopy (EIS) measurements. The vesicle fusion method was used to prepare a BLM.²¹⁷ Single-crystal Au(111) electrode (surface area of 0.7854 cm²) was used as the working electrode for electrochemical measurements. Before use, this electrode was pretreated according to the previously developed procedure.³²² Briefly, the electrode was rinsed with Milli-Q[®] water and then flame annealed using a Bunsen burner. After cooling down to room temperature, the electrode was immersed in a 0.4 mg ml⁻¹ 1-thio- β -D-glucose (Tg) solution from Sigma-Aldrich for 5 h. That way, a self-assembled monolayer of Tg (SAM-Tg) was formed on the gold surface. The SAM-Tg provides a hydrophilic cushion layer that enhances vesicle fusion and relieves the stress gold substrate imposes on the BLM.³²³ Moreover, it provides a water-rich layer underneath the lipid bilayer, thus mimicking the natural cell membrane environment. After SAM-Tg formation, the electrode was rinsed with Milli-Q[®] water and then immersed in the lipid vesicle solution (either containing or not containing A β O_s and K162) overnight. Finally, the electrodes were withdrawn from the solution, and then the excess of the solution was gently removed with a Kimtech wipe.

The all-glass three-electrode cell was used for all electrochemical measurements. An Au(111), Au wire, and saturated calomel electrode (SCE) were used as the working, counter, and reference electrode, respectively. Before each measurement, the solution was purged for 30 min with an Ar stream for deaeration. During the experiments, an Ar cushion was flowing over the solution. The Au(111) electrode coated with the BLM was assembled in the electrochemical cell in the hanging meniscus configuration (Figure 4.3). That is, the electrode was slowly lowered vertically toward the electrolyte solution until it touched it. Then, it was raised to form a meniscus between the electrode surface and the electrolyte.

Electrochemical impedance spectroscopy (EIS) measurements were conducted using VSP electrochemical interface (Biologic). The EIS spectra were acquired in the potential range of 0.30 to -0.40 V vs. SCE. During EIS measurements, an excitation sinusoidal voltage signal of the amplitude of 10 mV was applied, and the spectra were recorded in the frequency range of 10³ to 0.05 Hz. The EIS data were fitted using ZView software (Scribner Associates Inc.).

Atomic force microscopy (AFM) imaging. The BLM samples were imaged with AFM in the PeakForce quantitative nanomechanical mapping (PF-QNM) mode using a MultiMode 8 system (Bruker) equipped with an E scanner. The system was turned on and allowed to equilibrate for at least 30 min before each experiment. The BL-AC40TS (Olympus) and RTESPA300 (Bruker) cantilevers with spring constant of 0.1 and 40 N m⁻¹, and the resonance frequency of 50 and 300 kHz, respectively, were used for sample imaging in the liquid and air, respectively. The AFM cantilevers were cleaned by consecutive immersing in a detergent bath, 2-propanol, and Milli-Q[®] water for 10 min. Next, the cantilevers were ozonized in the UVC-1014 UV ozone cleaner (Nanobioanalytics, Berlin, Germany) for 10 min. Then, they were calibrated using the thermal tune method. The tip radius was determined by imaging the Ti roughness sample (Bruker), routinely used for tip radius determination.^{286,287} The V1 grade mica disks (Ted Pella, Inc.) were mounted on metallic disks using an adhesive tape. Afterward, mica was cleaned in ethanol and then in Milli-Q[®] water. After drying with an Ar stream, its top layer was piled off using adhesive tape, resulting in a clean and atomically flat surface. The samples were immediately deposited on the freshly-cleaned mica surface.

The PF-QNM in a fluid mode was used to study the morphology of BLM, BLM-A β Os, and BLM-A β Os-K162 in the PBS solution (pH = 7.4) at 21 °C. Before the imaging, the fluid cell and AFM accessories were cleaned in a detergent bath, followed by sequential rinsing with ethanol and then Milli-Q[®] water. A 30- μ l aliquot of the lipid vesicle solution (either without or with A β Os and K162) was deposited on a freshly cleaved mica substrate and then left for 45 min to form BLM on the substrate surface. Finally, the sample was rinsed with Milli-Q[®] water, filtered through a Whatman syringe filter (GE Healthcare Life Sciences) of 0.02 μ m porosity, and then mounted for AFM imaging.

The PF-QNM in air mode was used for monitoring A β aggregation in the absence and presence of K162. A freshly prepared A β M solution (either without or with K162) was deposited on a freshly cleaved mica substrate. After 5 min of deposition, the sample was rinsed with filtered Milli-Q[®] water, dried with a gentle stream of Ar, and subsequently mounted for AFM imaging. The imaging was performed at 21 °C.

All AFM images were processed and analyzed using Gwyddion software.²⁸⁸

Molecular dynamics (MD) simulations. To gain a molecular-level insight into the energetics of A β interaction with K162, we carried out molecular dynamics simulations and post-processed obtained trajectories using the Molecular Mechanics Poisson-Boltzmann Surface Area (MMPBSA)³⁵⁰ method. The A β M and A β D were constructed using the PDB: 6RHY structure.³⁵¹ The A β F structure was prepared using the PDB: 2NAO structure.³⁵² First, we simulated mixtures of A β M, A β D, or A β F with K162 in the molar ratio of A β :K162 equal to 1:10. We modeled solvent explicitly using the OPC3 water model,³⁵³ which provided a realistic description of solution dielectric properties and responses.³⁵⁴ The MD simulation procedure consisted of a sequence of the following steps (i) steepest descent optimization of initial configuration, (ii) heating to room

temperature, (iii) density optimization, and (iv) 50 ns production run within the isothermal-isobaric ensemble. The simulations were carried out under ambient conditions with the temperature controlled by stochastic Langevin thermostat (the collision frequency $\gamma = 2 \text{ ps}^{-1}$) and pressure controlled by Berendsen barostat (the coupling constant $\tau = 1 \text{ ps}$). Second, we extracted the bounded complexes of K162 with A β M, A β D, or A β F from the last configuration in the mixture production runs. These complexes were immersed in bulk water and simulated for another 50 ns. Finally, the single-complex trajectories were post-processed using the MMPBSA³⁵⁰ method to estimate the K162-A β binding energies. The interaction parameters for A β were assigned based on the residue-partitioning and connectivity using the Amber ff14SB³⁵⁵ force field. The interaction model for K162 was developed using the density function theory (theory level B3LYP/6-311++G**). This procedure included three steps, i.e., (i) geometry optimization, (ii) Merz-Singh-Kollman³⁵⁶ electrostatic potential partitioning into partial charges, and (iii) assignment of short-range interaction parameters and bonding terms from the GAFF³⁵⁷ force-field library. The first-principle calculations were carried using NWChem³⁵⁸ and Gaussian³⁵⁹ packages; the MD simulations were carried out using both Amber³⁶⁰ and Gromacs³⁶¹ packages.

5.3. Results and discussion

K162 inhibits BLM permeation by A β O_s - EIS studies. EIS measures the impedance of the BLM-coated electrode. The BLM is an insulating layer on the electrode surface. When the BLM integrity is compromised, the electrode impedance changes because of the ion transfer from the electrolyte solution bulk to the electrode surface. The impedance vs. frequency curve slope is constant for highly capacitive systems, including a non-permeable phospholipid bilayer. In contrast, the phase angle vs. frequency curve displays a plateau at a phase angle $\sim 90^\circ$ for a low-frequency region.^{320,362} These EIS features were observed for BLM in the absence of A β O_s and K162 (Figure 5.2).

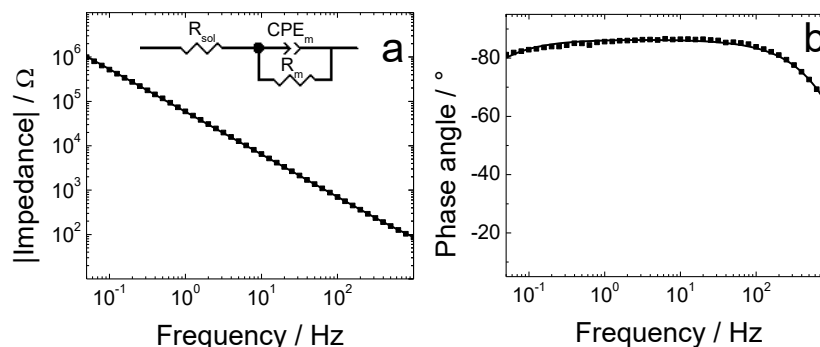


Figure 5.2. (a) Impedance and (b) phase angle as a function of frequency for BLM in the PBS (0.01 M phosphate buffer, 0.0027 M KCl, and 0.137 M NaCl, pH = 7.4) solution at 0 V vs. SCE. Symbols and lines of the same colors represent experimental data and results of fitting of parameters of the equivalent electrical circuits to the EIS data, respectively, for the same measurement at a single potential. The equivalent electric circuit, shown in Panel (a), is fitted to BLM's EIS data.

For BLM in the presence of A β O_s (BLM-A β O_s), the impedance vs. frequency curve displays the small "kink-like" feature below ~ 1 Hz (black curve in Figure 5.3a). The corresponding phase angle vs. frequency curve exhibits the minimum with the lowest phase angle of $\sim 74^\circ$ at ~ 0.4 Hz (black curve in Figure 5.3b). These results indicate the BLM permeation by A β O_s, in agreement with our previous study (Chapter 4, above). The pre-incorporation method was used to test whether K162 inhibits this permeation. That is, K162 was mixed with A β Ms and then allowed to interact with them for 24 h at 4 $^\circ$ C. Next, lipid vesicles were mixed with the A β -K162 solution at room temperature by 10-min sonication. Finally, the Tg-modified Au(111) electrode was immersed in the K162-A β -lipid mixture to allow for the overnight membrane deposition (for details, see the Experimental section).

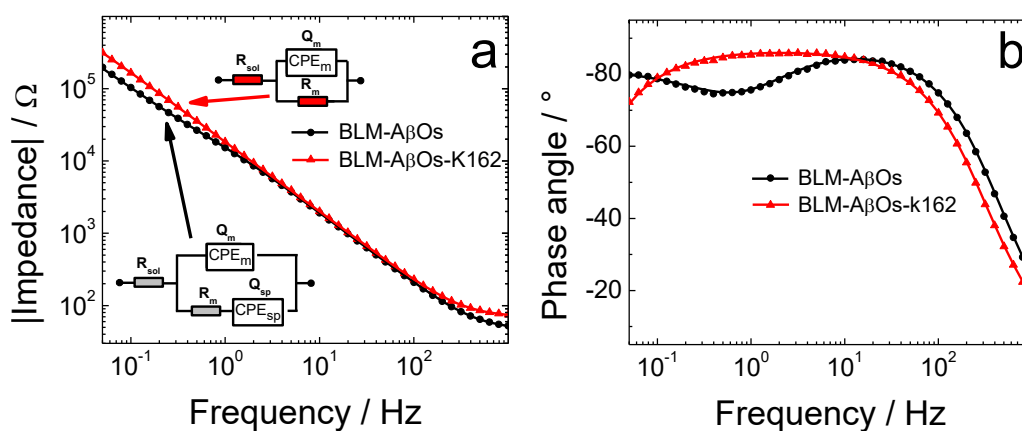


Figure 5.3. (a) Impedance and (b) phase angle as a function of frequency for (black curve) fBLM-A β O_s, and (red curve) fBLM-A β O_s-K162 in the PBS (0.01 M phosphate buffer, 0.0027 M KCl, and 0.137 M NaCl, pH = 7.4) solution at 0 V vs. SCE. Symbols and curves of the same colors represent experimental data and results of fitting of parameters of the equivalent electric circuits, shown as insets, to the EIS data, respectively, for the same measurement at a single potential. R_s and R_m – solution and membrane resistance, respectively; CPE_m and CPE_{sp} – constant-phase element for the membrane and submembrane (spacer) region, respectively.

For that sample, the impedance vs. frequency curve does not display the "kink-like" feature (red curve in Figure 5.3a). Moreover, there is no minimum in the phase angle vs. frequency curve, and the curve displays a plateau with a phase angle of $\sim 85^\circ$ (red curve in Figure 5.3b). These EIS features indicate that BLM-A β O_s-K162 is not permeated, and A β O_s are inactive towards BLM in the presence of K162. Presumably, K162 either interacts with A β Ms and prevents them from forming toxic A β O_s, or K162 interacts with toxic A β O_s and converts them into a non-toxic form.

The external addition procedure was utilized to test the second possibility. That is, K162 was added to a solution of pre-formed A β O_s and then allowed to interact with A β O_s for 24 h at 4 $^\circ$ C. Next, lipid vesicles were mixed with the A β O_s-K162 solution at room temperature by 10-min sonication. Finally, the Tg-modified Au(111) electrode was immersed in the K162-A β -lipid mixture

to allow for the overnight sample deposition (see details in the Experimental section). In this case, both the "kink-like" feature in the impedance vs. frequency curve (Figure 5.4a) and the minimum in the phase angle vs. frequency curve (Figure 5.4b) were absent. These EIS results confirm that K162 effectively inhibits the toxicity of preformed A β Os.

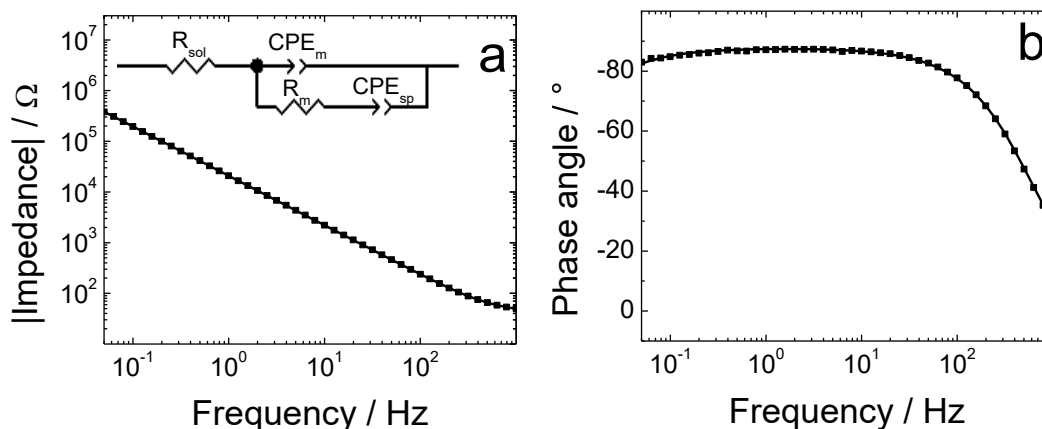


Figure 5.4. (a) Impedance and (b) phase angle as a function of frequency for BLM-A β Os-K162 (externally added) in the PBS (0.01 M phosphate buffer, 0.0027 M KCl, and 0.137 M NaCl, pH = 7.4) solution at 0 V vs. SCE. Symbols and lines of the same colors represent experimental data and results of fitting of parameters of the equivalent electric circuits to the EIS data, respectively, for the same measurement at a single potential. The equivalent electric circuit, shown in Panel (a), was fitted to the EIS data for BLM-A β Os-K162EA.

Equivalent electric circuits, shown as insets in Figures 5.3a, were fitted to the EIS data to determine membrane capacitance, Q_m , resistance, R_m , and their changes in the presence of toxins.¹⁴⁵ Results of the EIS fitting are shown in Table 5.1. As expected, Q_m is the lowest for BLM, equaling $\sim 3.72 \mu\text{F cm}^{-2}$. The addition of A β Os to BLM results in an increase in Q_m to $\sim 11.57 \mu\text{F cm}^{-2}$. The pre-incorporation or external addition of K162 does not change Q_m , i.e., Q_m is $\sim 11.79 \mu\text{F cm}^{-2}$ and $\sim 10.19 \mu\text{F cm}^{-2}$, respectively. A decrease in R_m is an excellent indicator of membrane permeation. As expected, R_m is the highest for BLM, amounting to $\sim 7.25 \text{ M}\Omega \text{ cm}^2$. The addition of A β Os to BLM (BLM-A β Os) results in a ~ 100 -fold decrease in R_m , i.e., to $\sim 0.079 \text{ M}\Omega \text{ cm}^2$. This result supports the conclusion that A β Os permeate the BLM. On the other hand, when K162 is pre-incorporated or externally added, R_m is ~ 0.954 and $3.29 \text{ M}\Omega \text{ cm}^2$, respectively, i.e., it is decreased much less than that for the non-permeated BLM. Overall, the EIS results indicate that K162 inhibits BLM permeation by A β Os.

Table 5.1. Numerical results of the equivalent electric circuits fittings to the EIS data for the BLM in the absence of both A β O_s and K162 (BLM), BLM in the presence of A β O_s (BLM-A β O_s), BLM-A β O_s in the presence of pre-incorporated K162 (BLM-A β O_s-K162PI), and BLM-A β O_s in the presence of externally-added K162 (BLM-A β O_s-K162EA) at 0 V vs. SCE in the PBS (0.01 M phosphate buffer, 0.0027 M KCl, and 0.137 M NaCl, pH = 7.4) solution. Q_m – membrane capacitance, α - an empirical constant related to the frequency dispersion, R_m – membrane resistance, and Q_{sp} – capacitance of the spacer region (SAM-Tg).

Sample	$Q_m / \mu\text{F cm}^{-2}$	α	$R_m / \text{M}\Omega \text{ cm}^2$	$Q_{sp} / \mu\text{F cm}^{-2}$	α_{sp}
BLM	3.72±0.01	0.96±0.01	7.25±0.41	/	/
BLM-A β O _s	11.57±0.05	0.97±0.01	0.079±0.005	2.47±0.05	0.796±0.007
BLM-A β O _s -K162 (K162 pre-incorporated)	11.79±0.01	0.96±0.001	0.954±0.011	/	/
BLM-A β O _s -K162 (K162 externally added)	10.19±0.01	0.97±0.01	3.29±0.1	/	/

K162 inhibits BLM permeation by A β O_s - AFM studies. EIS is a technique that provides averaged macroscopic information about the electrode-solution interface. Herein, high-resolution AFM imaging was used to complement the EIS results by providing molecular-level information about the A β interaction with BLM in the K162 absence and presence. In the absence of both A β O_s and K162, the BLM morphology is typical for lipid bilayers, i.e., it is a ~6-nm thick film with a smooth surface (Figures 5.5a and 5.5d).

Interestingly, a high-resolution image (inset in Figure 5.5a) shows that although BLM is only in a gel phase, it is not homogeneous. Instead, it consists of small domains. Such domains, also known as lipid clusters, have already been observed in cholesterol-containing ternary³⁶³ and quaternary³⁶⁴ lipid bilayer mixtures.^{365,366} Morphology of the BLM deposited and imaged immediately after the high-temperature preparation of lipid vesicle solution is shown in Figure 5.6a. This BLM consists of two domains with a thickness difference of ~1 nm (Figure 5.6b). The BLM mostly consists of DSPE and DPPC molecules (50% and 15%, respectively) with the melting temperature of 74 °C and 41 °C, respectively.^{367,368} The vesicle solution prepared at 50 °C contains DPPC molecules exhibiting a phase transition from the gel to the liquid crystalline phase. In the latter phase, lipid chains are melted. These lipids form the thinner (~5 nm thick) BLM domain. Under these conditions, DSPE remained in the gel phase with fully extended acyl chains. These lipid molecules form the thicker (~6 nm) BLM domain.

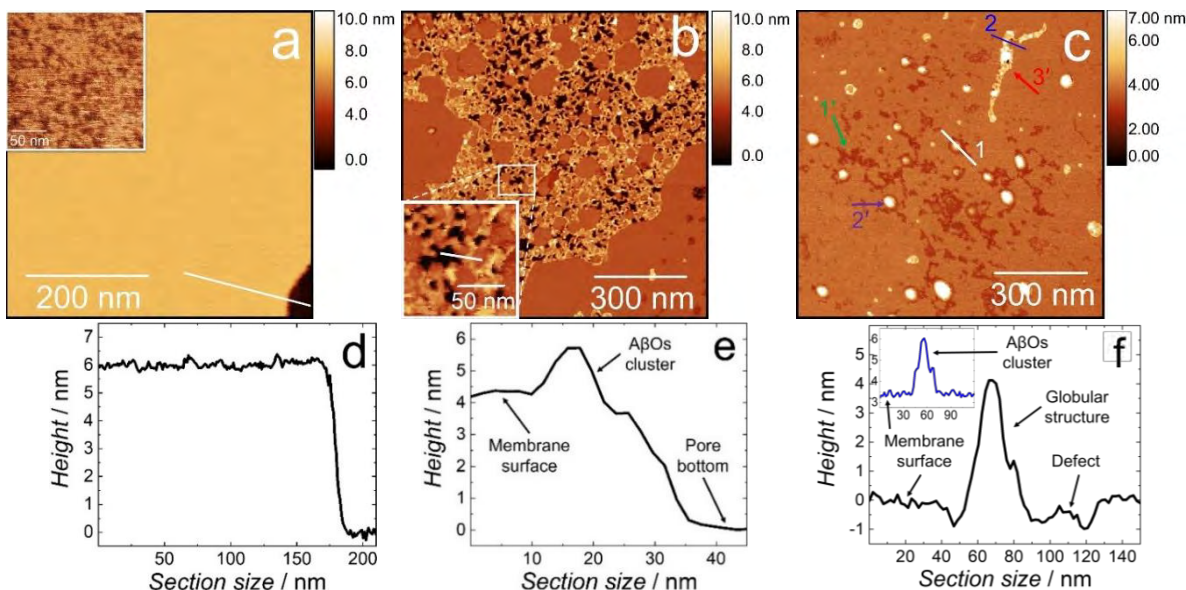


Figure 5.5. The AFM topography images of (a) BLM, (b) BLM in the presence of A β O, and (c) BLM in the presence of A β O and K162, in the PBS (0.01 M phosphate buffer, 0.0027 M KCl, and 0.137 M NaCl, pH = 7.4) solution at room temperature. Insets in Panels (a) and (b) are high-resolution AFM images of the BLM in the absence of A β O as well as the pores and A β O clusters formed in the BLM-A β O, respectively. (d) The cross-sectional profile measured along the line shown in Panel (a) presenting the BLM thickness. (e) Cross-sectional profile measured along the line shown in Inset of Panel (b) revealing the depth of a pore and the height of the A β O cluster protruding from the BLM surface. (f) The cross-sectional profile measured along line 1 in Panel (c), displaying the depth of defects and the height of globular structures. The inset in Panel (f) shows the cross-sectional profile measured along line 2 in Panel (c), displaying the A β O cluster's height present on the BLM-A β O-K162.

Domains of lipids in different phases (Figure 5.6a) are significantly larger than the small domains formed in the gel phased BLM (Inset in Figure 5.5a). Moreover, the thickness difference between small domains is ~ 0.3 nm (Inset in Figure 5.5a), which is significantly smaller than that of lipid domains in the gel and liquid crystalline phases (Figure 5.6). Phase diagrams for lipid bilayers composed of distearoylphosphatidylcholine (DSPC), dioleoylphosphatidylcholine (DOPC), and Chol were reported.^{363,364,366} At Chol mole fraction of ~ 0.4 - 0.7 , a single-phase BLM is formed in which lipid molecules are clustered into nanodomains. Although different lipids were used in this study, the Chol concentration was the same. Therefore, small domains formed in the gel-phase BLM are lipid clusters (Figure 5.5a).

Figure 5.5b depicts the BLM morphology in the presence of A β O (BLM-A β O). This morphology is significantly different from that of BLM in the A β O absence. In the A β O presence, a network of domains consisting of pores surrounded by A β O clusters is formed. This network occupies $\sim 40\%$ of the total surface area of the membrane. The pore depth is in the range of 3 to 4.5 nm, with the most populated pore depth of ~ 3.9 nm (Figures 5.5e and 5.7a). Our previous study

showed that A β O_s induce conformational changes of lipid acyl chains by increasing the number of *gauche* conformers characteristic for melted lipid acyl chains (Chapter 4, above). The thickness of the BLM with melted acyl chains, i.e., in the liquid crystalline phase, is \sim 5 nm (Figure 5.6). Therefore, the pore depth distribution (Figure 5.7a) shows that A β O_s entirely compromised the \sim 5-nm thick BLM's integrity (Figure 5.5b). The A β O clusters with an equivalent disk radius of \sim 5 nm (Figure 5.7b) protrude \sim 2-3 nm from the membrane surface (Figure 5.5e).

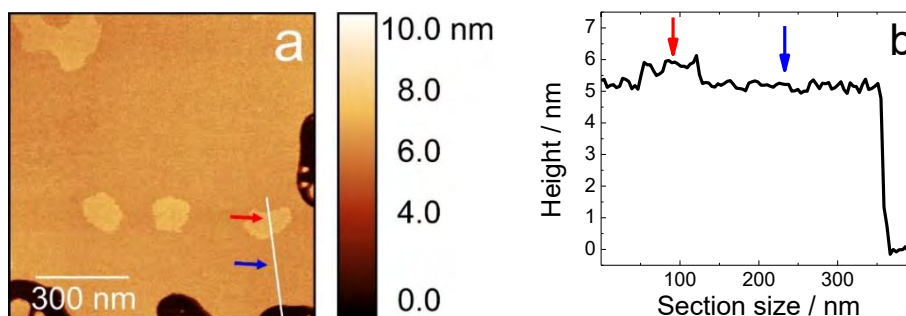


Figure 5.6. (a) The AFM image and (b) the corresponding cross-sectional profile of the BLM, deposited on a mica substrate immediately after lipid vesicle solution preparation and imaged in the PBS (0.01 M phosphate buffer, 0.0027 M KCl, and 0.137 M NaCl, pH = 7.4) solution. The BLM domains in gel and the liquid crystalline phase are indicated by red and blue arrows, respectively.

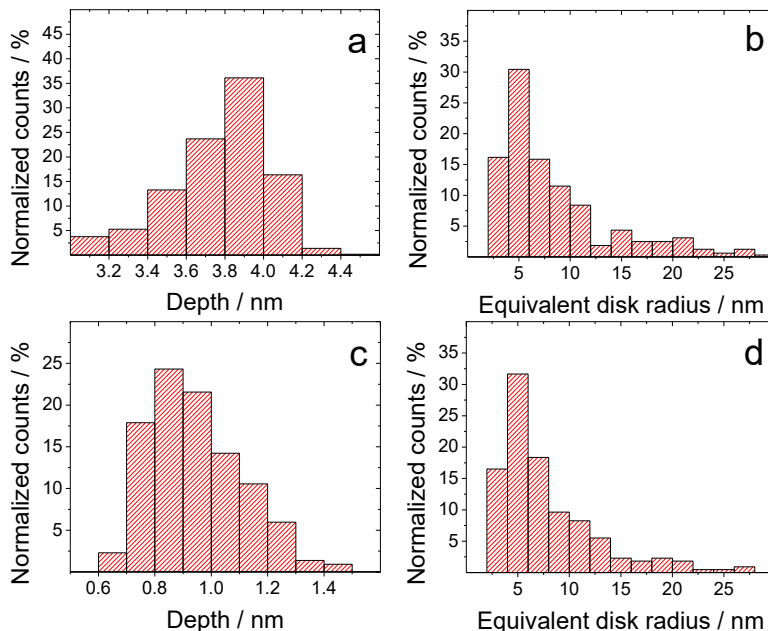


Figure 5.7. (a) The depth of pores and (b) equivalent disk radius of the A β O clusters surrounding the pores in BLM-A β O_s, deposited on a mica substrate and then imaged in the PBS (0.01 M phosphate buffer, 0.0027 M KCl, and 0.137 M NaCl, pH = 7.4) solution. (c) The depth and (d) equivalent disk radius of the defects in BLM-A β O_s-K162 deposited on a mica substrate and then imaged in the PBS (0.01 M phosphate buffer, 0.0027 M KCl, and 0.137 M NaCl, pH = 7.4) solution.

Figure 5.5c shows the BLM morphology in the presence of both A β O and K162 (BLM-A β O-K162). Evidently, K162 prevents A β O from forming the network of domains with pores passing through the entire BLM. Instead, three distinct features are visible on the BLM surface, i.e., defects of irregular shapes (indicated with green arrow 1'), globular particles (purple arrow 2'), and A β O clusters similar to those shown in Figure 2a (red arrow 3'). The defects are ~0.7-1.2 nm deep (Figures 5.5f and 5.7c), and they occupy ~7% of the BLM surface area. These defects are very shallow compared to the pores in BLM-A β O (Figure 5.5e and 5.7a). The globular structures with a height of ~4-6 nm (Figure 5.5f) occupy ~3% of the BLM surface area. The (~2-3)-nm thick A β O clusters (Inset in Figure 5.5f), similar to those in BLM-A β O in the absence of K162 (Figure 5.5b), also appear in the presence of K162, indicating that K162 does not inhibit A β O clustering on the BLM surface. The lack of pores in the K162 presence suggests that the resulting clusters do not permeate BLM, thus confirming the EIS results. In the presence of K162, there is no network of A β O clusters (Figure 5.5c) formed in the absence of K162 (Figure 5.5b). Instead, only a few separate A β O clusters and many large globular structures, mostly located in irregularly-shaped, shallow defects, are seen (Figure 5.5c). This observation indicates that the K162 molecules break the A β O cluster network and stimulate individual A β O clusters to shrink into globular structures. During this shrinking, A β O clusters leave defects on the BLM surface like imprints showing their location on the membrane surface before the shrinking. The formation of globular structures only in the K162 presence supports this explanation. Moreover, these structures are higher than A β O clusters (Figure 5.5c and Inset in Figure 5.5f), as expected, if the globular structure is formed by a mass accumulation of laterally long A β O clusters. Furthermore, the shape and radius of the defects (Figure 5.7e) are very similar to those of A β O clusters formed in the absence of K162 (Figure 5.7c), supporting the hypothesis that the defects are imprints of A β O clusters that shrank and diffused away from the BLM surface. This hypothesis could also account for the K162-induced inhibition of A β O binding to synapses.³⁴⁸

K162 affects the A β aggregation in solution – AFM studies. The EIS and AFM results showed that K162 inhibited BLM permeation by A β O, formed after 24 h of A β aggregation. The K162 inhibition mechanism was studied by monitoring the K162 influence on A β aggregation in membrane absence. Figure 5.8a shows the AFM image of A β molecules deposited on mica from a freshly prepared A β solution (0 h of aggregation) in the absence of K162. Globular structures are only visible. The most populated globules (~47%) with a height of ~0.3 nm correspond to A β M, while the remaining globules constitute a minor population of small A β O (Figure 5.8g and Table 5.2). These results are in excellent agreement with the literature data.¹⁸⁴ After 24 h of A β aggregation in the absence of K162 (Figure 5.8b), the A β M population significantly decreased from ~47% to ~19%, and two types of globular A β O, with their respective heights of ~1.2 and ~2.4 nm, were formed (Figure 5.8h and Table 5.2). Considering the A β M height, one can infer that the two populations of A β O presumably correspond to tetramers and octamers, respectively. The A β aggregation occurs via the so-called nucleated conversion mechanism.^{201,315} In this mechanism, two A β M molecules stack to produce an A β D, then two A β Ds stack to produce

a tetramer, and so on. This mechanism explains why A β Ms, A β Ds, tetramers, and octamers dominate over trimers, pentamers, hexamers, etc.

Table 5.2. The population of different A β forms after 0, 24, and 48 h of A β aggregation in the absence and presence of K162.

Aggregation time, h	A β monomers, %		A β dimers, %		A β tetramers, %		A β octamers, %	
	no K162	K162	no K162	K162	no K162	K162	no K162	K162
0	47	58	10	12	9	6	3	2
24	19	44	6	6	12	12	12	4
48	6	12	6	16	20	13	3	6

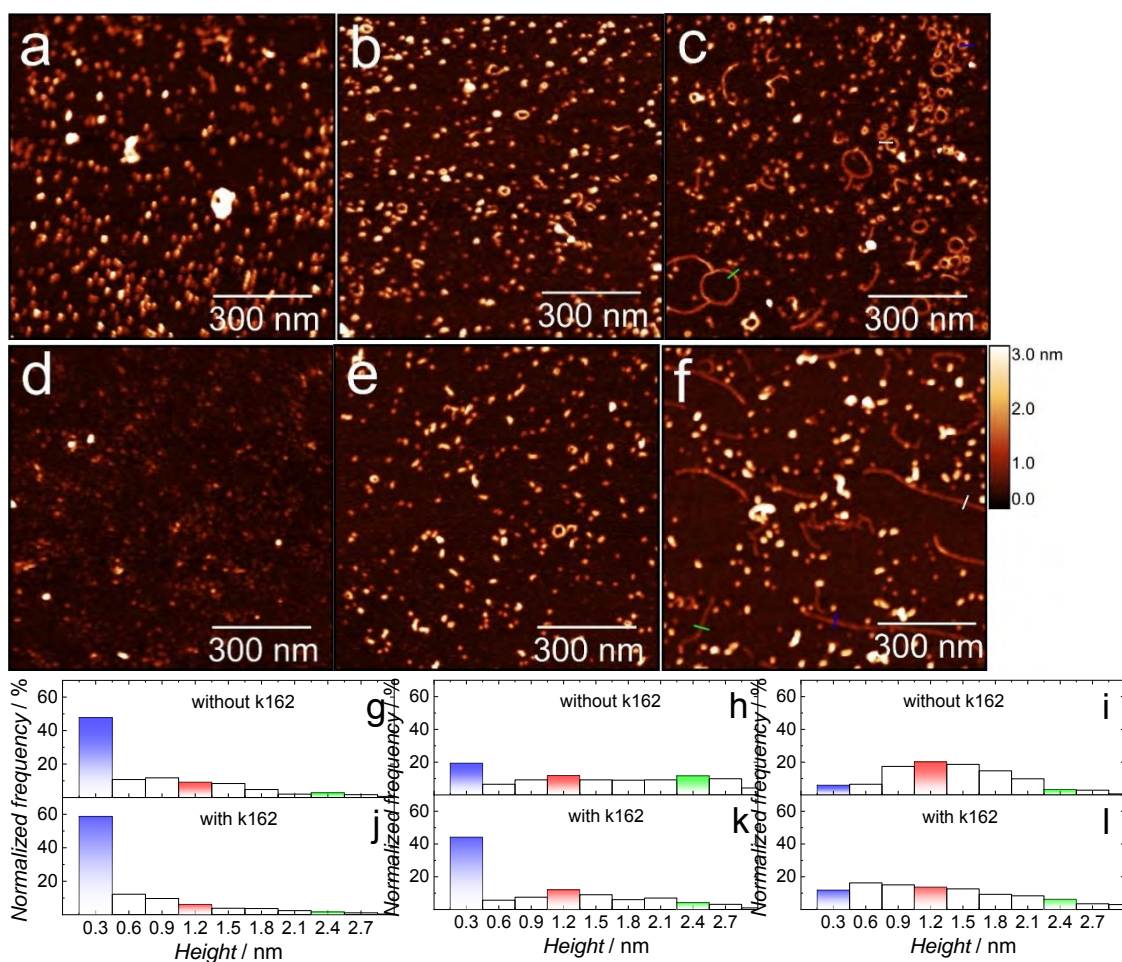


Figure 5.8. The AFM topography images of A β forms produced after (a, d) 0, (b, e) 24, and (c, f) 48 h of A β aggregation in the (a-c) absence and (d-f) presence of K162 in the PBS (0.01 M phosphate buffer, 0.0027 M KCl, and 0.137 M NaCl, pH = 7.4) solution at 4 °C. The corresponding height distributions of A β forms produced after (g, j) 0, (h, k) 24, and (i, l) 48 h of A β aggregation in the (g, h, i) absence and (j, k, l) presence of K162. Histograms corresponding to monomers, tetramers, and octamers of A β are colored in blue, red, and green, respectively.

In the presence of K162, a freshly prepared A β solution contains a slightly higher population of A β Ms (~58%) and a lower population of A β Os (Figures 5.8d and 5.8j) in comparison to those in the K162 absence (Figures 5.8a and 5.8g). After 24 h of A β aggregation in the K162 presence, only globular structures were formed (Figure 5.8e). The A β Ms population decreased from ~58% to ~44%, which is significantly lower than that in the absence of K162 (Figure 5.8k vs. 5.8h). Consequently, the population of A β Os formed in the K162 presence is lower than that in the K162 absence. Moreover, the height distribution of A β Os produced in the presence of K162 significantly differed from that in the K162 absence. That is, tetramers dominated over other A β O forms, and the number of octamers was negligible compared to the A β Os distribution in the K162 absence (Table 5.2). These results suggest that K162 substantially preserves A β Ms and inhibits their aggregation into membrane-permeating A β Os like tetramers, octamers, etc.

So far, we have demonstrated that K162 suppressed the formation of A β Os during the first 24 h of A β aggregation. However, it is unclear whether K162 merely delays or effectively inhibits the formation of toxic A β Os. In the former case, the BLM damage would be delayed but unavoidable, making K162 an ineffective therapeutic. Therefore, the A β aggregation in the absence and presence of K162 was monitored by AFM for 48 h. After 48 h of A β aggregation in the absence of K162, both globular and elongated structures were formed (Figure 5.8c and 5.9a). The A β Ms population decreased significantly (Figure 5.8i) compared to that observed after 24 h of A β aggregation (Figure 5.8h). Moreover, the most dominant A β Os were tetramers, while the octamer population decreased (Table 5.2). It might be surprising that globular A β aggregates formed after 48 h of aggregation (Figure 5.8i) were smaller than those formed after 24 h of aggregation (Figure 5.8h). However, a recent study showed that A β Os dissociated rather than grew into larger forms,³⁶⁹ even though A β Fs were formed later along the aggregation pathway. In the K162 absence, most elongated structures assumed a ring-like shape, while a minor population has an elongated shape typical for A β Fs (Figure 5.8c). The elongated structures' cross-sectional profile showed that their height was ~1.2 nm (Figure 5.9c), identical to the A β tetramers' height, indicating that these structures were formed lateral assembly of A β tetramers.

A β globules and A β Fs were formed after 48 h of aggregation in the K162 presence (Figures 5.8f and 5.9b), similarly as in the K162 absence (Figures 5.8c and 5.9a). However, the height distribution differed significantly between the two cases. In the K162 presence, A β Ms and A β Ds represented a substantial part of the A β aggregates (Figure 5.8l and Table 5.2). Interestingly, in the presence of K162, there were no ring-like structures. The cross-sectional profiles showed that A β Fs, formed in the presence of K162 (Figure 5.8f and 5.9d), were much longer and by ~50% thinner than the A β Fs formed in the K162 absence (Figures 5.8c and 5.9c). The height of the A β Fs formed in the presence of K162 indicated that they were composed of A β dimers (A β Ds), not tetramers, as in the K162 absence.

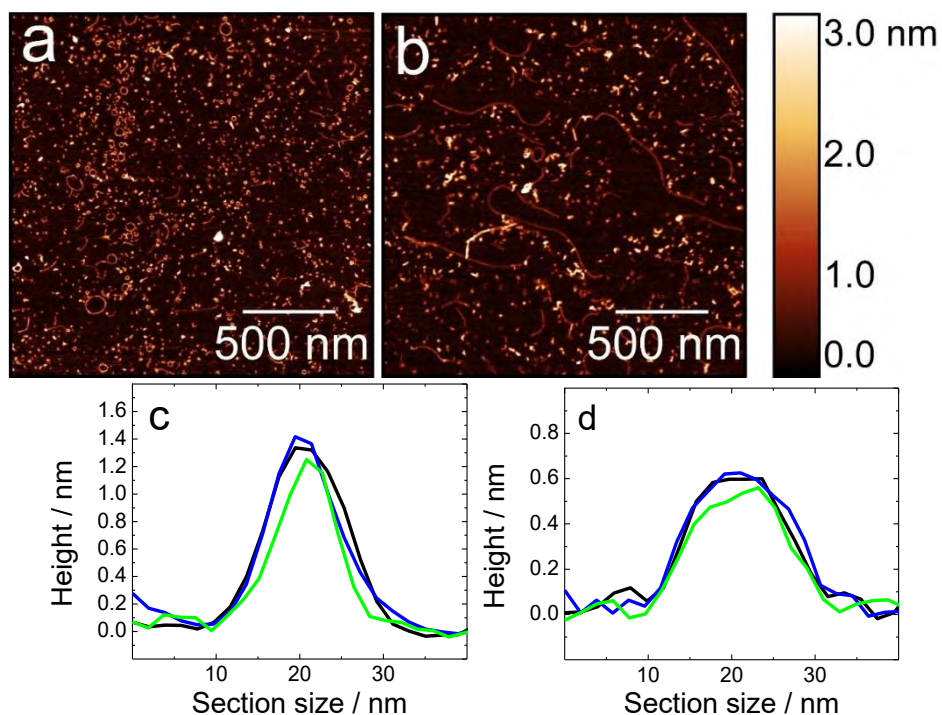


Figure 5.9. The AFM imaged topography of elongated A β aggregates formed in (a) the absence and (b) presence of K162 after 48 h of A β aggregation. Cross-sectional profiles of A β Fs shown in (c) Panel a and (d) Panel b.

K162 affects the A β aggregation in solution – MD simulations. Molecular dynamics (MD) simulations were performed to gain further insight into the K162 interaction with A β . Two different A β structures were used for the MD calculations. A β M and A β D are represented by the A β 42 that assumes a so-called β -hairpin structure with an antiparallel β -sheet arrangement.³⁵¹ This structure is typical for the prefibrillar A β forms, i.e., misfolded A β M and toxic A β O.^{44,195} For A β Fs, the structure of A β 42 fibrils with in-register parallel β -sheet architecture, composed of A β Ds, was used.³⁵² The in-register parallel β -sheet is typical for A β Fs.^{318,352,370,371} Interactions of these structures with K162 are shown in Figure 5.10.

MD identifies the binding sites and energies of the K162-A β interactions, thus providing information about the K162 affinity towards A β M, A β D, and A β F and its influence on A β aggregation. MD simulations show that K162 binds to all A β forms, i.e., A β M, A β D, and A β F, but also aggregates itself (Figure 5.10). In the K162-A β M complex (Figure 5.10a), K162 interacts with hydrophilic residues, i.e., 13-16, of A β M³⁷² via its Br terminal. In contrast to A β M, K162 binds to hydrophobic residues of A β D and A β F (Figures 5.10b and 5.10c, respectively) via its hydrophobic aromatic ring. The difference between K162-A β D and K162-A β F interactions is that K162 interacts with both the central part (residues 16-18) and the C-terminal side (residues 31-35) of A β Ds, while it binds only to the C-terminal part (residues 30-42) of A β Fs.

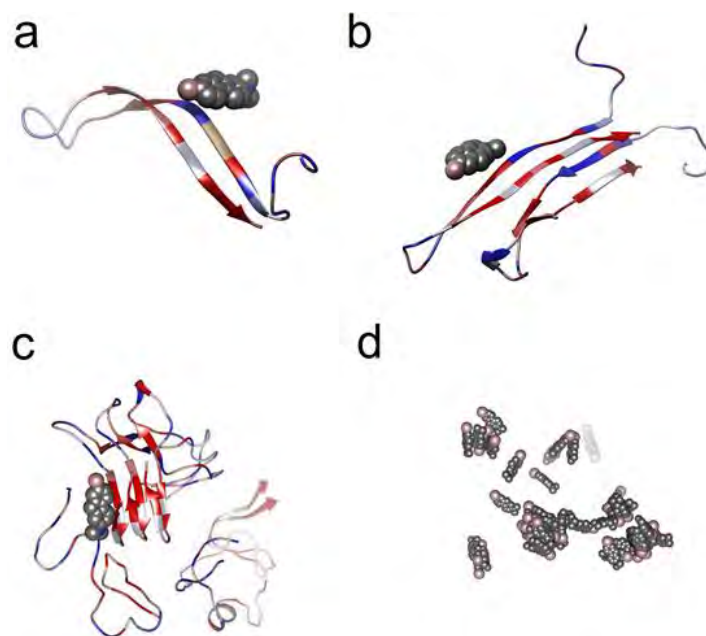


Fig. 5.10. The molecular dynamics modeled examples of configurations of the K162 complexes with (a) A β Ms, (b) A β Ds, (c) A β Fs, and (d) K162. K162 molecules are represented as spheres and colored by the type of element, i.e., carbon is grey, bromine is pink, and nitrogen is blue. All A β forms are shown as ribbon structures, and their residues are colored by lipophilicity, i.e., hydrophilic residues are blue, neutral residues are white, and hydrophobic residues are red.

The binding energy values for all A β -A β interactions in the K162 absence are negative, indicating a high A β ability to aggregate (Table 5.3). On the other hand, the positive binding energies of all A β -A β interactions in the K162 presence suggest that once the K162 binds to any A β form, its further aggregation is energetically unfavorable. However, AFM imaging shows that despite the K162 presence, A β aggregates are formed even at the K162 concentration ten-fold higher than that of A β (the K162:A β ratio is 10:1). K162 self-aggregates (Figure 5.10d), thus suggesting that not all K162 molecules bind to A β . Therefore, A β aggregation is not entirely prevented because K162 aggregation competes with the K162-A β interaction.

Moreover, K162 does not inhibit the aggregation of all A β forms equally because it does not bind to all of them with the same preference. The binding energy values for all K162-A β interactions indicate that the K162 affinity to different species in the order K162 < A β Fs < A β Ms < A β Ds (Table 5.3). This different affinity can be explained by considering structural changes of all A β forms produced during A β aggregation. The A β aggregation steps occur in the following order: (i) aggregation of misfolded A β Ms to A β Os rich in antiparallel β -sheets,^{44,53,195,351} (ii) conversion of A β Os to fibrillar seeds with in-register parallel β -sheets, and (iii) lateral assembly of fibril seeds to A β Fs with in-register parallel β -sheets.^{318,352,370,371} During A β aggregation, the hydrophobic residues of A β adopt the β -sheets conformation, thus are the main residues governing the A β

aggregation.³⁷² As A β aggregation proceeds, hydrophobic residues are gradually buried more deeply inside the A β aggregates, thus becoming less exposed and less accessible for K162.

Table 5.3. Binding energies of different A β -A β , K162-K162, and K162-A β interactions, calculated from the molecular dynamics simulations with explicit solvent and implicit-solvent postprocessing using the MMPBSA method.

System	Binding energy (kJ/mol)
K162 – K162	-5.72 \pm 0.21
K162 – A β M	-9.96 \pm 0.16
K162 – A β D	-15.71 \pm 0.21
K162 – A β F	-7.71 \pm 0.28
A β M – A β M (in the absence of K162)	-103.94 \pm 0.93
A β D – A β D (in the absence of K162)	-79.73 \pm 1.30
A β F – A β F (in the absence of K162)	-123.71 \pm 1.54
A β M – A β M (in the presence of K162)	4.63 \pm 0.01
A β D – A β D (in the presence of K162)	73.65 \pm 2.02
A β F – A β F (in the presence of K162)	26.79 \pm 1.34

AFM study showed that after 24 h of A β aggregation, a high amount of A β M was preserved (Figure 5.8k and Table 5.2). However, both A β Ds and A β Fs were formed after 48 h of A β aggregation (Figure 5.8l and Table 5.2). That is because K162 binds to the hydrophilic residues, not to aggregation-relevant hydrophobic residues of the A β M (Figure 5.10a). Therefore, K162 inhibits but does not entirely prevent A β M aggregation.

After 24-h A β aggregation in the K162 presence, a population of globular A β O, larger than A β Ds, was minor (Figure 5.8k and Table 5.2). This result demonstrates that K162 inhibits A β D oligomerization. After 48 h of A β aggregation in the K162 presence, A β Ds and A β Fs composed of A β Ds become the dominant structures (Figures 5.8f, 5.8l, and 5.9b). Apparently, some A β Ds managed to convert to fibril seeds and fibrillate in the K162 presence. Although K162 binds to aggregation-relevant hydrophobic residues of both A β Ds and fibril seeds/A β Fs (Figures 5.10b and 5.10c), the hydrophobic residues of A β Fs are more deeply buried, thus less accessible to K162. Therefore, the K162-A β D interaction is energetically more favorable than the K162-A β F

interaction (Table 5.3). Consequently, K162 more effectively prevents A β D oligomerization than fibrillation of A β D converted to fibril seeds.

Long A β Fs are formed in the K162 presence (Figures 5.8f and 5.9b), indicating that K162 cannot compromise them. The in-register parallel β -sheet arrangement in fibril seeds/A β Fs makes them very robust and stable, giving them a strength comparable to steel and mechanical stiffness comparable to that of silk³⁷³ that is significantly higher than that of A β O_s.³⁷⁴

Our results explain why only A β M_s and A β D_s were observed inside neurons.³⁴⁸ The only remaining types of A β aggregates formed in the K162 presence are non-toxic A β F_s, which adsorb on the BLM surface without destroying it (Figure 3.7). Thus, they cannot permeate the neuronal membrane and insert into neurons.³⁴⁸ Importantly, A β F_s are widely known as non-toxic because they are inactive towards various biosystems like lipid vesicles,⁶¹ PC12 cells,⁶² glial cells in CGC cultures, macrophage J774 cells,⁶³ MC65 cells, U18666A-treated neurons, and Tg6799 5xFAD mice.³⁴⁸ Moreover, our findings explain the influence of K162 on the formation of non-toxic A β D_s. In general, hydrophobic residues of A β O_s are essential for their toxicity. The higher the surface hydrophobicity of A β O_s, the higher their toxicity.^{191–193,216} The interaction of A β O hydrophobic residues with BLM's hydrophobic core leads to the BLM permeabilization. Our results show that K162 occupies the toxicity-relevant hydrophobic residues of A β D_s, thus inhibits BLM permeation by these A β O_s.

5.4. Conclusions

We have demonstrated that K162 inhibited BLM poration by A β O_s. The EIS results showed that BLM integrity was preserved in the presence of K162. This inference was confirmed by AFM imaging, showing no membrane's pores formed typically by A β O_s. The BLM protection from A β O_s by K162 resulted from K162 binding to hydrophobic residues of A β aggregates. These residues are not only responsible for A β O_s toxicity but also for A β aggregation. Once K162 binds to the A β molecule, its further aggregation is unfavorable. However, under the conditions used in the present study, K162 did not entirely prevent aggregation of all A β forms present in the solution because of competitive K162 self-aggregation. Therefore, K162 inhibited A β M_s aggregation, prevented A β D_s oligomerization, but allowed A β D_s fibrillation (Figure 5.11). As a result, non-toxic A β forms, i.e., A β M_s, A β D_s, and A β F_s, were only formed in the presence of K162. This way, the production of membrane-permeating A β O_s was bypassed. Unlike other A β toxicity inhibitors, K162 preserved neurologically beneficial A β M_s. However, it remains to be elucidated whether K162-bound A β M_s retain their neurologically-beneficial abilities. Even if they do not, the present findings describe a unique A β toxicity inhibition mechanism that may inspire the production of a novel type of AD therapeutics.

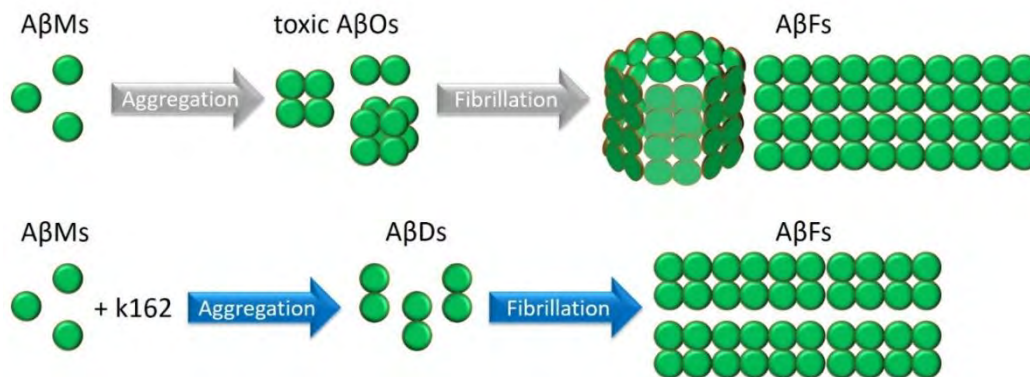


Figure 5.11. Schematic illustration of the A β aggregation pathways (grey arrows) in the absence and (blue arrows) presence of K162.

Chapter 6. Research summary and future perspectives

Amyloid β attracts researchers' widespread attention because it is linked to incurable AD, a global health problem. Understanding the mechanisms of amyloid proteins toxicity and aggregation is essential for developing effective AD treatments. Many discoveries have contributed to the understanding of $A\beta$ behavior. A significant turning point in amyloid toxicity investigation was when the research focus shifted from $A\beta$ Fs, initially thought to be toxic, to $A\beta$ O that exhibit various harmful abilities. The $A\beta$ O toxicity was demonstrated on many different biosystems ranging from lipid vesicles and cells to animal models. However, polymorphism and metastability of $A\beta$ O are significant challenges in $A\beta$ studies, attenuating further advancement in understanding their toxicity and aggregation mechanisms. Moreover, it is unclear why some $A\beta$ O are toxic, while others aggregate into non-toxic $A\beta$ Fs.

Therefore, this research's first step was to distinguish between toxic (membrane-permeating) and fibrillating $A\beta$ O and determine the mechanism of membrane permeation by $A\beta$ O. High-resolution AFM imaging revealed that $A\beta$ O formed at different aggregation stages behaved differently. Large $A\beta$ O aggregated on the membrane surface via both primary and secondary nucleation mechanisms. Most importantly, this kind of $A\beta$ O did not permeate the membrane. Unlike the large $A\beta$ O, small $A\beta$ O destroyed the lipid bilayer. The first step in this destruction is the formation of pores in the membrane. Next, the pores expand over time, and then small $A\beta$ O insert into the membrane through these pores. The final step involves the lipid extraction from the membrane, leading to the formation of $A\beta$ -lipid complexes that diffuse away from the membrane. Phospholipids from both BLM's leaflets are either extracted simultaneously or sequentially, i.e., first, lipids are extracted from the outer and then from the inner membrane leaflet. Interestingly, although large and small $A\beta$ O interact differently with the membrane, they both cause a $\sim 50\%$ decrease in the bilayers Young's moduli. This decrease indicates that both forms of $A\beta$ oligomers affect membrane stability, but each in a different way.

The next research step consisted of expanding the knowledge of the $A\beta$ O-induced membrane permeation by supplementing the AFM findings with electrochemical and IR spectroscopic analyses. Moreover, non-toxic $A\beta$ M were also studied, serving as the reference for comparing the difference between their and $A\beta$ O's behavior. Electrochemical measurements demonstrated that the electric BLM properties were significantly altered only in the $A\beta$ O presence because of membrane poration by $A\beta$ O. Moreover, these properties differed from those reported for lipid bilayers permeated by other toxins via the ion channel formation mechanism. This finding revealed the fundamental difference between pores formed by $A\beta$ O and ion channel-forming peptides. PM-IRRAS studies showed that both $A\beta$ M and $A\beta$ O caused significant lipid molecules disordering. It appeared that both $A\beta$ forms interacted with the membrane hydrophobic core. They increased the tilt angle of lipid acyl chains, increased the number of *gauche* conformers in the lipid acyl chains, decreased lipid acyl chains' mobility, and changed the lipid molecule packing. Although both $A\beta$ M and $A\beta$ O interacted with lipid acyl chains in the same manner, these

changes were more significant in the presence of A β O than in the presence of A β M. However, the respective interactions of A β M and A β O with lipid heads were different. A β M dehydrated lipid heads, but they did not affect their orientation, i.e., the angle of the C=O bond located in the lipid heads was not changed. In contrast, A β O changed the angle of the C=O bond, causing the reorientation of lipid heads without affecting their hydration. The 2D-COS spectroscopy results demonstrated that structural changes of lipids preceded those of A β . Moreover, these results indicated sequential changes of different secondary structure elements of A β O, in agreement with the A β aggregation mechanism.

After identifying the toxic kind of A β O and their membrane permeation mechanism, the final research step consisted of unraveling a potential inhibitor of A β O toxicity and deciphering the inhibition mechanism. K162 is a compound that decreases A β O toxicity *in vivo*, penetrates the blood-brain barrier, inhibits A β O binding to synapses, and decreases the amyloid load inside MC65 cells and hippocampus of 5xFAD mice brain. However, the mechanism of its inhibition was not provided. The EIS and AFM analyses show that BLM integrity is preserved in the presence of both A β O and K162. The MD study revealed that the BLM protection from A β O by K162 resulted from K162 binding to hydrophobic residues of A β aggregates. These residues are not only relevant for A β O toxicity but also for A β aggregation. Moreover, the MD study substantiated that once K162 was bound to the A β molecule, its further aggregation was unfavorable. However, K162 also self-aggregates. Under the conditions used in the present study, not all K162 molecules were bound to A β molecules. Consequently, K162 did not entirely prevent A β aggregation. Apparently, K162 inhibited A β M aggregation, prevented A β D oligomerization, but allowed partial A β D fibrillation. An important consequence was that the production of membrane-permeating A β O is bypassed because only non-toxic A β forms, i.e., A β M, A β D, and A β F, were formed in the presence of K162. The main advantage of K162 over other amyloid inhibitors is that it preserves neurologically beneficial A β M. The present findings describe a unique mechanism of A β toxicity inhibition by K162, which may inspire a novel AD therapeutic approach.

The findings presented herein brought new insight into A β toxicity, aggregation, and inhibition of both. However, along with the accumulated knowledge, further questions arise, which might be answered by future research.

1. What structural difference causes different A β O to interact with the membrane differently (i.e., large A β O fibrillate on the membrane surface, while small A β O permeate the membrane)?
2. Do different membrane lipid compositions of membrane stimulate membrane permeation or A β fibrillation?
3. Does the peptide-to-lipid ratio affect A β -lipid interaction?
4. Are there any other membrane components, e.g., membrane proteins, that affect A β -membrane interaction?

5. Does K162-bound A β Ms retain their beneficial neurological abilities? If not, what is the reason for this limitation? Are there any candidates that can overcome it?
6. Does the K162 inhibition efficiency depend on the K162 concentration?
7. Is it possible to provide conditions that will facilitate K162-A β interaction over the K162-K162 interaction, thus increasing the K162 inhibition efficiency?
8. Does the kinetics of the competing K162-K162 and K162-A β interactions affect the K162 inhibition efficiency?

Answering these questions will improve the understanding of not only A β but also other amyloid proteins because they share certain behavioral features. Such a molecular-level understanding of crucial pathogenic processes and factors affecting them will be a significant step toward developing efficient therapies for AD and other protein misfolding diseases.

References

- (1) OECD. *Health at a Glance 2019*; Health at a Glance; OECD, 2019.
- (2) Prusiner, S. B. Neurodegenerative Diseases and Prions. *N. Engl. J. Med.* **2001**, *344* (20), 1516–1526.
- (3) Hebert, L. E.; Weuve, J.; Scherr, P. A.; Evans, D. A. Alzheimer Disease in the United States (2010-2050) Estimated Using the 2010 Census. *Neurology* **2013**, *80* (19), 1778–1783.
- (4) Saunders, A. M.; Strittmatter, W. J.; Schmechel, D.; St. George-Hyslop, P. H.; Pericak-Vance, M. A.; Joo, S. H.; Rosi, B. L.; Gusella, J. F.; Crapper-MacLachlan, D. R.; Alberts, M. J.; et al. Association of Apolipoprotein E Allele 4 with Late-Onset Familial and Sporadic Alzheimer's Disease. *Neurology* **1993**, *43* (8), 1467–1467.
- (5) Green, R. C. Risk of Dementia Among White and African American Relatives of Patients With Alzheimer Disease. *JAMA* **2002**, *287* (3), 329.
- (6) 2020 Alzheimer's Disease Facts and Figures. *Alzheimer's Dement.* **2020**, *16* (3), 391–460.
- (7) Prince M, Wimo A, Guerchet M, A. D. I. World Alzheimer Report 2015: The Global Impact of Dementia | Alzheimer's Disease International. *World Alzheimer Rep. 2013* **2015**, 1–87.
- (8) Cummings, J. L. Alzheimer's Disease. *N. Engl. J. Med.* **2004**, *351* (1), 56–67.
- (9) Mohandas, E.; Rajmohan, V.; Raghunath, B. Neurobiology of Alzheimer's Disease. *Indian J. Psychiatry* **2009**, *51* (1), 55–61.
- (10) Alzheimer, A. Über Eine Eigenartige Erkankung Der Hirnrinde. *Allg. Zeitschrift für Psychiatr. und Psych. Med.* **1907**, No. 64, 146–148.
- (11) Grzybowski, A.; Pięta, A.; Pugaczewska, M. Teofil Simchowicz (1879–1957). *J. Neurol.* **2017**, *264* (8), 1831–1832.
- (12) Glenner, G. G. Reprint of "Alzheimer's Disease: Initial Report of the Purification and Characterization of a Novel Cerebrovascular Amyloid Protein." *Biochem. Biophys. Res. Commun.* **2012**, *425* (3), 534–539.
- (13) Kosik, K. S.; Joachim, C. L.; Selkoe, D. J. Microtubule-Associated Protein Tau (Tau) Is a Major Antigenic Component of Paired Helical Filaments in Alzheimer Disease. *Proc. Natl. Acad. Sci.* **1986**, *83* (11), 4044–4048.
- (14) Hardy, J.; Higgins, G. Alzheimer's Disease: The Amyloid Cascade Hypothesis. *Science (80-)*. **1992**, *256* (5054), 184–185.
- (15) Hardy, J.; Selkoe, D. J. The Amyloid Hypothesis of Alzheimer's Disease: Progress and Problems on the Road to Therapeutics. *Science (80-)*. **2002**, *297* (5580), 353–356.
- (16) Selkoe, D. J.; Hardy, J. The Amyloid Hypothesis of Alzheimer's Disease at 25 Years. *EMBO Mol. Med.* **2016**, *8* (6), 595–608.

- (17) O'Brien, R. J.; Wong, P. C. Amyloid Precursor Protein Processing and Alzheimer's Disease. *Annu. Rev. Neurosci.* **2011**, *34* (1), 185–204.
- (18) Vassar, R.; Bennett, B. D.; Babu-Khan, S.; Kahn, S.; Mendiaz, E. A.; Denis, P.; Teplow, D. B.; Ross, S.; Amarante, P.; Loeloff, R.; et al. β -Secretase Cleavage of Alzheimer's Amyloid Precursor Protein by the Transmembrane Aspartic Protease BACE. *Science* (80-.). **1999**, *286* (5440), 735 LP – 741.
- (19) Zhao, J.; Deng, Y.; Jiang, Z.; Qing, H. G Protein-Coupled Receptors (GPCRs) in Alzheimer's Disease: A Focus on BACE1 Related GPCRs. *Front. Aging Neurosci.* **2016**, *8* (MAR).
- (20) Pauwels, K.; Williams, T. L.; Morris, K. L.; Jonckheere, W.; Vandersteen, A.; Kelly, G.; Schymkowitz, J.; Rousseau, F.; Pastore, A.; Serpell, L. C.; et al. Structural Basis for Increased Toxicity of Pathological A β 42:A β 40 Ratios in Alzheimer Disease. *J. Biol. Chem.* **2012**, *287* (8), 5650–5660.
- (21) Butterfield, D. A.; Swomley, A. M.; Sultana, R. Amyloid β -Peptide (1–42)-Induced Oxidative Stress in Alzheimer Disease: Importance in Disease Pathogenesis and Progression. *Antioxid. Redox Signal.* **2013**, *19* (8), 823–835.
- (22) Jan, A.; Gokce, O.; Luthi-Carter, R.; Lashuel, H. A. The Ratio of Monomeric to Aggregated Forms of A β 40 and A β 42 Is an Important Determinant of Amyloid- β Aggregation, Fibrillogenesis, and Toxicity. *J. Biol. Chem.* **2008**, *283* (42), 28176–28189.
- (23) Kuperstein, I.; Broersen, K.; Benilova, I.; Rozenski, J.; Jonckheere, W.; Debulpaep, M.; Vandersteen, A.; Segers-Nolten, I.; Van Der Werf, K.; Subramaniam, V.; et al. Neurotoxicity of Alzheimer's Disease A β Peptides Is Induced by Small Changes in the A β 42 to A β 40 Ratio. *EMBO J.* **2010**, *29* (19), 3408–3420.
- (24) Bitan, G.; Kirkitadze, M. D.; Lomakin, A.; Vollers, S. S.; Benedek, G. B.; Teplow, D. B. Amyloid β -Protein (A β) Assembly: A β 40 and A β 42 Oligomerize through Distinct Pathways. *Proc. Natl. Acad. Sci.* **2003**, *100* (1), 330–335.
- (25) Côté, S.; Laghaei, R.; Derreumaux, P.; Mousseau, N. Distinct Dimerization for Various Alloforms of the Amyloid-Beta Protein: A β 1–40, A β 1–42, and A β 1–40 (D23N). *J. Phys. Chem. B* **2012**, *116* (13), 4043–4055.
- (26) Barz, B.; Urbanc, B. Dimer Formation Enhances Structural Differences between Amyloid β -Protein (1–40) and (1–42): An Explicit-Solvent Molecular Dynamics Study. *PLoS One* **2012**, *7* (4), e34345.
- (27) Bernabeu-Zornoza, A.; Coronel, R.; Palmer, C.; Monteagudo, M.; Zambrano, A.; Liste, I. Physiological and Pathological Effects of Amyloid- β Species in Neural Stem Cell Biology. *Neural Regen. Res.* **2019**, *14* (12), 2035.
- (28) Dobson, C. M.; Šali, A.; Karplus, M. Protein Folding: A Perspective from Theory and Experiment. *Angew. Chemie Int. Ed.* **1998**, *37* (7), 868–893.
- (29) Bradbury, J. Chaperones: Keeping a Close Eye on Protein Folding. *Lancet* **2003**, *361* (9364),

1194–1195.

- (30) Chaudhuri, T. K.; Paul, S. Protein-Misfolding Diseases and Chaperone-Based Therapeutic Approaches. *FEBS J.* **2006**, *273* (7), 1331–1349.
- (31) Hartl, F. U. Protein Misfolding Diseases. *Annu. Rev. Biochem.* **2017**, *86* (1), 21–26.
- (32) Moreno-Gonzalez, I.; Soto, C. Misfolded Protein Aggregates: Mechanisms, Structures, and Potential for Disease Transmission. *Semin. Cell Dev. Biol.* **2011**, *22* (5), 482–487.
- (33) Turoverov, K. K.; Kuznetsova, I. M.; Uversky, V. N. The Protein Kingdom Extended: Ordered and Intrinsically Disordered Proteins, Their Folding, Supramolecular Complex Formation, and Aggregation. *Prog. Biophys. Mol. Biol.* **2010**, *102* (2–3), 73–84.
- (34) Cohen, S. I. A.; Cukalevski, R.; Michaels, T. C. T.; Šarić, A.; Törnquist, M.; Vendruscolo, M.; Dobson, C. M.; Buell, A. K.; Knowles, T. P. J.; Linse, S. Distinct Thermodynamic Signatures of Oligomer Generation in the Aggregation of the Amyloid- β Peptide. *Nat. Chem.* **2018**, *10* (5), 523–531.
- (35) Walsh, D. M.; Lomakin, A.; Benedek, G. B.; Condron, M. M.; Teplow, D. B. Amyloid β -Protein Fibrillogenesis. *J. Biol. Chem.* **1997**, *272* (35), 22364–22372.
- (36) Butterfield, S. M.; Lashuel, H. A. Amyloidogenic Protein-Membrane Interactions: Mechanistic Insight from Model Systems. *Angew. Chemie Int. Ed.* **2010**, *49* (33), 5628–5654.
- (37) Tay, W. M.; Huang, D.; Rosenberry, T. L.; Paravastu, A. K. The Alzheimer's Amyloid- β (1–42) Peptide Forms Off-Pathway Oligomers and Fibrils That Are Distinguished Structurally by Intermolecular Organization. *J. Mol. Biol.* **2013**, *425* (14), 2494–2508.
- (38) Watanabe-Nakayama, T.; Ono, K.; Itami, M.; Takahashi, R.; Teplow, D. B.; Yamada, M. High-Speed Atomic Force Microscopy Reveals Structural Dynamics of Amyloid β 1–42 Aggregates. *Proc. Natl. Acad. Sci.* **2016**, *113* (21), 5835–5840.
- (39) Arosio, P.; Knowles, T. P. J.; Linse, S. On the Lag Phase in Amyloid Fibril Formation. *Phys. Chem. Chem. Phys.* **2015**, *17* (12), 7606–7618.
- (40) Mannini, B.; Chiti, F. Chaperones as Suppressors of Protein Misfolded Oligomer Toxicity. *Front. Mol. Neurosci.* **2017**, *10*, 98–106.
- (41) Sandberg, A.; Luheshi, L. M.; Sollvander, S.; Pereira de Barros, T.; Macao, B.; Knowles, T. P. J.; Biverstal, H.; Lendel, C.; Ekholm-Petterson, F.; Dubnovitsky, A.; et al. Stabilization of Neurotoxic Alzheimer Amyloid- β Oligomers by Protein Engineering. *Proc. Natl. Acad. Sci.* **2010**, *107* (35), 15595–15600.
- (42) Chiti, F.; Dobson, C. M. Protein Misfolding, Functional Amyloid, and Human Disease. *Annu. Rev. Biochem.* **2006**, *75* (1), 333–366.
- (43) Hoyer, W.; Grönwall, C.; Jonsson, A.; Ståhl, S.; Härd, T. Stabilization of a β -Hairpin in Monomeric Alzheimer's Amyloid- β Peptide Inhibits Amyloid Formation. *Proc. Natl. Acad.*

- Sci.* **2008**, *105* (13), 5099–5104.
- (44) Gu, L.; Liu, C.; Stroud, J. C.; Ngo, S.; Jiang, L.; Guo, Z. Antiparallel Triple-Strand Architecture for Prefibrillar A β 42 Oligomers. *J. Biol. Chem.* **2014**, *289* (39), 27300–27313.
- (45) Chandra, B.; Bhowmik, D.; Maity, B. K.; Mote, K. R.; Dhara, D.; Venkatramani, R.; Maiti, S.; Madhu, P. K. Major Reaction Coordinates Linking Transient Amyloid- β Oligomers to Fibrils Measured at Atomic Level. *Biophys. J.* **2017**, *113* (4), 805–816.
- (46) Gremer, L.; Schölzel, D.; Schenk, C.; Reinartz, E.; Labahn, J.; Ravelli, R. B. G.; Tusche, M.; Lopez-Iglesias, C.; Hoyer, W.; Heise, H.; et al. Fibril Structure of Amyloid- β (1–42) by Cryo-Electron Microscopy. *Science (80-)*. **2017**, *358* (6359), 116–119.
- (47) Serpell, L. C. Alzheimer's Amyloid Fibrils: Structure and Assembly. *Biochim. Biophys. Acta - Mol. Basis Dis.* **2000**, *1502* (1), 16–30.
- (48) Khurana, R.; Ionescu-Zanetti, C.; Pope, M.; Li, J.; Nielson, L.; Ramírez-Alvarado, M.; Regan, L.; Fink, A. L.; Carter, S. A. A General Model for Amyloid Fibril Assembly Based on Morphological Studies Using Atomic Force Microscopy. *Biophys. J.* **2003**, *85* (2), 1135–1144.
- (49) Ma, B.; Nussinov, R. Polymorphic C-Terminal β -Sheet Interactions Determine the Formation of Fibril or Amyloid β -Derived Diffusible Ligand-like Globulomer for the Alzheimer A β 42 Dodecamer. *J. Biol. Chem.* **2010**, *285* (47), 37102–37110.
- (50) Barghorn, S.; Nimmrich, V.; Striebinger, A.; Krantz, C.; Keller, P.; Janson, B.; Bahr, M.; Schmidt, M.; Bitner, R. S.; Harlan, J.; et al. Globular Amyloid Beta-Peptide1-42 Oligomer - a Homogenous and Stable Neuropathological Protein in Alzheimer's Disease. *J. Neurochem.* **2005**, *95* (3), 834–847.
- (51) Michaels, T. C. T.; Šarić, A.; Curk, S.; Bernfur, K.; Arosio, P.; Meisl, G.; Dear, A. J.; Cohen, S. I. A.; Dobson, C. M.; Vendruscolo, M.; et al. Dynamics of Oligomer Populations Formed during the Aggregation of Alzheimer's A β 42 Peptide. *Nat. Chem.* **2020**, *12* (5), 445–451.
- (52) Pettersen, E. F.; Goddard, T. D.; Huang, C. C.; Couch, G. S.; Greenblatt, D. M.; Meng, E. C.; Ferrin, T. E. UCSF Chimera-A Visualization System for Exploratory Research and Analysis. *J. Comput. Chem.* **2004**, *25* (13), 1605–1612.
- (53) Tomaselli, S.; Esposito, V.; Vangone, P.; van Nuland, N. A. J.; Bonvin, A. M. J. J.; Guerrini, R.; Tancredi, T.; Temussi, P. A.; Picone, D. The α -to- β Conformational Transition of Alzheimer's A β -(1-42) Peptide in Aqueous Media Is Reversible: A Step by Step Conformational Analysis Suggests the Location of β Conformation Seeding. *ChemBioChem* **2006**, *7* (2), 257–267.
- (54) Luhrs, T.; Ritter, C.; Adrian, M.; Riek-Loher, D.; Bohrmann, B.; Dobeli, H.; Schubert, D.; Riek, R. 3D Structure of Alzheimer's Amyloid- β (1-42) Fibrils. *Proc. Natl. Acad. Sci.* **2005**, *102* (48), 17342–17347.
- (55) Paravastu, A. K.; Leapman, R. D.; Yau, W.-M.; Tycko, R. Molecular Structural Basis for

- Polymorphism in Alzheimer's -Amyloid Fibrils. *Proc. Natl. Acad. Sci.* **2008**, *105* (47), 18349–18354.
- (56) Katzman, R.; Terry, R.; DeTeresa, R.; Brown, T.; Davies, P.; Fuld, P.; Renbing, X.; Peck, A. Clinical, Pathological, and Neurochemical Changes in Dementia: A Subgroup with Preserved Mental Status and Numerous Neocortical Plaques. *Ann. Neurol.* **1988**, *23* (2), 138–144.
- (57) Delaère, P.; Duyckaerts, C.; Masters, C.; Beyreuther, K.; Piette, F.; Hauw, J.-J. Large Amounts of Neocortical BA4 Deposits without Neuritic Plaques nor Tangles in a Psychometrically Assessed, Non-Demented Person. *Neurosci. Lett.* **1990**, *116* (1–2), 87–93.
- (58) Dickson, D. W.; Crystal, H. A.; Mattiace, L. A.; Masur, D. M.; Blau, A. D.; Davies, P.; Yen, S.-H.; Aronson, M. K. Identification of Normal and Pathological Aging in Prospectively Studied Nondemented Elderly Humans. *Neurobiol. Aging* **1992**, *13* (1), 179–189.
- (59) Aizenstein, H. J.; Nebes, R. D.; Saxton, J. A.; Price, J. C.; Mathis, C. A.; Tsopoulos, N. D.; Ziolkowski, S. K.; James, J. A.; Snitz, B. E.; Houck, P. R.; et al. Frequent Amyloid Deposition Without Significant Cognitive Impairment Among the Elderly. *Arch. Neurol.* **2008**, *65* (11), 1509.
- (60) Villemagne, V. L.; Pike, K. E.; Chételat, G.; Ellis, K. A.; Mulligan, R. S.; Bourgeat, P.; Ackermann, U.; Jones, G.; Szoeke, C.; Salvado, O.; et al. Longitudinal Assessment of A β and Cognition in Aging and Alzheimer Disease. *Ann. Neurol.* **2011**, *69* (1), 181–192.
- (61) Flagmeier, P.; De, S.; Wirthensohn, D. C.; Lee, S. F.; Vincke, C.; Muyldermans, S.; Knowles, T. P. J.; Gandhi, S.; Dobson, C. M.; Klenerman, D. Ultrasensitive Measurement of Ca²⁺ Influx into Lipid Vesicles Induced by Protein Aggregates. *Angew. Chemie Int. Ed.* **2017**, *56* (27), 7750–7754.
- (62) Ono, K.; Condrón, M. M.; Teplov, D. B. Structure-Neurotoxicity Relationships of Amyloid β -Protein Oligomers. *Proc. Natl. Acad. Sci.* **2009**, *106* (35), 14745–14750.
- (63) Cizas, P.; Budvytyte, R.; Morkuniene, R.; Moldovan, R.; Broccio, M.; Lösche, M.; Niaura, G.; Valincius, G.; Borutaite, V. Size-Dependent Neurotoxicity of β -Amyloid Oligomers. *Arch. Biochem. Biophys.* **2010**, *496* (2), 84–92.
- (64) He, Y.; Zheng, M.-M.; Ma, Y.; Han, X.-J.; Ma, X.-Q.; Qu, C.-Q.; Du, Y.-F. Soluble Oligomers and Fibrillar Species of Amyloid β -Peptide Differentially Affect Cognitive Functions and Hippocampal Inflammatory Response. *Biochem. Biophys. Res. Commun.* **2012**, *429* (3–4), 125–130.
- (65) Walsh, D. M.; Klyubin, I.; Fadeeva, J. V.; Cullen, W. K.; Anwyl, R.; Wolfe, M. S.; Rowan, M. J.; Selkoe, D. J. Naturally Secreted Oligomers of Amyloid β Protein Potently Inhibit Hippocampal Long-Term Potentiation in Vivo. *Nature* **2002**, *416* (6880), 535–539.
- (66) Shankar, G. M.; Li, S.; Mehta, T. H.; Garcia-Munoz, A.; Shepardson, N. E.; Smith, I.; Brett, F. M.; Farrell, M. A.; Rowan, M. J.; Lemere, C. A.; et al. Amyloid- β Protein Dimers Isolated Directly from Alzheimer's Brains Impair Synaptic Plasticity and Memory. *Nat. Med.* **2008**, *14* (8), 837–842.

- (67) Lesné, S.; Koh, M. T.; Kotilinek, L.; Kaye, R.; Glabe, C. G.; Yang, A.; Gallagher, M.; Ashe, K. H. A Specific Amyloid- β Protein Assembly in the Brain Impairs Memory. *Nature* **2006**, *440* (7082), 352–357.
- (68) LaFerla, F. M.; Green, K. N.; Oddo, S. Intracellular Amyloid- β in Alzheimer's Disease. *Nat. Rev. Neurosci.* **2007**, *8* (7), 499–509.
- (69) McDonald, J. M.; Savva, G. M.; Brayne, C.; Welzel, A. T.; Forster, G.; Shankar, G. M.; Selkoe, D. J.; Ince, P. G.; Walsh, D. M. The Presence of Sodium Dodecyl Sulphate-Stable A β Dimers Is Strongly Associated with Alzheimer-Type Dementia. *Brain* **2010**, *133* (5), 1328–1341.
- (70) Shankar, G. M.; Bloodgood, B. L.; Townsend, M.; Walsh, D. M.; Selkoe, D. J.; Sabatini, B. L. Natural Oligomers of the Alzheimer Amyloid- Protein Induce Reversible Synapse Loss by Modulating an NMDA-Type Glutamate Receptor-Dependent Signaling Pathway. *J. Neurosci.* **2007**, *27* (11), 2866–2875.
- (71) Lacor, P. N.; Buniel, M. C.; Furlow, P. W.; Sanz Clemente, A.; Velasco, P. T.; Wood, M.; Viola, K. L.; Klein, W. L. An Oligomer-Induced Aberrations in Synapse Composition, Shape, and Density Provide a Molecular Basis for Loss of Connectivity in Alzheimer's Disease. *J. Neurosci.* **2007**, *27* (4), 796–807.
- (72) Nimmrich, V.; Grimm, C.; Draguhn, A.; Barghorn, S.; Lehmann, A.; Schoemaker, H.; Hillen, H.; Gross, G.; Ebert, U.; Bruehl, C. Amyloid Oligomers (A 1-42 Globulomer) Suppress Spontaneous Synaptic Activity by Inhibition of P/Q-Type Calcium Currents. *J. Neurosci.* **2008**, *28* (4), 788–797.
- (73) Kroemer, G.; Jäättelä, M. Lysosomes and Autophagy in Cell Death Control. *Nat. Rev. Cancer* **2005**, *5* (11), 886–897.
- (74) Rosales-Corral, S.; Acuna-Castroviejo, D.; Tan, D. X.; López-Armas, G.; Cruz-Ramos, J.; Munoz, R.; Melnikov, V. G.; Manchester, L. C.; Reiter, R. J. Accumulation of Exogenous Amyloid- Beta Peptide in Hippocampal Mitochondria Causes Their Dysfunction: A Protective Role for Melatonin. *Oxid. Med. Cell. Longev.* **2012**, *2012*, 1–15.
- (75) Domínguez-Prieto, M.; Velasco, A.; Tabernero, A.; Medina, J. M. Endocytosis and Transcytosis of Amyloid- β Peptides by Astrocytes: A Possible Mechanism for Amyloid- β Clearance in Alzheimer's Disease. *J. Alzheimer's Dis.* **2018**, *65* (4), 1109–1124.
- (76) Tomiyama, T.; Matsuyama, S.; Iso, H.; Umeda, T.; Takuma, H.; Ohnishi, K.; Ishibashi, K.; Teraoka, R.; Sakama, N.; Yamashita, T.; et al. A Mouse Model of Amyloid Oligomers: Their Contribution to Synaptic Alteration, Abnormal Tau Phosphorylation, Glial Activation, and Neuronal Loss In Vivo. *J. Neurosci.* **2010**, *30* (14), 4845–4856.
- (77) Ferretti, M. T.; Bruno, M. A.; Ducatenzeiler, A.; Klein, W. L.; Cuellar, A. C. Intracellular A β -Oligomers and Early Inflammation in a Model of Alzheimer's Disease. *Neurobiol. Aging* **2012**, *33* (7), 1329–1342.
- (78) Lesné, S. E.; Sherman, M. A.; Grant, M.; Kuskowski, M.; Schneider, J. A.; Bennett, D. A.; Ashe, K. H. Brain Amyloid- β Oligomers in Ageing and Alzheimer's Disease. *Brain* **2013**, *136*

- (5), 1383–1398.
- (79) Gyure, K. A.; Durham, R.; Stewart, W. F.; Smialek, J. E.; Troncoso, J. C. Intraneuronal Abeta-Amyloid Precedes Development of Amyloid Plaques in Down Syndrome. *Arch. Pathol. Lab. Med.* **2001**, *125* (4), 489–492.
- (80) Lacor, P. N.; Buniel, M. C.; Chang, L.; Fernandez, S. J.; Gong, Y.; Viola, K. L.; Lambert, M. P.; Velasco, P. T.; Bigio, E. H.; Finch, C. E.; et al. Synaptic Targeting by Alzheimer's-Related Amyloid Oligomers. *J. Neurosci.* **2004**, *24* (45), 10191–10200.
- (81) Frackowiak, J.; Zoltowska, A.; Wisniewski, H. M. Non-Fibrillar β -Amyloid Protein Is Associated with Smooth Muscle Cells of Vessel Walls in Alzheimer Disease. *J. Neuropathol. Exp. Neurol.* **1994**, *53* (6), 637–645.
- (82) Esparza, T. J.; Zhao, H.; Cirrito, J. R.; Cairns, N. J.; Bateman, R. J.; Holtzman, D. M.; Brody, D. L. Amyloid-Beta Oligomerization in Alzheimer Dementia versus High-Pathology Controls. *Ann. Neurol.* **2013**, *73* (1), 104–119.
- (83) Cline, E. N.; Bicca, M. A.; Viola, K. L.; Klein, W. L. The Amyloid- β Oligomer Hypothesis: Beginning of the Third Decade. *J. Alzheimer's Dis.* **2018**, *64* (s1), S567–S610.
- (84) Pomorski, T. G.; Nylander, T.; Cárdenas, M. Model Cell Membranes: Discerning Lipid and Protein Contributions in Shaping the Cell. *Adv. Colloid Interface Sci.* **2014**, *205*, 207–220.
- (85) Singer, S. J.; Nicolson, G. L. The Fluid Mosaic Model of the Structure of Cell Membranes. *Science (80-.)*. **1972**, *175* (4023), 720–731.
- (86) Lombard, J. Once upon a Time the Cell Membranes: 175 Years of Cell Boundary Research. *Biol. Direct* **2014**, *9* (1), 1–35.
- (87) Tanford, C.; Sons, J. W. &. *The Hydrophobic Effect: Formation of Micelles and Biological Membranes*; Wiley-Interscience publication; Wiley, 1980.
- (88) Cooper, G. M. *The Cell : A Molecular Approach*; New York (NY) : Sinauer Associates : Oxford University Press, 2019.
- (89) Lodish, H. F.; Berk, A.; Kaiser, C.; Krieger, M.; Scott, M. P.; Bretscher, A.; Ploegh, H. L.; Matsudaira, P. T. *Molecular Cell Biology*; W.H. Freeman: New York, 2008.
- (90) Thudichum, J. L. W. *A treatise on the chemical constitution of the brain*; Bailliere, Tindall and Cox: London, 1884.
- (91) Ramstedt, B.; Slotte, J. P. Membrane Properties of Sphingomyelins. *FEBS Lett.* **2002**, *531* (1), 33–37.
- (92) Chan, R. B.; Oliveira, T. G.; Cortes, E. P.; Honig, L. S.; Duff, K. E.; Small, S. A.; Wenk, M. R.; Shui, G.; Di Paolo, G. Comparative Lipidomic Analysis of Mouse and Human Brain with Alzheimer Disease. *J. Biol. Chem.* **2012**, *287* (4), 2678–2688.
- (93) Tettamanti, G. Ganglioside/Glycosphingolipid Turnover: New Concepts. *Glycoconj. J.* **2003**, *20* (5), 301–317.

- (94) Posse de Chaves, E.; Sipione, S. Sphingolipids and Gangliosides of the Nervous System in Membrane Function and Dysfunction. *FEBS Lett.* **2010**, *584* (9), 1748–1759.
- (95) Chiricozzi, E.; Lunghi, G.; Di Biase, E.; Fazzari, M.; Sonnino, S.; Mauri, L. GM1 Ganglioside Is a Key Factor in Maintaining the Mammalian Neuronal Functions Avoiding Neurodegeneration. *Int. J. Mol. Sci.* **2020**, *21* (3), 1–29.
- (96) Vance, J. E. Dysregulation of Cholesterol Balance in the Brain: Contribution to Neurodegenerative Diseases. *DMM Dis. Model. Mech.* **2012**, *5* (6), 746–755.
- (97) Kruijff, B. de. Lipid Polymorphism and Biomembrane Function. *Curr. Opin. Chem. Biol.* **1997**, *1* (4), 564–569.
- (98) Seddon, J. M.; Templer, R. H. Polymorphism of Lipid-Water Systems; 1995; Vol. I, pp 97–160.
- (99) Koynova, R.; Tenchov, B. Transitions between Lamellar and Nonlamellar Phases in Membrane Lipids and Their Physiological Roles. *OA Biochem.* **2013**, *1* (1), 1–9.
- (100) Ces, O.; Mulet, X. Physical Coupling between Lipids and Proteins: A Paradigm for Cellular Control. *Signal Transduct.* **2006**, *6* (2), 112–132.
- (101) Frolov, V. A.; Shnyrova, A. V.; Zimmerberg, J. Lipid Polymorphisms and Membrane Shape. *Cold Spring Harb. Perspect. Biol.* **2011**, *3* (11), 1–14.
- (102) Epand, R. M. Lipid Polymorphism and Protein-Lipid Interactions. *Biochim. Biophys. Acta - Rev. Biomembr.* **1998**, *1376* (3), 353–368.
- (103) Keller, S. L.; Gruner, S. M.; Gawrisch, K. Small Concentrations of Alamethicin Induce a Cubic Phase in Bulk Phosphatidylethanolamine Mixtures. *Biochim. Biophys. Acta - Biomembr.* **1996**, *1278* (2), 241–246.
- (104) Brassaru, R.; Killian, J. A.; De Kruijff, B.; Ruyschaert, J. M. Conformational Analysis of Gramicidin-Gramicidin Interactions at the Air/Water Interface Suggests That Gramicidin Aggregates into Tube-like Structures Similar as Found in the Gramicidin-Induced Hexagonal HII Phase. *BBA - Biomembr.* **1987**, *903* (1), 11–17.
- (105) Killian, J. A.; Urry, D. W. Conformation of Gramicidin in Relation to Its Ability To Form Bilayers with Lysophosphatidylcholine. *Biochemistry* **1988**, *27* (19), 7295–7301.
- (106) Majewska, M.; Mrdenovic, D.; Pieta, I. S.; Nowakowski, R.; Pieta, P. Nanomechanical Characterization of Single Phospholipid Bilayer in Ripple Phase with PF-QNM AFM. *Biochim. Biophys. Acta - Biomembr.* **2020**, *1862* (9), 183347.
- (107) Ramkaran, M.; Badia, A. Gel-to-Fluid Phase Transformations in Solid-Supported Phospholipid Bilayers Assembled by the Langmuir-Blodgett Technique: Effect of the Langmuir Monolayer Phase State and Molecular Density. *J. Phys. Chem. B* **2014**, *118* (32), 9708–9721.
- (108) Kycia, A. H.; Su, Z.; Brosseau, C. L.; Lipkowski, J. In Situ PM-IRRAS Studies of Biomimetic

- Membranes Supported at Gold Electrode Surfaces. In *Vibrational Spectroscopy at Electrified Interfaces*; John Wiley & Sons, Inc.: Hoboken, NJ, USA, 2013; pp 345–417.
- (109) Akabori, K.; Nagle, J. F. Structure of the DMPC Lipid Bilayer Ripple Phase. *Soft Matter* **2015**, *11* (5), 918–926.
- (110) Jacobson, K.; Sheets, E. D.; Simson, R. Revisiting the Fluid Mosaic Model of Membranes. *Science (80-.)*. **1995**, *268* (5216), 1441–1442.
- (111) Brown, D. A. *Lipid Rafts*, 2nd ed.; Elsevier Inc., 2013.
- (112) Tsui-Pierchala, B. A.; Encinas, M.; Milbrandt, J.; Johnson, E. M. Lipid Rafts in Neuronal Signaling and Function. *Trends Neurosci.* **2002**, *25* (8), 412–417.
- (113) Pike, L. J. Lipid Rafts: Bringing Order to Chaos. *J. Lipid Res.* **2003**, *44* (4), 655–667.
- (114) Schengrund, C.-L. Lipid Rafts: Keys to Neurodegeneration. *Brain Res. Bull.* **2010**, *82* (1–2), 7–17.
- (115) Svennerholm, L.; Boström, K.; Jungbjer, B.; Olsson, L. Membrane Lipids of Adult Human Brain: Lipid Composition of Frontal and Temporal Lobe in Subjects of Age 20 to 100 Years. *J. Neurochem.* **1994**, *63* (5), 1802–1811.
- (116) Simpson, M. A.; Cross, H.; Proukakis, C.; Priestman, D. A.; Neville, D. C. A.; Reinkensmeier, G.; Wang, H.; Wiznitzer, M.; Gurtz, K.; Verganelaki, A.; et al. Infantile-Onset Symptomatic Epilepsy Syndrome Caused by a Homozygous Loss-of-Function Mutation of GM3 Synthase. *Nat. Genet.* **2004**, *36* (11), 1225–1229.
- (117) Svennerholm, L.; Gottfries, C. -G. Membrane Lipids, Selectively Diminished in Alzheimer Brains, Suggest Synapse Loss as a Primary Event in Early-Onset Form (Type I) and Demyelination in Late-Onset Form (Type II). *J. Neurochem.* **1994**, *62* (3), 1039–1047.
- (118) Molander-Melin, M.; Blennow, K.; Bogdanovic, N.; Dellheden, B.; Månsson, J. E.; Fredman, P. Structural Membrane Alterations in Alzheimer Brains Found to Be Associated with Regional Disease Development; Increased Density of Gangliosides GM1 and GM2 and Loss of Cholesterol in Detergent-Resistant Membrane Domains. *J. Neurochem.* **2005**, *92* (1), 171–182.
- (119) Blennow, K.; Davidsson, P.; Wallin, A.; Fredman, P.; Gottfries, C. G.; Månsson, J. E.; Svennerholm, L. Differences in Cerebrospinal Fluid Gangliosides between “Probable Alzheimer’s Disease” and Normal Aging. *Aging Clin. Exp. Res.* **1992**, *4* (4), 301–306.
- (120) Wood, W. G.; Li, L.; Müller, W. E.; Eckert, G. P. Cholesterol as a Causative Factor in Alzheimer’s Disease: A Debatable Hypothesis. *J. Neurochem.* **2014**, *129* (4), 559–572.
- (121) Solomon, A.; Kivipelto, M.; Wolozin, B.; Zhou, J.; Whitmer, R. A. Midlife Serum Cholesterol and Increased Risk of Alzheimer’s and Vascular Dementia Three Decades Later. *Dement. Geriatr. Cogn. Disord.* **2009**, *28* (1), 75–80.
- (122) Swiger, K. J.; Manalac, R. J.; Blumenthal, R. S.; Blaha, M. J.; Martin, S. S. Statins and

- Cognition: A Systematic Review and Meta-Analysis of Short- and Long-Term Cognitive Effects. *Mayo Clin. Proc.* **2013**, *88* (11), 1213–1221.
- (123) Wolozin, B.; Kellman, W.; Ruosseau, P.; Celesia, G. G.; Siegel, G. Decreased Prevalence of Alzheimer Disease Associated with 3-Hydroxy-3-Methylglutaryl Coenzyme A Reductase Inhibitors. *Arch. Neurol.* **2000**, *57* (10), 1439–1443.
- (124) Wood, W. G.; Eckert, G. P.; Igbavboa, U.; Müller, W. E. Amyloid Beta-Protein Interactions with Membranes and Cholesterol: Causes or Casualties of Alzheimer's Disease. *Biochim. Biophys. Acta - Biomembr.* **2003**, *1610* (2), 281–290.
- (125) Burns, M. P.; Rebeck, G. W. Intracellular Cholesterol Homeostasis and Amyloid Precursor Protein Processing. *Biochim. Biophys. Acta - Mol. Cell Biol. Lipids* **2010**, *1801* (8), 853–859.
- (126) Ong, W. Y.; Tanaka, K.; Dawe, G. S.; Ittner, L. M.; Farooqui, A. A. Slow Excitotoxicity in Alzheimer's Disease. *J. Alzheimer's Dis.* **2013**, *35* (4), 643–668.
- (127) Baumgart, T.; Offenhäusser, A. Spreading of Lipid Monolayers on Hydrophilic Substrates at Increased Relative Humidities. *Langmuir* **2002**, *18* (15), 5899–5908.
- (128) Parikha, A. N. Membrane-Substrate Interface: Phospholipid Bilayers at Chemically and Topographically Structured Surfaces. *Biointerphases* **2008**, *3* (2), FA22–FA32.
- (129) Hirtz, M.; Oikonomou, A.; Georgiou, T.; Fuchs, H.; Vijayaraghavan, A. Multiplexed Biomimetic Lipid Membranes on Graphene by Dip-Pen Nanolithography. *Nat. Commun.* **2013**, *4* (1), 2591.
- (130) MUELLER, P.; RUDIN, D. O.; TI TIEN, H.; WESCOTT, W. C. Reconstitution of Cell Membrane Structure in Vitro and Its Transformation into an Excitable System. *Nature* **1962**, *194* (4832), 979–980.
- (131) Giwa, A.; Hasan, S. W.; Yousuf, A.; Chakraborty, S.; Johnson, D. J.; Hilal, N. Biomimetic Membranes: A Critical Review of Recent Progress. *Desalination* **2017**, *420* (July), 403–424.
- (132) Castellana, E. T.; Cremer, P. S. Solid Supported Lipid Bilayers: From Biophysical Studies to Sensor Design. *Surf. Sci. Rep.* **2006**, *61* (10), 429–444.
- (133) Zwang, T. J.; Fletcher, W. R.; Lane, T. J.; Johal, M. S. Quantification of the Layer of Hydration of a Supported Lipid Bilayer. *Langmuir* **2010**, *26* (7), 4598–4601.
- (134) Böcking, T.; Gooding, J. J. Biomimetic Membranes in Biosensor Applications. *Nanobiotechnology Biomim. Membr.* **2007**, 127–166.
- (135) Groves, J. T.; Boxer, S. G. Micropattern Formation in Supported Lipid Membranes. *Acc. Chem. Res.* **2002**, *35* (3), 149–157.
- (136) Lagerholm, B. C.; Starr, T. E.; Volovyk, Z. N.; Thompson, N. L. Rebinding of IgE Fabs at Haptenated Planar Membranes: Measurement by Total Internal Reflection with Fluorescence Photobleaching Recovery. *Biochemistry* **2000**, *39* (8), 2042–2051.
- (137) Cremer, P. S.; Boxer, S. G. Formation and Spreading of Lipid Bilayers on Planar Glass

- Supports. *J. Phys. Chem. B* **1999**, *103* (13), 2554–2559.
- (138) Garcia-Manyes, S.; Redondo-Morata, L.; Oncins, G.; Sanz, F. Nanomechanics of Lipid Bilayers: Heads or Tails? *J. Am. Chem. Soc.* **2010**, *132* (37), 12874–12886.
- (139) Juhaniwicz, J.; Sek, S. Interaction of Melittin with Negatively Charged Lipid Bilayers Supported on Gold Electrodes. *Electrochim. Acta* **2016**, *197*, 336–343.
- (140) Le Bihan, T.; Pézolet, M. Study of the Structure and Phase Behavior of Dipalmitoylphosphatidylcholine by Infrared Spectroscopy: Characterization of the Pretransition and Subtransition. *Chem. Phys. Lipids* **1998**, *94* (1), 13–33.
- (141) Plant, A. L. Supported Hybrid Bilayer Membranes as Rugged Cell Membrane Mimics. *Langmuir* **1999**, *15* (15), 5128–5135.
- (142) Hillebrandt, H.; Wiegand, G.; Tanaka, M.; Sackmann, E. High Electric Resistance Polymer/Lipid Composite Films on Indium-Tin-Oxide Electrodes. *Langmuir* **1999**, *15* (24), 8451–8459.
- (143) Sigl, H.; Brink, G.; Seufert, M.; Schulz, M.; Wegner, G.; Sackmann, E. Assembly of Polymer/Lipid Composite Films on Solids Based on Hairy Rod LB-Films. *Eur. Biophys. J.* **1997**, *25* (4), 249–259.
- (144) Eeman, M.; Deleu, M. From Biological Membranes to Biomimetic Model Membranes. *Biotechnol. Agron. Soc. Environ.* **2010**, *14* (4), 719–736.
- (145) Valincius, G.; Mickevicius, M. Tethered Phospholipid Bilayer Membranes. In *Advances in Planar Lipid Bilayers and Liposomes*; Elsevier Inc., 2015; Vol. 21, pp 27–61.
- (146) McGillivray, D. J.; Valincius, G.; Vanderah, D. J.; Febo-Ayala, W.; Woodward, J. T.; Heinrich, F.; Kasianowicz, J. J.; Lösche, M. Molecular-Scale Structural and Functional Characterization of Sparsely Tethered Bilayer Lipid Membranes. *Biointerphases* **2007**, *2* (1), 21–33.
- (147) Junghans, A.; Köper, I. Structural Analysis of Tethered Bilayer Lipid Membranes. *Langmuir* **2010**, *26* (13), 11035–11040.
- (148) Leitch, J.; Kunze, J.; Goddard, J. D.; Schwan, A. L.; Faragher, R. J.; Naumann, R.; Knoll, W.; Dutcher, J. R.; Lipkowsky, J. In Situ PM-IRRAS Studies of an Archaea Analogue Thioliipid Assembled on an Au(111) Electrode Surface. *Langmuir* **2009**, *25* (17), 10354–10363.
- (149) Heinrich, F.; Ng, T.; Vanderah, D. J.; Shekhar, P.; Mihailescu, M.; Nanda, H.; Lösche, M. A New Lipid Anchor for Sparsely Tethered Bilayer Lipid Membranes. *Langmuir* **2009**, *25* (7), 4219–4229.
- (150) Girard-Egrot, A. P.; Blum, L. J. Langmuir-Blodgett Technique for Synthesis of Biomimetic Lipid Membranes. *Nanobiotechnology Biomim. Membr.* **2007**, 23–74.
- (151) Györvary, E.; Wetzer, B.; Sleytr, U. B.; Sinner, A.; Offenhäusser, A.; Knoll, W. Lateral Diffusion of Lipids in Silane-, Dextran-, and S-Layer-Supported Mono- And Bilayers.

- Langmuir* **1999**, *15* (4), 1337–1347.
- (152) Kycia, A. H.; Sek, S.; Su, Z.; Merrill, A. R.; Lipkowski, J. Electrochemical and STM Studies of 1-Thio- β -D-Glucose Self-Assembled on an Au(111) Electrode Surface. *Langmuir* **2011**, *27* (21), 13383–13389.
- (153) Abbasi, F.; Alvarez-Malmagro, J.; Su, Z.; Leitch, J. J.; Lipkowski, J. Pore Forming Properties of Alamethicin in Negatively Charged Floating Bilayer Lipid Membranes Supported on Gold Electrodes. *Langmuir* **2018**, *34* (45), 13754–13765.
- (154) Juhaniwicz-Dębińska, J.; Konarzewska, D.; Sęk, S. Effect of Interfacial Water on the Nanomechanical Properties of Negatively Charged Floating Bilayers Supported on Gold Electrodes. *Langmuir* **2019**, *35* (29), 9422–9429.
- (155) Lipkowski, J. Building Biomimetic Membrane at a Gold Electrode Surface. *Phys. Chem. Chem. Phys.* **2010**, *12* (42), 13874–13887.
- (156) Su, Z. F.; Leitch, J. J.; Lipkowski, J. Electrode-Supported Biomimetic Membranes: An Electrochemical and Surface Science Approach for Characterizing Biological Cell Membranes. *Curr. Opin. Electrochem.* **2018**, *12*, 60–72.
- (157) Liedberg, B.; Ivarsson, B.; Hegg, P. O.; Lundström, I. On the Adsorption of β -Lactoglobulin on Hydrophilic Gold Surfaces: Studies by Infrared Reflection-Absorption Spectroscopy and Ellipsometry. *J. Colloid Interface Sci.* **1986**, *114* (2), 386–397.
- (158) Kharazian, B.; Lohse, S. E.; Ghasemi, F.; Raoufi, M.; Saei, A. A.; Hashemi, F.; Farvadi, F.; Alimohamadi, R.; Jalali, S. A.; Shokrgozar, M. A.; et al. Bare Surface of Gold Nanoparticle Induces Inflammation through Unfolding of Plasma Fibrinogen. *Sci. Rep.* **2018**, *8* (1), 1–9.
- (159) Nakanishi, K.; Sakiyama, T.; Imamura, K. On the Adsorption of Proteins on Solid Surfaces, a Common but Very Complicated Phenomenon. *J. Biosci. Bioeng.* **2001**, *91* (3), 233–244.
- (160) Pan, H.; Qin, M.; Meng, W.; Cao, Y.; Wang, W. How Do Proteins Unfold upon Adsorption on Nanoparticle Surfaces? *Langmuir* **2012**, *28* (35), 12779–12787.
- (161) Arispe, N.; Rojas, E.; Pollard, H. B. Alzheimer Disease Amyloid Beta Protein Forms Calcium Channels in Bilayer Membranes: Blockade by Tromethamine and Aluminum. *Proc. Natl. Acad. Sci.* **1993**, *90* (2), 567–571.
- (162) Quist, A.; Doudevski, I.; Lin, H.; Azimova, R.; Ng, D.; Frangione, B.; Kagan, B.; Ghiso, J.; Lal, R. Amyloid Ion Channels: A Common Structural Link for Protein-Misfolding Disease. *Proc. Natl. Acad. Sci.* **2005**, *102* (30), 10427–10432.
- (163) Lin, H.; Bhatia, R.; Lal, R. Amyloid β Protein Forms Ion Channels: Implications for Alzheimer's Disease Pathophysiology. *FASEB J.* **2001**, *15* (13), 2433–2444.
- (164) Bode, D. C.; Freeley, M.; Nield, J.; Palma, M.; Viles, J. H. Amyloid- β Oligomers Have a Profound Detergent-like Effect on Lipid Membrane Bilayers, Imaged by Atomic Force and Electron Microscopy. *J. Biol. Chem.* **2019**, *294* (19), 7566–7572.

- (165) Michikawa, M.; Gong, J.; Fan, Q.; Sawamura, N.; Yanagisawa, K. A Novel Action of Alzheimer's Amyloid β -Protein (A β): Oligomeric A β Promotes Lipid Release. *J. Neurosci.* **2001**, *21* (18), 7226–7235.
- (166) Akinlolu, R. D.; Nam, M.; Qiang, W. Competition between Fibrillation and Induction of Vesicle Fusion for the Membrane-Associated 40-Residue β -Amyloid Peptides. *Biochemistry* **2015**, *54* (22), 3416–3419.
- (167) Delgado, D. A.; Doherty, K.; Cheng, Q.; Kim, H.; Xu, D.; Dong, H.; Grewer, C.; Qiang, W. Distinct Membrane Disruption Pathways Are Induced by 40-Residue β -Amyloid Peptides. *J. Biol. Chem.* **2016**, *291* (23), 12233–12244.
- (168) Qiang, W.; Akinlolu, R. D.; Nam, M.; Shu, N. Structural Evolution and Membrane Interaction of the 40-Residue β Amyloid Peptides: Differences in the Initial Proximity between Peptides and the Membrane Bilayer Studied by Solid-State Nuclear Magnetic Resonance Spectroscopy. *Biochemistry* **2014**, *53* (48), 7503–7514.
- (169) Lashuel, H. A.; Hartley, D.; Petre, B. M.; Walz, T.; Lansbury, P. T. Amyloid Pores from Pathogenic Mutations. *Nature* **2002**, *418* (6895), 291–291.
- (170) Kaye, R.; Pensalfini, A.; Margol, L.; Sokolov, Y.; Sarsoza, F.; Head, E.; Hall, J.; Glabe, C. Annular Protofibrils Are a Structurally and Functionally Distinct Type of Amyloid Oligomer. *J. Biol. Chem.* **2009**, *284* (7), 4230–4237.
- (171) Serra-Batiste, M.; Ninot-Pedrosa, M.; Bayoumi, M.; Gairí, M.; Maglia, G.; Carulla, N. A β 42 Assembles into Specific β -Barrel Pore-Forming Oligomers in Membrane-Mimicking Environments. *Proc. Natl. Acad. Sci.* **2016**, *113* (39), 10866–10871.
- (172) Jang, H.; Zheng, J.; Nussinov, R. Models of β -Amyloid Ion Channels in the Membrane Suggest That Channel Formation in the Bilayer Is a Dynamic Process. *Biophys. J.* **2007**, *93* (6), 1938–1949.
- (173) Jang, H.; Zheng, J.; Lal, R.; Nussinov, R. New Structures Help the Modeling of Toxic Amyloid β Ion Channels. *Trends Biochem. Sci.* **2008**, *33* (2), 91–100.
- (174) Arispe, N.; Pollard, H. B.; Rojas, E. Giant Multilevel Cation Channels Formed by Alzheimer Disease Amyloid Beta-Protein [A Beta P-(1-40)] in Bilayer Membranes. *Proc. Natl. Acad. Sci.* **1993**, *90* (22), 10573–10577.
- (175) Lin, H.; Zhu, Y. J.; Lal, R. Amyloid β Protein (1–40) Forms Calcium-Permeable, Zn²⁺-Sensitive Channel in Reconstituted Lipid Vesicles. *Biochemistry* **1999**, *38* (34), 11189–11196.
- (176) Rhee, S. K.; Quist, A. P.; Lal, R. Amyloid β Protein-(1–42) Forms Calcium-Permeable, Zn²⁺-Sensitive Channel. *J. Biol. Chem.* **1998**, *273* (22), 13379–13382.
- (177) Lee, J.; Kim, Y. H.; T. Arce, F.; Gillman, A. L.; Jang, H.; Kagan, B. L.; Nussinov, R.; Yang, J.; Lal, R. Amyloid β Ion Channels in a Membrane Comprising Brain Total Lipid Extracts. *ACS Chem. Neurosci.* **2017**, *8* (6), 1348–1357.

- (178) Bode, D. C.; Baker, M. D.; Viles, J. H. Ion Channel Formation by Amyloid- β 42 Oligomers but Not Amyloid- β 40 in Cellular Membranes. *J. Biol. Chem.* **2017**, *292* (4), 1404–1413.
- (179) Lindberg, D. J.; Wesén, E.; Björkeröth, J.; Rocha, S.; Esbjörner, E. K. Lipid Membranes Catalyse the Fibril Formation of the Amyloid- β (1–42) Peptide through Lipid-Fibril Interactions That Reinforce Secondary Pathways. *Biochim. Biophys. Acta - Biomembr.* **2017**, *1859* (10), 1921–1929.
- (180) Aisenbrey, C.; Borowik, T.; Byström, R.; Bokvist, M.; Lindström, F.; Misiak, H.; Sani, M.-A.; Gröbner, G. How Is Protein Aggregation in Amyloidogenic Diseases Modulated by Biological Membranes? *Eur. Biophys. J.* **2008**, *37* (3), 247–255.
- (181) Chi, E. Y.; Ege, C.; Winans, A.; Majewski, J.; Wu, G.; Kjaer, K.; Lee, K. Y. C. Lipid Membrane Templates the Ordering and Induces the Fibrillogenesis of Alzheimer's Disease Amyloid- β Peptide. *Proteins Struct. Funct. Bioinforma.* **2008**, *72* (1), 1–24.
- (182) Ewald, M.; Henry, S.; Lambert, E.; Feuillie, C.; Bobo, C.; Cullin, C.; Lecomte, S.; Molinari, M. High-Speed Atomic Force Microscopy to Investigate the Interactions between Toxic A β 1-42 Peptides and Model Membranes in Real Time: Impact of the Membrane Composition. *Nanoscale* **2019**, *11* (15), 7229–7238.
- (183) Qiang, W.; Yau, W.-M.; Schulte, J. Fibrillation of β Amyloid Peptides in the Presence of Phospholipid Bilayers and the Consequent Membrane Disruption. *Biochim. Biophys. Acta - Biomembr.* **2015**, *1848* (1), 266–276.
- (184) De, S.; Wirthensohn, D. C.; Flagmeier, P.; Hughes, C.; Aprile, F. A.; Ruggeri, F. S.; Whiten, D. R.; Emin, D.; Xia, Z.; Varela, J. A.; et al. Different Soluble Aggregates of A β 42 Can Give Rise to Cellular Toxicity through Different Mechanisms. *Nat. Commun.* **2019**, *10* (1), 1541.
- (185) De, S.; Whiten, D. R.; Ruggeri, F. S.; Hughes, C.; Rodrigues, M.; Sideris, D. I.; Taylor, C. G.; Aprile, F. A.; Muyldermans, S.; Knowles, T. P. J.; et al. Soluble Aggregates Present in Cerebrospinal Fluid Change in Size and Mechanism of Toxicity during Alzheimer's Disease Progression. *Acta Neuropathol. Commun.* **2019**, *7* (1), 120.
- (186) Scheltens, P.; Blennow, K.; Breteler, M. M. B.; de Strooper, B.; Frisoni, G. B.; Salloway, S.; Van der Flier, W. M. Alzheimer's Disease. *Lancet* **2016**, *388* (10043), 505–517.
- (187) Chen, G.; Xu, T.; Yan, Y.; Zhou, Y.; Jiang, Y.; Melcher, K.; Xu, H. E. Amyloid Beta: Structure, Biology, and Structure-Based Therapeutic Development. *Acta Pharmacol. Sin.* **2017**, *38* (9), 1205–1235.
- (188) Ahmed, M.; Davis, J.; Aucoin, D.; Sato, T.; Ahuja, S.; Aimoto, S.; Elliott, J. I.; Van Nostrand, W. E.; Smith, S. O. Structural Conversion of Neurotoxic Amyloid-B1–42 Oligomers to Fibrils. *Nat. Struct. Mol. Biol.* **2010**, *17* (5), 561–567.
- (189) Morris, C.; Cupples, S.; Kent, T. W.; Elbassal, E. A.; Wojcikiewicz, E. P.; Yi, P.; Du, D. N-Terminal Charged Residues of Amyloid- β Peptide Modulate Amyloidogenesis and Interaction with Lipid Membrane. *Chem. - A Eur. J.* **2018**, *24* (38), 9494–9498.

- (190) Wärmländer, S. K. T. S.; Österlund, N.; Wallin, C.; Wu, J.; Luo, J.; Tiiman, A.; Jarvet, J.; Gräslund, A. Metal Binding to the Amyloid- β Peptides in the Presence of Biomembranes: Potential Mechanisms of Cell Toxicity. *JBIC J. Biol. Inorg. Chem.* **2019**, *24* (8), 1189–1196.
- (191) Bolognesi, B.; Kumita, J. R.; Barros, T. P.; Esbjorner, E. K.; Luheshi, L. M.; Crowther, D. C.; Wilson, M. R.; Dobson, C. M.; Favrin, G.; Yerbury, J. J. ANS Binding Reveals Common Features of Cytotoxic Amyloid Species. *ACS Chem. Biol.* **2010**, *5* (8), 735–740.
- (192) Ladiwala, A. R. A.; Litt, J.; Kane, R. S.; Aucoin, D. S.; Smith, S. O.; Ranjan, S.; Davis, J.; Van Nostrand, W. E.; Tessier, P. M. Conformational Differences between Two Amyloid β Oligomers of Similar Size and Dissimilar Toxicity. *J. Biol. Chem.* **2012**, *287* (29), 24765–24773.
- (193) Ahmed, R.; Akcan, M.; Khondker, A.; Rheinstädter, M. C.; Bozelli, J. C.; Epand, R. M.; Huynh, V.; Wylie, R. G.; Boulton, S.; Huang, J.; et al. Atomic Resolution Map of the Soluble Amyloid Beta Assembly Toxic Surfaces. *Chem. Sci.* **2019**, *10* (24), 6072–6082.
- (194) Eckert, A.; Hauptmann, S.; Scherping, I.; Meinhardt, J.; Rhein, V.; Dröse, S.; Brandt, U.; Fändrich, M.; Müller, W. E.; Götz, J. Oligomeric and Fibrillar Species of β -Amyloid (A β 42) Both Impair Mitochondrial Function in P301L Tau Transgenic Mice. *J. Mol. Med.* **2008**, *86* (11), 1255–1267.
- (195) Cerf, E.; Sarroukh, R.; Tamamizu-Kato, S.; Breydo, L.; Derclaye, S.; Dufrêne, Y. F.; Narayanaswami, V.; Goormaghtigh, E.; Ruyschaert, J.-M.; Raussens, V. Antiparallel β -Sheet: A Signature Structure of the Oligomeric Amyloid β -Peptide. *Biochem. J.* **2009**, *421* (3), 415–423.
- (196) Stroud, J. C.; Liu, C.; Teng, P. K.; Eisenberg, D. Toxic Fibrillar Oligomers of Amyloid- β Have Cross- β Structure. *Proc. Natl. Acad. Sci.* **2012**, *109* (20), 7717–7722.
- (197) Vivoli Vega, M.; Cascella, R.; Chen, S. W.; Fusco, G.; De Simone, A.; Dobson, C. M.; Cecchi, C.; Chiti, F. The Toxicity of Misfolded Protein Oligomers Is Independent of Their Secondary Structure. *ACS Chem. Biol.* **2019**, *14* (7), 1593–1600.
- (198) Yasumoto, T.; Takamura, Y.; Tsuji, M.; Watanabe-Nakayama, T.; Imamura, K.; Inoue, H.; Nakamura, S.; Inoue, T.; Kimura, A.; Yano, S.; et al. High Molecular Weight Amyloid β 1-42 Oligomers Induce Neurotoxicity via Plasma Membrane Damage. *FASEB J.* **2019**, *33* (8), 9220–9234.
- (199) Sigurdsson, E. M. *Amyloid Proteins*; Humana Press: New Jersey, 2004; Vol. 299.
- (200) Nilsson, B. L.; Doran, T. M. *Peptide Self-Assembly*; Nilsson, B. L., Doran, T. M., Eds.; Methods in Molecular Biology; Springer New York: New York, NY, 2018; Vol. 1777.
- (201) Fu, Z.; Aucoin, D.; Davis, J.; Van Nostrand, W. E.; Smith, S. O. Mechanism of Nucleated Conformational Conversion of A β 42. *Biochemistry* **2015**, *54* (27), 4197–4207.
- (202) Henry, S.; Bercu, N. B.; Bobo, C.; Cullin, C.; Molinari, M.; Lecomte, S. Interaction of A β 1–42 Peptide or Their Variant with Model Membrane of Different Composition Probed by

- Infrared Nanospectroscopy. *Nanoscale* **2018**, *10* (3), 936–940.
- (203) Henry, S.; Vignaud, H.; Bobo, C.; Decossas, M.; Lambert, O.; Harte, E.; Alves, I. D.; Cullin, C.; Lecomte, S. Interaction of A β 1–42 Amyloids with Lipids Promotes “Off-Pathway” Oligomerization and Membrane Damage. *Biomacromolecules* **2015**, *16* (3), 944–950.
- (204) Ikeda, K.; Matsuzaki, K. Driving Force of Binding of Amyloid β -Protein to Lipid Bilayers. *Biochem. Biophys. Res. Commun.* **2008**, *370* (3), 525–529.
- (205) Ege, C.; Lee, K. Y. C. Insertion of Alzheimer’s A β 40 Peptide into Lipid Monolayers. *Biophys. J.* **2004**, *87* (3), 1732–1740.
- (206) Bokvist, M.; Lindström, F.; Watts, A.; Gröbner, G. Two Types of Alzheimer’s β -Amyloid (1–40) Peptide Membrane Interactions: Aggregation Preventing Transmembrane Anchoring Versus Accelerated Surface Fibril Formation. *J. Mol. Biol.* **2004**, *335* (4), 1039–1049.
- (207) Sciacca, M. F. M.; Kotler, S. A.; Brender, J. R.; Chen, J.; Lee, D.; Ramamoorthy, A. Two-Step Mechanism of Membrane Disruption by A β through Membrane Fragmentation and Pore Formation. *Biophys. J.* **2012**, *103* (4), 702–710.
- (208) Habchi, J.; Chia, S.; Galvagnion, C.; Michaels, T. C. T.; Bellaiche, M. M. J.; Ruggeri, F. S.; Sanguanini, M.; Idini, I.; Kumita, J. R.; Sparr, E.; et al. Cholesterol Catalyses A β 42 Aggregation through a Heterogeneous Nucleation Pathway in the Presence of Lipid Membranes. *Nat. Chem.* **2018**, *10* (6), 673–683.
- (209) de Planque, M. R. R.; Raussens, V.; Contera, S. A.; Rijkers, D. T. S.; Liskamp, R. M. J.; Ruyschaert, J.-M.; Ryan, J. F.; Separovic, F.; Watts, A. β -Sheet Structured β -Amyloid(1-40) Perturbs Phosphatidylcholine Model Membranes. *J. Mol. Biol.* **2007**, *368* (4), 982–997.
- (210) Ambroggio, E. E.; Kim, D. H.; Separovic, F.; Barrow, C. J.; Barnham, K. J.; Bagatolli, L. A.; Fidelio, G. D. Surface Behavior and Lipid Interaction of Alzheimer β -Amyloid Peptide 1–42: A Membrane-Disrupting Peptide. *Biophys. J.* **2005**, *88* (4), 2706–2713.
- (211) Korshavn, K. J.; Satriano, C.; Lin, Y.; Zhang, R.; Dulchavsky, M.; Bhunia, A.; Ivanova, M. I.; Lee, Y.-H.; La Rosa, C.; Lim, M. H.; et al. Reduced Lipid Bilayer Thickness Regulates the Aggregation and Cytotoxicity of Amyloid- β . *J. Biol. Chem.* **2017**, *292* (11), 4638–4650.
- (212) Fernández-Pérez, E. J.; Sepúlveda, F. J.; Peoples, R.; Aguayo, L. G. Role of Membrane GM1 on Early Neuronal Membrane Actions of A β during Onset of Alzheimer’s Disease. *Biochim. Biophys. Acta - Mol. Basis Dis.* **2017**, *1863* (12), 3105–3116.
- (213) Nakazawa, Y.; Suzuki, Y.; Williamson, M. P.; Saitô, H.; Asakura, T. The Interaction of Amyloid A β (1–40) with Lipid Bilayers and Ganglioside as Studied by ³¹P Solid-State NMR. *Chem. Phys. Lipids* **2009**, *158* (1), 54–60.
- (214) Chi, E. Y.; Frey, S. L.; Lee, K. Y. C. Ganglioside GM1-Mediated Amyloid-Beta Fibrillogenesis and Membrane Disruption†. *Biochemistry* **2007**, *46* (7), 1913–1924.
- (215) Cheng, Q.; Hu, Z.-W.; Doherty, K. E.; Tobin-Miyaji, Y. J.; Qiang, W. The On-Fibrillation-Pathway Membrane Content Leakage and off-Fibrillation-Pathway Lipid Mixing Induced by

- 40-Residue β -Amyloid Peptides in Biologically Relevant Model Liposomes. *Biochim. Biophys. Acta - Biomembr.* **2018**, *1860* (9), 1670–1680.
- (216) Mannini, B.; Mulvihill, E.; Sgromo, C.; Cascella, R.; Khodarahmi, R.; Ramazzotti, M.; Dobson, C. M.; Cecchi, C.; Chiti, F. Toxicity of Protein Oligomers Is Rationalized by a Function Combining Size and Surface Hydrophobicity. *ACS Chem. Biol.* **2014**, *9* (10), 2309–2317.
- (217) McConnell, H. M.; Watts, T. H.; Weis, R. M.; Brian, A. A. Supported Planar Membranes in Studies of Cell-Cell Recognition in the Immune System. *Biochim. Biophys. Acta - Rev. Biomembr.* **1986**, *864* (1), 95–106.
- (218) Lipowsky, R.; Seifert, U. Adhesion of Vesicles and Membranes. *Mol. Cryst. Liq. Cryst.* **1991**, *202* (1), 17–25.
- (219) Reviakine, I.; Brisson, A. Formation of Supported Phospholipid Bilayers from Unilamellar Vesicles Investigated by Atomic Force Microscopy. *Langmuir* **2000**, *16* (4), 1806–1815.
- (220) Jung, S. H.; Park, D.; Park, J. H.; Kim, Y. M.; Ha, K. S. Molecular Imaging of Membrane Proteins and Microfilaments Using Atomic Force Microscopy. *Exp. Mol. Med.* **2010**, *42* (9), 597–605.
- (221) Cappella, B.; Dietler, G. Force-Distance Curves by Atomic Force Microscopy. *Surf. Sci. Rep.* **1999**, *34* (1–3), 1–104.
- (222) Aoki, T.; Hiroshima, M.; Kitamura, K.; Tokunaga, M.; Yanagida, T. Non-Contact Scanning Probe Microscopy with Sub-Piconewton Force Sensitivity. *Ultramicroscopy* **1997**, *70* (1–2), 45–55.
- (223) Bizzarri, A. R.; Cannistraro, S. *Dynamic Force Spectroscopy and Biomolecular Recognition*; CRC Press, 2012.
- (224) *Atomic Force Microscopy in Molecular and Cell Biology*; Cai, J., Ed.; Springer Singapore: Singapore, 2018.
- (225) Pfreundschuh, M.; Martinez-Martin, D.; Mulvihill, E.; Wegmann, S.; Muller, D. J. Multiparametric High-Resolution Imaging of Native Proteins by Force-Distance Curve-Based AFM. *Nat. Protoc.* **2014**, *9* (5), 1113–1130.
- (226) Cross, S. E.; Jin, Y. S.; Rao, J.; Gimzewski, J. K. Nanomechanical Analysis of Cells from Cancer Patients. *Nat. Nanotechnol.* **2007**, *2* (12), 780–783.
- (227) Rosenbluth, M. J.; Lam, W. A.; Fletcher, D. A. Force Microscopy of Nonadherent Cells: A Comparison of Leukemia Cell Deformability. *Biophys. J.* **2006**, *90* (8), 2994–3003.
- (228) Hertz, H. Über Die Berührung Fester Elastischer Körper. *J. für die reine und Angew. Math.* **1881**, *92*, 156–171.
- (229) Derjaguin, B. .; Muller, V. .; Toporov, Y. . Effect of Contact Deformations on the Adhesion of Particles. *J. Colloid Interface Sci.* **1975**, *53* (2), 314–326.
- (230) Johnson, K. L.; Kendall, K.; Roberts, A. D. Surface Energy and the Contact of Elastic Solids.

- Proc. R. Soc. London. A. Math. Phys. Sci.* **1971**, 324 (1558), 301–313.
- (231) Sneddon, I. N. Boussinesq's Problem for a Rigid Cone. *Math. Proc. Cambridge Philos. Soc.* **1948**, 44 (4), 492–507.
- (232) Kontomaris, S.-V. The Hertz Model in AFM Nanoindentation Experiments: Applications in Biological Samples and Biomaterials. *Micro Nanosyst.* **2018**, 10 (1), 11–22.
- (233) Szymanski, J. M.; Zhang, K.; Feinberg, A. W. Measuring the Poisson's Ratio of Fibronectin Using Engineered Nanofibers. *Sci. Rep.* **2017**, 7 (1), 1–9.
- (234) Picas, L.; Rico, F.; Scheuring, S. Direct Measurement of the Mechanical Properties of Lipid Phases in Supported Bilayers. *Biophys. J.* **2012**, 102 (1), L01–L03.
- (235) Claesson, P. M.; Dobryden, I.; Li, G.; He, Y.; Huang, H.; Thorén, P.-A.; Haviland, D. B. From Force Curves to Surface Nanomechanical Properties. *Phys. Chem. Chem. Phys.* **2017**, 19 (35), 23642–23657.
- (236) Heath, G. R.; Scheuring, S. High-Speed AFM Height Spectroscopy Reveals Ms-Dynamics of Unlabeled Biomolecules. *Nat. Commun.* **2018**, 9 (1).
- (237) de Pablo, P. J.; Carrión-Vázquez, M. Imaging Biological Samples with Atomic Force Microscopy. *Cold Spring Harb. Protoc.* **2014**, 2014 (2), 167–177.
- (238) Kuznetsov, Y. G.; McPherson, A. Atomic Force Microscopy in Imaging of Viruses and Virus-Infected Cells. *Microbiol. Mol. Biol. Rev.* **2011**, 75 (2), 268–285.
- (239) Su, Z.; Juhaniewicz-Debinska, J.; Sek, S.; Lipkowski, J. Water Structure in the Submembrane Region of a Floating Lipid Bilayer: The Effect of an Ion Channel Formation and the Channel Blocker. *Langmuir* **2020**, 36 (1), 409–418.
- (240) Burgess, I.; Li, M.; Horswell, S. L.; Szymanski, G.; Lipkowski, J.; Majewski, J.; Satija, S. Electric Field-Driven Transformations of a Supported Model Biological Membrane - An Electrochemical and Neutron Reflectivity Study. *Biophys. J.* **2004**, 86 (3), 1763–1776.
- (241) Su, Z.; Leitch, J.; Lipkowski, J. Measurements of the Potentials of Zero Free Charge and Zero Total Charge for 1-Thio- β -D-Glucose and DPTL Modified Au(111) Surface in Different Electrolyte Solutions. *Zeitschrift fur Phys. Chemie* **2012**, 226 (9–10), 995–1009.
- (242) Kerner, Z.; Pajkossy, T. Impedance of Rough Capacitive Electrodes: The Role of Surface Disorder. *J. Electroanal. Chem.* **1998**, 448 (1), 139–142.
- (243) Krishna, G.; Schulte, J.; Cornell, B. A.; Pace, R. J.; Osman, P. D. Tethered Bilayer Membranes Containing Ionic Reservoirs: Selectivity and Conductance. *Langmuir* **2003**, 19 (6), 2294–2305.
- (244) Valincius, G.; Meškauskas, T.; Ivanauskas, F. Electrochemical Impedance Spectroscopy of Tethered Bilayer Membranes. *Langmuir* **2012**, 28 (1), 977–990.
- (245) Kwak, K. J.; Valincius, G.; Liao, W. C.; Hu, X.; Wen, X.; Lee, A.; Yu, B.; Vanderah, D. J.; Lu, W.; Lee, L. J. Formation and Finite Element Analysis of Tethered Bilayer Lipid Structures.

- Langmuir* **2010**, *26* (23), 18199–18208.
- (246) Valincius, G.; Mickevicius, M.; Penkauskas, T.; Jankunec, M. Electrochemical Impedance Spectroscopy of Tethered Bilayer Membranes: An Effect of Heterogeneous Distribution of Defects in Membranes. *Electrochim. Acta* **2016**, *222*, 904–913.
- (247) Su, Z.; Mrdenovic, D.; Sek, S.; Lipkowski, J. Ionophore Properties of Valinomycin in the Model Bilayer Lipid Membrane 1. Selectivity towards a Cation. *J. Solid State Electrochem.* **2020**, *24* (11–12), 3125–3134.
- (248) Tamm, L. K.; Tatulian, S. A. Infrared Spectroscopy of Proteins and Peptides in Lipid Bilayers. *Q. Rev. Biophys.* **1997**, *30* (4), 365–429.
- (249) Yang, H.; Yang, S.; Kong, J.; Dong, A.; Yu, S. Obtaining Information about Protein Secondary Structures in Aqueous Solution Using Fourier Transform IR Spectroscopy. *Nat. Protoc.* **2015**, *10* (3), 382–396.
- (250) Fahmy, K. Fourier Transform-Infrared Spectroscopy for Biophysical Applications: Technical Aspects. In *Encyclopedia of Biophysics*; Springer Berlin Heidelberg: Berlin, Heidelberg, 2018; pp 1–10.
- (251) Zamlynyy, V.; Lipkowski, J. Quantitative SNIFTIRS and PM IRRAS of Organic Molecules at Electrode Surfaces. In *Advances in Electrochemical Sciences and Engineering*; 2006; Vol. 9, pp 315–376.
- (252) Moskovits, M. Surface Selection Rules. *J. Chem. Phys.* **1982**, *77* (9), 4408–4416.
- (253) Baker, M. J.; Trevisan, J.; Bassan, P.; Bhargava, R.; Butler, H. J.; Dorling, K. M.; Fielden, P. R.; Fogarty, S. W.; Fullwood, N. J.; Heys, K. A.; et al. Using Fourier Transform IR Spectroscopy to Analyze Biological Materials. *Nat. Protoc.* **2014**, *9* (8), 1771–1791.
- (254) Mantsch, H. H. Biological Applications of Fourier Transform Infrared Spectroscopy: A Study of Phase Transitions in Biomembranes. *J. Mol. Struct.* **1984**, *113*, 201–212.
- (255) Lewis, R. N. A. H.; Mcelhaney, R. N. Biochimica et Biophysica Acta Membrane Lipid Phase Transitions, and Phase Organization Studied by Fourier Transform Infrared Spectroscopy ☆ *BBA - Biomembr.* **2013**, *1828* (10), 2347–2358.
- (256) Zawisza, I.; Bin, X.; Lipkowski, J. Potential-Driven Structural Changes in Langmuir-Blodgett DMPC Bilayers Determined by in Situ Spectroelectrochemical PM IRRAS. *Langmuir* **2007**, *23* (9), 5180–5194.
- (257) Damien, F.; Boncheva, M. The Extent of Orthorhombic Lipid Phases in the Stratum Corneum Determines the Barrier Efficiency of Human Skin in Vivo. *J. Invest. Dermatol.* **2010**, *130* (2), 611–614.
- (258) Champagne, A. M.; Pigg, V. A.; Allen, H. C.; Williams, J. B. Presence and Persistence of a Highly Ordered Lipid Phase State in the Avian Stratum Corneum. *J. Exp. Biol.* **2018**, *221* (11), 1–6.

- (259) Gooris, G. S.; Bouwstra, J. A. Infrared Spectroscopic Study of Stratum Corneum Model Membranes Prepared from Human Ceramides, Cholesterol, and Fatty Acids. *Biophys. J.* **2007**, *92* (8), 2785–2795.
- (260) Cameron, D. G.; Gudgin, E. F.; Mantsch, H. H. Dependence of Acyl Chain Packing of Phospholipids on the Head Group and Acyl Chain Length. *Biochemistry* **1981**, *20* (15), 4496–4500.
- (261) Blume, A.; Hiibner, W.; Messner, G. Fourier Transform Infrared Spectroscopy Of¹³C=O-Labeled Phospholipids Hydrogen Bonding To Carbonyl Groups. *Biochemistry* **1988**, *27* (21), 8239–8249.
- (262) Lewis, R. N.; McElhaneey, R. N.; Pohle, W.; Mantsch, H. H. Components of the Carbonyl Stretching Band in the Infrared Spectra of Hydrated 1,2-Diacylglycerolipid Bilayers: A Reevaluation. *Biophys. J.* **1994**, *67* (6), 2367–2375.
- (263) Kong, J.; Yu, S. Fourier Transform Infrared Spectroscopic Analysis of Protein Secondary Structures. *Acta Biochim. Biophys. Sin. (Shanghai)*. **2007**, *39* (8), 549–559.
- (264) Barth, A. Infrared Spectroscopy of Proteins. *Biochim. Biophys. Acta - Bioenerg.* **2007**, *1767* (9), 1073–1101.
- (265) Surewicz, W. K.; Mantsch, H. H. New Insight into Protein Secondary Structure from Resolution-Enhanced Infrared Spectra. *Biochim. Biophys. Acta - Protein Struct. Mol. Enzymol.* **1988**, *952*, 115–130.
- (266) Noda, I. Two-Dimensional Co-distribution Spectroscopy to Determine the Sequential Order of Distributed Presence of Species. *J. Mol. Struct.* **2014**, *1069* (1), 50–59.
- (267) Cameron, D. G.; Moffatt, D. J. Generalized Approach To Derivative Spectroscopy. *Appl. Spectrosc.* **1987**, *41* (4), 539–544.
- (268) Susi, H.; Michael Byler, D. Protein Structure by Fourier Transform Infrared Spectroscopy: Second Derivative Spectra. *Biochem. Biophys. Res. Commun.* **1983**, *115* (1), 391–397.
- (269) Ruggeri, F. S.; Mannini, B.; Schmid, R.; Vendruscolo, M.; Knowles, T. P. J. Single-Molecule Secondary Structure Determination of Proteins through Infrared Absorption Nanospectroscopy. *Nat. Commun.* **2020**, *11* (1), 2945.
- (270) Noda, I. Advances in Two-Dimensional Correlation Spectroscopy (2DCOS). In *Frontiers and Advances in Molecular Spectroscopy*; Elsevier, 2018; pp 47–75.
- (271) Domingo, J. C.; De Madariaga, M. A. Fourier Transform Infrared Spectroscopic Analysis of the Ester and Amide Bands of the Hydrated Dispersions of N-Acylethanolamine Phospholipids. *Chem. Phys. Lipids* **1996**, *84* (2), 147–153.
- (272) Allara, D. L.; Swalen, J. D. An Infrared Reflection Spectroscopy Study of Oriented Cadmium Arachidate Monolayer Films on Evaporated Silver. *J. Phys. Chem.* **1982**, *86* (14), 2700–2704.

- (273) Bertie, J. E.; Keefe, C. D. Infrared Intensities of Liquids XXII: Optical and Dielectric Constants, Molar Polarizabilities, and Integrated Intensities of Liquid Benzene-D₆ at 25°C between 5000 and 450 cm⁻¹. *Fresenius. J. Anal. Chem.* **1998**, *362* (1), 91–108.
- (274) Ordal, M. A.; Long, L. L.; Bell, R. J.; Bell, S. E.; Bell, R. R.; Alexander, R. W.; Ward, C. A. Optical Properties of the Metals Al, Co, Cu, Au, Fe, Pb, Ni, Pd, Pt, Ag, Ti, and W in the Infrared and Far Infrared. *Appl. Opt.* **1983**, *22* (7), 1099.
- (275) Brosseau, C. L.; Leitch, J.; Bin, X.; Chen, M.; Roscoe, S. G.; Lipkowski, J. Electrochemical and PM-IRRAS a Glycolipid-Containing Biomimetic Membrane Prepared Using Langmuir-Blodgett/Langmuir-Schaefer Deposition. *Langmuir* **2008**, *24* (22), 13058–13067.
- (276) Zawisza, I.; Bin, X.; Lipkowski, J. Potential-Driven Structural Changes in Langmuir-Blodgett DMPC Bilayers Determined by in Situ Spectroelectrochemical PM IRRAS. *Langmuir* **2007**, *23* (9), 5180–5194.
- (277) Leitch, J. J.; Brosseau, C. L.; Roscoe, S. G.; Bessonov, K.; Dutcher, J. R.; Lipkowski, J. Electrochemical and PM-IRRAS Characterization of Cholera Toxin Binding at a Model Biological Membrane. *Langmuir* **2013**, *29* (3), 965–976.
- (278) Pieta, P.; Majewska, M.; Su, Z.; Grossutti, M.; Wladyka, B.; Piejko, M.; Lipkowski, J.; Mak, P. Physicochemical Studies on Orientation and Conformation of a New Bacteriocin BacSp222 in a Planar Phospholipid Bilayer. *Langmuir* **2016**, *32* (22), 5653–5662.
- (279) Dante, S.; Hauß, T.; Steitz, R.; Canale, C.; Dencher, N. A. Nanoscale Structural and Mechanical Effects of Beta-Amyloid (1–42) on Polymer Cushioned Membranes: A Combined Study by Neutron Reflectometry and AFM Force Spectroscopy. *Biochim. Biophys. Acta - Biomembr.* **2011**, *1808* (11), 2646–2655.
- (280) Jao, S.-C.; Ma, K.; Talafous, J.; Orlando, R.; Zagorski, M. G. Trifluoroacetic Acid Pretreatment Reproducibly Disaggregates the Amyloid β -Peptide. *Amyloid* **1997**, *4* (4), 240–252.
- (281) Stine, W. B.; Jungbauer, L.; Yu, C.; LaDu, M. J. Preparing Synthetic A β in Different Aggregation States. In *Alzheimer's Disease and Frontotemporal Dementia: Methods and Protocols*; Roberson, E. D., Ed.; Humana Press: Totowa, NJ, United States, 2010; Vol. 670, pp 13–32.
- (282) Banerjee, S.; Hashemi, M.; Lv, Z.; Maity, S.; Rochet, J.-C.; Lyubchenko, Y. L. A Novel Pathway for Amyloids Self-Assembly in Aggregates at Nanomolar Concentration Mediated by the Interaction with Surfaces. *Sci. Rep.* **2017**, *7* (1), 45592.
- (283) Chromy, B. A.; Nowak, R. J.; Lambert, M. P.; Viola, K. L.; Chang, L.; Velasco, P. T.; Jones, B. W.; Fernandez, S. J.; Lacor, P. N.; Horowitz, P.; et al. Self-Assembly of A β 1-42 into Globular Neurotoxins. *Biochemistry* **2003**, *42* (44), 12749–12760.
- (284) Gurtovenko, A. A.; Anwar, J. Modulating the Structure and Properties of Cell Membranes: The Molecular Mechanism of Action of Dimethyl Sulfoxide. *J. Phys. Chem. B* **2007**, *111* (35), 10453–10460.

- (285) Notman, R.; Noro, M.; O'Malley, B.; Anwar, J. Molecular Basis for Dimethylsulfoxide (DMSO) Action on Lipid Membranes. *J. Am. Chem. Soc.* **2006**, *128* (43), 13982–13983.
- (286) Hutter, J. L.; Bechhoefer, J. Calibration of Atomic-force Microscope Tips. *Rev. Sci. Instrum.* **1993**, *64* (7), 1868–1873.
- (287) Lévy, R.; Maaloum, M. Measuring the Spring Constant of Atomic Force Microscope Cantilevers: Thermal Fluctuations and Other Methods. *Nanotechnology* **2002**, *13* (1), 33–37.
- (288) Nečas, D.; Klapetek, P. Gwyddion: An Open-Source Software for SPM Data Analysis. *Open Phys.* **2012**, *10* (1), 181–188.
- (289) Hermanowicz, P.; Sarna, M.; Burda, K.; Gabryś, H. AtomicJ: An Open Source Software for Analysis of Force Curves. *Rev. Sci. Instrum.* **2014**, *85* (6), 063703.
- (290) Vold, R. L.; Waugh, J. S.; Klein, M. P.; Phelps, D. E. Measurement of Spin Relaxation in Complex Systems. *J. Chem. Phys.* **1968**, *48* (8), 3831–3832.
- (291) Attwood, S. J.; Choi, Y.; Leonenko, Z. Preparation of DOPC and DPPC Supported Planar Lipid Bilayers for Atomic Force Microscopy and Atomic Force Spectroscopy. *Int. J. Mol. Sci.* **2013**, *14* (2), 3514–3539.
- (292) Ratto, T. V.; Longo, M. L. Obstructed Diffusion in Phase-Separated Supported Lipid Bilayers: A Combined Atomic Force Microscopy and Fluorescence Recovery after Photobleaching Approach. *Biophys. J.* **2002**, *83* (6), 3380–3392.
- (293) Shahin, V.; Datta, D.; Hui, E.; Henderson, R. M.; Chapman, E. R.; Edwardson, J. M. Synaptotagmin Perturbs the Structure of Phospholipid Bilayers. *Biochemistry* **2008**, *47* (7), 2143–2152.
- (294) Milhiet, P.-E.; Gubellini, F.; Berquand, A.; Dosset, P.; Rigaud, J.-L.; Le Grimellec, C.; Lévy, D. High-Resolution AFM of Membrane Proteins Directly Incorporated at High Density in Planar Lipid Bilayer. *Biophys. J.* **2006**, *91* (9), 3268–3275.
- (295) Chafekar, S. M.; Baas, F.; Scheper, W. Oligomer-Specific A β Toxicity in Cell Models Is Mediated by Selective Uptake. *Biochim. Biophys. Acta - Mol. Basis Dis.* **2008**, *1782* (9), 523–531.
- (296) Deshpande, A. Different Conformations of Amyloid Beta Induce Neurotoxicity by Distinct Mechanisms in Human Cortical Neurons. *J. Neurosci.* **2006**, *26* (22), 6011–6018.
- (297) Dahlgren, K. N.; Manelli, A. M.; Stine, W. B.; Baker, L. K.; Krafft, G. A.; LaDu, M. J. Oligomeric and Fibrillar Species of Amyloid- β Peptides Differentially Affect Neuronal Viability. *J. Biol. Chem.* **2002**, *277* (35), 32046–32053.
- (298) Taneja, V.; Verma, M.; Vats, A. Toxic Species in Amyloid Disorders: Oligomers or Mature Fibrils. *Ann. Indian Acad. Neurol.* **2015**, *18* (2), 138.
- (299) Sakono, M.; Zako, T. Amyloid Oligomers: Formation and Toxicity of A β Oligomers. *FEBS J.*

2010, 277 (6), 1348–1358.

- (300) Chimon, S.; Shaibat, M. A.; Jones, C. R.; Calero, D. C.; Aizezi, B.; Ishii, Y. Evidence of Fibril-like β -Sheet Structures in a Neurotoxic Amyloid Intermediate of Alzheimer's β -Amyloid. *Nat. Struct. Mol. Biol.* **2007**, 14 (12), 1157–1164.
- (301) Bitan, G.; Kirkitadze, M. D.; Lomakin, A.; Vollers, S. S.; Benedek, G. B.; Teplow, D. B. Amyloid-Protein (A) Assembly: A 40 and A 42 Oligomerize through Distinct Pathways. *Proc. Natl. Acad. Sci.* **2003**, 100 (1), 330–335.
- (302) Ryan, D. A.; Narrow, W. C.; Federoff, H. J.; Bowers, W. J. An Improved Method for Generating Consistent Soluble Amyloid-Beta Oligomer Preparations for in Vitro Neurotoxicity Studies. *J. Neurosci. Methods* **2010**, 190 (2), 171–179.
- (303) Bartolini, M.; Naldi, M.; Fiori, J.; Valle, F.; Biscarini, F.; Nicolau, D. V.; Andrisano, V. Kinetic Characterization of Amyloid-Beta 1-42 Aggregation with a Multimethodological Approach. *Anal. Biochem.* **2011**, 414 (2), 215–225.
- (304) Klein, W. L. A β Toxicity in Alzheimer's Disease: Globular Oligomers (ADDLs) as New Vaccine and Drug Targets. *Neurochem. Int.* **2002**, 41 (5), 345–352.
- (305) Stine, W. B.; Dahlgren, K. N.; Krafft, G. A.; LaDu, M. J. In Vitro Characterization of Conditions for Amyloid- β Peptide Oligomerization and Fibrillogenesis. *J. Biol. Chem.* **2003**, 278 (13), 11612–11622.
- (306) Parbhu, A.; Lin, H.; Thimm, J.; Lal, R. Imaging Real-Time Aggregation of Amyloid Beta Protein (1–42) by Atomic Force Microscopy. *Peptides* **2002**, 23 (7), 1265–1270.
- (307) Roher, A. E.; Chaney, M. O.; Kuo, Y.-M.; Webster, S. D.; Stine, W. B.; Haverkamp, L. J.; Woods, A. S.; Cotter, R. J.; Tuohy, J. M.; Krafft, G. A.; et al. Morphology and Toxicity of A β -(1-42) Dimer Derived from Neuritic and Vascular Amyloid Deposits of Alzheimer's Disease. *J. Biol. Chem.* **1996**, 271 (34), 20631–20635.
- (308) Cohen, S. I. A.; Linse, S.; Luheshi, L. M.; Hellstrand, E.; White, D. A.; Rajah, L.; Otzen, D. E.; Vendruscolo, M.; Dobson, C. M.; Knowles, T. P. J. Proliferation of Amyloid-B42 Aggregates Occurs through a Secondary Nucleation Mechanism. *Proc. Natl. Acad. Sci.* **2013**, 110 (24), 9758–9763.
- (309) Tashima, Y.; Oe, R.; Lee, S.; Sugihara, G.; Chambers, E. J.; Takahashi, M.; Yamada, T. The Effect of Cholesterol and Monosialoganglioside (GM1) on the Release and Aggregation of Amyloid β -Peptide from Liposomes Prepared from Brain Membrane-like Lipids. *J. Biol. Chem.* **2004**, 279 (17), 17587–17595.
- (310) Ditaranto, K.; Tekirian, T. L.; Yang, A. J. Lysosomal Membrane Damage in Soluble A β -Mediated Cell Death in Alzheimer's Disease. *Neurobiol. Dis.* **2001**, 8 (1), 19–31.
- (311) Jin, S.; Kedia, N.; Illes-Toth, E.; Haralampiev, I.; Prisner, S.; Herrmann, A.; Wanker, E. E.; Bieschke, J. Amyloid- β (1–42) Aggregation Initiates Its Cellular Uptake and Cytotoxicity. *J. Biol. Chem.* **2016**, 291 (37), 19590–19606.

- (312) Gregori, L.; Fuchs, C.; Figueiredo-Pereira, M. E.; Van Nostrand, W. E.; Goldgaber, D. Amyloid β -Protein Inhibits Ubiquitin-Dependent Protein Degradation in Vitro. *J. Biol. Chem.* **1995**, *270* (34), 19702–19708.
- (313) Oh, S.; Hong, H. S.; Hwang, E.; Sim, H. J.; Lee, W.; Shin, S. J.; Mook-Jung, I. Amyloid Peptide Attenuates the Proteasome Activity in Neuronal Cells. *Mech. Ageing Dev.* **2005**, *126* (12), 1292–1299.
- (314) Tseng, B. P.; Green, K. N.; Chan, J. L.; Blurton-Jones, M.; LaFerla, F. M. A β Inhibits the Proteasome and Enhances Amyloid and Tau Accumulation. *Neurobiol. Aging* **2008**, *29* (11), 1607–1618.
- (315) Fu, Z.; Aucoin, D.; Ahmed, M.; Ziliox, M.; Van Nostrand, W. E.; Smith, S. O. Capping of A β 42 Oligomers by Small Molecule Inhibitors. *Biochemistry* **2014**, *53* (50), 7893–7903.
- (316) Tieleman, D. P.; Berendsen, H. J. C. A Molecular Dynamics Study of the Pores Formed by Escherichia Coli OmpF Porin in a Fully Hydrated Palmitoylcholine Bilayer. *Biophys. J.* **1998**, *74* (6), 2786–2801.
- (317) Salveson, P. J.; Spencer, R. K.; Kreutzer, A. G.; Nowick, J. S. X-Ray Crystallographic Structure of a Compact Dodecamer from a Peptide Derived from A β 16–36. *Org. Lett.* **2017**, *19* (13), 3462–3465.
- (318) Colvin, M. T.; Silvers, R.; Ni, Q. Z.; Can, T. V.; Sergeev, I.; Rosay, M.; Donovan, K. J.; Michael, B.; Wall, J.; Linse, S.; et al. Atomic Resolution Structure of Monomorphic A β 42 Amyloid Fibrils. *J. Am. Chem. Soc.* **2016**, *138* (30), 9663–9674.
- (319) Pieta, P.; Mirza, J.; Lipkowski, J. Direct Visualization of the Alamethicin Pore Formed in a Planar Phospholipid Matrix. *Proc. Natl. Acad. Sci.* **2012**, *109* (52), 21223–21227.
- (320) Su, Z.; Ho, D.; Merrill, A. R.; Lipkowski, J. In Situ Electrochemical and PM-IRRAS Studies of Colicin E1 Ion Channels in the Floating Bilayer Lipid Membrane. *Langmuir* **2019**, *35* (25), 8452–8459.
- (321) Díaz, M.; Fabelo, N.; Ferrer, I.; Marín, R. “Lipid Raft Aging” in the Human Frontal Cortex during Nonpathological Aging: Gender Influences and Potential Implications in Alzheimer’s Disease. *Neurobiol. Aging* **2018**, *67*, 42–52.
- (322) Richer, J.; Lipkowski, J. Measurement of Physical Adsorption of Neutral Organic Species at Solid Electrodes. *J. Electrochem. Soc.* **1986**, *133* (1), 121–128.
- (323) Kycia, A. H.; Wang, J.; Merrill, A. R.; Lipkowski, J. Atomic Force Microscopy Studies of a Floating-Bilayer Lipid Membrane on an Au(111) Surface Modified with a Hydrophilic Monolayer. *Langmuir* **2011**, *27* (17), 10867–10877.
- (324) Hamm, U. W.; Kramer, D.; Zhai, R. S.; Kolb, D. M. The Pzc of Au(111) and Pt(111) in a Perchloric Acid Solution: An Ex Situ Approach to the Immersion Technique. *J. Electroanal. Chem.* **1996**, *414* (1), 85–89.
- (325) Li, M.; Chen, M.; Sheepwash, E.; Brosseau, C. L.; Li, H.; Pettinger, B.; Gruler, H.; Lipkowski,

- J. AFM Studies of Solid-Supported Lipid Bilayers Formed at an Au(111) Electrode Surface Using Vesicle Fusion and a Combination of Langmuir–Blodgett and Langmuir–Schaefer Techniques. *Langmuir* **2008**, *24* (18), 10313–10323.
- (326) Uchida, T.; Osawa, M.; Lipkowski, J. SEIRAS Studies of Water Structure at the Gold Electrode Surface in the Presence of Supported Lipid Bilayer Dedicated to Professor Kingo Itaya on the Occasion of His 65th Birthday and in Recognition of His Seminal Contributions to Electrochemistry. *J. Electroanal. Chem.* **2014**, *716*, 112–119.
- (327) Abbasi, F.; Leitch, J. J.; Su, Z. F.; Szymanski, G.; Lipkowski, J. Direct Visualization of Alamethicin Ion Pores Formed in a Floating Phospholipid Membrane Supported on a Gold Electrode Surface. *Electrochim. Acta* **2018**, *267*, 195–205.
- (328) Garcia-Araez, N.; Brosseau, C. L.; Rodriguez, P.; Lipkowski, J. Layer-by-Layer PMIRRAS Characterization of DMPC Bilayers Deposited on an Au(111) Electrode Surface. *Langmuir* **2006**, *22* (25), 10365–10371.
- (329) Snyder, R. G.; Strauss, H. L.; Elliger, C. A. C-H Stretching Modes and the Structure of n-Alkyl Chains. 1. Long, Disordered Chains. *J. Phys. Chem.* **1982**, *86* (26), 5145–5150.
- (330) Kirkitadze, M. D.; Condrón, M. M.; Teplow, D. B. Identification and Characterization of Key Kinetic Intermediates in Amyloid β -Protein Fibrillogenesis. *J. Mol. Biol.* **2001**, *312* (5), 1103–1119.
- (331) Ding, F.; Borreguero, J. M.; Buldyrey, S. V.; Stanley, H. E.; Dokholyan, N. V. Mechanism for the α -Helix to β -Hairpin Transition. *Proteins Struct. Funct. Genet.* **2003**, *53* (2), 220–228.
- (332) Sarroukh, R.; Cerf, E.; Derclaye, S.; Dufrêne, Y. F.; Goormaghtigh, E.; Ruyschaert, J.-M.; Raussens, V. Transformation of Amyloid β (1–40) Oligomers into Fibrils Is Characterized by a Major Change in Secondary Structure. *Cell. Mol. Life Sci.* **2011**, *68* (8), 1429–1438.
- (333) Benseny-Cases, N.; Cócera, M.; Cladera, J. Conversion of Non-Fibrillar β -Sheet Oligomers into Amyloid Fibrils in Alzheimer's Disease Amyloid Peptide Aggregation. *Biochem. Biophys. Res. Commun.* **2007**, *361* (4), 916–921.
- (334) Bagińska, K.; Makowska, J.; Wiczak, W.; Kasprzykowski, F.; Chmurzyński, L. Conformational Studies of Alanine-Rich Peptide Using CD and FTIR Spectroscopy. *J. Pept. Sci.* **2008**, *14* (3), 283–289.
- (335) Noda, I.; Dowrey, A. E.; Marcott, C.; Story, G. M.; Ozaki, Y. Generalized Two-Dimensional Correlation Spectroscopy. *Appl. Spectrosc.* **2000**, *54* (7), 236A–248A.
- (336) Thapa, A.; Jett, S. D.; Chi, E. Y. Curcumin Attenuates Amyloid- β Aggregate Toxicity and Modulates Amyloid- β Aggregation Pathway. *ACS Chem. Neurosci.* **2016**, *7* (1), 56–68.
- (337) Lopez del Amo, J. M.; Fink, U.; Dasari, M.; Grelle, G.; Wanker, E. E.; Bieschke, J.; Reif, B. Structural Properties of EGCG-Induced, Nontoxic Alzheimer's Disease A β Oligomers. *J. Mol. Biol.* **2012**, *421* (4–5), 517–524.
- (338) Ehrnhoefer, D. E.; Bieschke, J.; Boeddrich, A.; Herbst, M.; Masino, L.; Lurz, R.; Engemann,

- S.; Pastore, A.; Wanker, E. E. EGCG Redirects Amyloidogenic Polypeptides into Unstructured, off-Pathway Oligomers. *Nat. Struct. Mol. Biol.* **2008**, *15* (6), 558–566.
- (339) Cohen, S. I. A.; Arosio, P.; Presto, J.; Kurudenkandy, F. R.; Biverstål, H.; Dolfe, L.; Dunning, C.; Yang, X.; Frohm, B.; Vendruscolo, M.; et al. A Molecular Chaperone Breaks the Catalytic Cycle That Generates Toxic A β Oligomers. *Nat. Struct. Mol. Biol.* **2015**, *22* (3), 207–213.
- (340) Scheidt, T.; Łapińska, U.; Kumita, J. R.; Whiten, D. R.; Klenerman, D.; Wilson, M. R.; Cohen, S. I. A.; Linse, S.; Vendruscolo, M.; Dobson, C. M.; et al. Secondary Nucleation and Elongation Occur at Different Sites on Alzheimer's Amyloid- β Aggregates. *Sci. Adv.* **2019**, *5* (4), eaau3112.
- (341) Limbocker, R.; Chia, S.; Ruggeri, F. S.; Perni, M.; Cascella, R.; Heller, G. T.; Meisl, G.; Mannini, B.; Habchi, J.; Michaels, T. C. T.; et al. Trodusquemine Enhances A β 42 Aggregation but Suppresses Its Toxicity by Displacing Oligomers from Cell Membranes. *Nat. Commun.* **2019**, *10* (1), 225.
- (342) Bieschke, J.; Herbst, M.; Wiglenda, T.; Friedrich, R. P.; Boeddrich, A.; Schiele, F.; Kleckers, D.; Lopez del Amo, J. M.; Grüning, B. A.; Wang, Q.; et al. Small-Molecule Conversion of Toxic Oligomers to Nontoxic β -Sheet-Rich Amyloid Fibrils. *Nat. Chem. Biol.* **2012**, *8* (1), 93–101.
- (343) Yang, J.; Dear, A. J.; Yao, Q.-Q.; Liu, Z.; Dobson, C. M.; Knowles, T. P. J.; Wu, S.; Perrett, S. Amelioration of Aggregate Cytotoxicity by Catalytic Conversion of Protein Oligomers into Amyloid Fibrils. *Nanoscale* **2020**, *12* (36), 18663–18672.
- (344) Chen, Y.; Dong, C. A β 40 Promotes Neuronal Cell Fate in Neural Progenitor Cells. *Cell Death Differ.* **2009**, *16* (3), 386–394.
- (345) Bernabeu-Zornoza, A.; Coronel, R.; Palmer, C.; Calero, M.; Martínez-Serrano, A.; Cano, E.; Zambrano, A.; Liste, I. A β 42 Peptide Promotes Proliferation and Gliogenesis in Human Neural Stem Cells. *Mol. Neurobiol.* **2019**, *56* (6), 4023–4036.
- (346) Kim, J.; Onstead, L.; Randle, S.; Price, R.; Smithson, L.; Zwizinski, C.; Dickson, D. W.; Golde, T.; McGowan, E. A 40 Inhibits Amyloid Deposition In Vivo. *J. Neurosci.* **2007**, *27* (3), 627–633.
- (347) Giuffrida, M. L.; Caraci, F.; Pignataro, B.; Cataldo, S.; De Bona, P.; Bruno, V.; Molinaro, G.; Pappalardo, G.; Messina, A.; Palmigiano, A.; et al. β -Amyloid Monomers Are Neuroprotective. *J. Neurosci.* **2009**, *29* (34), 10582–10587.
- (348) Hong, H.-S.; Maezawa, I.; Budamagunta, M.; Rana, S.; Shi, A.; Vassar, R.; Liu, R.; Lam, K. S.; Cheng, R. H.; Hua, D. H.; et al. Candidate Anti-A β Fluorene Compounds Selected from Analogs of Amyloid Imaging Agents. *Neurobiol. Aging* **2010**, *31* (10), 1690–1699.
- (349) Kusumoto, Y.; Lomakin, A.; Teplow, D. B.; Benedek, G. B. Temperature Dependence of Amyloid -Protein Fibrillization. *Proc. Natl. Acad. Sci.* **1998**, *95* (21), 12277–12282.
- (350) Kollman, P. A.; Massova, I.; Reyes, C.; Kuhn, B.; Huo, S.; Chong, L.; Lee, M.; Lee, T.; Duan,

- Y.; Wang, W.; et al. Calculating Structures and Free Energies of Complex Molecules: Combining Molecular Mechanics and Continuum Models. *Acc. Chem. Res.* **2000**, *33* (12), 889–897.
- (351) Ciudad, S.; Puig, E.; Botzanowski, T.; Meigooni, M.; Arango, A. S.; Do, J.; Mayzel, M.; Bayoumi, M.; Chaignepain, S.; Maglia, G.; et al. A β (1-42) Tetramer and Octamer Structures Reveal Edge Conductivity Pores as a Mechanism for Membrane Damage. *Nat. Commun.* **2020**, *11* (1), 3014.
- (352) Wälti, M. A.; Ravotti, F.; Arai, H.; Glabe, C. G.; Wall, J. S.; Böckmann, A.; Güntert, P.; Meier, B. H.; Riek, R. Atomic-Resolution Structure of a Disease-Relevant A β (1–42) Amyloid Fibril. *Proc. Natl. Acad. Sci.* **2016**, *113* (34), E4976–E4984.
- (353) Izadi, S.; Onufriev, A. V. Accuracy Limit of Rigid 3-Point Water Models. *J. Chem. Phys.* **2016**, *145* (7), 074501.
- (354) Zarzycki, P.; Gilbert, B. Temperature-Dependence of the Dielectric Relaxation of Water Using Non-Polarizable Water Models. *Phys. Chem. Chem. Phys.* **2020**, *22* (3), 1011–1018.
- (355) Maier, J. A.; Martinez, C.; Kasavajhala, K.; Wickstrom, L.; Hauser, K. E.; Simmerling, C. Ff14SB: Improving the Accuracy of Protein Side Chain and Backbone Parameters from Ff99SB. *J. Chem. Theory Comput.* **2015**, *11* (8), 3696–3713.
- (356) Singh, U. C.; Kollman, P. A. An Approach to Computing Electrostatic Charges for Molecules. *J. Comput. Chem.* **1984**, *5* (2), 129–145.
- (357) Wang, J.; Wolf, R. M.; Caldwell, J. W.; Kollman, P. A.; Case, D. A. Development and Testing of a General Amber Force Field. *J. Comput. Chem.* **2004**, *25* (9), 1157–1174.
- (358) Aprà, E.; Bylaska, E. J.; de Jong, W. A.; Govind, N.; Kowalski, K.; Straatsma, T. P.; Valiev, M.; van Dam, H. J. J.; Alexeev, Y.; Anchell, J.; et al. NWChem: Past, Present, and Future. *J. Chem. Phys.* **2020**, *152* (18), 184102.
- (359) Frisch, M. J.; Trucks, G. W.; Schlegel, H. B.; Scuseria, G. E.; Robb, M. a.; Cheeseman, J. R.; Scalmani, G.; Barone, V.; Petersson, G. a.; Nakatsuji, H.; et al. Gaussian 16. 2016, p Gaussian 16, Revision C.01, Gaussian, Inc., Wallin.
- (360) Case, D. A.; Cheatham, T. E.; Darden, T.; Gohlke, H.; Luo, R.; Merz, K. M.; Onufriev, A.; Simmerling, C.; Wang, B.; Woods, R. J. The Amber Biomolecular Simulation Programs. *J. Comput. Chem.* **2005**, *26* (16), 1668–1688.
- (361) Berendsen, H. J. C.; van der Spoel, D.; van Drunen, R. GROMACS: A Message-Passing Parallel Molecular Dynamics Implementation. *Comput. Phys. Commun.* **1995**, *91* (1–3), 43–56.
- (362) Su, Z.; Shodiev, M.; Leitch, J. J.; Abbasi, F.; Lipkowski, J. Role of Transmembrane Potential and Defects on the Permeabilization of Lipid Bilayers by Alamethicin, an Ion-Channel-Forming Peptide. *Langmuir* **2018**, *34* (21), 6249–6260.
- (363) Heberle, F. A.; Wu, J.; Goh, S. L.; Petruzielo, R. S.; Feigenson, G. W. Comparison of Three

- Ternary Lipid Bilayer Mixtures: FRET and ESR Reveal Nanodomains. *Biophys. J.* **2010**, *99* (10), 3309–3318.
- (364) Konyakhina, T. M.; Wu, J.; Mastroianni, J. D.; Heberle, F. A.; Feigenson, G. W. Phase Diagram of a 4-Component Lipid Mixture: DSPC/DOPC/POPC/Chol. *Biochim. Biophys. Acta - Biomembr.* **2013**, *1828* (9), 2204–2214.
- (365) Heberle, F. A.; Feigenson, G. W. Phase Separation in Lipid Membranes. *Cold Spring Harb. Perspect. Biol.* **2011**, *3* (4), 1–13.
- (366) Ackerman, D. G.; Feigenson, G. W. Lipid Bilayers: Clusters, Domains, and Phases. *Essays Biochem.* **2015**, *57*, 33–42.
- (367) Kastantin, M.; Ananthanarayanan, B.; Karmali, P.; Ruoslahti, E.; Tirrell, M. Effect of the Lipid Chain Melting Transition on the Stability of DSPE-PEG (2000) Micelles. *Langmuir* **2009**, *25* (13), 7279–7286.
- (368) Biltonen, R. L.; Lichtenberg, D. The Use of Differential Scanning Calorimetry as a Tool to Characterize Liposome Preparations. *Chem. Phys. Lipids* **1993**, *64* (1–3), 129–142.
- (369) Dear, A. J.; Michaels, T. C. T.; Meisl, G.; Klenerman, D.; Wu, S.; Perrett, S.; Linse, S.; Dobson, C. M.; Knowles, T. P. J. Kinetic Diversity of Amyloid Oligomers. *Proc. Natl. Acad. Sci.* **2020**, *117* (22), 12087–12094.
- (370) Bertini, I.; Gonnelli, L.; Luchinat, C.; Mao, J.; Nesi, A. A New Structural Model of A β 40 Fibrils. *J. Am. Chem. Soc.* **2011**, *133* (40), 16013–16022.
- (371) Tycko, R. Solid-State NMR Studies of Amyloid Fibril Structure. *Annu. Rev. Phys. Chem.* **2011**, *62* (1), 279–299.
- (372) Abelein, A.; Abrahams, J. P.; Danielsson, J.; Gräslund, A.; Jarvet, J.; Luo, J.; Tiiman, A.; Wärmländer, S. K. T. S. The Hairpin Conformation of the Amyloid β Peptide Is an Important Structural Motif along the Aggregation Pathway. *JBIC J. Biol. Inorg. Chem.* **2014**, *19* (4–5), 623–634.
- (373) Smith, J. F.; Knowles, T. P. J.; Dobson, C. M.; MacPhee, C. E.; Welland, M. E. Characterization of the Nanoscale Properties of Individual Amyloid Fibrils. *Proc. Natl. Acad. Sci.* **2006**, *103* (43), 15806–15811.
- (374) Ruggeri, F. S.; Adamcik, J.; Jeong, J. S.; Lashuel, H. A.; Mezzenga, R.; Dietler, G. Influence of the β -Sheet Content on the Mechanical Properties of Aggregates during Amyloid Fibrillization. *Angew. Chemie Int. Ed.* **2015**, *54* (8), 2462–2466.



B.526/21

Biblioteka Instytutu Chemii Fizycznej PAN

F-B.526/21



80000000342007